POLITECNICO DI TORINO

SCUOLA DI DOTTORATO
Dottorato in Ambiente e Territorio – XXI Ciclo

Tesi di Dottorato

Non-Seismic Methods on Shallow Water Environments

Corrado Calzoni

Tutore	Coordinatore del corso di dottorato
Prof. Luigi Sambuelli	Prof. Sergio Dequa

Dicembre 2008

"Imagine a world in which every single person on the planet is given free access to the sum of all human knowledge."

Jimmy Wales,
Founder of Wikipedia

Index

Brief Comments on Notation

Note: The most common usage is listed; when specified a letter or symbol may have a local meaning within a section or chapter.

B magnetic excitation;

D electric excitation (electric displacement);

E electric field strength;

f frequency;

H magnetic field strength;

J density of current;

j imaginary unit;

k relative permittivity;

p loss factor;

P polarization field;

R amplitude reflection coefficient;

R_p power reflection coefficient;

t time;

T amplitude transmission coefficient;

T_p power transmission coefficient;

V velocity;

Z impedance;

α attenuation factor;

β phase factor;

γ propagation factor;

ε electrical permittivity;

λ wavelength;

μ magnetic permeability

ρ density of charge;

σ conductivity;

χ Magnetic susceptibility;

ω angular frequency;

$\vec{S}$ Poynting vector;

$\nabla \times$ curl operator;

$\nabla \cdot$ divergence operator;

c speed of light in free space.

1. Introduction

Characterization of shallow water environments is a topic of great interest due to the huge spectrum of potential applications such as: hydrogeology, environmental protection, water supply, flood prevention, river engineering, paleolimnology, archeology… In some case it is necessary to provide information about the water body: i.e. bathymetry, water discharge, bottom sediments composition, water detection under ice cover. Other times, the request could be focused about the water proximity, i.e. the geomorphology and sedimentology of the river system.

The investigation of shallow water environments could represent a serious challenge due to the particular conditions, i.e. the water depths, the nature of the sediments involved and the intense presence of human activities. Moreover the shallow water environments are very dynamic areas. In fact, there could be rapid changes in water discharge and in sedimentary fluxes. Consequently, the possibility of exploring these kinds of environments is a fascinating task and at present days not yet exists a set of methods able to resolve this task completely. However, applied geophysic boasts different techniques adapted to retrieve useful information about the shallow water environments. Often the characterization obtained by geophysical methods does not provide enough precision to project an intervention. However, geophysics in shallow water environment could be a cost effective solution to extend the interpretation of other disciplines or punctual information obtained by traditional sampling. Other times, applied geophysics could help to individuate particular area of interest at relative low cost, where could be focused further attentions with a better level of detail.

Of course, the most common traditional geophysical techniques used in these kinds of environments are the seismic methods. In fact, these tools are largely tested and they benefits the previously experiences in the oil industry. However there are some situations in which seismic methods could fails. For example at depths of less than

about 2 m, sonar may fail to profile bathymetry because reverberation can mask, and vegetation may degenerate, acoustic bottom reflections (Arcone et al., 2006). In addition, if the bottom is turbid, as a result of currents or the activities of bottom dwelling organisms, some sonar may not be able to clearly distinguish the bottom (Mellett, 1995). In fact, the presence of gas in the sediment could prevent seismic signal penetration (Delaney et al., 1992; Powers et al., 1999; Schwamborn et al., 2002). Finally, vertical temperature gradients alter water density, influencing velocity changes in the sonar pulse, and making less accurate the depth measurement (Mellett, 1995).

Other geophysical methods could provide complementary information to the seismic methods. Nowadays in water are been applied the majority of the geophysical methods developed in terrain environments. In fact, in many cases, performing a geophysical survey on water is simpler, quicker and therefore cheaper than a similar survey on land (Tóth, 2004). However, the methods mainly adopted in shallow water are geomagnetic, electrical and electromagnetic, in both low and high frequencies. We did not focus our attention on geomagnetic method because their application is more oriented on anomalies detection, i.e. archeological problem, and therefore they find limited application on environmental studies. We did not treat directly the electrical methods because we are not equipped for this kinds of surveys in water environments. In fact, as far we prefer to avoid the presence of instrumentations on the river bottom, we would have needed floating electrodes. However, we explored the bibliography on this topic, as we would like to effort this topic in the near future. Butler (2007) reviewed this argument starting by the pioneering works on towed multi-channel resistivity and induced polarization (IP) methods carried in the 1980's: the sub-bottom mapping of gravels in the relatively shallow Beaufort Sea, reported by Scott and Maxwell (1989), and the marine IP field trials targeting ilmenite on the continental shelf of the southeastern USA, described by Wynn (1988). The capabilities to characterize and map a buried groin in a shallow marine environment by Electrical Resistivity Tomography (ERT) was evaluated also by Losito et al.(2007). Orlando and Tramonti (2007) characterized the sediments setting and lithologies of the Tiber river bottom by ERT, focus their attention on the importance of the water thickness knowledge on the inversion uncertainties, especially in presence of conductive water. Furthermore, Allen and Dahlin (2007) shown as Electrical

Conductivity (EC) imaging is a very cost effective tool for imaging saline inflow to rivers and seepage loss control from canals as well as manages aquifer recharge and recover projects.

We then focused our attention on the applications of Ground Penetrating Radar (GPR) to shallow water environments, method widely handled in this work. Of course, the significant number of publications related to this topic testifies the growing interest of the geophysical community. The pioneer works of GPR in water environments (Annan and Davis, 1977; Kovacs, 1978) were carried out in low conductive media, such as melting water in arctic areas. A high penetration depth can be achieved in such low conductive water. There are many works, in frozen environments, aimed at obtaining bathymetric maps of ice-covered lakes (Moorman et al., 2001; Schwamborn et al., 2002) and reservoirs (Arcone et al., 1992; Hunter et al., 2003; Best et al., 2005). The improvements in GPR technologies, however, now also allow good penetration in conductive water (Arcone et al., 2006).

Thanks to its flexibility and potentiality, GPR is currently a reliable tool for bridge scour assessment (Davidson et al., 1995; Olimpio, 2000; Webb et al., 2000; Park et al., 2004), stream discharge monitoring (Haeni et al., 2000; Melcher et al., 2002; Cheng et al., 2004; Costa et al., 2006); sedimentological studies of bottom deposits (Buynevich and Fitzgerald, 2003; Fuchs et al., 2004; Shields et al., 2004); bathymetric mapping (Moorman and Michel, 1997; Powers et al., 1999; Jol and Albrecht, 2004), and for finding submerged objects like lumber (Jol and Albrecht, 2004). The versatility of GPR is due to the large flexibility of the surveying setups: case histories report the use of antennas directly coupled to water from the surface (Sellmann et al., 1992; Mellett, 1995); prototypes of submerged antennas (Meyers and Smith, 1998; Tóth, 2004); non contact systems such as helicopter-mounted (Melcher et al., 2002) or rope hanging systems (Costa et al., 2000; Haeni et al., 2000; Cheng et al., 2004); antennas placed on the bottom of non metallic boats (Jol and Albrecht, 2004; Park et al., 2004; Porsani et al., 2004; Bradford et al., 2005).

The potentiality of GPR to detect the composition of a riverbed was already mentioned in early studies (Ulriksen, 1982). In his work, Ulriksen suggested a qualitative approach to the analysis of basin bottom characteristics based on the observation of the radargram sections. Several authors (Beres and Haeni, 1991; Dudley and Giffen, 1999; Powers et al., 1999) tested and verified this procedure.

However, there seems to be a lack of documentation concerning the discrimination of sediments through a quantitative analysis of amplitude, our aim was to fill up this gap. In this thesis, we helped the reader to appreciate our work providing in chapter 2 the theoretical background on GPR. Of course, the purpose of chapter 2 is not to be an exhaustive theoretical dissertation on this mature subject, but it rather supplies a collection of concepts and knowledge to understand the following chapters 3 and 4.

Considering the complexity of the phenomena involved in the discrimination of sediments by GPR, we prefer to start our experience from acquisitions performed in controlled settings. In chapter 3, we described how we reproduced the field condition of a riverine GPR survey in laboratory experimentation. We selected a 1500 MHz GPR antenna, and we studied five types of riverine bottom sediments: a loam (<0.5 mm), a fine sand (<2 mm), a coarse sand (2-5 mm), a round (3-8 mm) and a round (5-15 mm). Before starting the experimentations with the sediments, we conducted a preliminary calibration in air and an in depth calibration study in water with two different types of bottom reflectors: the high-density polyethylene of a tank and an aluminum sheet. When the calibration studies were consolidated, we developed two different approaches to interpret the GPR responses of the sediments: the velocity and the amplitude analysis. The velocity method is almost recognized in literature but it is difficulty suitable in field condition, due to the general lack of knowledge about the sediments thickness. Instead the amplitude analysis developed by us is particularly innovative and fit very well the field requirements. We tried to estimate the sediments porosities by some mixing rules by the electromagnetic properties founded with both the analysis performed. The comparison among the porosities provided by the GPR measurements and the porosities measured by direct methods confirm the accuracy of the velocity analysis and it highlights the poor reliability of the amplitude analysis.

Then, chapter 4 shows how in a riverine survey we taken advantage of the experiences reach in the laboratory experimentation. In fact, we described the integrated geophysical survey on a stretch of the river Po in order to check the GPR ability to discriminate the variability of riverbed sediments through an analysis of the bottom reflection amplitudes. We acquired continuous profiles with a 200MHz GPR system and a handheld broadband electromagnetic sensor. A conductivity meter and a TDR provided punctual measurements of the water conductivity, permittivity and

temperature. The GPR measurements provided maps of the bathymetry and of the bottom reflection amplitude, that we correlated with the results of a direct sampling campaign.

We then focused our attention on the electromagnetic techniques. Among all the geophysical methods, the electromagnetic must have the broadest range of different instrumental system of any (Reynolds, 1997). Like the GPR and on the contrary of the electrical methods, one of the main advantages of the electromagnetic methods is that the process of induction does not require direct contact with the water. In the following paragraphs, we give an overview of the main electromagnetic used in shallow water environments.

We start this brief review from the Time Domain Electromagnetic (TDEM) technique. Goldman (2004) described the results of an extensive TDEM survey covering the Sea of Galilee in order to image the distribution of saline groundwater beneath the lake. The TDEM survey suggested different salt transport mechanisms from the sediments to the central part of the lake and from regional aquifers to the margins of the lake. Analogously Barrett et al. (2005) mapped by towed TDEM the influx of saline water through sub-riverbed sediments in Australia. The interpretation of the TDEM results correlates very well regions of high-resistivity in the riverbed sediments with saline-aquifer borehole pumping locations. Considering the efficient cost, the technique is now used for routine mapping of the Murray river systems in Australia.

Concerning multi-frequency electromagnetic survey, Paine et al. (2007) evaluated salinity sources, the extent of salinization and the migration mechanisms in a shallow stream draining on the Texas Coastal Plain. They combined airborne, ground, and borehole electromagnetic induction measurements with surface-water chemical analyses. Concerning these applications, Butler et al. (2004) carried out a survey to delineate the recharge area to a river valley aquifer on the Saint Joint River (City of Fredericton, New Brunswick) using a combination of three geophysical surveys: resistivity imaging along the shoreline, seismic and electromagnetic methods carried above the water subsurface. The results of the research were successful and the geophysical interpretations were confirmed by drilling. Greenwood and Swarzenski (2006) employed the low induction approximation to develop a first order correction to the apparent conductivities provided by multi-frequency electromagnetic measures. They highlighted the potential of the method

for locating high-contrast zones and other pore water salinity anomalies in areas not accessible to conventional marine- or land-based resistivity arrays. Mansoor et al. (2006) applied the same procedure to an urban wetland, affected by point and nonpoint sources of pollution. To finish the review of low frequency electromagnetic methods, Evans (2007) reported the application of a towed electromagnetic system to map the uppermost 20 m of seafloor in a variety of settings ranging from near shore regions in water depths of approximately 10 m on the continental shelf out to water depths of 1300 m.

One of the aims of this thesis was to verify the applicability of low induction number electromagnetic multi-frequency soundings carried out from a boat in riverine surveys. In particular, our intent was to determine if this technique could be effectively used to define the typology of sediments and to obtain an estimate of the stratigraphy below a riverbed. In chapter 5 we analyzed the acquisition of the handheld broadband electromagnetic sensor of the integrated geophysical survey described previously in chapter 4. We analyzed the induction number, the depth of investigation and the sensitivity of our experimental setup by forward modeling varying the water depth, the frequency and the bottom sediment resistivity. The simulations led to an optimization of the choice of the frequencies that could be reliably used for the interpretation. We applied a bathymetric correction to the conductivity data using the water depths obtained from the GPR data. We plotted a map of the river bottom resistivity and compared this map to the results of a direct sediment sampling campaign. The resistivity values (from 120 to 240 Ωm) were compatible with the saturated gravel with pebbles in a sandy matrix that resulted from the direct sampling, and with the known geology.

2. The Ground Penetrating Radar

Aim of this chapter is to give an overview of the Ground Penetrating Radar (GPR) and to supply a set of basilar concepts and knowledge necessary to appreciate the following chapters. Then, we start to give a brief description of GPR functional principles, a short history of its development and a list of common applications.

The possibility of exploring the ground and its contents, like buried objects, is a challenge that had always fascinated scientists and engineers. Nowadays there not yet exists a single method able to resolve this task completely. However applied geophysic boasts different techniques adapted to retrieve useful information about the underground. Ground penetrating radar is one of the very few methods available to inspect objects which are hidden beneath an optically opaque surface (Daniels, 2004).

2.1. Principle of Operations

GPR is one of the radio echo sounding techniques, its principle has several
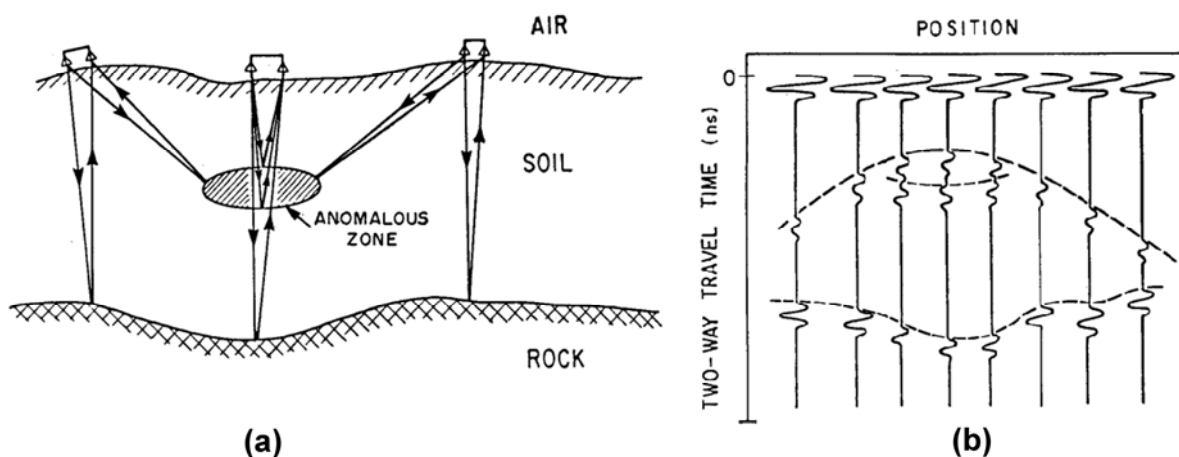

Figure 2.1: (a) Conceptual illustration of a GPR used in the reflection profiling mode. (b) Resulting radar data record obtained. (Davis and Annan, 1989)

analogies to reflection seismic and sonar techniques. Simplistically, the GPR transmitting antenna produces a short pulsed electromagnetic signal of high frequency, typically between 10MHz and 1000MHz (Davis and Annan, 1989). The electromagnetic energy is transmitted into the subsurface, changes in the under ground electromagnetic properties produces the scattering of the energy. The back scattered signal is picked up by the receiving antenna, and after an opportune amplification is stored for the following processing operation.

Figure 2.1a and Figure 2.1b give respectively a conceptual illustration of a GPR reflection profiling mode and the resulting data record. Viewed in the frequency domain the pulsed signal energy of GPR is spread over a wide spectrum (Daniels, 1996), most of the energy is concentrated around the antenna central frequency. The frequency dependent electrical properties of the ground influence the propagation of the radar signal. Then in order to obtain a profitable resolution and penetration depth is necessary to correctly design the central frequency of the survey antenna. This is one reason that pushed manufacturers to build GPR systems operable at different frequencies, simply changing the transmitting and receiving antennas.

2.2. History

The first use of electromagnetic signals to determine the presence of remote terrestrial metal objects is attributed to Hülsmeyer in 1904, but only in the 1910 Leimbach and Löwy in their patent gave a published description of a system to locate buried objects. These forerunners used continuous wave transmissions (CW). We need to wait until Hülsenbeck (1926) to see the first use of a pulsed techniques. Thanks to its unusually wide bandwidth, which offers interesting challenges, the impulse radar became soon the most widely popular system (Skolnik, 1990). Though nowadays various modulation techniques are available in the market of the GPR. The early civilian application of pulsed radar were in probing considerable depths in polar ice sheets (Steenson, 1951; Cook, 1960; Evans, 1963; Evans, 1965; Swithinbank, 1968), salt deposits (Unterberger, 1978), desert sand and rock formations (Morey, 1974; Kadaba, 1976). Different attempts were performed also on rock and coal formations (Cook, 1974; Cook, 1975; Roe and Ellerbruch, 1979), although it was clear that in these environments GPR could reach only lower penetration depths due to the higher attenuation of these materials.

Lunar programs had strongly encouraged the development of GPR, from 1970s a significant number of works were carried out to testify the potentiality of radar techniques in planet exploration (Evans, 1969; Brown, 1972; Hagfors and Campbell, 1973; Simmons et al., 1973; Porcello et al., 1974; Olhoeft and Strangway, 1975; Gary and Keihm, 1978; Peeples et al., 1978; Pettengill, 1978; Thompson, 1979; Ostro, 1993). In particular what had led to consider GPR an attractive tool is its ability to investigate the ground with remote non-contacting transducers.

Thanks to the continuing technical advances from the 1970s until present day there has been a continuous growth of GPR applications in several fields. Manufacturers have been developing purpose-built equipment for a various set of applications (Daniels, 2004). Moreover the pulsed techniques, born and developed in GPR application is beginning to be employed in other radar fields: for example impulsive or carrier-free radar developed for anti-Stealth capabilities (Kingsley and Quegan, 1992).

2.3. Applications

GPR has been used obtaining success in the following applications (Daniels, 2004): archaeological investigations, borehole inspections, bridge deck analysis, building condition assessment, contaminated land investigation, detection of buried mines (anti-personnel and anti-tank), evaluation of reinforced concrete, forensic investigations, geophysical investigations, medical imaging, pipes and cable detection, planetary exploration, rail track and bed inspection, remote sensing from aircraft and satellites, road condition survey, security applications, snow, ice and glacier, timber condition tunnel linings, wall, abandoned anti-personnel land mines and unexploded ordnance, geological strata ranging (in special case like: artic area, granite...).

2.4.   Theoretical Background: Preface

Although GPR has achieved some spectacular successes, it would be unrealistic to leave the impression that GPR is the complete solution to the users perceived problems (Daniels, 2004). The GPR could detect changes in electrical impedance in the material under investigation, within the limits of the physics of propagation. Then, in order to design a correct GPR survey and better understand its results, it is necessary to have knowledge of the physical principles that controls the electromagnetic wave propagation. This section is not an exhaustive theoretical dissertation on the physical principles behind this mature subject, but its aim is rather to supply a collection of basilar concepts and knowledge necessary to appreciate the following chapters. For the reader interested to go into this subject, the author invites to browse the plentiful literature available, for example starting from the sources listed in the reference section. The author does not attempt to make this list comprehensive, so he is sure that there are many more, excellent books with equivalent content that could have been included.

2.5.   Maxwell's Equation

In everyday life we can experiment with phenomena related to the interactions between fields and electric charge, including electromagnetism and wave propagation. Understanding the interactions between electromagnetic fields and materials allows helping the characterization of the material itself. Interactions between electrical fields and charged particles, particularly the electron, influence the material electrical properties.

We can distinguish firstly the electrical conduction, described by the electrical conductivity (σ) and related to charge motion in response to an electric field and implying energy dissipation due to conversion to heat (Reynolds, 1997). Secondly the electrical polarization, measured by the electrical permittivity (ε), arises when a force displaces a charge from some equilibrium position and thus storing energy (Santamarina, 2001). Both the electrical energy loss and storage are frequency dependent phenomena. Finally we can identify the magnetic polarization, defined by the magnetic permeability (μ) or susceptibility (χ_m), and represented by the alignment of the magnetic dipoles of the material with the applied magnetic field, and also resulting in a energy loss and storage (Balanis, 1989).

Electrical and magnetic processes are strongly coupled, for example a charged particle is surrounded by an electric field that exercises a forced on other charges, causing them to move, and moreover the electric charge movement in an electric field produces a magnetic field proportional to the charge speed. These coupling fields are so called electromagnetic (EM) field.

The electromagnetic theory is described by a set of basic laws formulated primarily through experiments conducted until the nineteenth century by many scientists like Faraday, Ampere, Gauss, Lenz, Coulomb, Volta and others. Prior to the early nineteenth century, the phenomena associated with electrostatics, magnetism and optics were largely thought to be independent (Smith, 1997). Maxwell had the intuition to combined all the previous contributions into a consistent set of vector equations (Maxwell, 1873), these widely acclaimed Maxwell's equations are: Gauss' law of electricity, Gauss' law of magnetism, Faraday's law of induction and Ampere-Maxwell' law. These fundamental equations, reported in Table 2.2, govern static charges, moving charges and time-varying electrical and magnetic fields (Santamarina, 2001).

Maxwell's equations could be enunciated both in differential and integral form. The differential form is the most widely used representation to solve boundary-value electromagnetic problems. It is used to describe and relate the field vectors, current densities (J) and charge densities (ρ) at any point in space at any time. Instead integral form describes the relation of the field vectors over an extended region of space. They have limited applications and are usually utilized only to solve electromagnetic boundary-value problems that posses complete symmetry (such as rectangular, cylindrical, spherical, etc., symmetries). The integral form can be derived from its differential form by utilizing the Stokes' and divergence theorems (Balanis, 1989).

The integrals in the equation of Table 2.2 are referred to an open surface (S) with contour (C) in the space, we defined $d\vec{l}$ an infinitesimal vector locally tangent to C. Analogously considering a volume (V) with closed surface S, we defined $d\vec{S}$ a differential surface area vector. All the other terms expressed in
are explained in Table 2.1.

Table 2.1: *Electromagnetic quantities and their units (Smith, 1997).*

Quantity	Definition	SI unit	
		In term of other units	In term of base units
$\vec{E}$	Electric field strength	V/m	$m \cdot kg \cdot s^{-3}$
$\vec{B}$	Magnetic field strength	T	$kg \cdot s^{-2} \cdot A^{-1}$
$\vec{D}$	Electric excitation (electric displacement)	C/m^2	$m^{-2} \cdot s \cdot A$
$\vec{H}$	Magnetic excitation	A/m	$m^{-1} \cdot A$
$\vec{J}$	Volume density of current	A/m^2	$m^{-2} \cdot A$
ρ	Volume density of charge	C/m^3	$m^{-3} \cdot s \cdot A$
$\vec{J_s}$	Surface density of current	A/m	$m^{-1} \cdot A$
ρ_s	Surface density of charge	C/m^2	$m^{-2} \cdot s \cdot A$
ε_0	Permittivity of free space $(8.8541 \ldots \cdot 10^{-12})$	F/m	$m^{-3} \cdot kg^{-1} \cdot s^4 \cdot A^2$
μ_0	Permeability of free space $(4 \cdot \pi \cdot 10^{-7})$	H/m	$m \cdot kg \cdot s^{-2} \cdot A^{-2}$
c	Speed of light in free space $(2.9979 \ldots \cdot 10^8)$	-	$m \cdot s^{-1}$
$\vec{S}$	Poynting vector	W/m^2	$kg \cdot s^{-3}$
$\nabla \times$	Curl operator		
$\nabla \cdot$	Divergence operator		

Table 2.2: *Maxwell's equations.*

Name	Equation	
	Integral form	Differential form
Faraday's law of induction	$\oint_c \vec{E} \cdot d\vec{l} = -\iint_s \frac{\partial \vec{B}}{\partial t} \cdot d\vec{S}$	$\nabla \times \vec{E} = -\frac{\partial \vec{B}}{\partial t}$
Ampère-Maxwell law	$\oint_c \vec{H} \cdot d\vec{l} = \iint_s \vec{J} \cdot d\vec{S} + \iint_s \frac{\partial \vec{D}}{\partial t} \cdot d\vec{S}$	$\nabla \times \vec{H} = \vec{J} + \frac{\partial \vec{D}}{\partial t}$
Gauss' electric law	$\oiint_s \vec{D} \cdot d\vec{S} = \iiint_v \rho \, dV$	$\nabla \cdot \vec{D} = \rho$
Gauss' magnetic law	$\oiint_s \vec{B} \cdot d\vec{S} = 0$	$\nabla \cdot \vec{B} = 0$

Briefly the Faraday's law of induction enunciates that the electromagnetic force or line integral of the electric field around the closed circuit C (left-hand side) is equal to the negative of the time rate of change of the magnetic flux through the surface S (right-hand side) closed on C. The negative sign reflects the empirical observation called Lenz's law, whereby the current induced by the electromagnetic force tends to counteract the change in magnetic field (Jackson, 2003).

About the Ampère-Maxwell law: in its historically original form, Ampère's Circuital law, relates the magnetic field to its source, the current density. Maxwell's correction to Ampère's law was particularly important (Maxwell, 1861). With its inclusion of the displacement current term, the laws state that a changing electric field could produce a magnetic field, and vice-versa.

The Gauss' electric law followed the Coulomb's work. Gauss showed that the divergence of the electric field is proportional to the charge density. Upon integration, Gauss' electric law states that the electric flux through a closed surface S is proportional to the charge enclosed by the surface (Casanova Alig, 2003).

The final Maxwell equation, the Gauss' magnetic law, states that the magnetic field B is a solenoidal vector field (divergence equal to zero). This law embodies the fact that, as far as it is presently known, there are no magnetic charges or magnetic charge density, then the total magnetic flux emerging from a closed surface S vanishes (Jackson, 2003). Rather than "magnetic charges", the basic entity for magnetism is the magnetic dipole.

2.6. *Constitutive Parameters and Relations*

In a material medium the electric field polarizes the medium itself, if the medium is electrically linear and isotropic this polarization P is linearly dependent on the intensity of the applied electric field E:

$$\vec{P} = \chi_e \cdot \varepsilon_0 \cdot \vec{E} \tag{2.1}$$

where χ_e is the electrical susceptibility. Thus we can define the first constitutive relation, which describes the electric displacement:

$$\vec{D} = \varepsilon_0 \cdot \vec{E} + \vec{P} = \varepsilon_0 \cdot (1 + \chi_e) \cdot \vec{E} = \varepsilon \cdot \vec{E} \tag{2.2}$$

where ε is the permittivity of the medium (Santamarina, 2001). The permittivity of a homogeneous material is usually given relative to that of free space, the relative permittivity (or dielectric constant) ε is:

$$k = \frac{\varepsilon}{\varepsilon_0} \quad [-] \tag{2.3}$$

and in geological material it is included between 1 (air) to 81 (water).

Analogously when a material medium is placed within a magnetic induction field (B), the bodies becomes magnetized. The auxiliary magnetic field (H) represents how a magnetic field (B) influences the organization of magnetic dipoles in the given medium, including dipole migration and magnetic dipole reorientation. This relation could be described like:

$$\vec{B} = \mu_0 \cdot (1 + \chi_m) \cdot \vec{H} = \mu \cdot \vec{H} \tag{2.4}$$

This is the second constitutive relation, where μ is the magnetic permeability of the medium. Also the magnetic permeability could be given relative to that of free space, the relative magnetic permeability μ_r is:

$$\mu_r = \frac{\mu}{\mu_0} \quad [-] \tag{2.5}$$

The third constitutive relation is Ohm's law. It relates the current densities J to the electric field E:

$$\vec{J} = \sigma \cdot \vec{E} \tag{2.6}$$

where σ is the electrical conductivity of the medium, expressed in $\Omega^{-1} \cdot m^{-1}$. If σ=0, the medium is a perfect dielectric (Santamarina, 2001).

Whereas equations (2.2), (2.4), (2.6) are referred to as the constitutive relations, ε, μ, σ are referred to as the constitutive parameters, which are in general functions of the applied field strength, the position within the medium, the direction of the applied field, and the frequency of operation (Balanis, 1989). Hence, the electromagnetic properties of material are frequency dependent. Furthermore, the response is partially out-of-phase with the excitation; therefore both the phase and amplitude of the response must be captured (Santamarina, 2001). This can be done by defining the complex constitutive parameters, ε* and μ*, which vary with frequency:

$$\varepsilon^* = \varepsilon' - j\varepsilon'' \tag{2.7}$$

$$\mu^* = \mu' - j\mu'' \tag{2.8}$$

Consequently we can define also the complex relative permittivity

$$k^* = \frac{\varepsilon^*}{\varepsilon_0} = k' - jk'' \tag{2.9}$$

and the complex magnetic permeability

$$\mu_r^* = \frac{\mu^*}{\mu_0} = \mu_r' - j\mu_r'' \tag{2.10}$$

2.7. *Electromagnetic Wave Equations*

The manipulation of the Maxwell's equations led to the electromagnetic wave equation that predicts the variation of electric and magnetic fields in space and time. We start modifying the Faraday's law of induction in differential form, reported in Table 2.2, using the second constitutive relation (2.4), assuming the constancy of the magnetic permeability in the time:

$$\nabla \times \vec{E} = -\mu \cdot \frac{\partial \vec{H}}{\partial t} \tag{2.11}$$

Analogously we rewrite the Ampère-Maxwell law, reported in Table 2.2, using the first constitutive relation (2.2), the third constitutive relation (2.6) and assuming the constancy of the dielectric permittivity in the time:

$$\nabla \times \vec{H} = \sigma \cdot \vec{E} + \varepsilon \cdot \frac{\partial \vec{E}}{\partial t} \tag{2.12}$$

Taking the curl operator of both sides of each of equation (2.11) and (2.12), we can write that:

$$\nabla \times \left(\nabla \times \vec{E}\right) = \nabla \times \left(-\mu \cdot \frac{\partial \vec{H}}{\partial t}\right) \qquad (2.13)$$

$$\nabla \times \left(\nabla \times \vec{H}\right) = \nabla \times \left(\vec{J} + \varepsilon \cdot \frac{\partial \vec{E}}{\partial t}\right) \qquad (2.14)$$

and assuming a homogeneous medium, we can rewrite as:

$$\nabla \times \left(\nabla \times \vec{E}\right) = -\mu \cdot \frac{\partial \left(\nabla \times \vec{H}\right)}{\partial t} \qquad (2.15)$$

$$\nabla \times \left(\nabla \times \vec{H}\right) = \nabla \times \left(\vec{J} + \varepsilon \cdot \frac{\partial \vec{E}}{\partial t}\right) \qquad (2.16)$$

We introduce the vector identity

$$\nabla \times \left(\nabla \times \vec{F}\right) = \nabla \left(\nabla \cdot \vec{F}\right) - \overrightarrow{\nabla^2 F} \qquad (2.17)$$

where $\overrightarrow{\nabla^2}$ is the Laplace operator, a second order differential operator in the n-dimensional Euclidean space defined as the divergence $(\nabla \cdot)$ of the gradient (∇F). Using the vector identity (2.17) into the left sides of equations (2.15) we can rewrite

$$\nabla \left(\nabla \cdot \vec{E}\right) - \overrightarrow{\nabla^2 E} = -\mu \cdot \frac{\partial \left(\nabla \times \vec{H}\right)}{\partial t} \qquad (2.18)$$

Substituting the first constitutive relation (2.1) in the Gauss' electric law, reported in Table 2.2, we can assert that

$$\nabla \cdot \vec{E} = \frac{\rho}{\varepsilon} \qquad (2.19)$$

that is constant in a homogeneous medium with no excess free charge, and consequently the contribution of the first member of the equation (2.18) is null. Substituting the Ampère-Maxwell law like expressed in equation (2.12) in the (2.18) and rearranging its terms, we have that

$$\overrightarrow{\nabla^2 E} = \mu \cdot \sigma \cdot \frac{\partial \vec{E}}{\partial t} + \mu \cdot \varepsilon \cdot \frac{\partial^2 \vec{E}}{\partial t^2} \qquad (2.20)$$

which is recognized as an uncoupled second-order differential equation for $\vec{E}$.

In a similar manner, by substituting the third constitutive relation (2.6) into the right side of (2.16) and using the vector identity (2.17) in the left side of (2.16), we can write it as

$$\nabla\left(\nabla\cdot\vec{H}\right) - \overrightarrow{\nabla^2 H} = \nabla\times\left(\sigma\cdot\vec{E} + \varepsilon\cdot\frac{\partial\vec{E}}{\partial t}\right) \tag{2.21}$$

and with assumption of medium homogeneity

$$\nabla\left(\nabla\cdot\vec{H}\right) - \overrightarrow{\nabla^2 H} = \sigma\cdot\left(\nabla\times\vec{E}\right) + \varepsilon\cdot\frac{\partial\left(\nabla\times\vec{E}\right)}{\partial t} \tag{2.22}$$

Substituting the second constitutive relation (2.4) in Gauss' magnetic law, reported in Table 2.2, we can assert that

$$\nabla\cdot\vec{B} = \mu\cdot\nabla\cdot\vec{H} = 0 \Rightarrow \nabla\cdot\vec{H} = 0 \tag{2.23}$$

then the contribution of the first member of the equation (2.22) is null. Substituting the Faraday's law of induction in term of H, equation (2.11), in equation (2.22) and rearranging its terms, we have that

$$\overrightarrow{\nabla^2 H} = \mu\cdot\sigma\cdot\frac{\partial\vec{H}}{\partial t} + \mu\cdot\varepsilon\cdot\frac{\partial^2\vec{H}}{\partial t^2} \tag{2.24}$$

which is recognized as an uncoupled second-order differential equation for $\vec{H}$.

Equations (2.20) and (2.24) are referred to as the vector wave equations for $\vec{E}$ and $\vec{H}$ (Balanis, 1989).

2.8. *Time Harmonic Electromagnetic Wave Propagation*

In this paragraph we deduce the wave equation for the case of a time-harmonic electromagnetic field propagating in a linear, isotropic and homogeneous medium with no excess free charge. The sinusoidal assumption is not restrictive, considering that any discrete signal can be Fourier transformed and expressed as the summation of sinusoids, within the assumption of linear time-invariant material behavior (Santamarina, 2001).

We start from the time harmonic electromagnetic fields expressed in the Euler form

$$E_{(t)} = E_0 e^{j\omega t} = E_0\left[\cos(\omega t) + j\sin(\omega t)\right] \tag{2.25}$$

$$H_{(t)} = H_0 e^{j\omega t} = H_0\left[\cos(\omega t) + j\sin(\omega t)\right] \tag{2.26}$$

where t is the time and ω is the angular frequency

$$\omega = 2 \cdot \pi \cdot f \quad \left[rad/s \right] \tag{2.27}$$

expressed in term of the frequency f.

We can rewrite equations (2.25) and (2.26) as

$$\overrightarrow{\nabla^2 E} = \mu\sigma j\omega E_0 e^{j\omega t} - \mu\varepsilon\omega^2 E_0 e^{j\omega t} = \left(j\omega\mu\sigma - \omega^2\mu\varepsilon \right) E_{(t)} = \gamma^2 E_{(t)} \tag{2.28}$$

$$\overrightarrow{\nabla^2 H} = \mu\sigma j\omega H_0 e^{j\omega t} - \mu\varepsilon\omega^2 H_0 e^{j\omega t} = \left(j\omega\mu\sigma - \omega^2\mu\varepsilon \right) \cdot H_{(t)} = \gamma^2 H_{(t)} \tag{2.29}$$

where γ is the propagation constant

$$\gamma^2 = j\omega\mu\sigma - \omega^2\mu\varepsilon \tag{2.30}$$

The term γ could be expressed also as

$$\gamma = \alpha + j\beta = \sqrt{-\omega^2\mu\varepsilon + j\omega\mu\sigma} \tag{2.31}$$

where α is the attenuation constant (Np/m) and β is the phase constant (rad/m) (Balanis, 1989).

Squaring equation (2.31) and equating real and imaginary from both sides reduces it to

$$\alpha^2 - \beta^2 = -\omega^2\mu\varepsilon \tag{2.32}$$

$$2\alpha\beta = \omega\mu\sigma \tag{2.33}$$

Solving equations (2.32) and (2.33) simultaneously, we can write α and β as

$$\alpha = \omega\sqrt{\frac{\mu\varepsilon}{2}\left[\sqrt{1+\left(\frac{\sigma}{\omega\varepsilon}\right)^2}-1\right]} \quad \left[\frac{Np}{m}\right] \tag{2.34}$$

$$\beta = \omega\sqrt{\frac{\mu\varepsilon}{2}\left[\sqrt{1+\left(\frac{\sigma}{\omega\varepsilon}\right)^2}+1\right]} \quad \left[\frac{rad}{m}\right] \tag{2.35}$$

The attenuation factor α is often expressed in decibels per meter (dB/m), the conversion between the two systems is

$$\left| \alpha\left(Np/m\right) \right| = \frac{1}{8.68}\left| \alpha\left(dB/m\right) \right| \tag{2.36}$$

We can now express the solutions of equations (2.28) and (2.29) function of the attenuation and phase factors,

$$E_{(z,t)} = E_0 e^{-\alpha z} e^{j(\omega t - \beta z)} \tag{2.37}$$

$$H_{(z,t)} = H_0 e^{-\alpha z} e^{j(\omega t - \beta z)} \tag{2.38}$$

These represents waves, polarized in the XY plane, that travels in the z direction as determined by the propagation term $e^{j(\omega t - \beta z)}$, and it decay in the same direction according to the attenuation term $e^{-\alpha z}$ (Ulriksen, 1982).

Several references highlight to the term

$$p = \frac{\sigma}{\omega \varepsilon} \quad [-] \tag{2.39}$$

of equations (2.34) and (2.35), like the loss factor p (Reynolds, 1997). Media whose the loss factor p is much less than unity are referred to as good dielectrics and those whose p is much greater than unity are referred to as good conductors (Paris and Hurd, 1969).

2.9. *Far Field Condition*

In order to treat with simplified theory and formulation, it is common to deal with GPR assuming wave propagation in the far field condition.

The far field (or far zone) is defined in several different ways, but generally could be considered the distance at which the field generated by the antenna could be approximated as a plane wave. Actually the field radiates by antennas of finite dimensions are spherical waves (Balanis, 1989).

Moreover for a localized target in the ground, besides the reflected and refraction signals, explained in the following chapters, there can be several other possible paths that energy can travel from a transmitter to the receiver: the direct signal in the air and the direct signal in the ground (Annan, 2001).

The distance at which the transition from near field to far field occurs is dependent on the wavelength, the geometry and size of the antenna, and the electromagnetic properties of the ground. Balanis (1996) suggests that the far field region for a radiator is defined as the region whose smallest radial distance is

$$R_{ff} = \frac{2D^2}{\lambda} \ [m]$$
(2.40)

where D is the largest dimension of the radiator and λ is the wavelength of the signal. However the application of this formula in GPR application needs particular attention considering that antenna usually emitted a broadband signal and consequently the wavelength of the signal is not univocally determined.

2.10. Velocity

The velocity of the electromagnetic waves propagate with phase velocity V

$$V = \frac{\omega}{\beta} = \frac{1}{\sqrt{\frac{\mu\varepsilon}{2}\left[\sqrt{1+\left(\frac{\sigma}{\omega\varepsilon}\right)^2}+1\right]}} \quad \left[\frac{m}{s}\right]$$ (2.41)

described by the speed of light in the material. In a material the speed of light is always slower than the speed of light in vacuum (c=2.9979…·10^8 m/s). The angular frequency ω remains in the equation (2.41), therefore the wave velocity is frequency dependent (Santamarina, 2001). This aspect is particular evident in dispersive material, where the electromagnetic properties vary strongly with frequency (Xiong and Tripp, 1997). For instance, the high permittivity of water, which is due to the orientational polarization of water molecules, is not sustained at high frequency when the field reverses faster than the water molecules can rotate (Powers, 2004). On the contrary at low frequencies other processes, such as interfacial polarization of ions drifting against barriers, take longer to accomplish and then create variations in relative permittivity (Powers, 1997).

Simplified relations of the phase velocity can be readily obtained for the case of low-loss material, where the loss factor p is negligible. Equation (2.41) became

$$V = \frac{1}{\sqrt{\mu \cdot \varepsilon}}$$ (2.42)

We can verify equation (2.42) if we substitute the magnetic permeability μ_0 and the dielectric permittivity ε_0 of the free space, in fact we obtained the well know value of the velocity in the free space c reported in Table 2.2. From equation (2.42) we can express the velocity of electromagnetic waves in non ferromagnetic ($\mu \approx \mu_0$) and low-loss medium ($p \approx 0$) in term of the material relative permittivity k:

$$V = \frac{c}{\sqrt{k}}$$ (2.43)

The wavelength λ, the spatial distance traversed by one period (or cycle) of the propagating electromagnetic wave, is related to the velocity by

$$\lambda = \frac{2 \cdot \pi}{\beta} = \frac{V}{f} \quad [m]$$ (2.44)

Table 2.3: *Review of the electromagnetic properties of the most common geological material.*

Material	Dieletric costant			DC electrical conductivity	Tipical Velocity
	Davis & Annan (1989)	*Daniels (1996)*	*Ulriksen (1982)*	*Ulriksen (1982)*	*Moorman et al. (2001)*
	ε_r	ε_r	ε_r	σ [mS/m]	V [m/ns]
Air	1	1	1	0	0.3
Distilled	80				0.033
Fresh water	80	81	81	10^{-4} to $3*10^{-2}$	0.033
Sea water	80		81	4	0.01
Fresh water	3-4	4	4	10^{-3}	
Sea water ice		4-8	4-8	10^{-2} to 10^{-1}	
Snow		8-12	1.4	10^{-6} to 10^{-5}	
Permafrost		4-8	4-8	10^{-5} to 10^{-2}	
Sand, dry	3-5	4-6	4-6	10^{-7} to 10^{-3}	
Sand,	20-30	10-30	30	10^{-4} to 10^{-2}	0.06
Sandstone,		2-3			
Sandstone,		5-10	6	$4*10^{-2}$	
Limestone	4-8				0.12
Limestone,		7	7	10^{-9}	
Limestone		8	8	$2.5*10^{-2}$	
Shales	5-15				0.09
Shale, wet		6-9	7	10^{-1}	
Silt, saturated	10		10	10^{-3} to 10^{-2}	0.09
Clays	5-40				0.06
Clay, dry		2-6			
Clay,		15-40	8-12	10^{-1} to 1	0.09
Soil, sandy		4-6	2.6	$1.4*10^{-4}$	
Soil, sandy		15-30	25	$6.9*10^{-3}$	
Soil, loamy		4-6	2.5	$1.1*10^{-4}$	
Soil, loamy		10-20	19	$2.1*10^{-2}$	
Soil, clayey		4-6	2.4	$2.7*10^{-4}$	
Soil, clayey		10-15	15	$5.0*10^{-2}$	
Coal, dry		3.5			
Coal, wet		8			
Granite	4-6				0.13
Granite, dry		5	5	10^{-8}	
Granite, wet		7	7	10^{-3}	
Salt, dry	5-6	4-7			
Basalt, wet			8	10^{-2}	
Alluminium			1	10^{7}	

2.11. Impedance

The electromagnetic impedance of a medium Z is the relation between the electric field E and the magnetic field H:

$$Z = \frac{\vec{E}}{\vec{H}} = \sqrt{\frac{j\omega\mu}{\sigma + j\omega\mu}} \quad [\Omega] \tag{2.45}$$

Note that Z is a complex number, therefore the variations of E and H are in general out-of-phase (Santamarina, 2001). The magnitude $|Z|$ and the phase shift θ are calculated like (Ulriksen, 1982)

$$|Z| = \frac{\sqrt{\frac{\mu}{\varepsilon}}}{\sqrt[4]{1 + \left(\frac{\sigma}{\omega\varepsilon}\right)^2}} \quad [\Omega] \tag{2.46}$$

$$\theta = \frac{1}{2}\tan^{-1}\left(\frac{\sigma}{\omega\varepsilon}\right) \quad [rad] \tag{2.47}$$

2.12. Reflection and Transmission

When electromagnetic waves travel in materials could encounter boundaries, scatters and other objects. We can take into account the effects of an interface introducing reflection and transmission coefficients. These coefficients are in general complex quantities and they are functions of the constitutive parameters of the two media, the angle of incidence of the wave, and the wave polarization (Balanis, 1989).

2.12.1. Normal Incidence

This condition is very common dealing with ground penetrating radar, considering in a lot of applications the transmitter and receiver dipoles are placed in the same antenna case, the dipole distance is negligible respect the investigated object depth (near-zero offset condition).

Consider two media with finite conductivities and a plane electromagnetic wave approaching the interface with normal incidence. At the interface, part of the incident energy is transmitted on the second medium and part of it is scattered back in the first medium (Santamarina, 2001). The resulting fields are

$$E_i^{\langle 1 \rangle} + E_r^{\langle 1 \rangle} = E_t^{\langle 2 \rangle} \tag{2.48}$$

$$H_i^{\langle 1 \rangle} + H_r^{\langle 1 \rangle} = H_t^{\langle 2 \rangle} \tag{2.49}$$

where the index 'i', 'r', 't' refer respectively to incident, reflected and transmitted, while the apexes <1> and <2> refer to the media.

The terms of equations (2.48) and (2.49) could be expressed function of the electromagnetic impedance Z, we obtain:

$$E_r = R \cdot E_i \tag{2.50}$$

$$E_t = T \cdot E_i \tag{2.51}$$

where R is the reflection coefficient

$$R = \frac{Z_2 - Z_1}{Z_1 + Z_2} \quad [-] \tag{2.52}$$

and T is the transmission coefficient

$$T = \frac{2Z_2}{Z_1 + Z_2} \quad [-] \tag{2.53}$$

We can found a simplified formulations for low loss media (p<<1) of the reflection coefficient R function of the relative permittivity of the two media (Gloaguen et al., 2001)

$$R = \frac{\sqrt{k_1} - \sqrt{k_2}}{\sqrt{k_2} + \sqrt{k_1}} \quad [-] \tag{2.54}$$

In term of power we introduce the power reflectivity R_p, or power reflection coefficient, that identify the amount of energy reflected from an electromagnetic interface (Telford et al., 1990)

$$R_p = \frac{P_r}{P_i} = \left| \frac{E_r}{E_i} \right|^2 = \left(\frac{Z_2 - Z_1}{Z_1 + Z_2} \right)^2 = R^2 \quad [-] \tag{2.55}$$

Analogously the power transmittivity T_p, or power transmission coefficient is

$$T_p = \frac{4Z_1 Z_2}{\left(Z_1 + Z_2 \right)^2} = T^2 \frac{Z_1}{Z_2} \quad [-] \tag{2.56}$$

2.12.2. Oblique Incidence

To examine reflections and transmissions at oblique angles of incidence for a general wave polarization, it is most convenient to decompose the electric field into its perpendicular and parallel components (relative to the plane of incidence) and

analyze each one of them individually. The total reflected and transmitted field will be the vector sum from each one of these two polarizations (Balanis, 1989).

We define the plane of incidence as the plane formed by a unit vector normal to the reflecting interface and the vector in the direction of incidence. We referred to perpendicular polarization $E_\perp$ (or horizontal or E polarization) when the electric filed is perpendicular to the plane of incidence. Adopting the conventions previously defined for the index 'i', 'r', 't' and the apexes $<1>$ and $<2>$, the reflection and transmission coefficient for the perpendicular polarization could be expressed like

$$R_\perp = \frac{E_\perp^r}{E_\perp^i} = \frac{\sqrt{\dfrac{\mu_2}{\varepsilon_2}}\cos\theta_i - \sqrt{\dfrac{\mu_1}{\varepsilon_1}}\cos\theta_t}{\sqrt{\dfrac{\mu_2}{\varepsilon_2}}\cos\theta_i + \sqrt{\dfrac{\mu_1}{\varepsilon_1}}\cos\theta_t} \quad [-] \tag{2.57}$$

$$T_\perp = \frac{E_\perp^t}{E_\perp^i} = \frac{2\sqrt{\dfrac{\mu_2}{\varepsilon_2}}\cos\theta_i}{\sqrt{\dfrac{\mu_2}{\varepsilon_2}}\cos\theta_i + \sqrt{\dfrac{\mu_1}{\varepsilon_1}}\cos\theta_t} \quad [-] \tag{2.58}$$

Analogously we refers to parallel polarization $E_\parallel$ (or vertical or H polarization) when the electric field is parallel to the plane of incidence. The reflection and transmission coefficient for the parallel polarization according to Balanis (1989) are

$$R_\parallel = \frac{E_\parallel^r}{E_\parallel^i} = \frac{-\sqrt{\dfrac{\mu_1}{\varepsilon_1}}\cos\theta_i + \sqrt{\dfrac{\mu_2}{\varepsilon_2}}\cos\theta_t}{\sqrt{\dfrac{\mu_1}{\varepsilon_1}}\cos\theta_i + \sqrt{\dfrac{\mu_2}{\varepsilon_2}}\cos\theta_t} \quad [-] \tag{2.59}$$

$$T_\parallel = \frac{E_\parallel^t}{E_\parallel^i} = \frac{2\sqrt{\dfrac{\mu_2}{\varepsilon_2}}\cos\theta_i}{\sqrt{\dfrac{\mu_1}{\varepsilon_1}}\cos\theta_i + \sqrt{\dfrac{\mu_2}{\varepsilon_2}}\cos\theta_t} \quad [-] \tag{2.60}$$

Using the Snell's law of reflection

$$\theta_r = \theta_i \quad [rad] \tag{2.61}$$

and the Snell's law of refraction

$$\beta_1 \sin\theta_i = \beta_2 \sin\theta_t \tag{2.62}$$

it is possible to demonstrate that, if the magnetic permeability of the two medium is almost the same of free space, there exists no real incidence angle that will reduce

the reflection coefficient for perpendicular polarization to zero. Instead the incidence angle θ_i which reduces the reflection coefficient for parallel polarization to zero, is referred to as the Brewster angle θ_B

$$\theta_B = \sin^{-1}\left(\sqrt{\frac{\varepsilon_2}{\varepsilon_1 + \varepsilon_2}}\right) \; [rad] \tag{2.63}$$

then in this condition there is the total transmission.

The opposite situation is the total reflection condition, that occur when the incidence angle is higher than the critical angle θ_c

$$\theta_c = \sin^{-1}\left(\sqrt{\frac{\varepsilon_2}{\varepsilon_1}}\right) \; [rad] \tag{2.64}$$

For two media with identical magnetic permeabilities the critical angle exists only if the wave propagates from a medium with higher permittivity to a medium with lower permittivity ($\varepsilon_2 < \varepsilon_1$).

2.12.3.   Reflection and Transmission in a Thin Layer

In thin-layered media (thin compared to a wavelength), the classical Fresnel reflection coefficient requires modification because the response amplitude is proportional to the layer thickness (Annan et al., 1988).

The normal incidence amplitude reflection coefficient R_{thin} for a plane layer of thickness t_h with a relative permittivity k_2, embedded in a medium with relative permittivity k_1, is given by

$$R_{thin} = \frac{R\left(1 - e^{jB}\right)}{1 - R^2 e^{jB}} \; [-] \tag{2.65}$$

where R is the Fresnel normal-incidence amplitude reflection coefficient for a plane wave incident from a half space with relative permittivity k_1, onto a half space with relative permittivity k_2, calculated according equation (2.52). B is the phase shift that the wave suffers traveling a two-way path through the layer and is expressed as

$$B = \frac{4\pi t_h}{\lambda_2} \; [-] \tag{2.66}$$

where λ_2 is the wavelength in the layer.

2.13. Energy Loss and Attenuation

There are many factors that influence the signal strength as radio waves propagate through sub-surface: intrinsic attenuation, geometrical spreading, scattering, dispersion, multipathing and so on. In the next sections we summarize the principal causes of loss encountered dealing with ground penetrating radar.

2.13.1. Intrinsic Attenuation

Attenuation is one of the most important causes of energy loss. This energy loss occurs as a transformation from electromagnetic energy to thermal energy, the resultant losses are exhibited as temperature rise in the material for the ohmic dissipation (Annan, 2001). This conversion is due to the movement of charge or particles under the effect of the electric field, the same phenomena that occur during the microwave cooking.

Attenuation is a complex function of the dielectric and electrical properties of the media through which the radar signal is travelling. In particular real and imaginary parts of the complex magnetic permeability and complex dielectric permittivity describe the storage (real part) and loss or transformation (imaginary part) of energy.

The attenuation phenomena is defined by the attenuation factor α defined in equation (2.34), this term is dependent upon the electric, magnetic and dielectric properties of the media through which the signal is propagating. Moreover, considering the pulse frequency ω remains in the attenuation constant, the attenuation is a frequency dependent phenomenon.

The depth at which the field strength of a plane wave decays to *1/e* is called the skin depth δ and could be derived from equations (2.37) and (2.38):

$$\delta = \frac{1}{\alpha} = \frac{1}{\omega \sqrt{\frac{\mu \varepsilon}{2} \left[\sqrt{1 + \left(\frac{\sigma}{\omega \varepsilon} \right)^2} - 1 \right]}} \quad [m] \tag{2.67}$$

Considering only the intrinsic attenuation, we can related the amplitude *A,* at a given distance *r* from the source, to the amplitude of the source A_0 by the relation (Cook, 1975)

$$A = A_0 \cdot e^{-\alpha \cdot r} \tag{2.68}$$

2.13.2. Geometrical Spreading

We assumed the electromagnetic field radiates by antennas of finite dimensions are spherical waves (Balanis, 1989). Analogously what happens in seismology, getting out from the source there is a progressive diminution in amplitude due to geometrical spreading. Contrarily what happens with the intrinsic losses, the energy is still electromagnetic and it is not transformed to other form, but it is following a path that is no longer detectable from the receiver.

In order to appreciate the geometrical attenuation, we can image the total energy emitted from the source E spread out over the surface of a spherical shell, with a radius r that increases with the distance from the source. Actually the emission lobe of a GPR antenna is more similar to a cone with the base idealizable to a spherical cap. We define the energy density E_d like the energy per unit area

$$E_d = \frac{E}{4\pi r^2} \quad \left[\frac{J}{m^2} \right]$$

(2.69)

The energy density diminishes in proportion to $1/r^2$, consequently the amplitude, which is proportional to the square root of the energy density, varies in proportion to $1/r$ (Reynolds, 1997).

2.13.3. Scattering

When the electromagnetic waves travels in medium and encounter a change in electrical or magnetic material properties its energy is scattered. The functional principle of ground penetrating radar is based on the detection of scattering; without it, there would be nothing for the radar to measure.

We defined previously the energy scattered by reflection when the electromagnetic waves encounter a planar interface. In this section we want to highlight also the scattering by object due to diffraction phenomena. Considering the randomly direction of this energy, it is difficultly measureable by the antenna receiver, then for our scope it could be considerable a loss. We define clutter those signals that are unrelated to the target scattering characteristics but occur in the same sample time window and have similar spectral characteristics to the target wavelet (Daniels, 2004).

We consider a monostatic GPR antenna (transmitter and receiver are the same antenna) illuminating a target: the target intercepts a portion of the incident energy

irradiated by the antenna and re-radiates it. The measure of the incident power intercepted by the target and radiated back toward the receiver is called the radar cross section (RCS) (Kingsley and Quegan, 1992). In other worlds the RCS is a measure of the target apparent area as perceived by the radar.

The RCS of a target is partly dependent on the signal wavelength investing it. For target sizes remarkably bigger than the wavelength, the RCS is roughly the same size as the real area of the target; we identify this condition as the optical region because we can deal the electromagnetic propagation with the optics theory. For target size comparable with the wavelength, the RCS, and consequently the backscattered energy, varies wildly with changes in wavelength; this condition is known as the resonance or Mie region. Finally for target sizes relevantly smaller than the wavelength, the RCS is roughly proportional to λ^{-4}; we indentify this condition as the Rayleigh region (Kingsley and Quegan, 1992). The Rayleigh scattering allows us to consider the heterogeneous material as being homogeneous.

When dealing with scattering problems, it is usual to define a size factor (x) that for a give sphere target with radius *r* is (Skolnik, 1990)

$$x = \frac{2 \cdot \pi \cdot r}{\lambda}$$
(2.70)

The log-log plot of Figure 2.2 shows the variation of the RCS of a sphere as a function of the wavelength. The graph reveals the rapid RCS rise in the Rayleigh region (0<x<1), the RCS floating variation in the Mie region (1<x<10) and finally the optical region (x>10) where the RCS approaches the optical cross section (Skolnik, 1981).
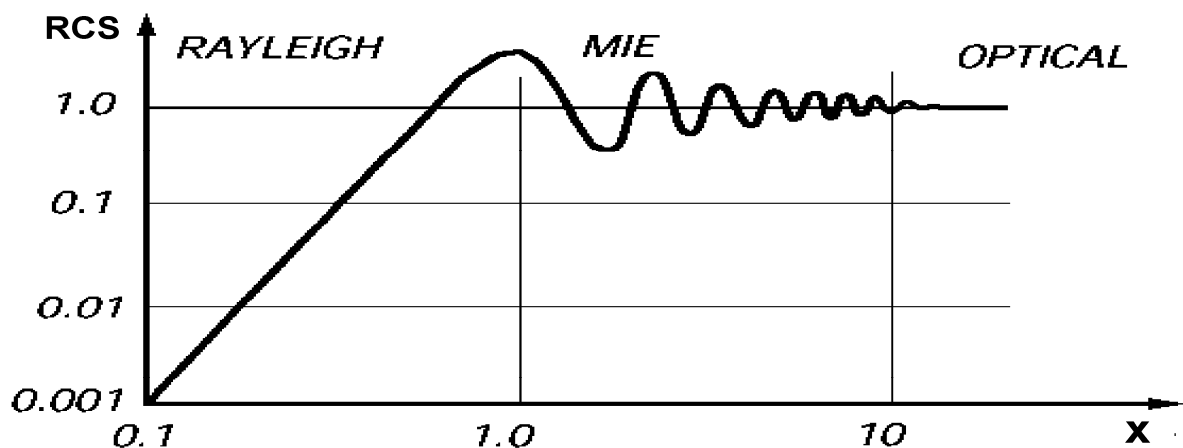
Figure 2.2: *Radar Cross Section of a perfectly conducting sphere as a function of its size factor (Skolnik, 1990).*

2.14. Radar Equation

Perhaps the single most useful description of the factors influencing radar performance is the radar equation which gives the range of a radar in terms of the radar characteristics (Skolnik, 1990).

Radar equation describes how electromagnetic waves irradiated by the transmitter antenna, and propagated in the material, are measured by the antenna receiver.

Ps: Source power

$P_{Rx} = \eta_{Rx} \cdot P_7$: Power to the receiver electronics

η_{Tx}: Transmitter efficiency

η_{Rx}: Receiver efficiency

$P_1 = \eta_{Tx} \cdot P_s$: radiated power

$P_8 = G_{Rx} \cdot P_7$: power at the receiver

G_{Tx}: transmitter gain

G_{RX}: receiver gain

$P_2 = G_{Tx} \cdot P_1$: power radiated in target direction

$P_7 = \eta_{CRx} \cdot P_6$: power directed to the receiver

η_{CTx}: transmitter-ground coupling efficiency

η_{CRx}: ground-receiver coupling efficiency

$P_3 = \eta_{CTx} \cdot P_2$: power entering in the ground

$P_6 = e^{-\alpha z}/(4\pi z^2) \cdot P_5$: power reaching the ground surface

$e^{-\alpha z}$: intrinsic losses

$e^{-\alpha z}$: intrinsic losses

$1/(4\pi z^2)$: geometrical spreading

$1/(4\pi z^2)$: geometrical spreading

$P_4 = e^{-\alpha z}/(4\pi z^2) \cdot P_3$: power reaching the target

$P5 = RCS \cdot P4$: power scattered by the target in the receiver **d**irection

RCS: Radar Cross Section

Figure 2.3: *Block diagram illustrating the factor influencing the radar equation.*

Radar equation thus takes in account: transmitter antenna properties (gain, pattern, frequency dependence), antenna-ground coupling losses (efficiency, frequency dependence), geometric spreading losses, materials intrinsic attenuation, scattering, and receiving antenna properties. In Figure 2.3 we schematized the factors influencing the radar equation. Some parameters are to some extent under the control of the radar designer (i.e. antenna gain and efficiency), instead other factors are characteristics of the survey conditions (i.e. intrinsic attenuation, spreading losses and RCS).

The radar equations highlights that if we want reach long ranges, the transmitted power must be large, the radiated energy must be concentrated into a narrow beam (high transmitter gain), the received echo energy must be collected with a large antenna aperture (also synonymous with high gain), and the receiver must be sensitive to weak signals (Skolnik, 1981).

In practice, however, the simple radar equation does not predict the range performance of actual radar equipments to a satisfactory degree of accuracy. The discrepancy is due to several factors like the difficulty to include and quantify all type of losses. For example in conventional free-space radar the target is in the far field of the antenna and spreading loss is proportional to the inverse fourth power of distance, instead in many situations relating to ground penetrating radar the target is in near field condition and the relationship is no longer valid (Daniels, 2004). Moreover usually radar performances are experienced in laboratory test and not in the field. Finally several parameters like RCS have a statistical or unpredictable nature (Skolnik, 1981).

2.15. Resolution

The resolution tells how far apart two targets have to be before we can see that there are indeed two targets rather a large one (Kingsley and Quegan, 1992). Dealing with GPR it is common define both the vertical (or depth, or longitudinal) and horizontal (or plan, or lateral) resolution.

2.15.1. Depth Resolution

The depth resolution is a measure of the ability to differentiate between two signals adjacent to each other in time. For example if two interfaces are separated a

measure less than the depth resolution, the tail of the first reflection signal could be mask the second reflection.

Simplistically, vertical resolution is a function of frequency (Reynolds, 1997). The maximum vertical resolution is usually considered to be one-quarter of the predominant wavelength (Martinez and Byrnes, 2001). Considering a material characterized by velocity V and using equation (2.44), we can evaluate the depth resolution like

$$\lambda_{1/4} = \frac{V}{4f} \quad [m]$$

(2.71)

We need to take care that this value is the best that could be achieved theoretically. In reality, the resolution is usually less considering the complex nature of the source waveform and the ground responses (Reynolds, 1997). In fact the earth acts as a low pass filter, then in order to define the depth resolution it is important to consider the bandwidth of the received signal rather the bandwidth of the transmitted signal (Daniels et al., 1988).

2.15.2. Plan Resolution

The plan resolution of a ground penetrating radar system is important when localized targets are sought and when there is a need to distinguish between more than one at the same depth (Daniels, 2004).

The plan resolution is influenced by the area of the region illuminated by the antenna, this area is usually referred to be the Fresnel zone or antenna footprint. Considering a bistatic dipole antennas, the antenna footprint at depth z could be approximated with an ellipse which major semi axes is

$$r_h = \sqrt{\frac{\lambda^2}{16} + \frac{\lambda z}{2}} \quad [m]$$

(2.72)

and the minor semi axis is half of the major semi axes (Reynolds, 1997).

3. Laboratory experiments on the possibility to discriminate sediments by GPR

3.1. Abstract

We performed some GPR experimentations in controlled laboratory conditions with sediments and water. We investigated the correlations between the particulate media properties, like grain sizes distributions or porosities, and the GPR responses. We started from laboratory experimentations in order to work in a well known environment, where it could be easily to mitigate noises and disturbs on the radar measurements. With this research, we aimed to prepare the following integrated geophysical survey in riverine environment.

We performed an in-depth calibration work in water with different types of reflectors, before going into the sediment experimentations. Besides to prepare a processing model to treat the GPR acquisitions in water, the mainly goals of the calibration tests were the estimations of the electromagnetic pulse velocity in water ($V_W=0.0327\pm0.001$ m·ns^{-1}), the water attenuation term in time domain ($\alpha=2.68\pm0.01$ m^{-1}) and the spectra in frequency domain of the water attenuation term. From the GPR measurements in water with the sediments, we developed two different approaches: the velocity and the amplitude analysis, which take in account the two-way-travel-times and the amplitude respectively. We investigated by these two methods five different types of riverine sediments. For each of this particulate media the two analyses provided an estimation of the bulk sediments permittivities and the water-sediments reflection coefficients. The correlation by some mixing rules of the sediments porosities with the electromagnetic properties, founded by the two approaches, highlighted the reliability of the velocity analysis and the high uncertainties of the amplitude analysis.

3.2.   Introduction

The GPR applied in shallow water environments is a flexible and powerful tool, which could provide complementary information to other geophysical techniques and disciplines. Starting from the early works documented by Annan and Davis (1977) and Kovacs (1978), it is now available a plentiful literature of GPR applications in water. For the reader interested to go into this subject, the author invites to browse the interesting and important bibliography proposed in the Introduction section of chapter 4.

In particular, we were interested to testify the potentiality of GPR to detect the composition of a riverbed. This topic was already explored in the early studies by Ulriksen (1982) with a qualitative approach. In his work, Ulriksen suggested that fine sediments could be identified from strong and smooth reflectors, and moraine from speckled and weak signals, while boulders may produce hyperbolic diffractions. This method has positively been adopted and tested by others (Beres and Haeni, 1991; Dudley and Giffen, 1999; Powers et al., 1999). However, we believed there is a lack of documentation concerning the discrimination of sediments through a quantitative analysis of amplitude.

At the begin of our experiences, the idea of a quantitative analysis of the sediments bottom reflections amplitudes was born by the observation of the high constancy of the main bang (the first reflection event in a radargram acquired with a near zero offset bistatic antenna) obtained from the water surface. If the main bang signal remains constant among different tests, we can consider as constant the amount of energy entering the water, and consequently compare the amplitude of the bottom signal reflections among different reflectors. The main bang repeatability is particularly true for GPR measurements in water thanks to the constant coupling between antenna and water. Contrarily in terrain GPR measurements it is difficult maintain a constant electromagnetic coupling between the antenna and the ground because of the surface heterogeneities.

Considering the complexity of the phenomena involved, we preferred to start our experience from GPR acquisitions performed in controlled settings. Then, we tried to reproduce the field condition of a GPR survey in laboratory experimentations. In this way, we could maintain constant among the tests the electromagnetic properties of

the water and we could choose the grain sizes distributions of the sediments. We adopted for our experiments a tank able to contain a 15 cm sediments thick layer on the tank bottom and a 30 cm water depth. According to the specifications explained in Experimental Design section we selected a 1500 MHz GPR antenna, and we studied five types of riverine bottom sediments: a loam (<0.5 mm), a fine sand (<2 mm), a coarse sand (2-5 mm), a round (3-8 mm) and a round (5-15 mm).

Before starting the experimentations with the sediments, we conducted a preliminary calibration in air and an in depth calibration study in water. In the calibration work in water, we studied two different types of bottom reflectors: the high-density polyethylene of the tank and an aluminum sheet. Thanks to the calibration measurements, we evaluated the velocity of the electromagnetic pulse in water and the water attenuation term in time domain, both physical parameters necessary to the following analysis on the sediments. Moreover the aluminum reflector allowed us to find an indirect estimation of the amount of energy emitted by the antenna transmitter and entered in the water. Other interesting results are showed in the calibration part. We performed a time-frequency analysis of the GPR traces acquired and we evaluated the amplitude spectra of the bottom reflection signals in frequency domain. Thanks to these amplitude spectra, we estimated the spectrum of the water attenuation term in frequency domain.

When the calibration studies were consolidated, we developed two different approaches to interpret the GPR responses of the sediments: the velocity and the amplitude analysis. The velocity method is almost recognized in literature but it is difficulty suitable in field condition, due to the general lack of knowledge about the sediments thickness. Instead the amplitude analysis developed by us is particularly innovative and fit very well the field requirements. Then, we were curious to test its reliability. By both the approaches, we evaluated the sediments bulk permittivities and the water-reflection coefficients. Finally, we tried to estimate the sediments porosities by some mixing rules and the electromagnetic properties founded with both the analysis performed. The comparison among the porosities provided by the GPR measurements and the porosities measured by direct methods confirm the accuracy of the velocity analysis and it highlights the poor reliability of the amplitude analysis.

3.3. Experimental Design

As far we have provided the theoretical background to effort and understand a GPR survey. We are now ready to explain and justify the experimental design of the GPR laboratory experimentations, which provided useful elements to prepare the following GPR survey on the field.

In order to reproduce in a laboratory the field condition of a shallow water environment we need to take in account the geometrical scaling properties. In field condition we expect to investigate bathymetric depth on a metric scale, roughly from 0 to 5 m. On the contrary, the logistic conditions of a laboratory test impose water depths lower than 0.5 m. We need to verify and possibly quantify the influences of the geometrical scaling on the physical properties measured by GPR. The geometrical scaling could be performed focusing the attention on three main aspects: the water depth, the signal wavelength in water and finally the granulometric dimension distribution of the bottom sediments. In our case a 10 times downscale of the water depth corresponds to an upscale of 10 times of the signal frequency and a 10 times downscale of the grain size distribution.

We choose the antenna frequency considering two contrasting criterion: on the one hand we had a preference for an antenna frequency that could be as much as possible near to the survey condition of a river measurement. On the other hand, we need a frequency that could be meaningful at the small scale condition of the tank experiments. In a field survey condition is suitable a low frequency antenna (100-200MHz), which could obtain high penetration depth thanks to the lower intrinsic attenuation of the water in this frequency range. Instead in laboratory conditions we need a high frequency antenna, in order to obtain short wavelength and reduce the near field effect. At the end we choose a 1500 MHz antenna.

Coming back on the geometrical scaling, if we consider suitable in field condition a 200MHz central frequency antenna and a velocity of the radar signal in water of 0.033 m/ns, by equation (2.44) we can evaluate a wavelength in water of 16.5 cm. In the laboratory tests for a 1500 MHz central frequency antenna, then 7.5 times higher than the frequency suitable in the field, corresponds a wavelength of roughly 2÷2.5 cm. We need to take in account that the scaling of the wavelength is not linear. In fact, the water acts like a low pass filter of the electromagnetic signal, similarly to

other geological materials. In water the higher frequencies are more attenuated than the lower frequencies. Consequently, the central frequency of the power spectrum shifts down. In the wavelength domain, this phenomenon corresponds to a shift toward higher wavelengths. This aspect should be taken in account when we consider the electromagnetic cluttering of the bottom sediments. Actually, in section 2.13, we showed as the radar cross section of a target is strongly dimensionally dependent on the signal wavelength. If we consider equation (2.70), we infer that to a rise in the wavelength λ corresponds a fall of the size factor x. Consequently, it could be possible the transition from the Optic or Mie region toward the Rayleigh region (Figure 2.2). Then we could infer that scattering is affected by the geometrical scaling, in particular we expect in the field a lower level of cluttering with respect to the lab condition.

We focus now our attention on the water depth: we wanted it one order of magnitude higher than the wavelength of the radar wave in water ($\lambda \approx 2.5$ cm), then at least 25 cm. We need to take care that this water depth does not satisfy the far field condition. Let us assume the 1.5 GHz antenna dipoles 8 cm long. Then, from equation (2.40), we could verify as the far field condition requires roughly 65 cm of water depth. However, we could not reproduce this water depth for logistic reasons and we come to a compromise. The tank would have contained also a 15 cm sediment layer besides the water. Then, the tank height should have been at least 40 cm.

In field conditions, the bottom sediments dimensions are strongly dependent to the type of water environment. For example, the riverbed of the PO river near Turin is covered by a pebbly layer coated by a thin silty film. The pebbly layer occurs during the flood events, when the water speed is high enough to shift along the riverbed coarse clasts. After the flood, during low water regime, the fine suspended sediments deposit to form a thin silty film. Then we expected in the field a wide band of bottom sediments dimensions, which changes from submillimeter to roughly one decimeter. In laboratory we chose sediments dimensions roughly 10 times smaller than the sediments expected in the field. Then, we selected the following 5 sediments types: a loam (<0.5 mm), a fine sand (<2 mm), a coarse sand (2-5 mm), a round (3-8 mm) and a round (5-15 mm). We have a preference to test materials with mineralogical

properties similar to the sediment encountered in the following test in the field. For this criterion, we choose sediments provided from a quarry near the Po river.

3.4. Experimental setup

According to the requirements of the experimental design we needed a tank able to contain and resist without significant deformation a water depth of at least 25cm and a bottom sediments layer of 15cm. We would have liked a tank made by a material with a minimal electromagnetic interference. Consequently we absolutely avoided metallic material, considering the commercial availability we preferred plastic materials. At the end we choose a

Figure 3.1: *Experimental setup of the GPR equipments for the measurement in water. In particular it is visible the HDPE tank, the GPR GSSI SIR-2 and the antenna.*

1.05×0.64×0.668m High-Density PolyEthylene (HDPE) tank, showed in Figure 3.1. We wanted to change the water depth during the experiment and then we performed a homemade system to raise the antenna height, keeping constant the coupling between antenna and water. The antenna was immerged roughly half centimeter in the water. The realization is shown in Figure 3.2, Figure 3.3 and Figure 3.7.

Figure 3.2: *Tank filled with 8cm of water and with the aluminum plate on the bottom.*


Figure 3.3: *Tank filled with 40cm of water, without the aluminum plate on the bottom.*

We performed an experiment on the water with a perfect reflector on the bottom of the tank. For this test we choose an aluminum plate, 0.5 cm thick that covered completely the area of the tank.

Considering the influence of the temperature on the water electromagnetic properties, we monitored it using a thermometer with ±0.1°C accuracy.

GPR and Accessories

We used for these experiments a GSSI SIR-2 (Geophysical Survey Systems Inc, 1996), a portable GPR, shown in fig 4.2. It does not need a computer to acquire measurements, because it is an embedded MS-DOS system. We interfaced the GPR to a laptop to download the measurements, and to check the measurements with the Sandmeier's software Reflex 3.5.7.

We improve the repeatability among the different experiments adopting the same GPR data collection configuration for all the tests; Table 3.1 summarizes the setting parameters.

Table 3.1: *GSSI SIR-2 Setup "Data Collection" adopted for the experiments.*

Parameters		Values
Samples/Scan		2048
Bits/Sample		16
Scans/Second		8
Stacking		0
Units		Meters
Scans/Unit		20
Unit/Mark		5
Dielectric		1
Position		170 ns
Range		50 ns
Gain		0
Vertical Filters	Low Pass	2.5 GHz
	High Pass	0.3 GHz
Horizontal Filters	Smoothing	4 scans
	Background Removal	0 scans

We give now a brief description of the Table 3.1 parameters, and we deduce the argumentations that have influenced the setting of their values.

Samples/Scan: it is the number of samples in a GPR trace, in the GSSI SIR-2it could be set to 128, 256, 1024, 2048. Considering the small dimension of our

measurements we set this parameter to the high value in order to obtain the highest sampling frequency possible.

Bits/Sample: it is the number of bits used to represent the amplitude values, it coud be set to 8 or 16. We set to the highest value to obtain the best digital resolution of the amplitude data.

Scans/Second: it is the number of traces obtained in a second.

Stacking: this parameter improves the signal-to-noise ratio (SNR). Considering all our measurements are acquired in static condition this parameter does not have influence, then we set it to zero.

Units: It control the system of measurements, we define the meter value to be consistent to the International System of Units (SI).

Scans/Unit: it sets the horizontal sampling, usually in survey condition the horizontal dimension is a distance, but in our case of static measurements it is a time.

Unit/Mark: this value determines how often distance marks are placed on the data display.

Dielectric: it is the value of the dielectric constant used to convert two-way travel time to depth in the data viewing window of the GSSI SIR-2.

Position: it controls the vertical position of the main bang in the data viewing window. In general we identified with main bang the signal produced when the radar pulse leaves the antenna, and enters the subsurface. It can therefore be considered to be "time zero", and its position should be at the top of the scan. We changed the default value to record the entire waveform of the main bang.

Range: it is a time value in nanoseconds; it controls how long the record of the received reflected signals is, after the sent out of the radar pulse. The choose of this parameter is a trade-off between a high value, to record all the phenomenon, and a short record in order to obtain an high sampling rate. We set the range to 50ns, obtaining a sampling rate of roughly 40GHz, that is nearly 25 times the central frequency of the antenna. Moreover with a 50ns range, it could be possible obtain information in a water medium from a depth higher than 1.5m.

Gain: usually if the data acquired is too low in amplitude and difficult to interpret, this parameter is used to apply an additional gain constant to the data files. We preferred don not used this feature to obtain as much as possible raw data.

Vertical Low Pass Filters: this three pole IIR (Infinite Impulse Response) filter is used to eliminate high frequency noise from the data. It should be set roughly to the double of the antenna center frequency, as the value of this filter is decreased, more filtering occurs and more data will be removed by the filter. We did not apply any filter.

Vertical High Pass Filters: it is a three pole IIR filter used to eliminate low frequency noise (e.g., tilt) from the data. The value of this parameter should be set according to 1/6 of the antenna center frequency, as the value of this filter is increased, more filtering occurs and more data will be removed by the filter. We did not apply any filter.

Horizontal Smoothing: It is an IIR running average filter; it process the data horizontally eliminating random noise, smoothing the data and emphasizing continuous layers. The input value is number of Scans. In the static condition of our experiments this parameter is not relevant.

Background Removal: It is used to improve the recognition of small targets and dipping reflectors. This process filters the data horizontally by removing horizontal noise bands and reflecting layers. It is important to do not use this filter because it removes the surface reflection and any other real horizontal reflections.

3.5. Calibration: Measurements in Air

Before starting the experiments in water we performed, with the same GPR configuration, a measurement in air with the antenna directed toward the sky. Aim of the test was to compare the main bang waveform (the signal produced when the radar pulse leaves the antenna and enters the subsurface) obtained in air, with the one obtained in water. Moreover we wanted to verify the presence of possible anomalies in the radar signals.
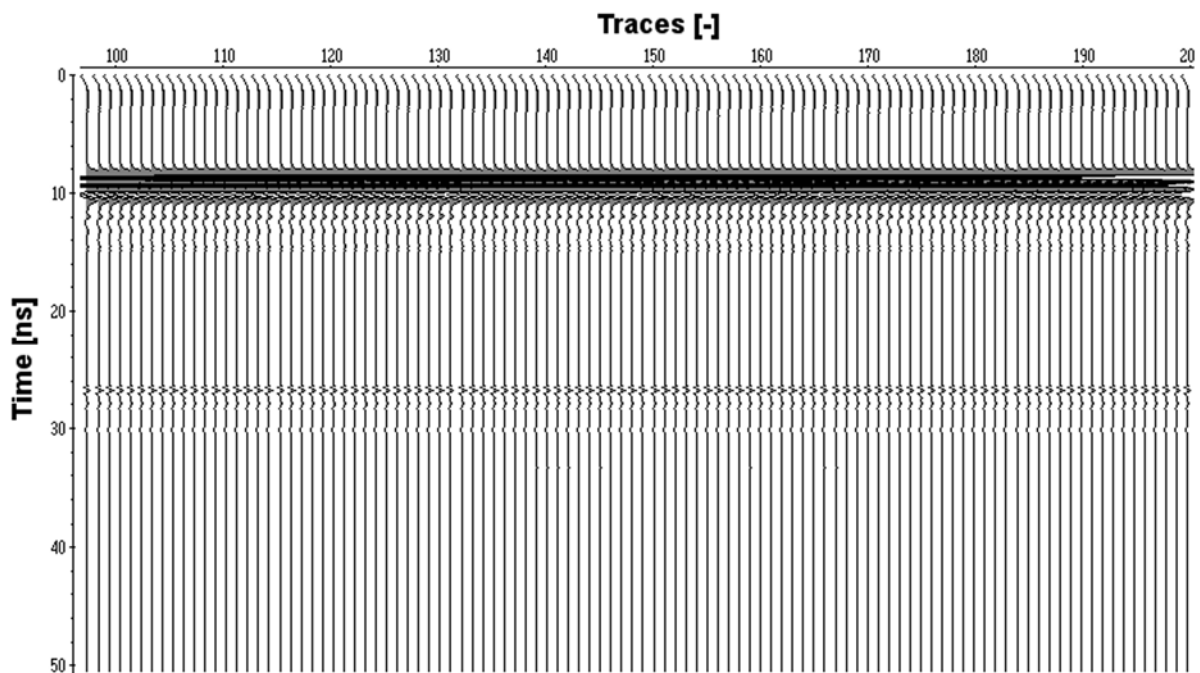
Figure 3.4: *Radargram relative to the GPR measurement in air with the antenna directed toward the sky and kept still. The radargrams shows the 100 central traces of the test. The only processing applied to the data was to remove the first and the last 100 traces.*

We performed two measurements with the antenna kept still and taking care to direct the antenna emission cone far from possible scattering targets, like building. We acquired for each measure 300 radar traces, and both the tests were characterized by high repeatability. Figure 3.4 shown the 100 central radar traces relative to the first radargrams acquired, imported and processed with the Sandmeier's Reflex Win software. The main bang signal is positioned nearly 8ns far from the zero time, moreover it is visible an unforeseen signal positioned roughly at 27ns. Figure 3.5a shown the zoom of the main bang event relative to the 1st trace of Figure 3.4. This signal is similar in the waveform to the main bang relative to the measurement in

water, but with strong difference in the amplitude value, due to the different impedance contrasts between the antenna-air and antenna-water coupling.
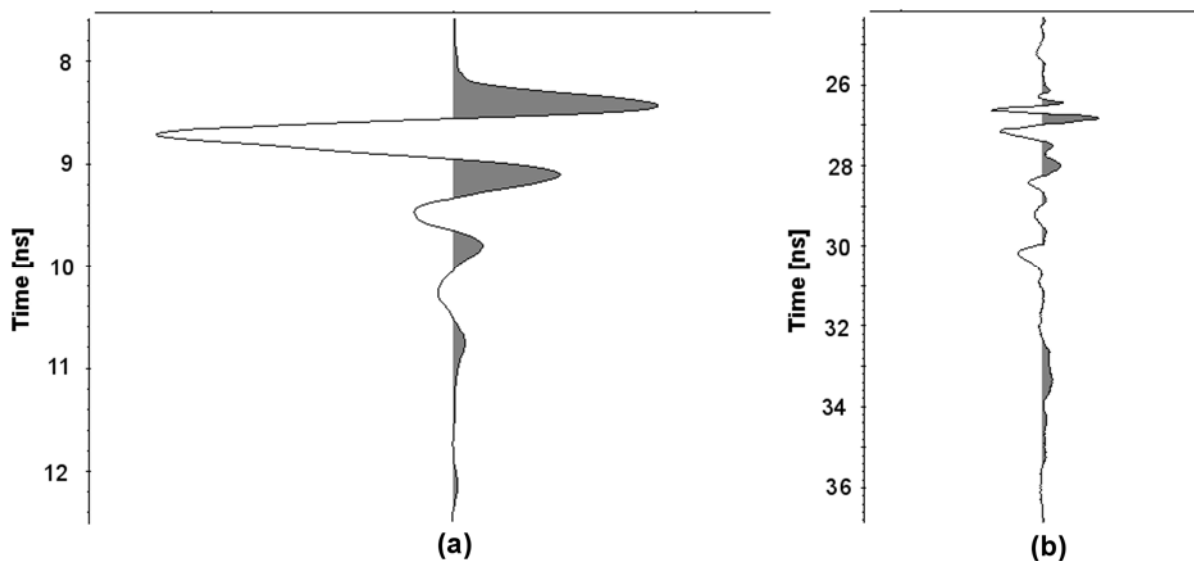
Figure 3.5: *On the left zoom of the main bang signal of a trace relative to the measurements in air, with the antenna directed toward the sky (a). On the right zoom of the noise signal encountered in the same measurements (b).*

We selected one trace from the radargrams and we computed its spectrogram, the result is shown in Figure 3.6. The spectrogram can be defined as an intensity plot of the Short-Time Fourier Transform (STFT) magnitude (Smith, 2007). The STFT is a sequence of Fast Fourier transforms (FFTs) of windowed data segments, where the windows are usually allowed to overlap in time, typically by 25-50% (Allen and Rabiner, 1977). The spectrogram in the air measurements highlight only the main bang, because the noise shown Figure 3.5 has a lower energy.

Figure 3.5b provides a zoom of this noise signal. In order to understand the origin of this signal, we carried out different trials, changing the GSSI SIR-2 data collection setup, the materials investigated. In all these tests the noise could be identifiable and constant in position and waveform. Instead the amplitude of the signal changed in the different tests. With these elements we deduced that the signal could be due to a defect in the cable that provides the link between the radar system and the antenna. The discovery of this anomaly was an important aspect, because it influenced the next experiments in water. In fact we take care of it, excluding from the interpretation all the measurements where the reflection phenomena of the tank bottom could be interfere with this noise.
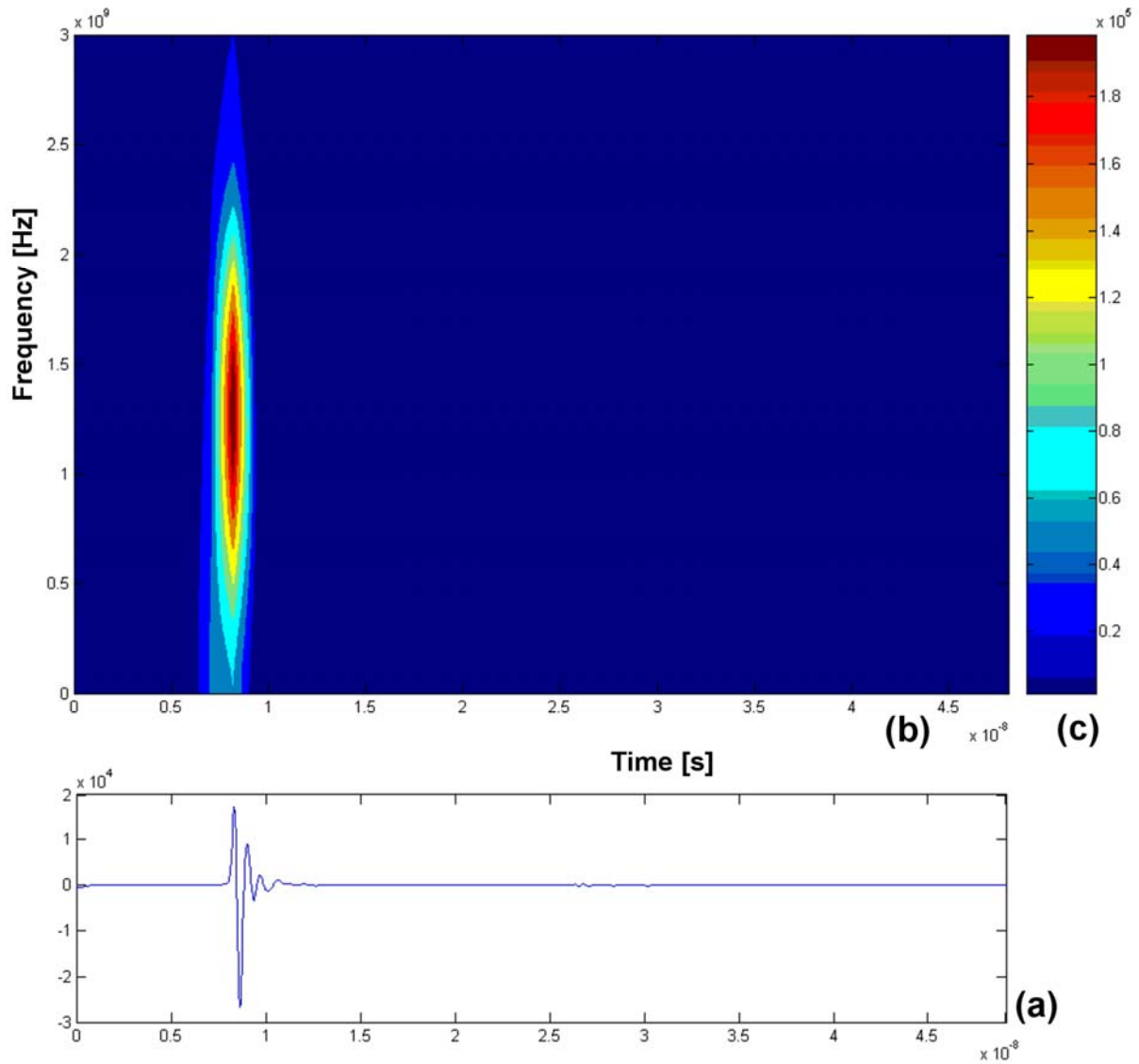
Figure 3.6: *(a) GPR trace relative to the measurements in air, with the antenna directed toward the sky. (b) Spectrogram of the trace shown in (a) and its magnitude color bar (c).*

3.6. Calibration: Measurements in Water

Before starting the water experiments with the sediments on the bottom of the tank, we carried out some calibration tests with the same experimental setup, but without sediments. Aims of these measurements were to optimize the experimental setup, to design the processing flow of the data, to estimate the velocity of the radar pulse in water, to estimate the intrinsic attenuation coefficient in Time Domain (TD) and to evaluate the intrinsic attenuation coefficient in Frequency Domain (FD).

The propagation velocity of the radar pulse in water and the intrinsic attenuation of the water are two parameters dependently by several physical properties of the water but independently by the water depth. Then to investigate these two parameters we carried out different measurements varying the water depth in the tank, with the antenna positioned on the water surface. We adopted for these tests two different bottom reflectors, characterized by different electromagnetic impedances: the HDPE of the tank and an aluminum plate.

We estimated the velocity of the radar pulse in water ($v=0.0327\pm0.001$ m/ns) by a linear regression on the Two Way Travel Times (TWT) versus the water depths. We found a good agreement among both the results of the two tests, corresponding to different reflectors, and the values available in literature. We evaluated the water attenuation coefficient ($\alpha=2.68\pm0.1$ m^{-1}) in TD by a linear regression on the processed amplitude data versus the water depths. We explored the water attenuation coefficient in FD studying at different water depth, both the spectra of the isolated bottom reflection signals, and the spectrograms of the complete radar traces.

3.6.1. Methods

The calibration test with the water was started placing the aluminum plate on the bottom of the tank, and then filling the tank with 8cm of water depth. We excluded lower water depths, in order to avoid strong near field effect. Considering the influence of the temperature on the water permittivity, we monitored this parameter with a 0.1°C accuracy thermometer. Then we dipped roughly 0.5cm the bottom of the antenna under the water surface. We took care to maintain in all the measurements the same antenna dip, because in some preliminary tests we verified the influence of the antenna coupling on the main bang signal amplitudes. When the GPR measurements with the aluminum plate were finished, we removed the plate and we

replaced the antenna on the water to acquire GPR measurements with the water and the HDPE bottom of the tank. After a positive preliminary check of these two measurements, we filled the tank with other 5cm of water and we acquired two measurements with and without the aluminum plate. We could change the vertical position of the antenna with the home made slide shown in Figure 3.7. Then we continued the test adding 5cm of water and acquiring GPR measurements, until reaching a 48cm water depth. To summarize, we acquired 16 GPR measurements, 8 with an aluminum plate on the bottom of the tank and 8 without, with the following water depth: 8, 14, 19, 24, 29, 34, 40 and 48 cm.
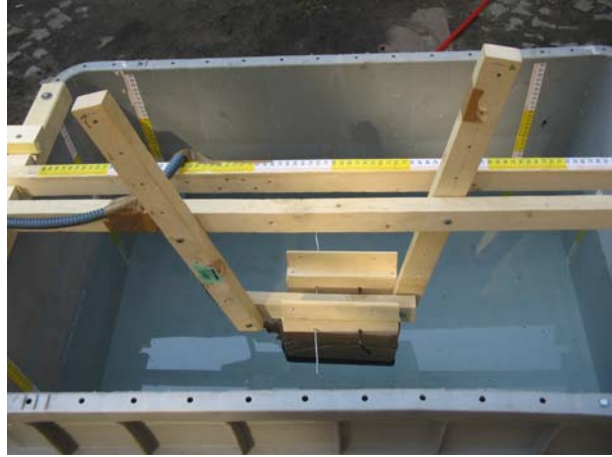
Figure 3.7: *Particular of the system to anchor the antenna and raise it, to keep constant the antenna coupling with the water.*

3.6.2. Processing Summary

Objectives of the data processing was to estimate the velocity value of the radar pulse in water, the water attenuation coefficient in TD, the spectra of the water attenuation coefficient in FD and finally the spectrograms of the GPR signals acquired at the different positions. We applied the data processing flow, shown in Figure 3.8, to the measurements acquired with and without the aluminum plate on the bottom of the tank.

Velocity analysis: We started the processing downloading the GPR measurements from the GSSI SIR-2 to a PC and importing the raw data in the Sandmeier's software Reflex, step (1) in Figure 3.8. From the different radargrams we picked the time values of the main bang (2) and of the bottom reflection event (3). We need to take care that the radargrams show the two way travel (TWT) times: the time elapsed from the transmission instant and the receiver detection instant, then relative to the there and back paths. We evaluated the Time of Flight (ToF) of the radar pulse in water (4) by difference between the bottom reflection and the main bang times. Then the ToF in water is the time taken by the radar pulse to propagate from the water surface to the bottom of the tank and to come back to the water surface.

We graphed the ToF in water depth versus the distance covered by the radar signal (7). In this graph we evaluated the velocity of the radar pulse in water (6) by the linear regression (5) of the available points.

Attenuation coefficient in Time Domain: In order to estimate the attenuation coefficient in time domain we previously performed a uniformity control of the main bangs (8) among all the 16 measurements relative to the 2 reflector types and the 8 different water depths. If this control would have highlighted data dispersion among the measurements we would have applied the amplitude normalization (14). However thanks to the optimal coupling among the measurements we did not applied any normalization. After this control we removed the firsts and lasts 100 traces from each radargram in order to avoid transitory due to the turn on or turn off the GPR (9). Then we picked the reflection amplitude relative to the tank bottom (11). The amplitude data collected were recovered for the geometrical losses (11) according to the criteria shown in section 2.13. The processed amplitude data were graphed versus the distance covered (7) in order to find the linear regression of the points (12). Then the absolute value of the angular coefficient of the interpolation line represents the attenuation coefficient in time domain of the water (13).

Attenuation coefficient in Frequency Domain: we started by the extraction from the radargrams of the reflection signals relative to the tank bottom (15). This operation was performed by the amplitude muting above and below the reflection signals. Then we evaluated the amplitude spectrum (16) of the isolated reflection signal, from 0 to 3000 MHz with a sampling frequency of 20 MHz, and we plotted the amplitude spectra (21). For each amplitude value of the spectra we iterated the processing flow performed in the time domain analysis. Thus we recovered the geometrical losses (17), and we founded the linear regression of the amplitude data versus the distance covered (18), obtaining the attenuation coefficient of the water from 0 to 3000 MHz (19) by the absolute value of the regression line angular coefficient.

Finally we made a time-frequency analysis (20), by the spectrogram of the traces, in order to describe the frequency variations of the signal reflection at the different water depth.
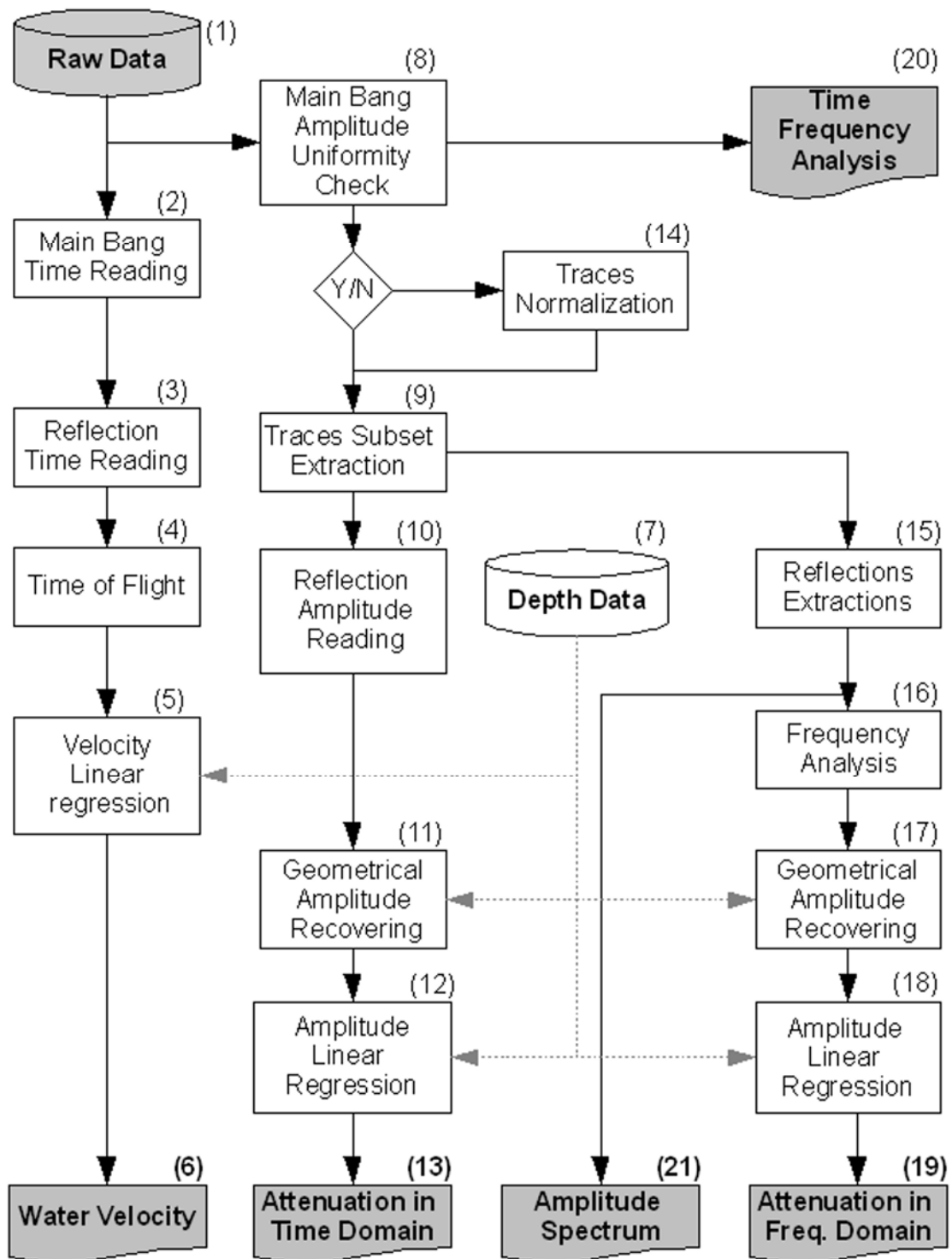
Figure 3.8: *Processing flow designated to interpret the calibration measurements in water.*

3.6.3. Results

Velocity Analysis

The velocity of the electromagnetic pulse in water could be estimated by the time of flight in water Δtwt and the water depth data h. The time of flight Δtwt, relative to the there and back paths in water, is estimated by difference of the bottom reflection time t_R and the main bang event time t_{MB}

$$\Delta twt = t_R - t_{MB} \quad [ns] \tag{3.1}$$

The main bang time is different from zero because we inserted a delay in the GPR traces, like it is described in section 3.3. For each water depth we can estimate a velocity value

$$v = \frac{2h}{\Delta twt} \quad \left[\frac{m}{ns}\right] \tag{3.2}$$

In Table 3.2 we summarized all the data about the estimation of the electromagnetic velocity in water, both with and without the aluminum sheet placed on the bottom. We reported respectively: the progressive number of the antenna position, the time of flight Δtwt estimated by equation (3.1), the distance covered by the electromagnetic pulse 2·h, the standard deviation of both the time of flight σ(Δtwt) and the distance covered σ(2·h), and finally the velocity v estimated by equation (3.2). From the analysis of the reflection amplitude we discover that the measurements of some antenna positions were affected by systematic error, and then we discarded them; we underlined these values in Table 3.2. The uncertainty of the water depth data σ(2·h) were estimated taking in account the deformation of the lateral side of the tank, due to the water thrust, were we placed the rule. The time of flight uncertainties σ(Δtwt) were estimated with the propagation error analysis of the main bang σ(Δt_{MB}) and reflection σ(Δt_R) picking times standard deviations

$$\sigma^2{}_{(\Delta twt)} = \left(\frac{\partial(\Delta twt)}{\partial t_R}\right)^2 \cdot \sigma^2{}_{(t_R)} + \left(\frac{\partial(\Delta twt)}{\partial t_{t_{MB}}}\right)^2 \cdot \sigma^2{}_{(t_{MB})} \tag{3.3}$$

$$\sigma_{(\Delta twt)} = \sqrt{\sigma^2{}_{(t_R)} + \sigma^2{}_{(t_{MB})}} \tag{3.4}$$

Table 3.2: *Experimental data of the calibration test in water performed for the estimation of the electromagnetic velocity in water. The X values represent time of flight of the electromagnetic pulse in water, the Y values the distance covered. The velocity values V are estimated by equation (3.2).The underlined data are discarded because affected by systematic error.*

Pos	Bottom Reflector: Aluminum Sheet				
	X	Y	σ(X)	σ(Y)	V
	Δtwt [ns]	2h [m]	σ(Δtwt) [ns]	σ(2h) [m]	[m/ns]
8	<u>28.2852</u>	<u>0.9660</u>	<u>0.0373</u>	<u>0.01</u>	<u>0.0342</u>
7	<u>23.4388</u>	<u>0.8080</u>	<u>0.0236</u>	<u>0.01</u>	<u>0.0345</u>
6	19.9354	0.6840	0.0192	0.01	0.0343
5	16.7134	0.5720	0.0207	0.01	0.0342
4	13.4766	0.4800	0.0078	0.01	0.0356
3	10.5955	0.3760	0.0057	0.01	0.0355
2	7.5211	0.2760	0.0068	0.01	0.0367
1	<u>4.4275</u>	<u>0.1600</u>	<u>0.0117</u>	<u>0.01</u>	<u>0.0361</u>
Pos	Bottom Reflector: HDPE Tank				
	X	Y	σ(X)	σ(Y)	V
	Δtwt [ns]	2h [m]	σ(Δtwt) [ns]	σ(2h) [m]	[m/ns]
8	<u>29.9321</u>	<u>0.9600</u>	<u>0.0390</u>	<u>0.01</u>	<u>0.0321</u>
7	25.0874	0.8020	0.0224	0.01	0.0320
6	<u>21.4632</u>	<u>0.6780</u>	<u>0.0239</u>	<u>0.01</u>	<u>0.0316</u>
5	18.1332	0.5660	0.0205	0.01	0.0312
4	14.8725	0.4740	0.0137	0.01	0.0319
3	11.7444	0.3700	0.0128	0.01	0.0315
2	8.4472	0.2700	0.0016	0.01	0.0320
1	<u>5.0866</u>	<u>0.1480</u>	<u>0.0145</u>	<u>0.01</u>	<u>0.0291</u>

From Table 3.2 we can highlight that the uncertainties on the water depth data are more relevant than the time of flight uncertainties.

We improved the precision of the velocity values expressed in Table 3.2 by a linear regression of the data retained reliable, we performed the interpolation by a home-

made statistical routine. Given the X and Y values with their standard deviations, the routine gives back the linear interpolation defined by:

- a: the intercept of the linear interpolation with the Y axes;
- b; the angular coefficient of the line;
- $\sigma(a)$: the intercept standard deviation;
- $\sigma(b)$: the angular coefficient standard deviation;
- χ^2: the value of the homonymous test;
- q: the probability that the interpolation is linear.

Moreover we estimated for each interpolation the coefficient of determination R^2, the proportion of variability in a data set that is accounted for by a statistical model, with Microsoft Excel.

We performed the linear regression of the 2 data sets, each consisting of 5 values, relative to the measurements with and without the aluminum sheet, the results of the statistical tests are summarized in Table 3.3 and the interpolations is showed in Figure 3.9. Assuming a normal distribution of the errors, almost all (actually, 99.7%) of the values lie between the mean minus 3 times the standard deviation and the mean plus 3 times the standard deviation.

We can observe from Figure 3.9 the two data sets are fitted very well by the linear regressions, in fact both the coefficient of determination R^2 in Table 3.3 confirm the low dispersion of the data.

Table 3.3: *Results of the statistical tests for the estimation of the radar velocity in water.*

Bottom reflector	a	b	$\sigma(a)$	$\sigma(b)$	χ^2	q	R^2
Aluminum	0.0314	0.0327	0.0149	0.0010	1.0294	0.7941	0.999
HDPE	-0.0030	0.0319	0.0132	0.0008	1.3280	0.7225	0.9992

From Figure 3.9 we can highlight that the two data sets have a vertical shift lower than the 3 times of their standard deviations. In both case the linear regressions of the velocity do not intercept the axis origin. Lambot et al. (2004) suggests that for a monostatic antenna exists a point, non correspondent to the antenna position, that represent the virtual source of the irradiated field. In order to obtain a linear

regression crossing the axis origin we should fix the distance between the virtual source and the irradiated object.
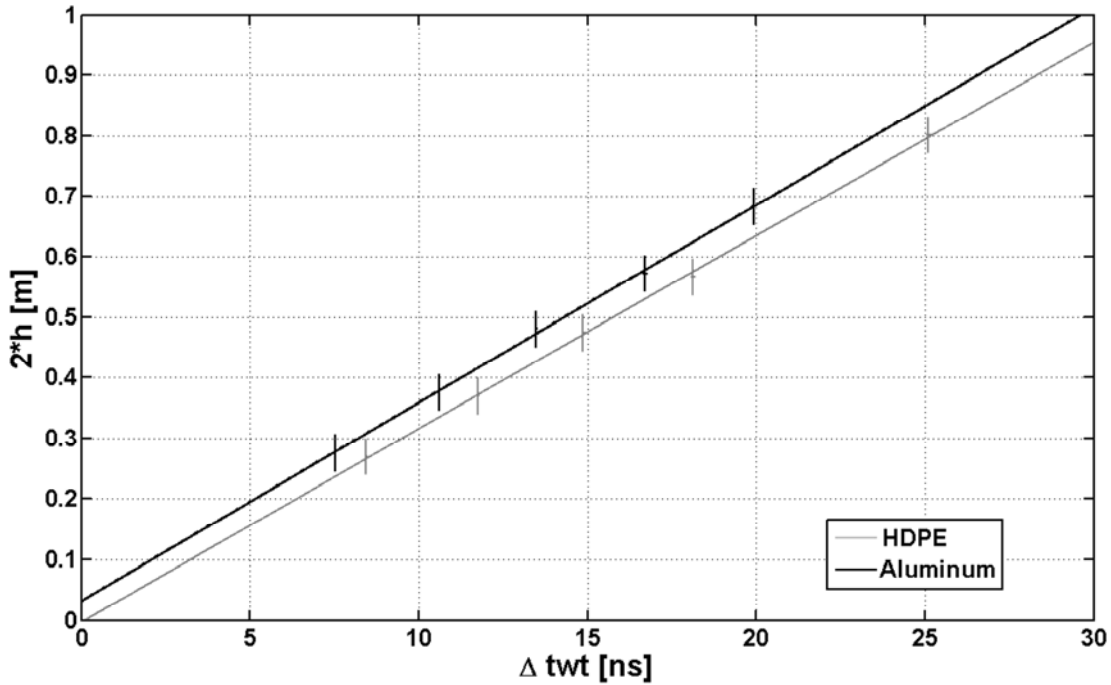
Figure 3.9: Linear regression of the data retained reliable of Table 3.2 for the estimation of the radar velocity in water. The black line refers to the measurements with the aluminum sheet on the bottom, the gray line refers to the HDPE tank bottom. The error bars represent 3 times the standard deviations.

We focus now our attention on the results of our goal: the velocity of the electromagnetic pulse in water, that it is represented by the angular coefficients of the interpolations. We can assert that the two values obtained are closed, in fact their distance are smaller than their standard deviation. Moreover the estimated value agrees with the typical velocity of water available in literature, listed in Table 2.3. Considering the better statistical results obtained from the tests on the aluminum reflector, for the following interpretation of the laboratory experiments we'll take in account its velocity value

$$V = 0.0327 \pm 0.001 \left[\frac{m}{ns} \right] \qquad (3.5)$$

Main Bang Repeatability Check

Before starting the analysis on the signal amplitude we check the repeatability of the main bang signals among different measurements. If the main bang signal remains constant among different tests we can consider constant the amount of energy entering the water as constant and consequently compare the amplitude of the bottom signal reflection among different reflectors and water depths. The main bang repeatability is particularly true in water GPR measurements thanks to the constant coupling between antenna and water. Contrarily in terrain GPR measurements it is difficult maintain a constant electromagnetic coupling between the antenna and the ground because of the surface heterogeneities.

In order to check the main bang repeatability, we picked the amplitude values of the main bang signals and we compared them among different measurements. Successively we isolated the main bang signals, by muting above and below the GPR traces. We performed a frequency analysis on the isolated main bang signals and we compared them, Figure 3.10 shows 4 amplitude spectra corresponding to different bottom reflectors and different water depths. Our analysis confirms the good repeatability of the main bang signals among different tests.
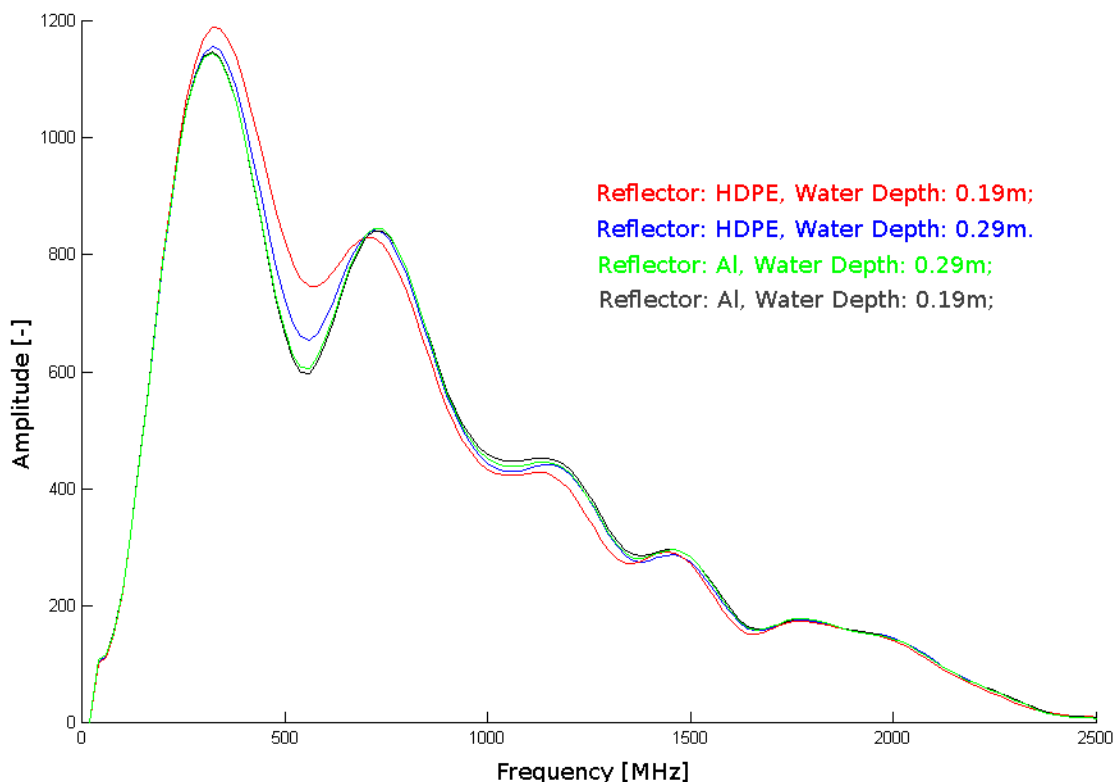
Figure 3.10: *Main Bang amplitude spectra of 4 different measurements.*

Signal Phase Inversion on the Aluminum Reflector

Now we want focus the reader attention on the comparison between the reflection signals relative to the aluminum and HDPE reflectors. The analysis of Figure 3.11 highlight two signals in phase opposition and a time shift of roughly 1ns. The phase inversion is explicable if we estimate the reflection coefficients of the two impedance contrasts: water-aluminum and water-HDPE.
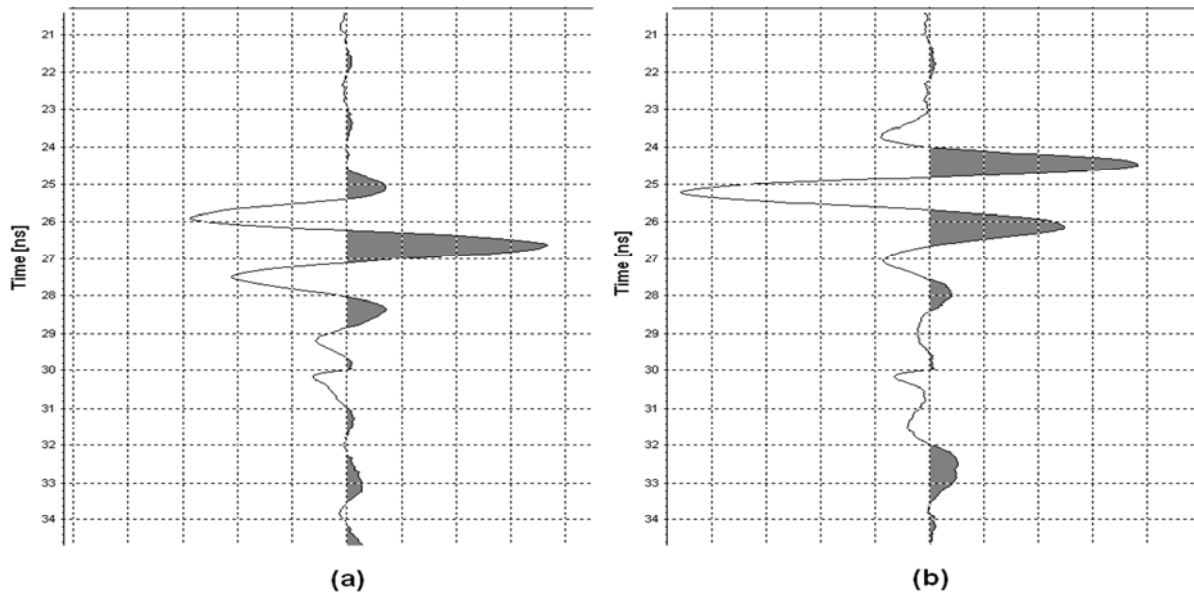
Figure 3.11: *Comparison between the reflection signals relative to the aluminum sheet (a) and the HDPE tank bottom (b).*

Table 3.4: *Electromagnetic properties of the material used in the calibration tests.*

			Water	**Aluminum**	**HDPE**
Electrical conductivity	σ	$\left[\dfrac{1}{\Omega \cdot m}\right]$	0.2	10^7	10^{-7}
Relative magnetic permeability	μ_R	[-]	1	1	1
Magnetic permeability	μ	$\left[\dfrac{H}{m}\right]$	$1.257 \cdot 10^{-6}$	$1.257 \cdot 10^{-6}$	$1.257 \cdot 10^{-6}$
Relative permittivity	ε_R	[-]	79	1	2
Permittivity	ε	$\left[\dfrac{F}{m}\right]$	$6.985 \cdot 10^{-10}$	$8.841 \cdot 10^{-12}$	$1.768 \cdot 10^{-11}$

In Table 3.4 we summarized the electromagnetic properties of the media involved in the experiment, by the definitions (2.45) and (2.45) we can estimate the material impedances for water Z_w, aluminum Z_{Al} and HDPE Z_{HDPE}

$$Z_W = \sqrt{\frac{i \cdot \omega \cdot \mu_W}{\sigma_W + i \cdot \omega \cdot \varepsilon_W}} = 23.91 + 0.5445i \quad [\Omega] \tag{3.6}$$

$$Z_{Al} = \sqrt{\frac{i \cdot \omega \cdot \mu_{Al}}{\sigma_{Al} + i \cdot \omega \cdot \varepsilon_{Al}}} = 0.0112 + 0.0112i \quad [\Omega] \tag{3.7}$$

$$Z_{HDPE} = \sqrt{\frac{i \cdot \omega \cdot \mu_{HDPE}}{\sigma_{HDPE} + i \cdot \omega \cdot \varepsilon_{HDPE}}} = 150.4 + 0.68 \cdot 10^{-4}i \quad [\Omega] \tag{3.8}$$

If we assume a near zero offset condition, we can evaluate the reflection coefficients for the water-aluminum $R_{W\text{-}Al}$ and water-HDPE $R_{W\text{-}HDPE}$ with the relation (2.52) valid for normal incidence

$$R_{W-Al} = \frac{Z_{Al} - Z_W}{Z_{Al} + Z_W} = -0.999 + 9.15 \cdot 10^{-4}i \tag{3.9}$$

$$R_{W-HDPE} = \frac{Z_{HDPE} - Z_W}{Z_{HDPE} + Z_W} = 0.726 + 5.39 \cdot 10^{-3}i \tag{3.10}$$

From the relations (3.9) we can highlight a negative reflection coefficient of the water-aluminum interface and its absolute value is practically unitary, in fact the aluminum is a perfect electromagnetic reflector. Instead relation (3.10) tells that the water-HDPE impedance contrast is characterized by a positive reflection coefficient and the amount of energy reflected in water is lower than the aluminum case. This analytical result is well distinguishable in Figure 3.11, where over the phase opposition of the two signals, we can also remark the reflected amplitude from the aluminum higher than from the HDPE.

Taking in account the phase opposition, the goal of the picking operation on the water-aluminum interface is the local maximum of the first negative amplitude peak encountered in the signal reflection; contrarily in the water-HDPE case we picked the first positive amplitude maximum.

Nevertheless from the reflection coefficients analysis we can not explain the time shift between the two signals, observable in Figure 3.11. Even if we consider the 5mm aluminum sheet thick, we can evaluate a 0.15ns advance of the reflection signal, which can not explain the 1ns shift between the traces.

Attenuation Factor in Time Domain

In this section we explain the analysis performed to estimate the attenuation coefficient in Time Domain. In order to compare the bottom reflection amplitudes relative to different types of reflector and water depths we deduced a simplified version of the radar equation described in section 2.14. The comprehensive radar equation takes in account a broad range of aspects: the source energy, the transmitter and receiver gains and efficiencies, the transmitter-ground and receiver-ground couplings, the intrinsic and geometrical losses and finally the reflector behaviors. In all our tests we maintained a constant experimental setup: we then used always the same antenna and GPR configuration and we guaranteed a constant antenna-water coupling; the Main Bang Repeatability Check section gives confirm of this aspect. In our experiments we changed only the water depth, which influences the geometrical and intrinsic losses, and the type of reflector, which individuation represents our goal. Thus we can rewrite the radar equation taking in account only these two elements. The source amplitude entering in the water A_0 in the 2h distance covered by the electromagnetic pulse is attenuated for the intrinsic dissipation by a factor $e^{-2\alpha h}$. The geometrical losses required special attentions; section 2.13 defines for a punctual reflector in far field condition a geometrical attenuation inversely proportional to $1/h^2$. But in our experiment the far field condition is not verified and the reflector is planar, then we preferred to consider the geometrical losses inversely proportional to $1/2h$. This attenuation factor could be justified if we consider the conceptual idealization showed in Figure 3.12. The real experiment situation is schematized in Figure 3.12a, only for the geometrical attenuation we considered the situation of Figure 3.12b. We suppose to have the transmitter position placed on a virtual point specular to the real transmitter position with respect to the plane reflector. Assuming a spherical wave, we

Figure 3.12: *Conceptual idealization for the explanation of the geometrical attenuation factor.*

consider the geometrical attenuation inversely proportional to the distance virtually covered 2h by the electromagnetic pulse.

Now we are able to express the amplitude at the receiver A function of the amplitude entering in water A_0, the water depth h, the water-bottom amplitude reflection coefficient R and the water attenuation coefficient α

$$A = A_0 R \frac{1}{2h} e^{-2\alpha h}$$
(3.11)

We can rewrite equation (3.11) in the following linearized form

$$Y = a + bX$$
(3.12)

exploiting the logarithmic properties in order to obtain the linearized simplified radar equation

$$\ln(A) + \ln(2h) = \ln(A_0 R) - 2\alpha h$$
(3.13)

The sum of the two addends on the left of equation (3.13) represent the natural logarithm of the receiver amplitude covered for the geometrical attenuation. The addend $\ln(A_0 R)$ on the right of equation (3.13) is function only of the amplitude entering in water and of the reflection coefficient. We already asserted about the source amplitude constancy, moreover in each experiment the reflector was the same, thus we can consider the term $\ln(A_0 R)$ constant in each experiment. Thus equation (3.13) describes a straight line in the distance versus corrected amplitude space, that intercepts the amplitude axes on the $\ln(A_0 R)$ value and which slope is defined by the water attenuation coefficient. Moreover assuming the aluminum like a perfect reflector (unitary water-aluminum reflection coefficient) we are allowed to infer the amplitude entering in water A_0 from the interception of the linear regression with the amplitude axes in the case of the aluminum reflector experiments.

In Table 3.5 we reported for each position of the two calibration tests the distances covered by the electromagnetic pulse 2h and the amplitude data covered for the geometrical attenuation A^* evaluated according to

$$A^* = \ln(A) + \ln(2h)$$
(3.14)

We also reported the distance standard deviation σ(2h), estimated like in the velocity analysis, and the amplitude standard deviation σ(A*), estimated by the error propagation analysis on equation (3.14)

$$\sigma\left(A^*\right) = \left|\frac{\partial(A^*)}{\partial(A)}\right| \cdot \sigma_{(A)} + \left|\frac{\partial(A^*)}{\partial(h)}\right| \cdot \sigma_{(h)} = \frac{\sigma_{(A)}}{A} + \frac{\sigma_{(h)}}{h}$$
(3.15)

We excluded some experimental data affected by systematic errors, we underlined these values in Table 3.5. In particular the position 1 of both the experiments was too near to the reflectors; instead the amplitudes relative to the positions 8 were too noised and dispersed. Finally the picking relatives to position 7 on the aluminum reflector experiment and position 6 on HDPE reflector test had fallen near the noise described in detail in section 3.5.

Table 3.5: *Experimental data of the calibration test in water performed for the estimation of the water attenuation coefficient with their standard deviation. The X values represent the distance covered by the electromagnetic pulse in water 2h, the Y values repesent the amplitude of the bottom reflection corrected for the geometrical attenuation A^*. The underlined data are discarded because affected by systematic error.*

	Bottom Reflector: Aluminum Sheet				Bottom Reflector: HDPE Tank			
	X	Y	σ(X)	σ(Y)	X	Y	σ(X)	σ(Y)
Pos	2h [m]	A^*	σ(2h) [m]	σ(A^*) [-]	2h [m]	A^* [-]	σ(2h) [m]	σ(A^*) [-]
8	0.9660	5.3454	0.01	0.0098	0.9600	5.1587	0.01	0.0329
7	0.8080	5.7817	0.01	0.0022	0.8020	5.7102	0.01	0.0244
6	0.6840	6.1251	0.01	0.0059	0.6780	5.9252	0.01	0.0247
5	0.5720	6.3756	0.01	0.0105	0.5660	6.1326	0.01	0.0269
4	0.4800	6.6674	0.01	0.0136	0.4740	6.4384	0.01	0.0264
3	0.3760	6.9636	0.01	0.0210	0.3700	6.6962	0.01	0.0329
2	0.2760	7.1828	0.01	0.0294	0.2700	6.9663	0.01	0.0430
1	0.1600	7.3077	0.01	0.0550	0.1480	7.1632	0.01	0.0746

With the statistical utility Myfitexy, described in detail in the velocity analysis section, we found the linear interpolation showed in Figure 3.13, which equations are for the aluminum reflector test

$$\ln(A^*) = 7.94 - 2.68 \cdot 2h \tag{3.16}$$

and for the HDPE reflector

$$\ln(A^*) = 7.55 - 2.35 \cdot 2h \tag{3.17}$$

The comprehensive results of the linear regression are reported in Table 3.6. The observation of Figure 3.13 and the results of the statistical tests highlight a worse interpolation on the amplitude data respect the velocity analysis. In particular the HDPE reflector gives a low accurate interpolation, like testified by the bad result of

the χ^2 test and by the low probability that the regression is effectively linear q. The bad interpolation on the HDPE experiment is due to the high dispersion of the amplitude data. Thus in the following analysis we consider for the water attenuation coefficient te value estimated with the aluminum sheet reflector

$$\alpha = 2.68 \pm 0.1 \left[\frac{1}{m} \right] \tag{3.18}$$

Table 3.6: *Results of the statistical tests performed for the estimation of the water attenuation coefficient.*

| Reflector	a	b	σ(a)	σ(b)	χ^2	q	R^2
Aluminum	7.9456	-2.6843	0.0538	0.1029	2.8230	0.4197	0.9963
HDPE	7.5537	-2.3550	0.0542	0.0961	8.9573	0.0299	0.9873
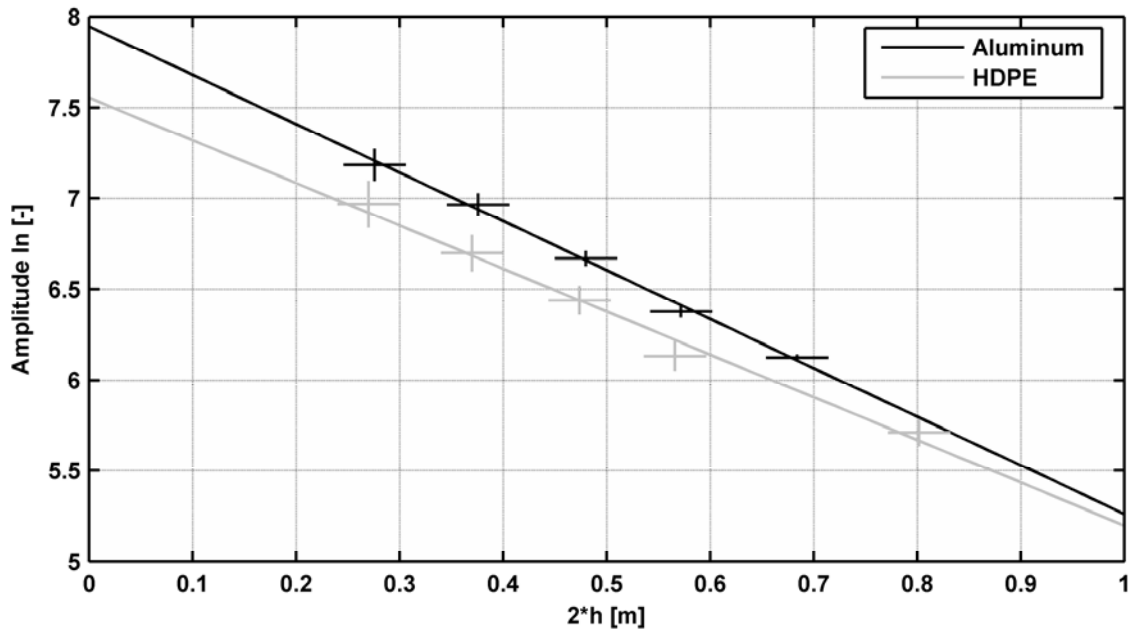
Figure 3.13: *Linear regression of the data retained reliable of Table 3.5 for the estimation of the water attenuation coefficient. The black line refers to the measurements with the aluminum sheet on the bottom, the gray line refers to the HDPE tank bottom. The error bars represent 3 times the standard deviations.*

Amplitude Spectra of the Reflection signals

In order to estimate the water attenuation coefficient in frequency domain, we performed a frequency analysis of the reflection signals relatives to the bottom of the tank. We firstly isolated the bottom reflections by muting the traces above and below the reflection signals. Figure 3.14a shows one of the GPR traces acquired on the aluminum reflector over a water depth of 13.8cm, we can identify the main bang event roughly at 8ns, the bottom reflection signals at 15ns and finally the multiple of the same reflection at 22ns. In Figure 3.14b, after the muting processing, remains only the bottom reflection event.
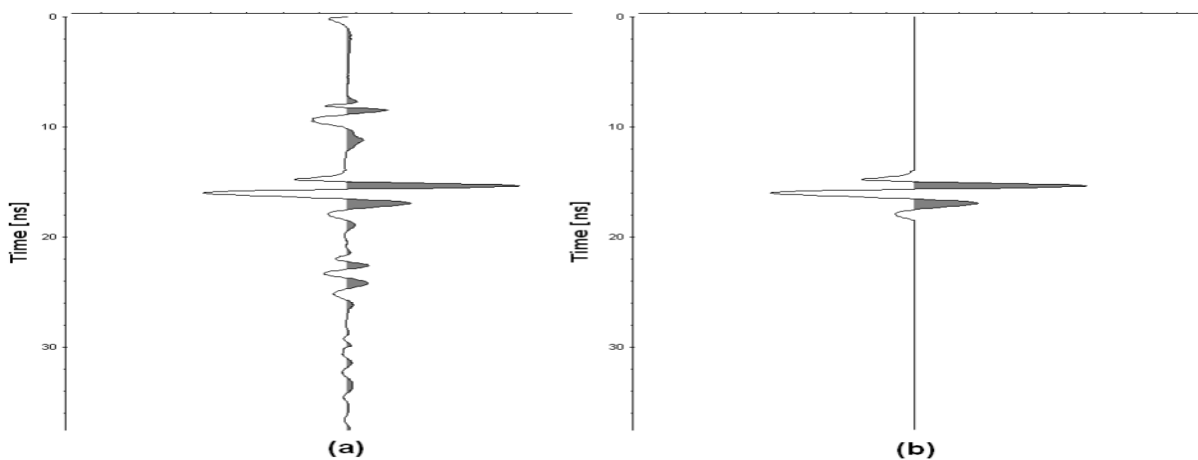
Figure 3.14: *Extraction of the reflection signal relative to the aluminum reflector (Pos 2, water depth 13.8 cm), for the estimation of the amplitude spectrum. On the left it is showed the trace before the muting processing (a), on the right the isolated bottom reflection signal (b).*

We estimated by the Sandmeier Reflex Win[©] Software the amplitude spectra from 0 to 2500 MHz of the isolated reflection signals, obtaining a 20MHz frequency sampling. We performed this process for all the traces acquired on each position with both the bottom reflectors. We disposed for each of the 16 measurements roughly 250 traces, then for each of them we have estimated the mean and the standard deviation of the amplitude spectrum. Figure 3.15a and Figure 3.15b compare respectively the amplitude spectra obtained by the measurements with and without the aluminum sheet on the tank bottom. We excluded from these comparisons the spectra relatives to the position 7, because the measurement performed on the aluminum reflector is affected by the noise described in section 3.5. The noise influences is well highlighted in Figure 3.16, where we can observe the abnormally broadband amplitude spectrum of this position with respects to all the other spectra.

However the low dispersion of the amplitude spectrum tells us the high repeatability of the noise. These observations confirm our choice of avoiding, in the velocity and attenuation analysis, the data acquired on the aluminum reflector relatives to position 7 (0.404 m water depth).

From Figure 3.16 we can infer for frequency higher than 1200 MHz all the estimation of the amplitude spectra are not accurate, in fact we can observe high standard deviations.

All the estimated amplitude spectra show their maxima in the 300÷700 MHZ frequency range. This result was expected because we adopted a 1500 MHz central frequency antenna, but the water acts like a low pass filter on the electromagnetic signals. The proof of this water behavior is also evident comparing the different spectra, in fact for higher water depth the amplitude spectra are more attenuated, moreover the higher frequency are more attenuated than the lower frequency.
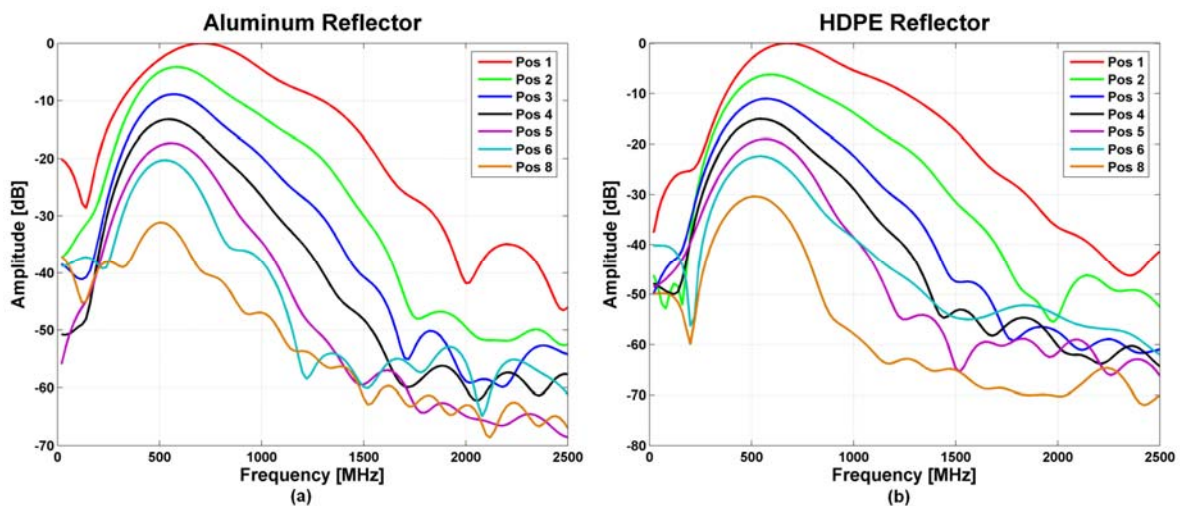
Figure 3.15: *Amplitude spectra of the isolated bottom reflection signals relatives to the acquisitions performed with the aluminum sheet (a) and with only the HDPE tank(b).*
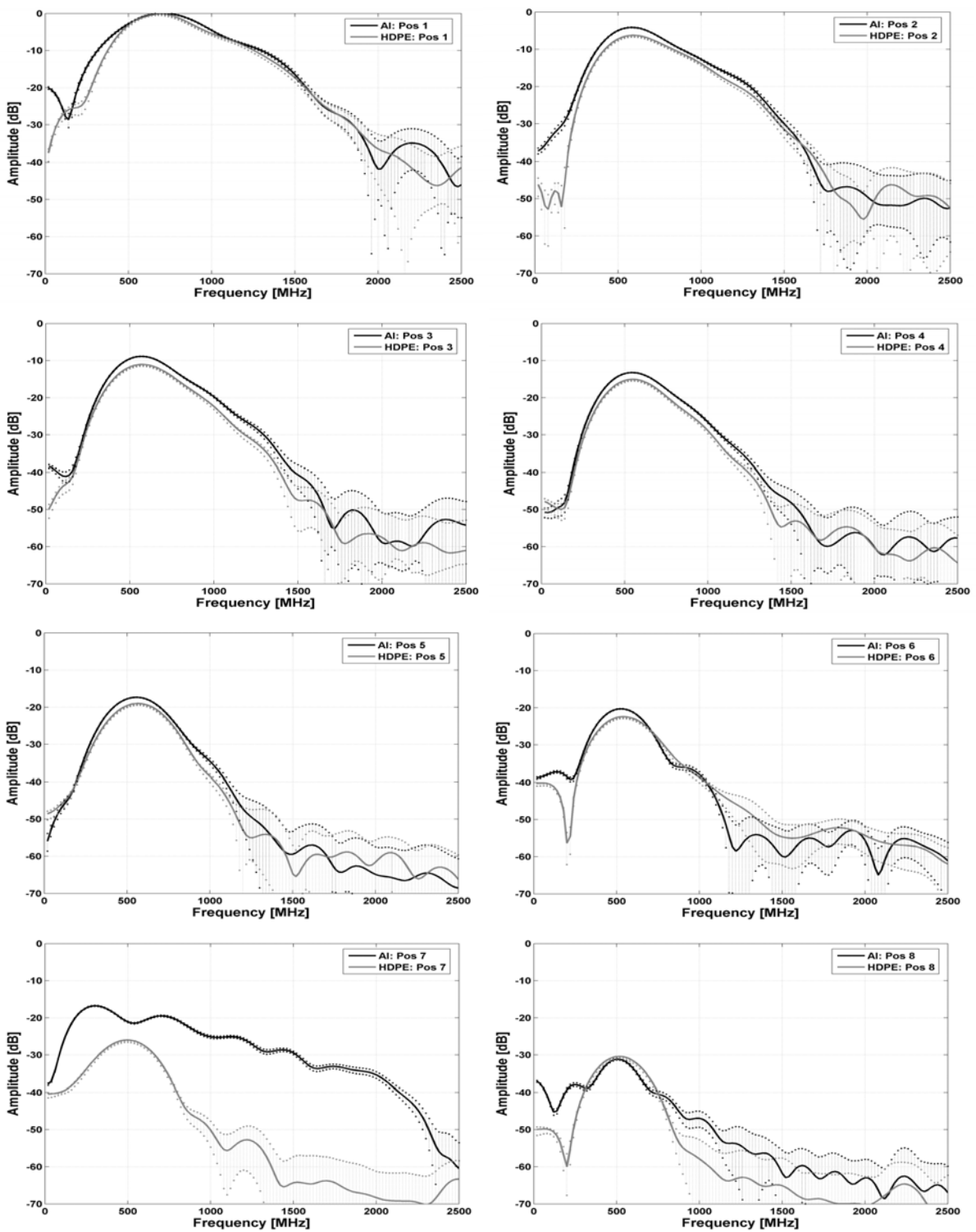
Figure 3.16: *Comparison between the amplitude spectra of the isolated reflection signals on the aluminum and HDPE reflectors, for each water depth acquired in the calibration tests.*

Time-Frequency Analysis of the Reflection Signals

The time-frequency analysis of the signals acquired in water allows us to recover important qualitative information about the propagation of the electromagnetic signal in water. Figure 3.17 and Figure 3.18 show the spectrograms relative to the measurements acquired respectively on the aluminum and HDPE reflectors. In all the showed plots are visible two main events: the main bang, placed roughly at 8ns, and the bottom reflection, placed from 12 to 36 ns dependent from the water depths. Moreover we could highlight the multiple of the bottom reflection when it occurs in the acquisition range. Considering the wide dynamic of the signals, we can not adopt the same color scale for all the graphs. However it is clear that the power of bottom reflection signal decrease for higher water depths. Moreover we have the confirm that higher frequencies of the reflection signals are more attenuated than lower frequencies, the same experimental evidence highlighted in the analysis of the amplitude spectra of the reflection signals in the previous section.

We could compare by the spectrograms the frequency content of the main bangs relative to the measurements in water and the measurement in air, showed in section 3.5. From the comparison we can assert that the main bang in air has a dominant frequency closed to the nominal frequency of the antenna (1500 MHz). Instead in water we could verify a shift of the main bang dominant frequency roughly toward 700 MHz.
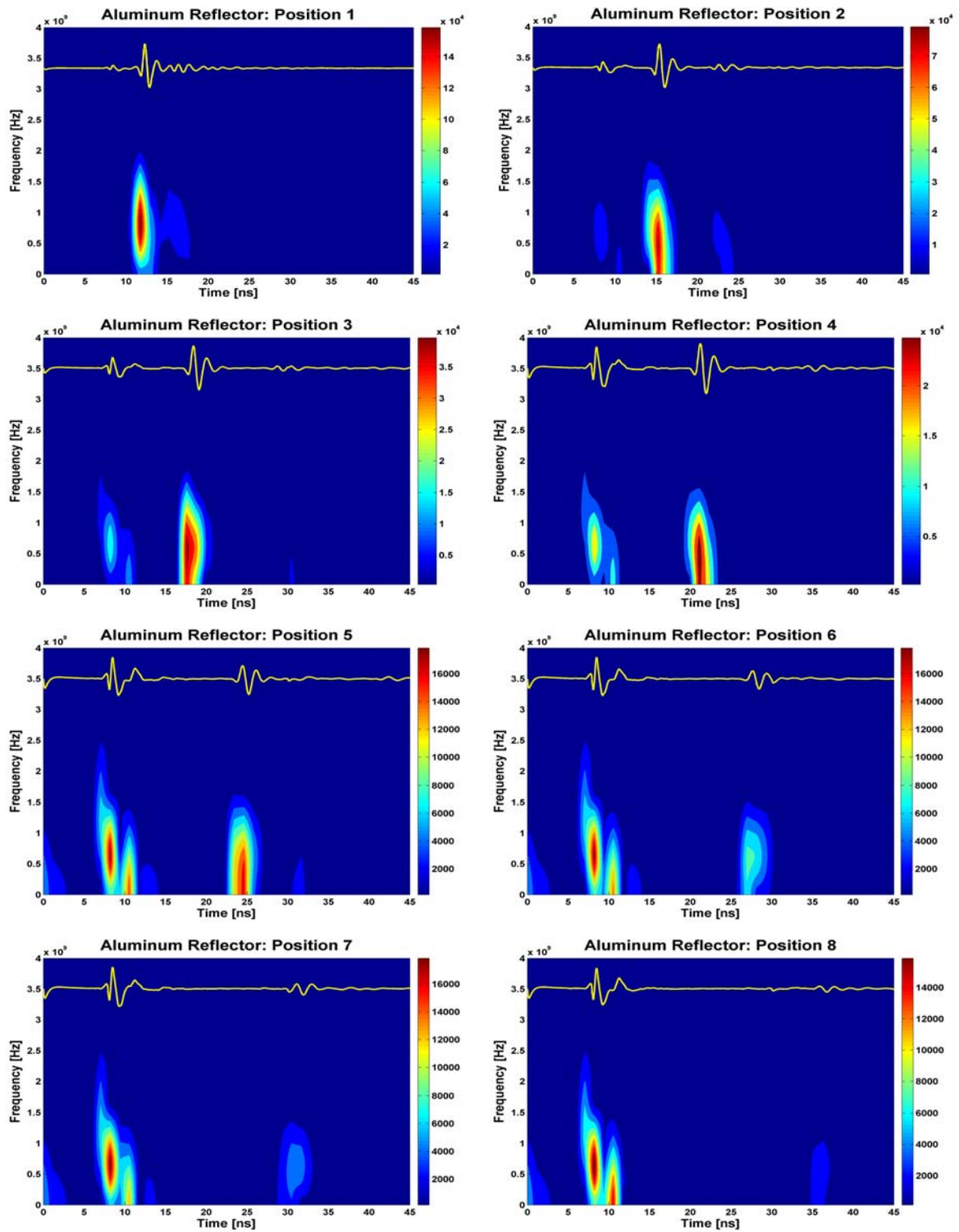
Figure 3.17: *Spectrograms of the signals acquired in the calibration tests for different water depths on the aluminum reflector. The yellow plots represent the average traces used for the spectrograms computation.*
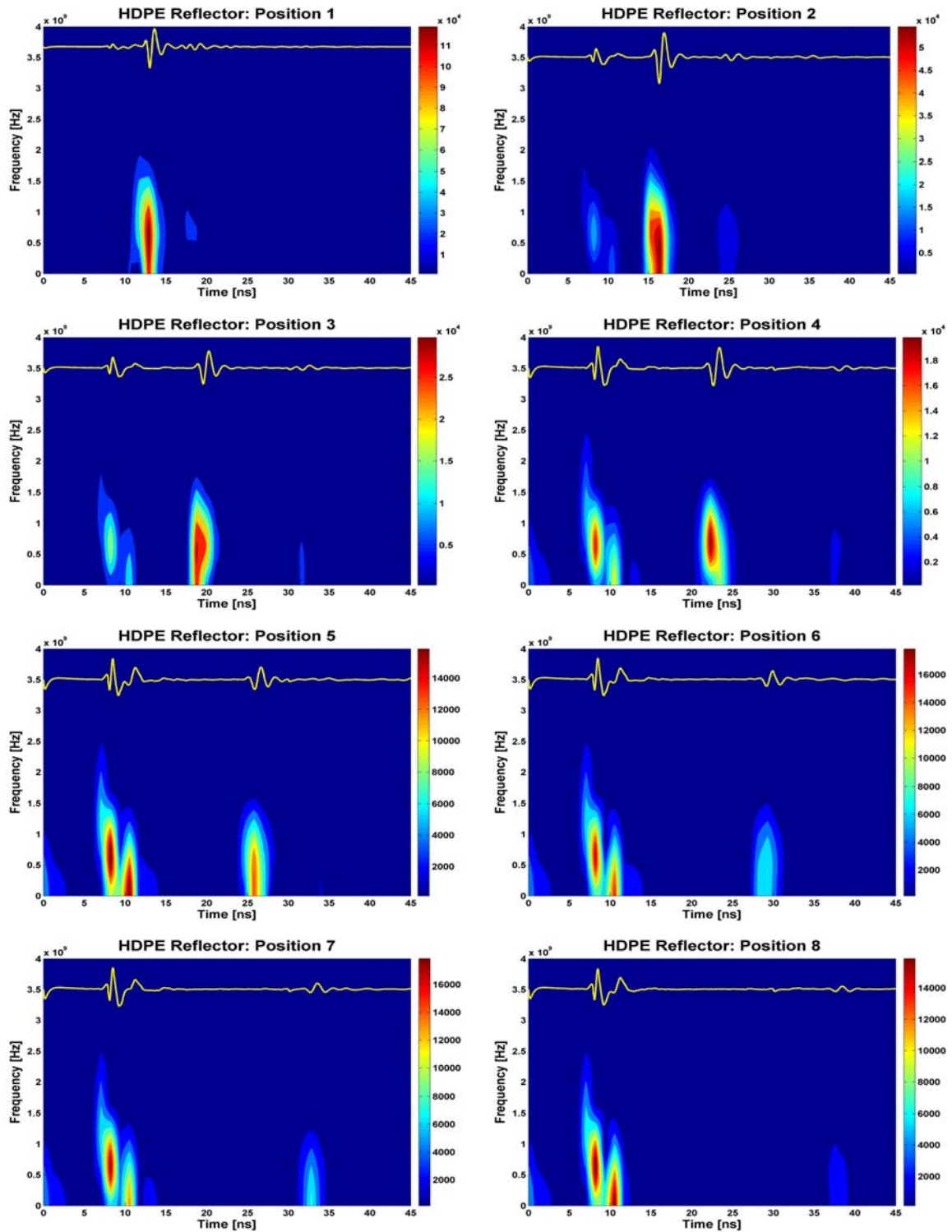
Figure 3.18: *Spectrograms of the signals acquired in the calibration tests for different water depths on the HDPE reflector. The yellow plots represent the average traces used for the spectrograms computation.*

Water Attenuation Factor in Frequency Domain

In the two previous sections from the observation of both the trace spectrograms and the reflection amplitude spectra we analyzed qualitatively the attenuation of the electromagnetic signal in water. Now we are ready to quantify the attenuation coefficient in frequency domain. In order to realize this task we started from the amplitude spectra of the isolated reflection signals showed in Figure 3.16. From the amplitude spectra we can collect the amplitude values of the bottom reflection from 0 to 2500 MHz with 20 MHz step. Then with the statistical utility, we iterated for each frequency available the linear regression on the reflection amplitude relative to different water depths, a process analogous to the analysis performed to find the attenuation coefficient in time domain. In Figure 3.19 we graphed the values of the water attenuation coefficient estimated by linear interpolation, with the relative uncertainties, of the experimental data acquired for different water depth with the aluminum and the HDPE reflectors.
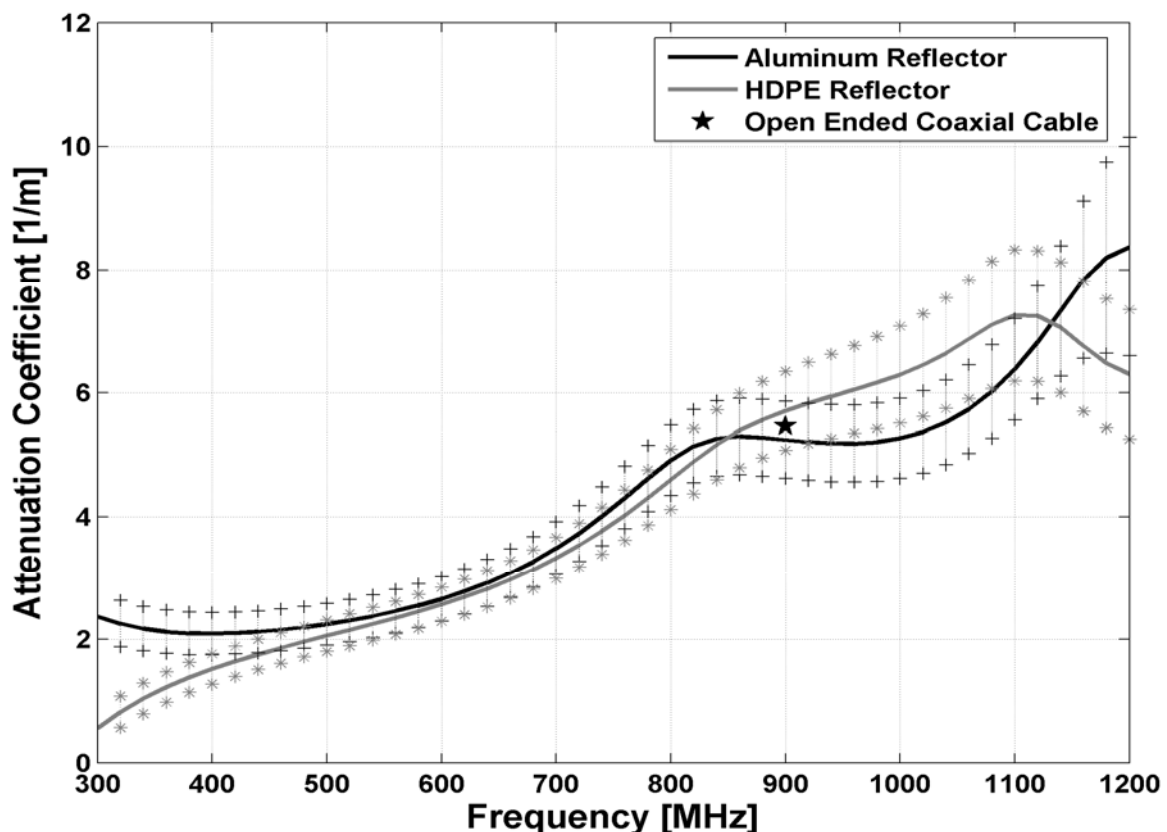
Figure 3.19: *Comparison between the water attenuation spectra estimated from the measurements acquired with the aluminum reflector (black line) and with the HDPE reflector (gray line). The error bars represents 3 times the standard deviations. The black star is the value founded with the Open Ended Coaxial Cable test.*

We concentrate our analysis on the frequency range 300-1200MHz because out of this band the amplitude spectra of the refection are affected by high noise. A previously test of the water attenuation coefficient, performed with an Open Ended Coaxial Cable (OECC), was available. The OECC test provides us a water attenuation of 5.24±0.21 1/m for the frequency value corresponding to 900 MHz. From Figure 3.19 we can highlight that in the frequency band 500-900MHz both the tests with different bottom reflectors provide values of the water attenuation includes in the respectively error intervals (±3 times the standard deviations). Moreover the value provided by the OECC is included in both the error intervals.

3.7.   Measurements with the Sediments

As far the calibration studies are consolidated, we are now ready to enter in the core of this chapter: the GPR experimentations in water with the sediments on the bottom of the tank. We start this section describing the particulate media chose for the experiments. In particular in section 3.7.1 we reported all the sediments specifications provided by the quarry and the grain size distribution analysis. The following section 3.7.2 describes the GPR data acquisition methods and the porosities measurements conducted on the sediments in the GPR experimentation conditions. Before the presentation of the result, we presented in section 3.7.3 the processing flow planned to allow the interpretation of the GPR measurements on the bottom sediments. The understanding of the overall processing flow let us to appreciate the results and interconnection among the physical properties obtained in section 3.7.4.

3.7.1.   Materials

We explained in the Experimental Design section the criterion of sediments selection. First of all we have a preference to study particulate media with characteristics as close as possible to the riverine bottom sediments. Then, we located an open quarry on the alluvial deposits near the PO river in Moncalieri, roughly 10 km far from the site of the following riverine survey described in chapters 4 and 5. We selected from the products of the open quarry five sediments: a loam (<0.5 mm), a fine sand (<2 mm), a coarse sand (2-5 mm), a round (3-8 mm) and a round (5-15 mm). The above materials were products extracted by the quarry and did not sustain any manufacturing process.

We selected the five sediments types to investigate a broad grain size distribution, without granulometric interference among the classes itself. About the smallest dimension, we avoided clay materials, because they have complexes electromagnetic behaviors. Instead the bigger dimension was selected with regard to the wavelength of the GPR signal in water. We explained in the Experimental Design section that for a 1500 MHz central frequency antenna correspond a wavelength of roughly 2÷2.5 cm. Then we selected all sediments smaller than this limit.

Loam (<0.5mm)

Table 3.7: *Petrographic description of the loam.*

Simplified petrographic description UNI EN 932-3		
Commercial denomination: Sabbia Finissima.		
Sample Description	Petrographic and geological identification	
Sample weight: 0.6kg;	Definition: sedimentary aggregate;	
Maximum grain dimension: 3mm;	Minerals composition %:	
Grain surface: rough;		Quartz 40%,
Grain shape: irregular;		femic and mica 35%,
Roundness: absent;		feldspar 25%,
Shattering degree: absent.	Shell fragments: traces,	
	Extraneous elements: absents;	
	Formation: alluvium;	
	Geological era: quaternary.	
Final denomination: Quartzofeldspathic heterogeneous sand.		

Table 3.8: *Analysis of the loam organic impurity.*

Organic impurity UNI EN 1744-1		
Dried mass (g):	M_9	379.3
Mass of light particles (g):	M_{10}	0
Light particles percentage	M_{LPC}	0

Table 3.9: *Fine fraction definition of the loam.*

Effective diameter (mm):	D_{10}	0.08
Uniformity coefficient (mm):	$U=D_{60}/D_{10}$	2.5

Grain size distribution analysis UNI EN 933-1 of the loam (<0.5mm)

Sample weight analyzed: 1068.2 g;

Sample weight retained: 1053.0 g.

Table 3.10: *Grain size distribution analysis of the loam*

Granulometric class	Retained mass	Passed mass	Retained mass (elementary frequency)	Retained mass (cumulative frequency)
[mm]	[g]	[g]	[%]	[%]
1		1053	0.00	100.00
0.5-1	51.6	1016.6	4.90	100.00
0.25-0.5	714.3	302.3	67.83	95.10
0.125-0.25	232.1	70.2	22.04	27.26
0.063-0.0125	55	15.2	5.22	5.22
Total:	1053.00			
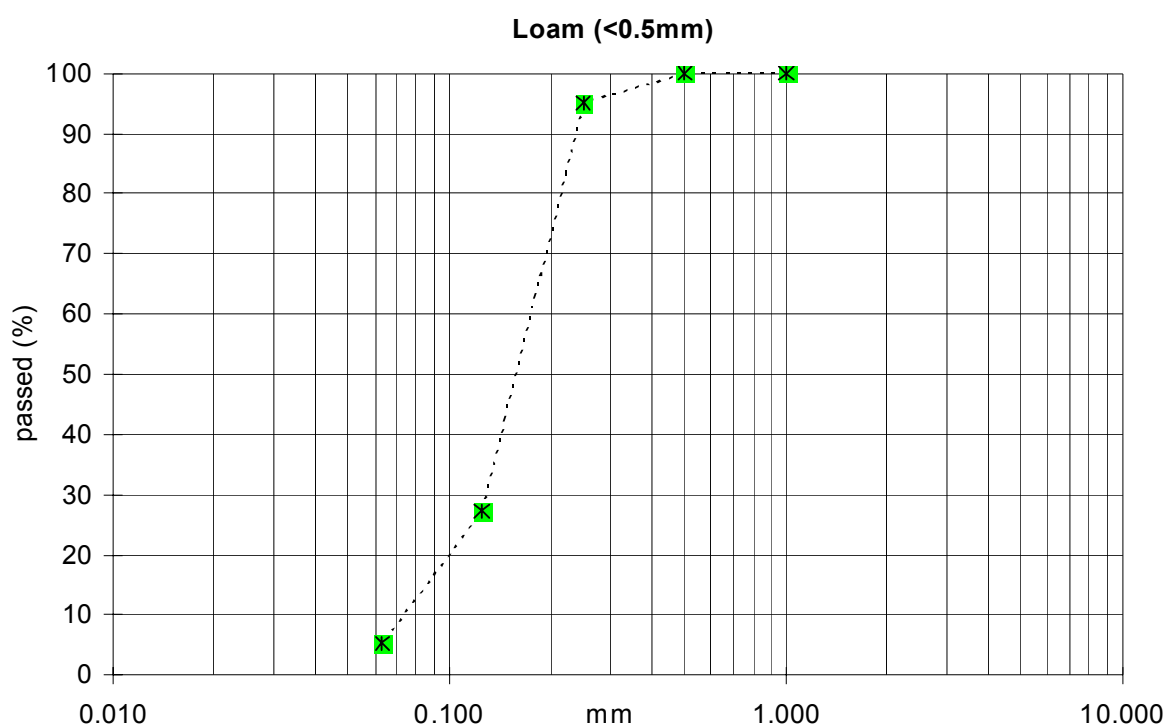
Figure 3.20: *Grain size distribution curve of the loam.*

Fine Sand (<2mm)

Table 3.11: *Petrographic description of the fine sand (<2mm).*

Simplified petrographic description UNI EN 932-3		
Commercial denomination: Sabbia 0.2.		
Sample Description	Petrographic and geological identification	
Sample weight: 0.6kg;	Definition: sedimentary aggregate;	
Maximum grain dimension: 3mm;	Minerals composition %:	
Grain surface: rough;		Quartz 40%,
Grain shape: irregular;		femic and mica 35%,
Roundness: absent;		feldspar 25%,
Shattering degree: absent.	Shell fragments: traces,	
	Extraneous elements: absents;	
	Formation: alluvium;	
	Geological era: quaternary.	
Final denomination: Quartzofeldspathic heterogeneous sand.		

Table 3.12: *Analysis of the fine sand (<2mm) organic impurity.*

Organic impurity UNI EN 1744-1		
Dried mass (g):	M_9	362.3
Mass of light particles (g):	M_{10}	1.1
Light particles percentage	M_{LPC}	0.3

Table 3.13: *Fine fraction definition of the fine sand (<2mm).*

Effective diameter (mm):	D_{10}	0.22
Uniformity coefficient (mm):	$U=D_{60}/D_{10}$	3.6

Grain size distribution analysis UNI EN 933-1 of the fine sand (<2mm)

Sample weight analyzed: 1107.7 g;

Sample weight retained: 1097.7 g.

Table 3.14: *Grain size distribution analysis of the fine sand (<2mm)*

Granulometric class	Retained mass	Passed mass	Retained mass (elementary frequency)	Retained mass (cumulative frequency)
[mm]	[g]	[g]	[%]	[%]
4		1097.70	0.00	100.00
4 - 2	10.2	1087.50	0.93	99.07
2 - 1	229.1	858.40	20.89	78.20
1 - 0.5	521.7	336.70	47.57	30.67
0.5 - 0.25	261.9	74.80	23.88	6.81
0.25 - 0.125	63.9	10.90	5.83	0.99
0.125 - 0.063	9.9	1.00	0.90	0.09
Totale:	1097.70			

Fine Sand (<2mm)
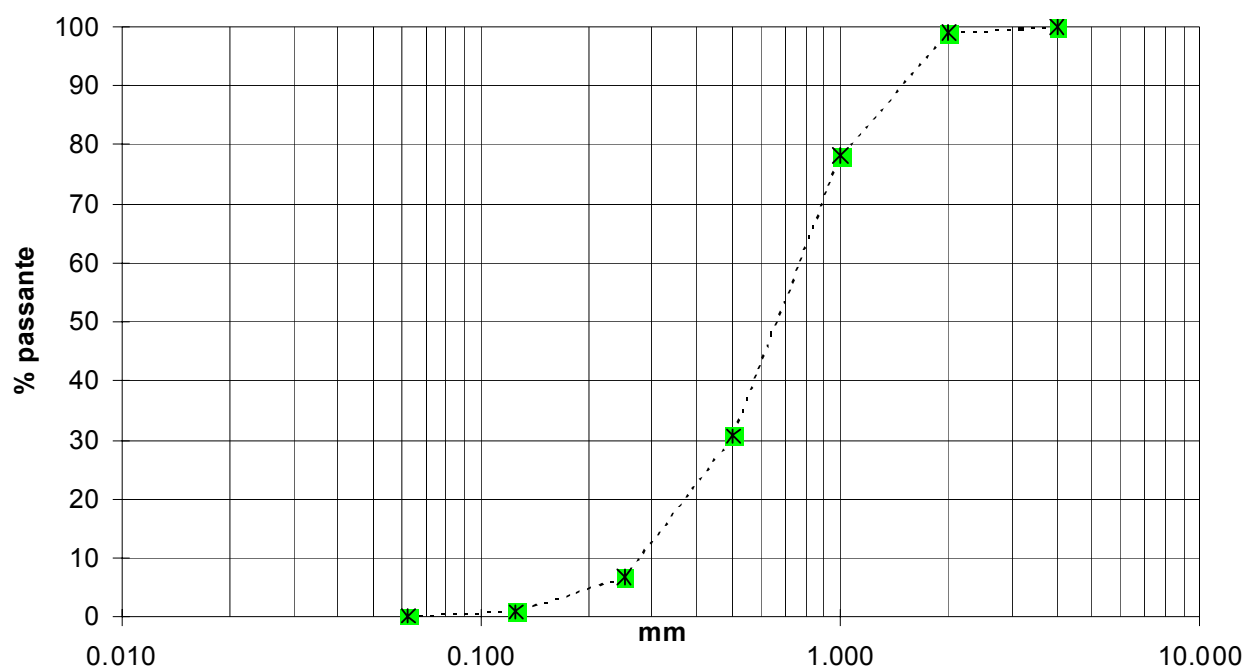
Figure 3.21: *Grain size distribution curve of the fine sand (<2mm).*

Coarse Sand (2-5mm)

Table 3.15: *Petrographic description of the coarse sand (2-5mm).*

Petrographic and geological identification
Definition: sedimentary aggregate;
Minerals composition %:
Basic rocks and greenschist 30%,
Quartzite40%,
Carbonates 20%,
Gneiss 10%.

Table 3.16: *Fine fraction definition of the* coarse sand (2-5mm)*.*

Effective diameter (mm):	D_{10}	0.1
Uniformity coefficient (mm):	$U=D_{60}/D_{10}$	10

Grain size distribution analysis UNI EN 933-1 of the coarse sand (2-5mm)

Sample weight analyzed: 1291.51 g;

Sample weight retained: 1290.51 g.

Table 3.17 *Grain size distribution analysis of the* coarse sand (2-5mm)

Granulometric class	*Retained mass*	*Passed mass*	*Retained mass (elementary frequency)*	*Retained mass (cumulative frequency)*
[mm]	*[g]*	*[g]*	*[%]*	*[%]*
>5.613	1.50	1291.51	0.12	100.00
5.153-4	128.01	1163.50	9.91	99.88
4-3.35	161.72	1001.78	12.52	89.97
3.35-2	571.94	429.84	44.28	77.45
2.0-1.0	371.54	58.30	28.77	33.17
1.0-0.063	56.7	1.60	4.39	4.40
<0.063	0.1	1.50	0.01	0.01
Total:	1291.51			

coarse sand (2-5mm)
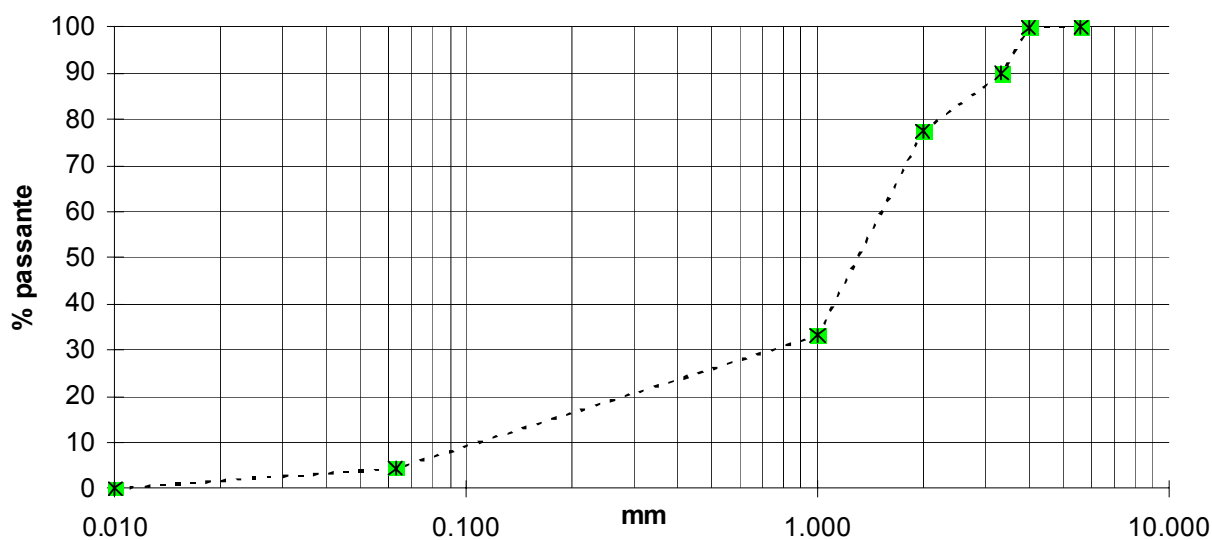
Figure 3.22: *Grain size distribution curve of the coarse sand (2-5mm).*

Round (3-8mm)

Table 3.18: *Petrographic description of the round (3-8mm).*

Petrographic and geological identification
Definition: sedimentary aggregate;
Minerals composition %:
Basic rocks 25%,
Quartzite 40%,
Carbonates 25%,
Gneiss 10%.

Table 3.19: *Fine fraction definition of the round (3-8mm).*

Effective diameter (mm):	D_{10}	0.1
Uniformity coefficient (mm):	$U=D_{60}/D_{10}$	10

Grain size distribution analysis UNI EN 933-1 of the _round (3-8mm)_

Sample weight analyzed: 1737.12 g;

Table 3.20 _Grain size distribution analysis of the round (3-8mm)._

Granulometric class	Retained mass	Passed mass	Retained mass (elementary frequency)	Retained mass (cumulative frequency)
[mm]	[g]	[g]	[%]	[%]
>7.925	84.60	1737.12	4.87	100.00
7.925-6.3	506.68	1230.44	29.17	95.13
6.3-5.6	441.3	789.14	25.40	65.96
5.6-4.75	310.63	478.51	17.88	40.56
4.75-4	228.95	249.56	13.18	22.68
4-3.35	100.1	149.46	5.76	9.50
<3.35	64.86	84.60	3.73	3.73
Totale:	1737.12			

Round (3-8mm)
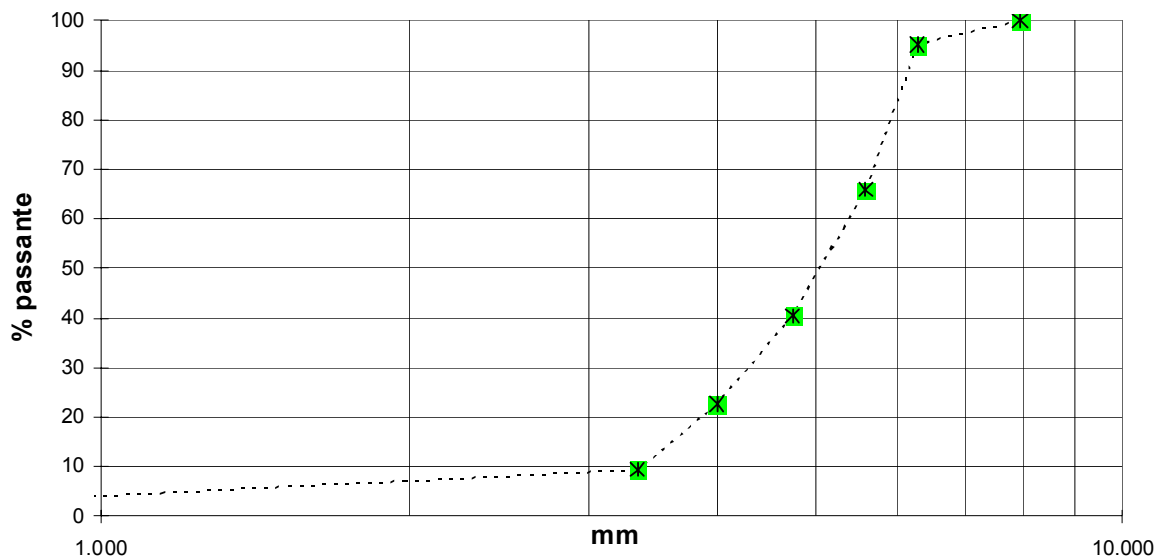
Figure 3.23: _Grain size distribution curve of the round (3-8mm)._

Round (5-15mm)

Table 3.21: *Petrographic description of the round (5-15mm).*

Simplified petrographic description UNI EN 932-3		
Commercial denomination: Sabbia Finissima.		
Sample Description	Petrographic and geological identification	
Sample weight: 20 kg;	Definition: sedimentary aggregate;	
Maximum grain dimension: 25mm;	Minerals composition %:	
Grain surface: from smooth to moderate roughly;		Quartz and similar 25%,
Grain shape: irregular;		Greenschist 75%,
Roundness: present;		
Shattering degree: traces on ophiolitic emerging.	Shell fragments: absents,	
	Extraneous elements: absents;	
	Formation: alluvium gravel;	
	Geological era: quaternary.	
Final denomination: Gravel of greenschist and quartz.		

Table 3.22: *Organic impurity analysis of the round (5-15mm).*

Organic impurity UNI EN 1744-1		
Dried mass (g):	M_9	402.8
Mass of light particles (g):	M_{10}	0
Light particles percentage	M_{LPC}	0

Table 3.23: *Fine fraction definition of the round (5-15mm).*

Effective diameter (mm):	D_{10}	0.8
Uniformity coefficient (mm):	$U=D_{60}/D_{10}$	1.4

### *Grain size distribution analysis UNI EN 933-1 of the round (5-15mm)*

Sample weight analyzed: 1648.2 g;

Sample weight retained: 1643.6 g.

Table 3.24: *Grain size distribution analysis of the round (5-15mm).*

Granulometric class	Retained mass	Passed mass	Retained mass (elementary frequency)	Retained mass (cumulative frequency)
[mm]	[g]	[g]	[%]	[%]
22.4		1643.60	0.00	100.00
22.4-16	51.2	1592.40	3.12	96.88
16-11.2	856	736.40	52.17	44.80
11.2-8	441.4	295.00	26.90	17.95
11-5.6	292.2	2.80	17.81	0.17
Totale:	1640.80			
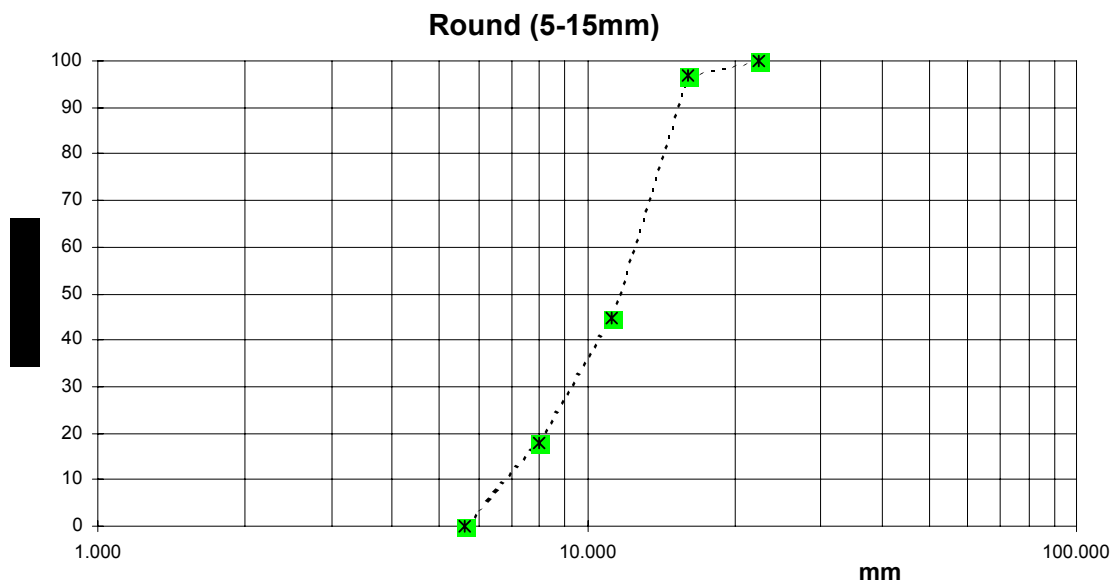
Figure 3.24: *Grain size distribution curve of the round (5-15mm).*

Table 3.25: *Volumic mass and water adsorbtion of the round (5-15mm).*

Volumic mass and water adsorbtion UNI EN 1097-6		
Mass in air of the particulate with dry surface (g)	M_1	1140.2
Apparent mass in water of the basket with the saturated sample (g)	M_2	5970.0
Apparent mass in water of the empty basket (g)	M_3	5264.8
Apparent mass in aria of the dried sample (g)	M_4	1135.9
Apparent volumetric mass of grain (kg/m^3)	ρ_A	2.64
Volumetric mass of the pre-dried grains (kg/m^3)	ρ_{RD}	2.61
Volumetric mass of the saturated grains with dried surface (kg/m^3)	ρ_{SSD}	2.62
Water adsorption (% on the dried mass)	WA_{24}	0.38

Table 3.26: *Results of the Los Angeles Test on the round (5-15mm).*

Fragmentation resistance definition UNI EN 1097-2		
Sample initial weight (g)	P1	5000.00
Retained weight at the end of the test with the 1.6mm sieve (g)	P2	3764.40
L.A.%	$\dfrac{P_1 - P_2}{P_1} \cdot 100$	24.71%

3.7.2. Methods

GPR Measurements

In this section we want to describe the experimental setup and procedure that we followed to carried out the GPR measurement with the sediments. The conceptual idea is the same of the calibration tests in water: we acquired several GPR measurements correspondent to different water depths, but in these tests the bottom reflector was a layer of sediments instead the HDPE or the aluminum sheet. Firstly we'll describe how we set up the tank with the particulate media on the bottom and after we'll focus our attention on the GPR acquisition procedures.

In these measurements we used the same tank adopted in the calibration test in water. We take care to realize a mattress of sediments that could be as much as possible homogeneous. In particular we want to avoid that different area of the tank was characterized by different granulometric distribution, due for example to different compacting. We were aware that with an accurate filling of the tank we could avoid horizontally variation of the sediments distribution. On the other hand we canned not control vertical gradient of the granulometric distribution especially in the finest sediments, however we tried to minimize this negative effect. We wanted to avoid also the formation air bubbles trapped in the sediments voids. In order to minimize all these possible inconvenient we firstly fill the tank with a little water depth, and then we filled the bottom of the tank with a rain of sediments. When the sediments reached the surface of the water we add a further water depth, with a low intensity water stream, and then we added new sediments. We iterate this process until the sediments mattress reached a thickness of 16-17 cm. After the preparation of the sediments mattress we fill the tank almost completely with water, and we wait between 1 to 3 days in order to allow the deposition of the finest fraction of the sediments dispersed in the water. We adopted this because the water turbidity could influences the electromagnetic parameters that we had previously estimated in the calibration tests, in particular the water permittivity and attenuation. The preparation process above-mentioned was adopted in all the materials investigated with the exclusions of the finest, the loam (<0.5mm). In fact this material was problematic due to the high time of deposition. In this case we firstly created the mattress of dried loam and then we add the water until we filled the tank. Successively we stirred the

bottom materials in order to obtain as much we can a regular surface, but due to the high turbidity we canned not see the bottom. After waiting 3 days the finest fraction was completely deposited and we discovered the not perfectly leveling of the sediments top. However we were content of this result and we did not repeat the mattress preparation because improbably we canned reach a better arrangement.

Figure 3.25: *Acquisition of the GPR measurements with the loam (<0.5mm).*

Figure 3.26: Detail of the antenna immersion in the tests with the loam (<0.5mm).

For each material investigated we acquired GPR measurements from 4 to 6 positions correspondent to different water depth, roughly included from 10 to 30 cm. In a different way respect the calibration test, we acquired from higher versus lower water depths, in order to avoid the raising of the finest sediment due to the water stream. In order to obtain an uncertainly range, for each water depth we acquired 3 GPR measurements, each one with 300 radar traces. During the tests we used thermometer, with ±0.1°C accuracy, to monitoring the water temperature. Finished the GPR measurements we downloaded the data and we perform a preliminary check on the amplitude and on the wave form of the radar traces acquired. Finished the quality control we then carried out the porosity measurements by direct methods.

Porosity Measurements

We estimated the porosity of the particulate materials in the experimental condition of the GPR measurements in order to compare the result of the GPR interpretations with a porosity value estimated direct methods.

The porosity of a particulate medium is the volume of voids per unit volume of the medium, where the voids may contain, for example, air or water (Santamarina, 2001). The porosity is defined by the ratio

$$n = \frac{V_V}{V} \hspace{3cm} (3.19)$$

where V_V is the volume of void space and V is the total or bulk volume of the material. In the general case of a three-phase system formed by solid, water and air the volume of voids is the sum of the water ad air volumes. Saturated sediments are two-phase system formed by only solid and water, and the volume of voids is then defined by the water volume. Considering the neglected air trapped among the grains, we can assume our experiments in saturated condition.

Figure 3.27: *Sediment in saturated condition before the weighting.*

Figure 3.28: *Zoom of the sediment surface before the weighting.*

In our case the main problem concerning the porosity estimation was the extraction of an undisturbed sample from the sediments used in the GPR experimentation. In fact the sampling of a particulate material is a challenging task, because small variation in the grain distribution could provide wide porosity variations. We examined three different procedures for the porosity estimation. The first solution taken in account was to perform the porosity estimation of the whole tank used for the GPR measurements. Considering the dimension of the tank the main disadvantage was

the large amount of sediment to be treat, however the accuracy of this method is the best achievable. The second possibility was the sampling of a significant volume of sediment, but we just commented about the difficulties to obtain an undisturbed sample. The last procedure available was to recreate the grain size distribution in a smaller scale using the same method adopted to fill the tank. Also this method is logistically an easy task but we could obtain doubtful results. Finally we preferred the first procedure above-mentioned, the estimation of the porosity using all the material available in the tank.

When all the GPR acquisitions on a particulate material were finished, with a siphon, we take away the water from the tank until the water level reached the top of the sediments, like is shown in Figure 3.27 and Figure 3.28. Finished the water siphoning we measured the height of the sediment with a ruler. Then with the help of a travelling hand-crane we weighted the tank filled with sediments, like is shown in Figure 3.29. In this way, by difference with the weight of the empty tank, we deduced the sediments weight in saturated condition. After we remove all the possible water with the siphon and then in order to dry the particular material we place all in an oven for a period included from 1 to 3 days, like is shown in Figure 3.30. Finally when we tested that the drying was completed, we weighted the dried materials in order to obtain the weight of the solid part.

Figure 3.29: Weighting operation of the tank with the sediment in saturated condition.

Figure 3.30: *Sediments arranged in the oven for the drying process.*

For the porosity computation n we compared two different formulations, the first formula taken in account is

$$n_1 = \left(\frac{P_w}{\rho_w} \right) \cdot \frac{1}{V} \qquad (3.20)$$

where P_w is the weight of the water part and ρ_w is its specific weight equal to 1005 ± 0.01 kg/m^3. For the porosity n_1 defined by equation (3.20) we deduced the standard deviation

$$\sigma(n_1) = \sqrt{\frac{1}{(\rho_w \cdot V)^2}\sigma^2(P_w) + \frac{P_w^2}{\rho_w^2 \cdot V}\sigma^2(\rho_w) + \frac{P_w^2}{\rho_w \cdot V^2}\sigma^2(V)} \tag{3.21}$$

that is function of $\sigma(P_w)$, $\sigma(\rho_w)$, $\sigma(V)$, the standard deviation respectively of the water weigth P_w, and specific weight ρ_w and of the total volume V. The water weight P_w was estimated by difference between the saturated and the dry conditions, and we imposed its uncertainly $\sigma(\rho_w)$ equal to 0.6 kg considering the balance accuracy. Introducing the weight of the solid part P_S, with its standard deviation $\sigma(P_S)$ and the specific weight of the solid part ρ_S with its standard deviation $\sigma(\rho_S)$, we deduced the second formula for the porosity n

$$n_2 = \frac{\dfrac{P_w}{\rho_w}}{\dfrac{P_S}{\rho_S} + \dfrac{P_w}{\rho_w}} \tag{3.22}$$

and the relative uncertainly

$$\sigma(n_2) = \sqrt{\begin{array}{l} \left[\rho_S \cdot P_S \dfrac{\rho_w}{(P_S \cdot \rho_w + P_w \cdot \rho_S)^2}\right]^2 \sigma^2(P_w) + \cdots \\[4mm] \cdots + \left[\rho_S \cdot P_w \dfrac{P_S}{(P_S \cdot \rho_w + P_w \cdot \rho_S)^2}\right]^2 \sigma^2(\rho_w) + \cdots \\[4mm] \cdots + \left[\rho_w \cdot P_w \dfrac{\rho_S}{(P_S \cdot \rho_w + P_w \cdot \rho_S)^2}\right]^2 \sigma^2(P_S) + \cdots \\[4mm] \cdots + \left[P_w P_S \dfrac{\rho_w}{(P_S \cdot \rho_w + P_w \cdot \rho_S)^2}\right]^2 \sigma^2(\rho_S) \end{array}} \tag{3.23}$$

We impose the specific weight of the solid part ρ_S equal to 2700 kg/m^3, and its standard deviation equal to 100 kg/m^3, to include in the uncertainly interval nearly all the typical specific weights of minerals.

Table 3.27: Data for the porosity evaluation of the particulate media in the GPR measurements conditions.

	Water Weight		Solid Weight		Total Volume		Porosity [according to (3.20)]		Porosity [according to (3.22)]	
	P_w	$\sigma(P_w)$	P_s	$\sigma(P_s)$	V	$\sigma(V)$	n_1	$\sigma(n_1)$	n_2	$\sigma(n_2)$
	[kg]	[kg]	[kg]	[kg]	[m³]	[m³]				
Loam (<0.5mm)	28.75	0.6	139.25	0.6	0.0858	0.006	0.333	0.025	0.357	0.01
Fine Sand (<2mm)	33.6	0.6	141.9	0.6	0.0912	0.006	0.367	0.025	0.389	0.01
Coarse Sand (2-5mm)	23.3	0.6	139.3	0.6	0.0858	0.006	0.27	0.02	0.31	0.01
Round (3-8mm)	33	0.6	145	0.6	0.0858	0.006	0.383	0.028	0.379	0.01
Round (5-15mm)	33.5	0.6	150	0.6	0.0912	0.006	0.365	0.025	0.375	0.01

Comparing the uncertainties of the two proposed methods to estimate the porosity, presented   in

Table 3.27, we inferred that the equation (3.22) gave more accurate values affected by lower uncertainties. Then in the nest sections we adopted the results of equation (3.22) to interpreter and compare the GPR results with the porosity estimated by direct methods.

3.7.3.   Processing Summary

Thanks to the theoretical background exposed in chapter 2 and to the knowledge acquired in the calibration analysis, we designed a processing to interpret the GPR measurements performed with the granular sediments. The objectives of this processing were to:

-    verify the results obtained in the calibration tests in water, in particular focusing our attention on the velocity of the electromagnetic pulse in water, the attenuation factor in the time domain and the spectra of the attenuation factor in frequency domain;

-    estimate the value of the bulk permittivity of the saturated sediments;

-    estimate the reflection coefficient of the interface between the water and the sediments.

In order to reach our goals, we designed two different processing flows. The first, shown in Figure 3.31, is based on the time analysis of the GPR reflections. The second method is shown in Figure 3.32 and is based on the amplitude analysis of the reflection events. All the processing operations are performed with the same software previously adopted for the interpretation of the calibration tests: the Sandmeier Reflex Win$^{©}$, the Mathworks™ Matlab$^{®}$ and the homemade utility Myfitexy.

Velocity Analysis Processing Flow

Now we enter in the details of the processing flow shown in Figure 3.31, based on the velocity analysis. We started the processing by the extraction from the raw data (1) of a significant set of traces (2). At each position, we acquired 3 GPR measurements, each one consists of roughly 300 traces. In order to remove possible transient phenomena, due to the turn-on and turn-off of the GPR system, we removed from each measurement the first and final 100 traces. Then, for each position remain roughly 100 traces. From these set of traces, we picked the times of three distinct events: the main bang of the antenna (3), the reflection from the sediments top (4), and finally the reflection from the sediments bottom (5). We estimated the velocity of the electromagnetic wave in water (9) in the same manner of the calibration tests. Firstly we evaluated the time of flight of the radar pulse in water (6) by difference from the reflection time of the sediments top and the main bang time. After we graphed the water depth data versus the time of flight in water,

and then with the statistical utility Myfitexy we found the interpolation of the experimental data (7). Finally we compared the angular coefficient of the linear regression (10), which is an estimate of the electromagnetic velocity, with the value previously founded in the calibration tests in water (11).
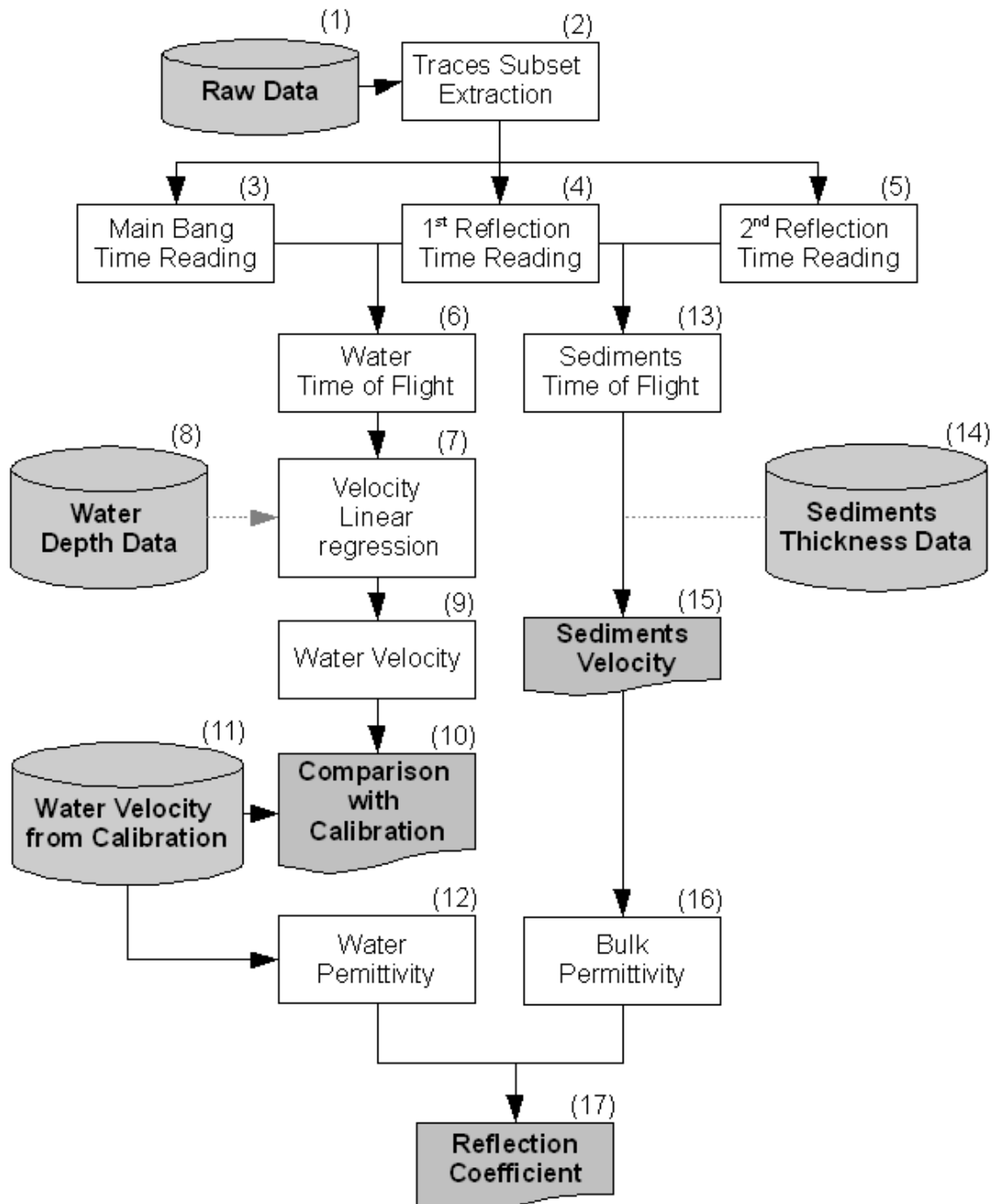

Figure 3.31: Processing flow adopted in order to estimate, by the velocity analysys, the reflection coefficient of the interface between water and sediments.

In order to evaluate the velocity of the GPR pulse in the saturated sediments (15) we needed the information of the sediment thickness (14), available from the direct measurements, and the time of flight in the sediment layer (13). We estimated the time of flight of the GPR pulse in the particulate media by difference from the reflection times of the sediments top (4) and bottom (5). The simplified relation expressed in equation (2.43), allows us to find both the bulk permittivities of the saturated sediments (16) and the water permittivity (12) by the velocity of the electromagnetic pulse in the particulate media and in water respectively. Finally, knowing the water and saturated sediments, we determined the reflection coefficient of the sediment top interface using the simplified relation expressed in equation (2.54).

Amplitude Analysis Processing Flow

By the amplitude analysis of the reflection from the sediments top, summarized in Figure 3.32, we estimated the bulk permittivity of the particulate media (39) and the reflection coefficients of the interface between water and sediments (36). Then, we compared these values with the ones previously founded in the velocity analysis. Moreover, we evaluated the attenuation factor in time domain (30) and its spectra in frequency domain (24), and we compared the results with the ones obtained in the calibration tests in water.

We analyzed the same traces subset of the raw data (18), previously extracted in the time analysis (19). From these traces, we picked the amplitude of reflection due to the impedance contrast between water and sediments (27). In order to find the attenuation factor in time domain, we recovered the divergence loss on the amplitude of reflection using the water depths information (28). We then graphed for each material, the recovered amplitude of reflections for each water depth, versus the distance covered by the electromagnetic pulse. Then, we founded the linear interpolation of the experimental data with the statistical utility Myfitexy (29). Finally, we compared the angular coefficient of the regression line (32), which is an estimate of the attenuation factor (30), with the value founded in the calibration tests (31).

We then founded the spectra of the attenuation factor in frequency domain. We extracted from the selected traces subset the reflection signal due to the sediments top by muting the traces above and below the reflection event (20). For each material and position we computed the amplitude spectrum of the isolated reflection

signals (21) and we recovered these values for the geometrical loss (22), with the water depth information. We then iterated the linear interpolation (23), performed also in the time domain analysis, in order to find the attenuation factor for each frequency sampled in the amplitude spectra, and we compared these results (26) with the ones founded in the calibration tests (25). These comparisons were performed mainly to obtain quality indication of the data acquired. After, we started the processing in order to obtain information on the sediments EM properties, by the interpretation of the amplitude of reflection.

We derived the reflection coefficients of the impedance contrast between the water and the particulate media adopting the simplified version of the radar equation (3.11). In fact, from this relation, we could estimate the reflection coefficients of the sediment top knowing two terms: the amplitude emitted from the antenna transmitter and entered in the water (35), and the amplitude of reflection of the sediment top recovered for the geometrical (34) and intrinsic losses (33). We obtained an estimate of the amplitude entered in the water indirectly, by the interpretation of the calibration in water on the aluminum reflector. In addition, we corrected the amplitude of reflection for the two losses take in account knowing the water depth and the attenuation factor estimated in the calibration tests.

Moreover, knowing the water permittivity (38), estimable from the water velocity (37) using the simplified relation (2.43), and the reflection coefficient of the sediment top we derive from equation (2.54) an estimate of the bulk permittivity of the saturated sediments (39).
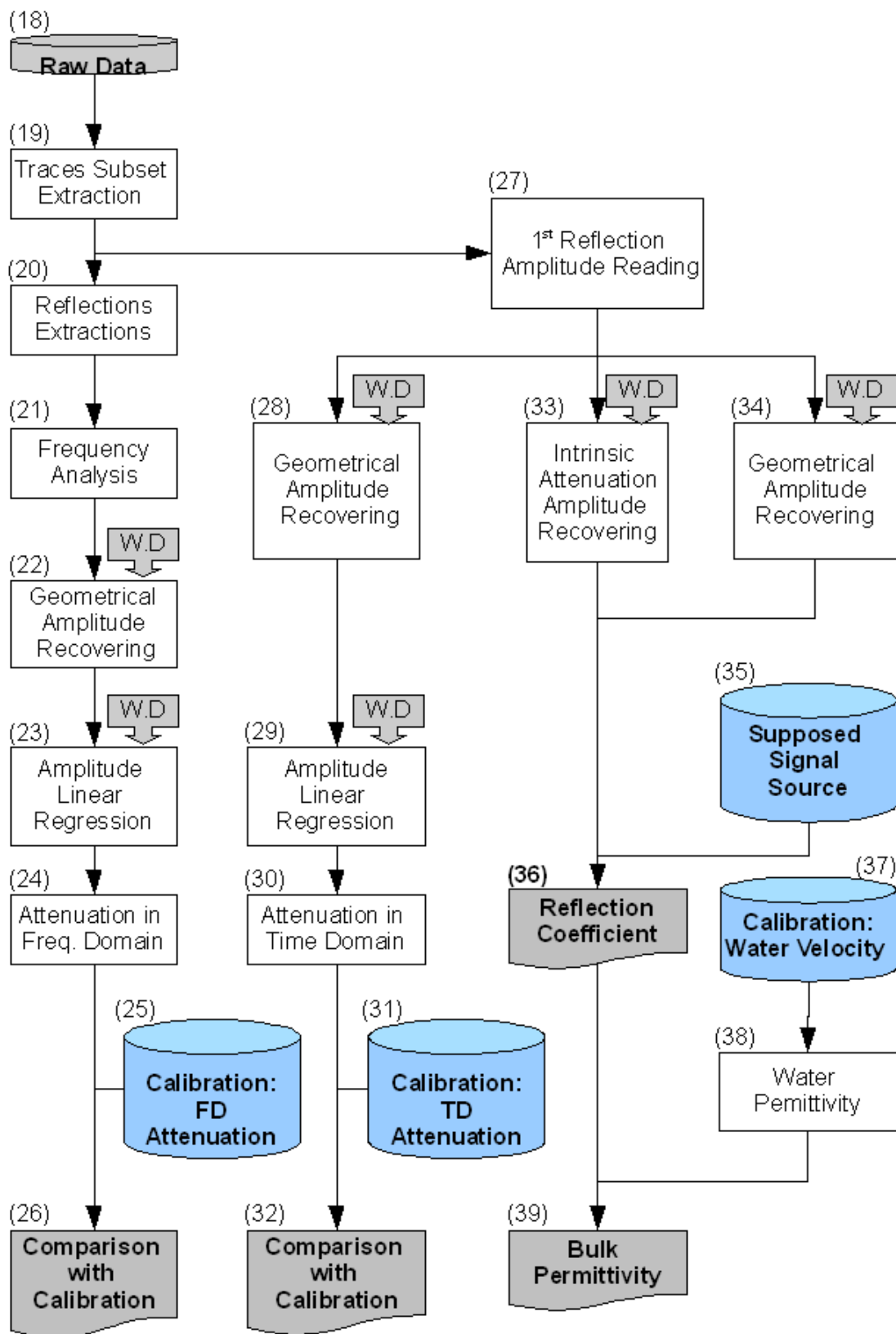
Figure 3.32: *Processing flow adopted in order to estimate, by the amplitude analysys, the reflection coefficient of the interface between water and saturated sediments and the bulk permittivity of the particulate media. The arrow callouts marked by W.D. represent the water depth data input.*

3.7.4. Results

Now we present the results of the GPR measurements analyzed with the processing flows described in section 3.7.3. Firstly, we want to start from the presentation of some examples of raw data acquired. In particular, for each particulate material investigated and for each antenna position, correspondent to the water depths reported in Table 3.28, we selected from the center of the first radargrams acquired one GPR trace. Figure 3.33 shows all the 101st GPR traces extracted by the radargrams.

Table 3.28: *Summary of the measurements performed on the sediments. For each material and position it is reported: the distance measured between the antenna and the bottom tank h_T; the sediment thickness h_B measured; the water depth h_W estimated by difference between h_T and h_B; and finally the relative uncertainties $\sigma(h_T)$ $\sigma(h_B)$ and $\sigma(h_W)$.*

Material	Position	h_T [m]	$\sigma(h_T)$ [m]	h_B [m]	$\sigma(h_B)$ [m]	h_W [m]	$\sigma(h_w)$ [m]
Loam (<0.5mm)	Pos 1	0.455	0.005	0.16	0.005	0.295	0.01
	Pos 2	0.405	0.005	0.16	0.005	0.245	0.01
	Pos 3	0.358	0.005	0.16	0.005	0.198	0.01
	Pos 4	0.316	0.005	0.16	0.005	0.156	0.01
Fine Sand (<2 mm)	Pos 1	0.477	0.005	0.17	0.005	0.307	0.01
	Pos 2	0.425	0.005	0.17	0.005	0.255	0.01
	Pos 3	0.404	0.005	0.17	0.005	0.234	0.01
	Pos 4	0.357	0.005	0.17	0.005	0.187	0.01
	Pos 5	0.303	0.005	0.17	0.005	0.133	0.01
	Pos 6	0.256	0.005	0.17	0.005	0.086	0.01
Coarse Sand (2-5 mm)	Pos 1	0.463	0.005	0.16	0.005	0.303	0.01
	Pos 2	0.423	0.005	0.16	0.005	0.263	0.01
	Pos 3	0.396	0.005	0.16	0.005	0.236	0.01
	Pos 4	0.362	0.005	0.16	0.005	0.202	0.01
	Pos 5	0.309	0.005	0.16	0.005	0.149	0.01
	Pos 6	0.257	0.005	0.16	0.005	0.097	0.01
Round (3-8 mm)	Pos 1	0.46	0.005	0.16	0.005	0.3	0.01
	Pos 2	0.392	0.005	0.16	0.005	0.232	0.01
	Pos 3	0.352	0.005	0.16	0.005	0.192	0.01
	Pos 4	0.286	0.005	0.16	0.005	0.126	0.01
Round (5-15 mm)	Pos 1	0.459	0.005	0.17	0.005	0.289	0.01
	Pos 2	0.401	0.005	0.17	0.005	0.231	0.01
	Pos 3	0.355	0.005	0.17	0.005	0.185	0.01
	Pos 4	0.308	0.005	0.17	0.005	0.138	0.01

From Figure 3.33 we can observe that the main bang event remain constant in position and amplitude among all the measurements. On the other hand, in all the experiments the reflections from the top and the bottom of the sediments became more attenuated for higher water depth. However all the measurements are not noised and the bottom reflections are always clear.
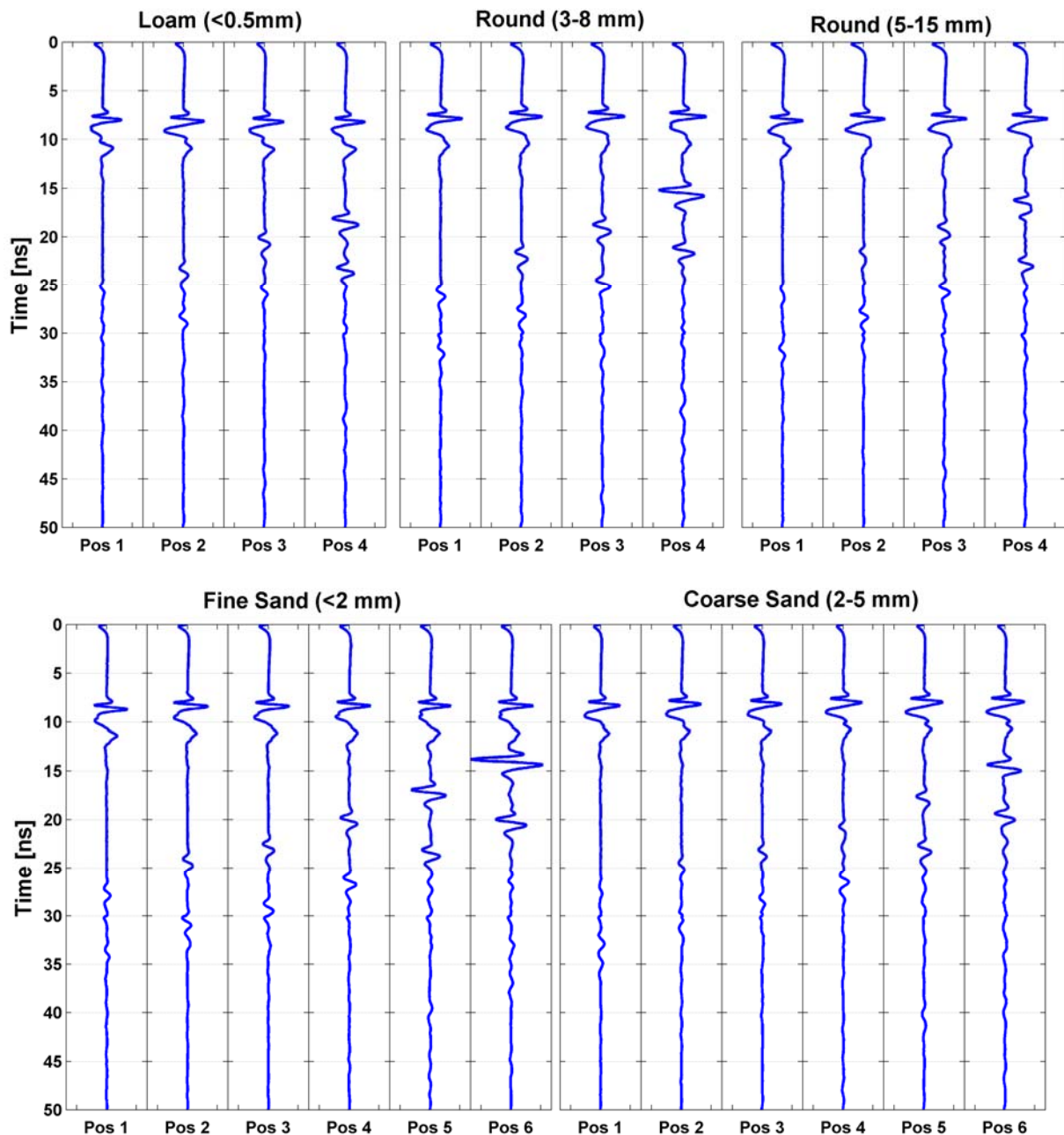
Figure 3.33: *Example of GPR raw data acquired with the particulate media on the bottom of the tank. For each material and position (Pos) we selected the 101st trace of the nearly 300 traces acquired. All the traces are plotted with the same amplitude magnification.*

Velocity of the GPR signal in water

Now we are going to estimate the velocity of the GPR pulse in water, with the same procedure adopted in the calibration tests: firstly we estimate the velocity values for each antenna positions and after one more robust value will be estimate by the linear regression of the distances covered by the electromagnetic pulse versus the time of flights.
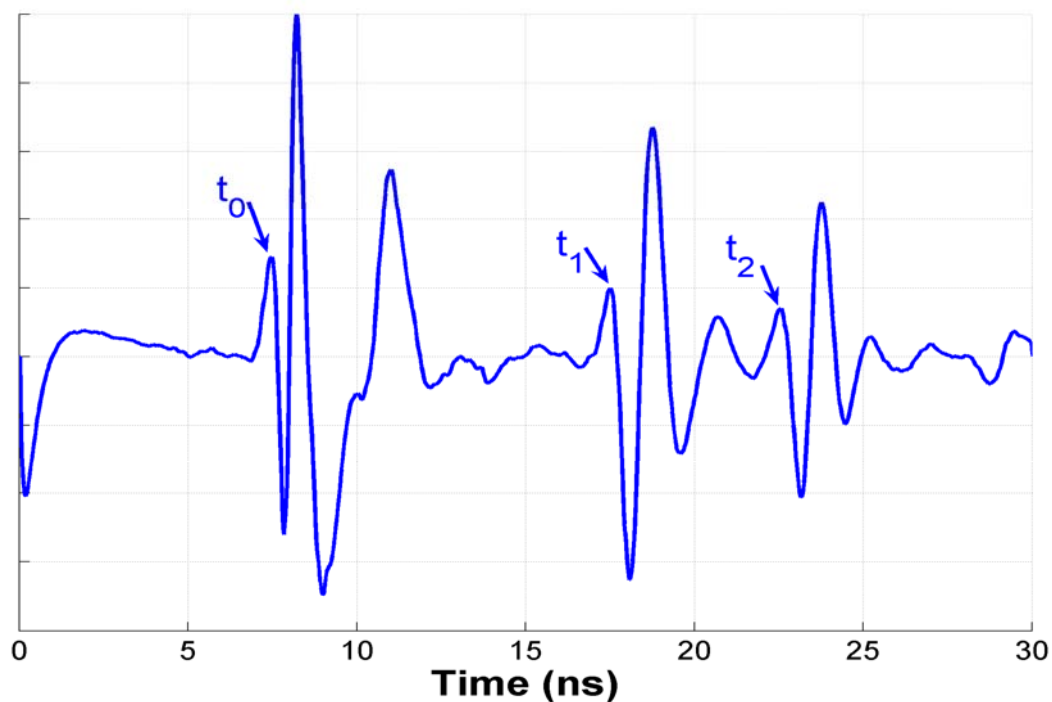
Figure 3.34: *Mean trace of the GPR signals relative to the 1st measurement in position 4 with the Loam (< 0.5mm) on the bottom of the tank. The arrows refer to the picking on the man bang event (t_0), on the sediments top (t_1) and on the tank bottom (t_2) respectively.*

In order to estimate the electromagnetic velocity in water, we need the water depth data h_W for each antenna position and its uncertainties $\sigma(h_W)$. We did not measure the water depths directly, and we deducted its values by difference between the antenna distance h_T from the bottom of the tank and the thickness of the sediments layer h_B. We assume the uncertainties of both the antenna height $\sigma(h_T)$ and the sediments thickness $\sigma(h_B)$ equal to 0.5 cm according to the precision expected by the direct measurements with a ruler. Then, we evaluated the water depth data h_W ,reported in Table 3.28, by:

$$h_W = h_T - h_B \quad [m] \tag{3.24}$$

and the relative uncertainty $\sigma(h_W)$ by:

$$\sigma(h_W) = \sigma(h)_T + \sigma(h_B) \quad [m] \tag{3.25}$$

From the radargrams we picked the main bang times t_0 and the reflections times t_1 from the top of the sediment layer, like is shown in Figure 3.34. We then estimated the time of flights TOF_W in water of the electromagnetic pulse, by difference between the reflection times t_1 and the main bang times t_0.

$$TOF_W = t_1 - t_0 \quad [ns] \tag{3.26}$$

We need to take in account that the time of flights in water TOF_W refers to the entire distance covered by the electromagnetic pulse in water, then the there and back paths between antenna and top of the sediments.

We estimated the standard deviation of both the main bang times $\sigma(t_0)$ and the reflection times $\sigma(t_1)$ from the picked time data. We then propagated this uncertainty in order to find the uncertainty relative to the time of flights in water $\sigma(TOF_W)$.

$$\sigma(TOF_W) = |\sigma(t_1) + \sigma(t_0)| \quad [ns] \tag{3.27}$$

Now we are ready to evaluate the velocity of the electromagnetic pulse V_W in water for each GPR measurement by

$$V_W = \frac{2 \cdot h_W}{TOF_W} \quad \left[\frac{m}{ns} \right] \tag{3.28}$$

with its uncertainty $\sigma(V_W)$

$$\sigma(V_W) = \left| \frac{2}{TOF_W} \right| \cdot \sigma(h_W) + \left| \frac{2 \cdot h_W}{TOF_W^2} \right| \cdot \sigma(TOF_W) \quad \left[\frac{m}{ns} \right] \tag{3.29}$$

We reported in Table 3.29 the values of the electromagnetic velocity in water estimated by equation (3.29) for each one of the GPR measurements acquired. From Table 3.29 we can observe that for the same particulate media we obtained dispersed velocity values. We need to take in account that for the same bottom sediments, all the measurements are acquired in a small temporal interval, and then we excepted a water media with the same electromagnetic properties. On the other hand, we can accept wider variations of the water electromagnetic properties among tests performed with different bottom sediments. In fact, these tests are carried out in different days and then external factors, like temperature, could have influenced the water properties. Consequently, the high dispersion of the velocity values in Table 3.29 among tests with different positions on the same bottom material, tells us that this first procedure to estimate the EM velocity is affected by low precision.

Table 3.29: *Velocity values of the electromagnetic pulse in water estimated by equation (3.28) for each GPR measurements acquired.*

Material	Position	1st Measurement V [m/ns]	σ(V) [m/ns]	2nd Measurement V [m/ns]	σ(V) [m/ns]	3rd Measurement V [m/ns]	σ(V) [m/ns]
Loam (<0.5mm)	Pos 1	0.0328	0.0012	0.0328	0.0012	0.0328	0.0012
	Pos 2	0.0309	0.0013	0.031	0.0013	0.031	0.0013
	Pos 3	0.0315	0.0017	0.0316	0.0017	0.0316	0.0017
	Pos 4	0.0296	0.002	0.0297	0.002	0.0296	0.002
Fine Sand (<2 mm)	Pos 1	0.032	0.0011	0.032	0.0011	0.032	0.0011
	Pos 2	0.0312	0.0013	0.0312	0.0013	0.0312	0.0012
	Pos 3	0.0317	0.0014	0.0317	0.0014	0.0317	0.0014
	Pos 4	0.0309	0.0017	0.031	0.0017	0.031	0.0017
	Pos 5	0.0291	0.0023	0.0291	0.0022	0.0291	0.0022
	Pos 6	0.0287	0.0034	0.0286	0.0033	0.0286	0.0034
Coarse Sand (2-5 mm)	Pos 1	0.0313	0.0011	0.0313	0.0011	0.0313	0.0011
	Pos 2	0.0309	0.0012	0.0309	0.0012	0.0309	0.0012
	Pos 3	0.0302	0.0013	0.0302	0.0013	0.0302	0.0013
	Pos 4	0.0302	0.0016	0.0302	0.0016	0.0302	0.0016
	Pos 5	0.0288	0.002	0.0292	0.002	0.0292	0.002
	Pos 6	0.0276	0.0029	0.0277	0.0029	0.0276	0.0029
Round (3-8 mm)	Pos 1	0.0327	0.0011	0.0327	0.0011	0.0327	0.0011
	Pos 2	0.0317	0.0014	0.0318	0.0014	0.0318	0.0014
	Pos 3	0.0326	0.0018	0.0325	0.0018	0.0325	0.0017
	Pos 4	0.0311	0.0025	0.0311	0.0025	0.031	0.0025
Round (5-15 mm)	Pos 1	0.0316	0.0012	0.0316	0.0012	0.0316	0.0012
	Pos 2	0.032	0.0015	0.032	0.0015	0.032	0.0015
	Pos 3	0.031	0.0017	0.0309	0.0018	0.031	0.0018
	Pos 4	0.0295	0.0022	0.0295	0.0022	0.0295	0.0022

We can evaluated, for each test with a particulate media on the bottom of the tank, a more reliable velocity estimation by the interpolation of the data relatives to different water depths. The same approach adopted in the calibration tests.

In Table 3.30 we reported the input data required to find the regression line of the distances $2 \cdot h_W$ covered by the electromagnetic pulse in water versus the correspondent times of flight TOF_W, for each type of bottom sediments. The interpolation could be expressed in the form

$$Y[m] = a[m] + b[m/s] \cdot X[s] \tag{3.30}$$

Table 3.30: *Input data of the linear regressions, distance covered 2·h_W versus the time of flight in water TOF_W, performed in order to find the velocities of the electromagnetic pulse in water for each of the 5 tests with different bottom materials.*

Material	Position	X TOF_W [ns]	Y 2h_W [m]	σ(X) σ(TOF_W) [ns]	σ(Y) σ(2h_W) [m]	Position	X TOF_W [ns]	Y 2h_W [m]	σ(X) σ(TOF_W) [ns]	σ(Y) σ(2h_W) [m]
Loam (<0.5mm)	POS 1	17.98	0.59	0.057	0.02	POS 3	12.58	0.40	0.039	0.02
		17.98	0.59	0.035	0.02		12.54	0.40	0.032	0.02
		17.99	0.59	0.042	0.02		12.54	0.40	0.038	0.02
	POS 2	15.84	0.49	0.036	0.02	POS 4	10.54	0.31	0.035	0.02
		15.81	0.49	0.041	0.02		10.51	0.31	0.030	0.02
		15.81	0.49	0.027	0.02		10.54	0.31	0.023	0.02
Fine Sand (<2 mm)	POS 1	19.19	0.61	0.031	0.02	POS 4	12.08	0.37	0.010	0.02
		19.19	0.61	0.025	0.02		12.08	0.37	0.014	0.02
		19.19	0.61	0.028	0.02		12.08	0.37	0.022	0.02
	POS 2	16.35	0.51	0.025	0.02	POS 5	9.15	0.27	0.022	0.02
		16.35	0.51	0.015	0.02		9.15	0.27	0.009	0.02
		16.35	0.51	0.014	0.02		9.15	0.27	0.011	0.02
	POS 3	14.76	0.47	0.029	0.02	POS 6	6.00	0.17	0.008	0.02
		14.77	0.47	0.026	0.02		6.01	0.17	0.003	0.02
		14.77	0.47	0.025	0.02		6.00	0.17	0.007	0.02
Coarse Sand (2-5 mm)	POS 1	19.35	0.61	0.040	0.02	POS 4	13.39	0.40	0.028	0.02
		19.37	0.61	0.028	0.02		13.38	0.40	0.029	0.02
		19.37	0.61	0.031	0.02		13.39	0.40	0.028	0.02
	POS 2	17.02	0.53	0.029	0.02	POS 5	10.34	0.30	0.026	0.02
		17.04	0.53	0.034	0.02		10.22	0.30	0.019	0.02
		17.03	0.53	0.031	0.02		10.22	0.30	0.013	0.02
	POS 3	15.61	0.47	0.017	0.02	POS 6	7.04	0.19	0.022	0.02
		15.61	0.47	0.024	0.02		7.01	0.19	0.005	0.02
		15.61	0.47	0.029	0.02		7.03	0.19	0.007	0.02
Round (3-8 mm)	POS 1	18.31	0.58	0.057	0.02	POS 3	11.79	0.38	0.030	0.02
		18.27	0.58	0.050	0.02		11.80	0.38	0.030	0.02
		18.29	0.58	0.052	0.02		11.80	0.38	0.019	0.02
	POS 2	14.43	0.46	0.060	0.02	POS 4	8.12	0.25	0.018	0.02
		14.43	0.46	0.040	0.02		8.09	0.25	0.018	0.02
		14.43	0.46	0.041	0.02		8.12	0.25	0.022	0.02
Round (5-15 mm)	POS 1	18.33	0.60	0.026	0.02	POS 3	11.94	0.37	0.024	0.02
		18.36	0.60	0.031	0.02		11.96	0.37	0.032	0.02
		18.36	0.60	0.024	0.02		11.94	0.37	0.030	0.02
	POS 2	14.61	0.46	0.021	0.02	POS 4	9.37	0.28	0.029	0.02
		14.58	0.46	0.022	0.02		9.36	0.28	0.026	0.02
		14.57	0.46	0.031	0.02		9.37	0.28	0.015	0.02

We performed the interpolation with the homemade utility Myfitexy, previously described in the calibration tests. This utility gives us the coefficients a and b of the interpolation line with the relative uncertainties σ(a) and σ(b), the result of the χ^2 test

and the probability q that the interpolation is linear. In Table 3.31 we reported the output of the statistical test together with the coefficients of determination R^2 of the same interpolations, estimated with Microsoft Excel. Moreover in Table 3.31 we reported the water temperature measured during the tests with a thermometer and, for comparison purpose, also the data relative to the calibration tests performed on the aluminum and HDPE reflectors.
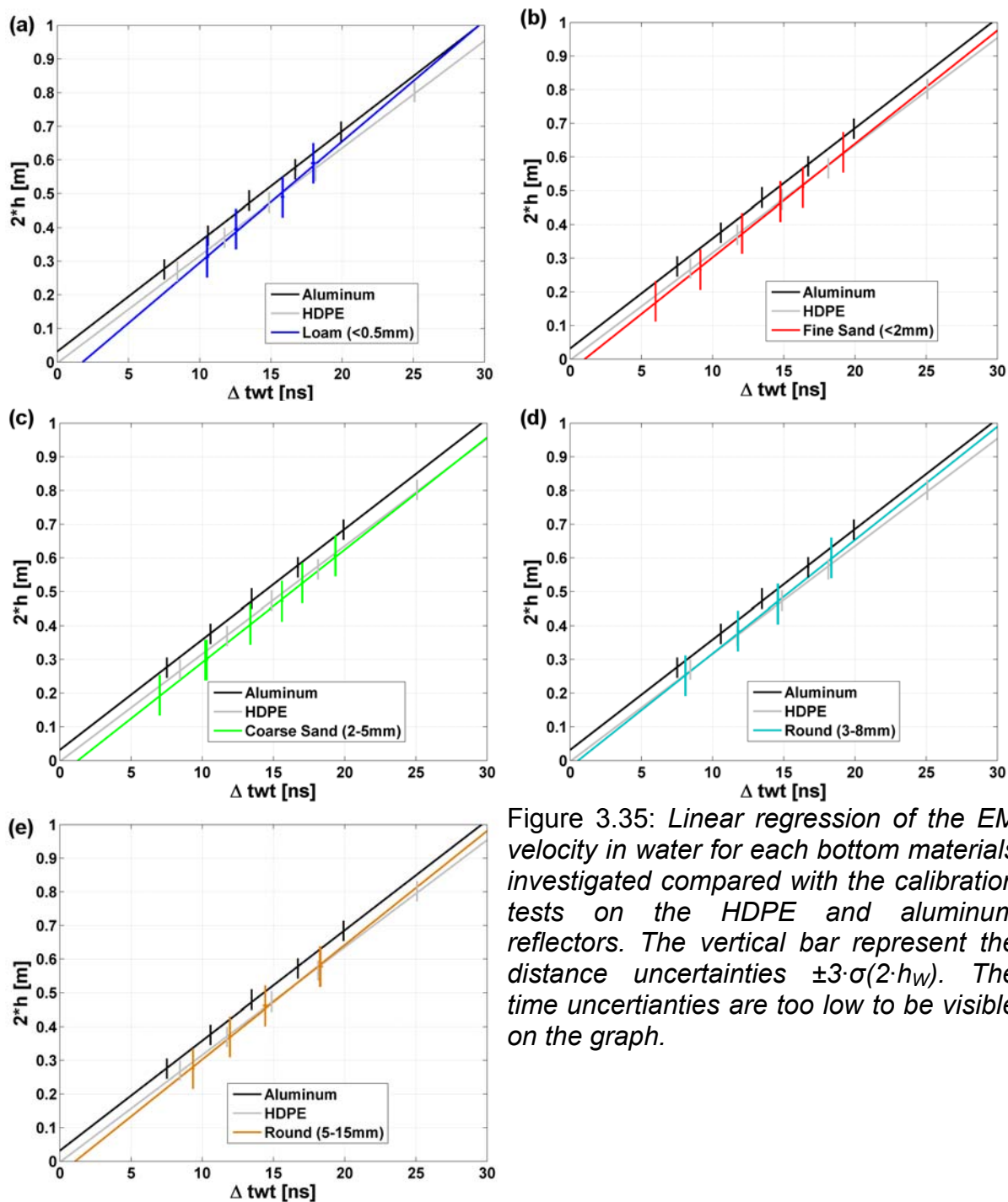

Figure 3.35: *Linear regression of the EM velocity in water for each bottom materials investigated compared with the calibration tests on the HDPE and aluminum reflectors. The vertical bar represent the distance uncertainties $\pm 3 \cdot \sigma(2 \cdot h_W)$. The time uncertianties are too low to be visible on the graph.*

Table 3.31: *Statistical results of the linear regression in order to find the electromagnetic velocity in water. All the tests with different bottom materials are taken in account, together with the calibration tests. The last two column report respectively the water temperature during the tests and the water permittivity estimated by the velocity values.*

Material	a ± σ(a) [m]	b ± σ(b) [m/ns]	χ^2	q	R^2	T [°C]	k±σ(k) [-]
Loam (<0.5mm)	-0.064 ±0.0293	0.0359 ±0.002	2.659	0.9884	0.9917	23	69.7 +7.77
Fine Sand (<2 mm)	-0.0346 ±0.0148	0.0337 ±0.0011	1.1167	1	1	20	79.1 +5.17
Coarse Sand (2-5 mm)	-0.0424 ±0.0163	0.0333 ±0.0011	0.405	1	0.9995	19	81 +5.35
Round (3-8 mm)	-0.0191 ±0.0213	0.0336 ±0.0015	0.7812	0.9999	0.9984	26	79.6 +7.11
Round (5-15 mm)	-0.0368 ±0.0246	0.0339 ±0.0018	1.0746	0.9998	0.9971	28	78.2 +8.31
Aluminum	0.0314 ±0.0149	0.0327 ±0.0010	1.0294	0.7941	0.999	16	84.1 +5.14
HDPE	-0.0030 ±0.0132	0.0319 ±0.0008	1.3280	0.7225	0.9992	16	88.3 +4.43

In Figure 3.35 we plotted the results of the interpolations for each bottom materials investigated, and we compared it with the interpolations founded in the calibration analysis. The comparison among the velocity of the electromagnetic pulse in water relative to all the tests performed with different type of bottom reflectors is shown in Figure 3.36. In order to justify the dispersion of the velocity founded, we have analyzed the influence of the water temperature on our data set. Firstly we have estimated the water permittivity k_W from the water velocity V_W values by the simplified relation (2.43):

$$k_W = \left(\frac{c}{V_W} \right)^2 \qquad (3.31)$$

and its uncertainties

$$\sigma\left(k_W\right) = \left|\frac{2c^2}{V_W^3}\right| \cdot \sigma\left(V_W\right) \tag{3.32}$$

considering for the standard deviation of the velocity in water $\sigma(V_W)$ the values $\sigma(b)$ obtained with the statistical utilities Myfitexy, and the uncertainties of the speed of light c equals to zero.

Then we compared the water permittivity values founded experimentally with the relation proposed by Malberg and Maryott (1956). This law studies the influence of the temperature T on the water permittivity K_W in the range from 0 to 100°C

$$k_W = 87.74 - 0.4008 \cdot T + 9.398 \cdot 10^{-4} \cdot T^2 - 1.41 \cdot 10^{-6} \cdot T^3 \tag{3.33}$$

In Figure 3.37 we compared the water permittivity values estimated for the tests with different reflectors by the equations (3.31) and (3.32), together with the water permittivity value calculated with the theoretical relation (3.33). This graph tell us firstly that the water temperature play a not negligible role in the water permittivity. Secondly the water permittivity estimated could be considered reliable, with the exclusion of the tests carried out with the loam (<0.5 mm) that is too low. However the uncertainties of the water permittivity estimated with this method is affected by high uncertainties.
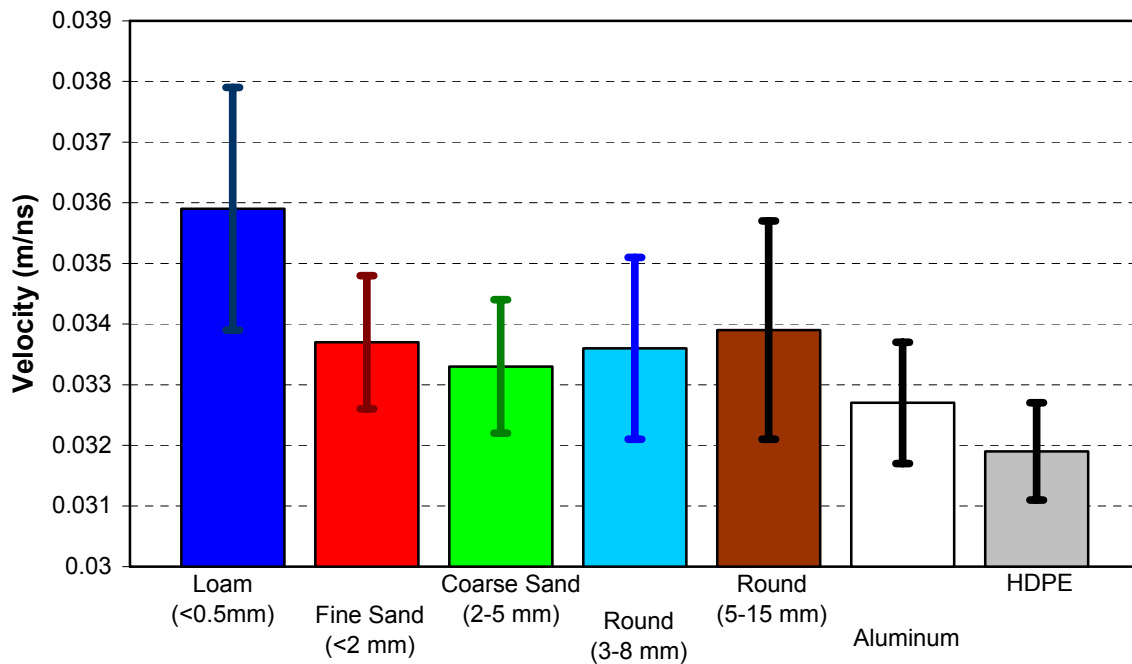
Figure 3.36: *Comparison among the different velocity values of the EM pulse in water, obtained from the GPR measurements with different bottom reflectors.*
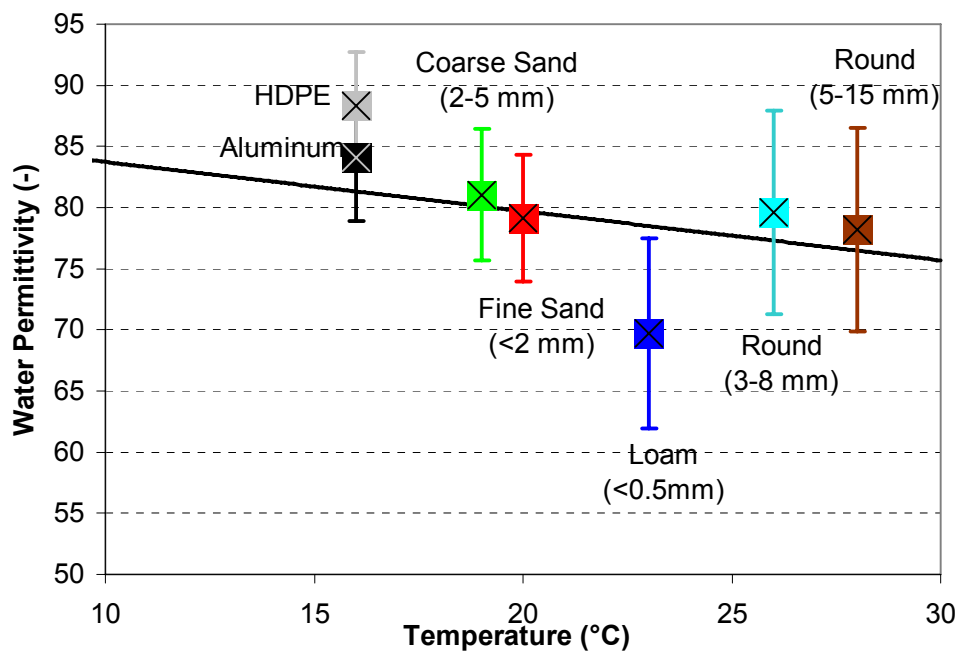
Figure 3.37: *Comparison among the water permittivity values estimated experimentally by the velocity analysis of the EM puse in water in the different tests, the coloured cross with its uncertainties ±σ(k$_W$), and the theoretical value calculated by the relation of Malberg and Maryott (1956) the continuous black line.*

Sediments Permittivity by Velocity Analysis

In this section, we want to show how we estimated the permittivity of the bottom materials by the interpretation of the EM pulse velocity in the particulate media.

Then, the first step is the estimation of the velocity in the sediments. We started from picking the reflection time values t_1 of the sediments top and the reflection time t_2 due to the bottom of the tank, like is shown in Figure 3.34. We need to take care that the picking of the sediments bottom it is affected by an implicit error. In fact the bottom of the tank is separated from the pavements by roughly 20 cm of air, like it is visible in Figure 3.1. Considering that the velocity of the EM pulse in air is 0.3 m/ns, the reflection from the pavement is nearly 1 ns after the reflection from the bottom of the tank. Consequently the pavement reflection interferes with the reflection from the tank bottom, and the removal of this interference is not an easy task by standard signal processing techniques. We would have avoided this undesirable effect if we would have positioned a perfect reflector between the sediments layer and the bottom of the tank, like the aluminum sheet settled in the calibration tests. In fact in this case the reflector would have reflected back all the energy, avoiding the reflection from the pavement. We considered acceptable the inaccuracy on the sediments bottom reflection time and we evaluated the time of flight in the sediments as

$$TOF_B = t_2 - t_1 \quad [ns]$$
(3.34)

with its uncertainties $\sigma(TOF_B)$

$$\sigma(TOF_B) = \left| \sigma(t_2) + \sigma(t_1) \right| \quad [ns]$$
(3.35)

evaluating from the picking time data both the standard deviations $\sigma(t_1)$ and $\sigma(t_2)$ of the sediments top and bottom reflection times respectively.

We estimated the velocity of the EM pulse in the sediments V_B by the ratio between distance covered $2 \cdot (h_B)$ in the sediments, and the relative time of flights

$$V_B = \frac{2 \cdot h_B}{TOF_B} \quad \left[\frac{m}{ns} \right]$$
(3.36)

We evaluated the velocity uncertainties $\sigma(V_B)$ by propagating the uncertainties on the time of flight in the sediments $\sigma(TOF_B)$ and the thickness of the sediments layer (h_B)

$$\sigma(V_B) = \left| \frac{2}{TOF_B} \right| \cdot \sigma(h_B) + \left| \frac{2 \cdot h_B}{TOF_B^2} \right| \cdot \sigma(TOF_B) \quad \left[\frac{m}{ns} \right]$$
(3.37)

In Table 3.32 we summarized all the data taken in account for the estimation of the velocity in the sediments and the velocity values founded. In Table 3.33 we reported for each particulate media the mean values of the velocity estimated from the data in Table 3.32.

Now we know the velocity in the sediments V_B, and then we are able to obtain a first estimation of the sediments permittivity k_B using the simplified relation (2.43)

$$k_B = \left(\frac{c}{V_B}\right)^2 \qquad (3.38)$$

With the same criteria choosen for the estimation of the water permittivity in the previous section, we estimated the uncertainties of the sediments permittivity evaluated

$$\sigma(K_B) = \left|\frac{2c^2}{V_B^3}\right| \cdot \sigma(V_B) \qquad (3.39)$$

Table 3.32 summarizes the sediments permittivities estimated for each GPR measurement. Table 3.33 reports the mean permittivity evaluated for each particulate media investigated, that are graphed in Figure 3.39. We need to take care that this method for the sediments permittivity estimation is affected by two weaknesses: firstly we obtain the permittivity from the picked time of the bottom sediments that is inaccurate for the interference with the pavement reflection. Secondly this permittivity is simply evaluated by the mean of different measurements and not by the more accurate method of the linear regression adopted for the estimation of the water permittivity. In fact we available only one sediment thickness for each particulate media.

Table 3.32: *EM properties of the sediments estimated by the velocity analysis. For each particulate media it is reported: the time of flights in the sediments TOF$_B$, the sediments thickness h$_B$, the velocity of the EM pulse in the sediments V$_B$ and the sediments permittivity k$_B$.*

Mat	Pos	TOF$_B$ [ns]	σ(TOF$_B$) [ns]	h$_B$ [m]	σ(h$_B$) [m]	V$_B$ [m/ns]	σ(V$_B$) [m/ns]	k$_B$ [-]	σ(k$_B$) [-]
Loam (<0.5mm)	POS 1	5.141	0.0667	0.16	0.005	0.0622	0.0028	23.202	2.0523
		5.128	0.0407	0.16	0.005	0.0624	0.0024	23.078	1.809
		5.138	0.0605	0.16	0.005	0.0623	0.0027	23.167	1.9938
	POS 2	5.051	0.0429	0.16	0.005	0.0634	0.0025	22.39	1.7799
		5.101	0.0499	0.16	0.005	0.0627	0.0026	22.841	1.8744
		5.096	0.0415	0.16	0.005	0.0628	0.0025	22.79	1.7953
	POS 3	5.206	0.0413	0.16	0.005	0.0615	0.0024	23.79	1.8645
		5.233	0.0428	0.16	0.005	0.0611	0.0024	24.04	1.8959
		5.226	0.0336	0.16	0.005	0.0612	0.0023	23.975	1.8069
	POS 4	4.993	0.0358	0.16	0.005	0.0641	0.0025	21.883	1.6813
		5.003	0.0323	0.16	0.005	0.064	0.0024	21.966	1.6565
		4.987	0.0209	0.16	0.005	0.0642	0.0023	21.827	1.5475
Fine Sand (<2 mm)	POS 1	6.364	0.0421	0.17	0.005	0.0534	0.0019	31.489	2.2685
		6.353	0.0459	0.17	0.005	0.0535	0.002	31.379	2.2996
		6.346	0.0461	0.17	0.005	0.0536	0.002	31.315	2.2965
	POS 2	6.197	0.0307	0.17	0.005	0.0549	0.0019	29.862	2.0527
		6.199	0.0372	0.17	0.005	0.0548	0.0019	29.876	2.1155
		6.199	0.0325	0.17	0.005	0.0548	0.0019	29.877	2.0711
	POS 3	6.350	0.0385	0.17	0.005	0.0535	0.0019	31.35	2.2241
		6.331	0.0364	0.17	0.005	0.0537	0.0019	31.16	2.1915
		6.334	0.0354	0.17	0.005	0.0537	0.0019	31.192	2.1839
	POS 4	6.318	0.0275	0.17	0.005	0.0538	0.0018	31.04	2.0964
		6.317	0.0315	0.17	0.005	0.0538	0.0019	31.023	2.1346
		6.321	0.0323	0.17	0.005	0.0538	0.0019	31.062	2.1449
	POS 5	6.251	0.0238	0.17	0.005	0.0544	0.0018	30.384	2.0183
		6.247	0.0173	0.17	0.005	0.0544	0.0018	30.344	1.9527
		6.243	0.0211	0.17	0.005	0.0545	0.0018	30.302	1.987
	POS 6	6.203	0.0076	0.17	0.005	0.0548	0.0017	29.919	1.8332
		6.197	0.0131	0.17	0.005	0.0549	0.0017	29.858	1.8823
		6.199	0.017	0.17	0.005	0.0549	0.0018	29.874	1.9215
Coarse Sand (2-5 mm)	POS 1	5.207	0.0443	0.16	0.005	0.0615	0.0024	23.801	1.8924
		5.196	0.0496	0.16	0.005	0.0616	0.0025	23.697	1.9336
		5.183	0.0607	0.16	0.005	0.0617	0.0027	23.575	2.0257
	POS 2	5.259	0.0407	0.16	0.005	0.0609	0.0024	24.272	1.893
		5.256	0.0396	0.16	0.005	0.0609	0.0024	24.245	1.8806
		5.263	0.0404	0.16	0.005	0.0608	0.0024	24.312	1.8926

Table 3.32: *following from previous page.*

Mat	Pos	TOF$_B$ [ns]	σ(TOF$_B$) [ns]	h$_B$ [m]	σ(h$_B$) [m]	V [m/ns]	σ(V) [m/ns]	ε$_R$ [-]	σ(ε$_R$) [-]
Coarse Sand (2-5 mm)	POS 3	4.979	0.0358	0.16	0.005	0.0643	0.0025	21.756	1.673
		4.983	0.0406	0.16	0.005	0.0642	0.0025	21.797	1.7174
		4.985	0.038	0.16	0.005	0.0642	0.0025	21.812	1.6955
	POS 4	5.077	0.0391	0.16	0.005	0.063	0.0025	22.625	1.7628
		5.077	0.0324	0.16	0.005	0.063	0.0024	22.625	1.7025
		5.085	0.031	0.16	0.005	0.0629	0.0024	22.692	1.6947
	POS 5	5.020	0.0349	0.16	0.005	0.0637	0.0024	22.12	1.6905
		5.077	0.024	0.16	0.005	0.063	0.0023	22.628	1.6279
		5.075	0.0264	0.16	0.005	0.0631	0.0023	22.607	1.6478
	POS 6	5.047	0.0225	0.16	0.005	0.0634	0.0023	22.359	1.5968
		5.059	0.0132	0.16	0.005	0.0633	0.0021	22.464	1.5208
		5.041	0.0192	0.16	0.005	0.0635	0.0022	22.303	1.5637
Round (3-8 mm)	POS 1	5.947	0.0395	0.16	0.005	0.0538	0.002	31.047	2.3529
		5.914	0.0448	0.16	0.005	0.0541	0.0021	30.696	2.3838
		5.945	0.0409	0.16	0.005	0.0538	0.0021	31.024	2.3656
	POS 2	5.881	0.0315	0.16	0.005	0.0544	0.002	30.352	2.2218
		5.892	0.0415	0.16	0.005	0.0543	0.0021	30.472	2.3333
		5.900	0.0363	0.16	0.005	0.0542	0.002	30.554	2.286
	POS 3	5.718	0.0377	0.16	0.005	0.056	0.0021	28.699	2.1719
		5.711	0.0335	0.16	0.005	0.056	0.0021	28.628	2.125
		5.707	0.0316	0.16	0.005	0.0561	0.0021	28.582	2.1032
	POS 4	5.923	0.0217	0.16	0.005	0.054	0.0019	30.794	2.1504
		5.932	0.0242	0.16	0.005	0.0539	0.0019	30.881	2.1824
		5.920	0.0228	0.16	0.005	0.0541	0.0019	30.759	2.1593
Round (5-15 mm)	POS 1	5.875	0.0746	0.17	0.005	0.0579	0.0024	26.84	2.2601
		5.924	0.0788	0.17	0.005	0.0574	0.0025	27.283	2.331
		5.911	0.1	0.17	0.005	0.0575	0.0027	27.169	2.5171
	POS 2	6.009	0.0808	0.17	0.005	0.0566	0.0024	28.071	2.4062
		5.999	0.0583	0.17	0.005	0.0567	0.0022	27.981	2.1895
		6.000	0.0571	0.17	0.005	0.0567	0.0022	27.992	2.1797
	POS 3	5.952	0.0404	0.17	0.005	0.0571	0.0021	27.54	1.9942
		5.929	0.039	0.17	0.005	0.0573	0.0021	27.331	1.9671
		5.953	0.0332	0.17	0.005	0.0571	0.002	27.55	1.9283
	POS 4	5.777	0.0413	0.17	0.005	0.0589	0.0022	25.951	1.8975
		5.781	0.0345	0.17	0.005	0.0588	0.0021	25.982	1.8386
		5.780	0.029	0.17	0.005	0.0588	0.002	25.971	1.788

Table 3.33: *Summary of the EM pulse velocity in the sediments investigated, and the sediments permittivity estimated by the velocity analysis.*

| Sediments	V_B [m/ns]	$\sigma(V_B)$ [m/ns]	k_B [-]	$\sigma(k_B)$ [-]
Loam (<0.5mm)	0.0627	0.0025	22.9	1.8
Fine Sand (<2 mm)	0.0542	0.0019	30.6	2.1
Coarse Sand (2-5 mm)	0.0627	0.0024	22.9	1.8
Round (3-8 mm)	0.0546	0.0020	30.2	2.2
Round (5-15 mm)	0.0576	0.0022	27.1	2.1
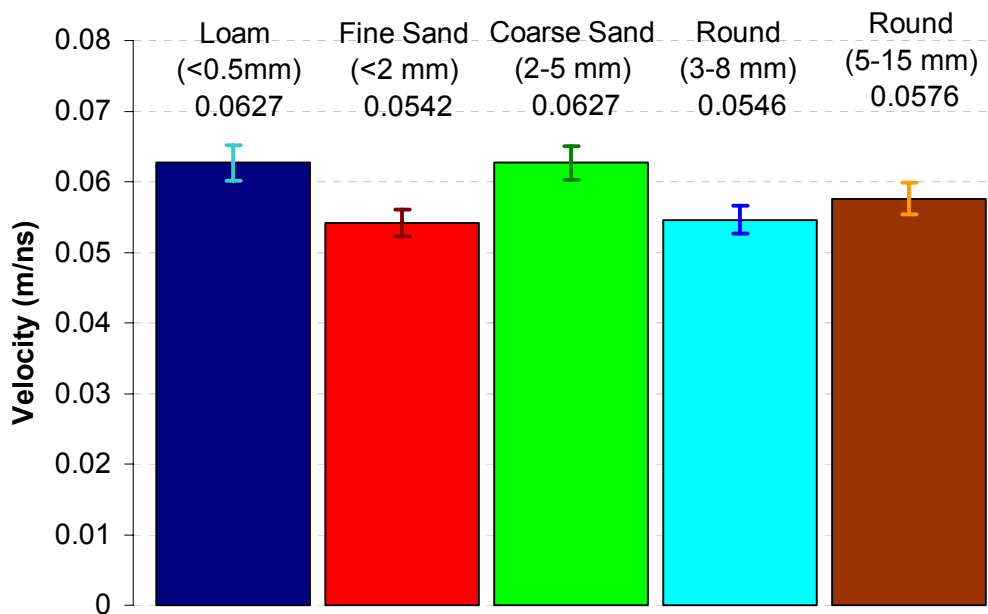
Figure 3.38: *EM velocity in the sediments investigated, the vertical bar are the uncertainties range ±σ.*
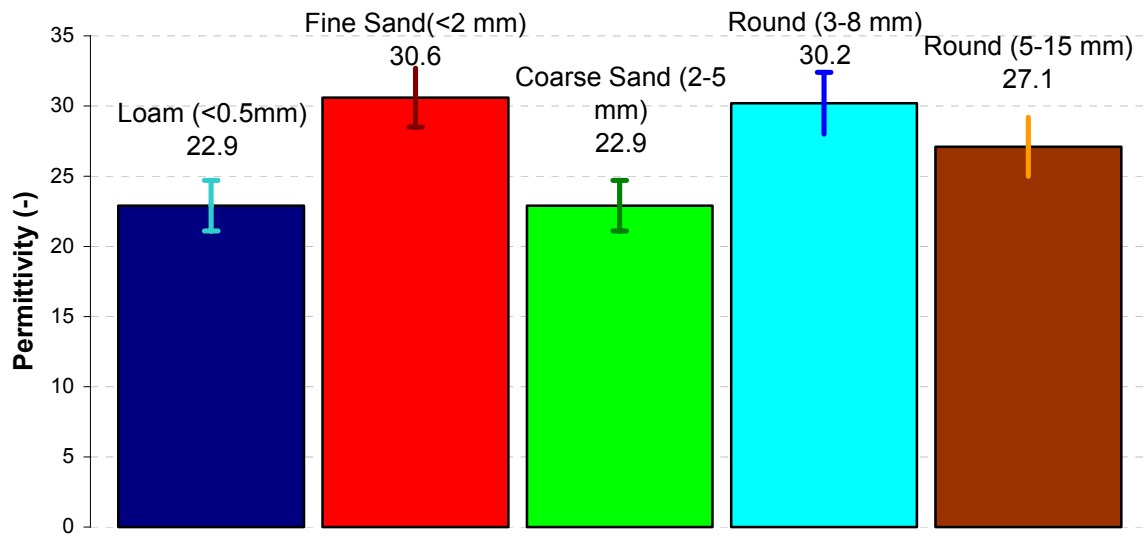
Figure 3.39: *Sediments permittivity estimated by the velocity analysis, the vertical bars represent the uncertainties range ±σ.*

Water-Sediments Reflection Coefficient by Velocity Analysis

In this section we estimate the reflection coefficient of the interface between water and sediments by the first method taken in account: the velocity analysis.

Equation (2.54) defines an approximation of the reflection coefficient by the permittivity of the two media facing the interface. We adopted the simplified relation (2.54) because we assume for both the two media a low electrical conductivity and a unitary relative magnetic permeability. Then, knowing the water permittivity k_W and the bulk permittivity of the sediments k_B, we can evaluate the correspondent reflection coefficient as

$$r = \frac{\sqrt{k_W} - \sqrt{k_B}}{\sqrt{k_W} + \sqrt{k_B}} \qquad (3.40)$$

From relation (3.40), we can propagate the uncertainties of the water permittivity $\sigma(k_W)$ and of the bulk permittivity of the sediments $\sigma(k_B)$ in order to evaluate the standard deviation of the reflection coefficient $\sigma(r)$ estimated by the velocity analysis.

$$\sigma(r) = \left| \frac{2k_W - 3k_W^{1/2}k_B^{1/2} + k_W^{-1/2}k_B^{3/2}}{(k_W - k_B)^2} \right| \cdot \sigma(k_W) + \dots$$

$$\dots + \left| \frac{2k_B - 3k_W^{1/2}k_B^{1/2} + k_W^{3/2}k_B^{-1/2}}{(k_W - k_B)^2} \right| \cdot \sigma(k_B) \qquad (3.41)$$

In order to solve equations (3.40) and (3.41) we selected the water permittivity value estimated from the velocity of the radar pulse in water during the calibration tests with the aluminum reflector. In Table 3.34 we reported the reflection coefficients and the relative uncertainties estimated for each one of the GPR measurements performed with the sediments. From the data of Table 3.34 we evaluated a value of the water-sediments reflection for each particulate media investigated, the results are summarized in Table 3.35.

Table 3.34: *Sediment-water reflection coefficient values, for each GPR measurements performed, estimated by the velocity analysis.*

Material	Position	1st Measurement		2nd Measurement		3rd Measurement	
		r	σ(r)	r	σ(r)	r	σ(r)
Loam (<0.5mm)	Pos 1	0.311	0.109	0.313	0.104	0.312	0.108
	Pos 2	0.319	0.105	0.315	0.106	0.315	0.105
	Pos 3	0.306	0.104	0.303	0.105	0.304	0.103
	Pos 4	0.324	0.104	0.324	0.103	0.325	0.101
Fine Sand (<2 mm)	Pos 1	0.241	0.101	0.242	0.101	0.242	0.102
	Pos 2	0.253	0.099	0.253	0.1	0.253	0.1
	Pos 3	0.242	0.1	0.243	0.1	0.243	0.1
	Pos 4	0.244	0.098	0.244	0.099	0.244	0.099
	Pos 5	0.249	0.098	0.25	0.097	0.25	0.098
	Pos 6	0.253	0.095	0.253	0.096	0.253	0.097
Coarse Sand (2-5 mm)	Pos 1	0.306	0.105	0.307	0.106	0.308	0.108
	Pos 2	0.301	0.104	0.301	0.104	0.301	0.104
	Pos 3	0.326	0.104	0.325	0.105	0.325	0.104
	Pos 4	0.317	0.104	0.317	0.103	0.316	0.103
	Pos 5	0.322	0.104	0.317	0.101	0.317	0.102
	Pos 6	0.32	0.101	0.319	0.1	0.32	0.101
Round (3-8 mm)	Pos 1	0.244	0.103	0.247	0.104	0.244	0.103
	Pos 2	0.249	0.101	0.249	0.103	0.248	0.102
	Pos 3	0.263	0.103	0.263	0.102	0.264	0.102
	Pos 4	0.246	0.1	0.245	0.1	0.246	0.1
Round (5-15 mm)	Pos 1	0.278	0.107	0.274	0.108	0.275	0.111
	Pos 2	0.268	0.108	0.268	0.104	0.268	0.104
	Pos 3	0.272	0.101	0.274	0.101	0.272	0.1
	Pos 4	0.286	0.102	0.286	0.101	0.286	0.1

Table 3.35: *Sediments-water reflection coefficients estimated by the velocity analysis.*

Material	r	σ(r)
Loam (<0.5mm)	0.3142	0.0879
Fine Sand (<2 mm)	0.2473	0.0989
Coarse Sand (2-5 mm)	0.3146	0.1034
Round (3-8 mm)	0.2506	0.1019
Round (5-15 mm)	0.2756	0.1038

Water Attenuation Factor in Time Domain

From this section, we start to take in account the amplitude data acquired in the experiments with the sediments on the tank bottom. Before starting the amplitude analysis to characterize the sediments by the water-sediment reflection coefficient or the sediments permittivity, we focus our attention on the water medium. In fact we could estimate the attenuation factor of the water because we collected GPR measurements on different water depth. On the other hand, we can not estimate the sediments attenuation factor with a similar analysis because we worked with a constant sediment thickness. The explanation of this procedure is omitted in this section and we invite the reader to go into the calibration tests section for further details.

We can evaluate the water attenuation factor α in time domain from the simplified radar equation

$$A = rA_0 \cdot \frac{1}{2h_w} \cdot e^{-2 \cdot \alpha \cdot h_w} \tag{3.42}$$

where A is the amplitude of the water-sediments reflection, r is the reflection coefficient, A_0 the amplitude entered in water and h_w the water depth. We can made linear equation (3.42) in the form

$$Y[-] = a[-] + b[1/m] \cdot X[m] \tag{3.43}$$

by the logarithmic properties, obtaining:

$$\ln(A) + \ln(2h_w) = \ln(A_0 r) - 2\alpha h_w \tag{3.44}$$

We used equation (3.44) to interpret the interpolation of the amplitude data of the water-sediments reflection, corrected for the geometrical losses, versus the water depth. Table 3.36 summarized all the input data necessary to perform the linear regression of the amplitude, with the statistical utility Myfitexy. The results of the interpolation founded for the GPR measurements with the sediments are reported in Table 3.37 together with the results of the calibration tests with the HDPE and aluminum reflectors. From the quality of the interpolations shown in Figure 3.40 and the statistical test summarized in Table 3.37 we can assert that the interpolations on the sediments reflection are worst than the same interpolation founded in calibration tests. We ca explain this result because in the case of the sediments measurements we acquired a littler number of positions, then we computed the regression using all

the data available. Instead in the calibration tests we discarded some data, in particular when the reflection was affected by noise or when the reflection was in near field condition, like is explained in the calibration section.
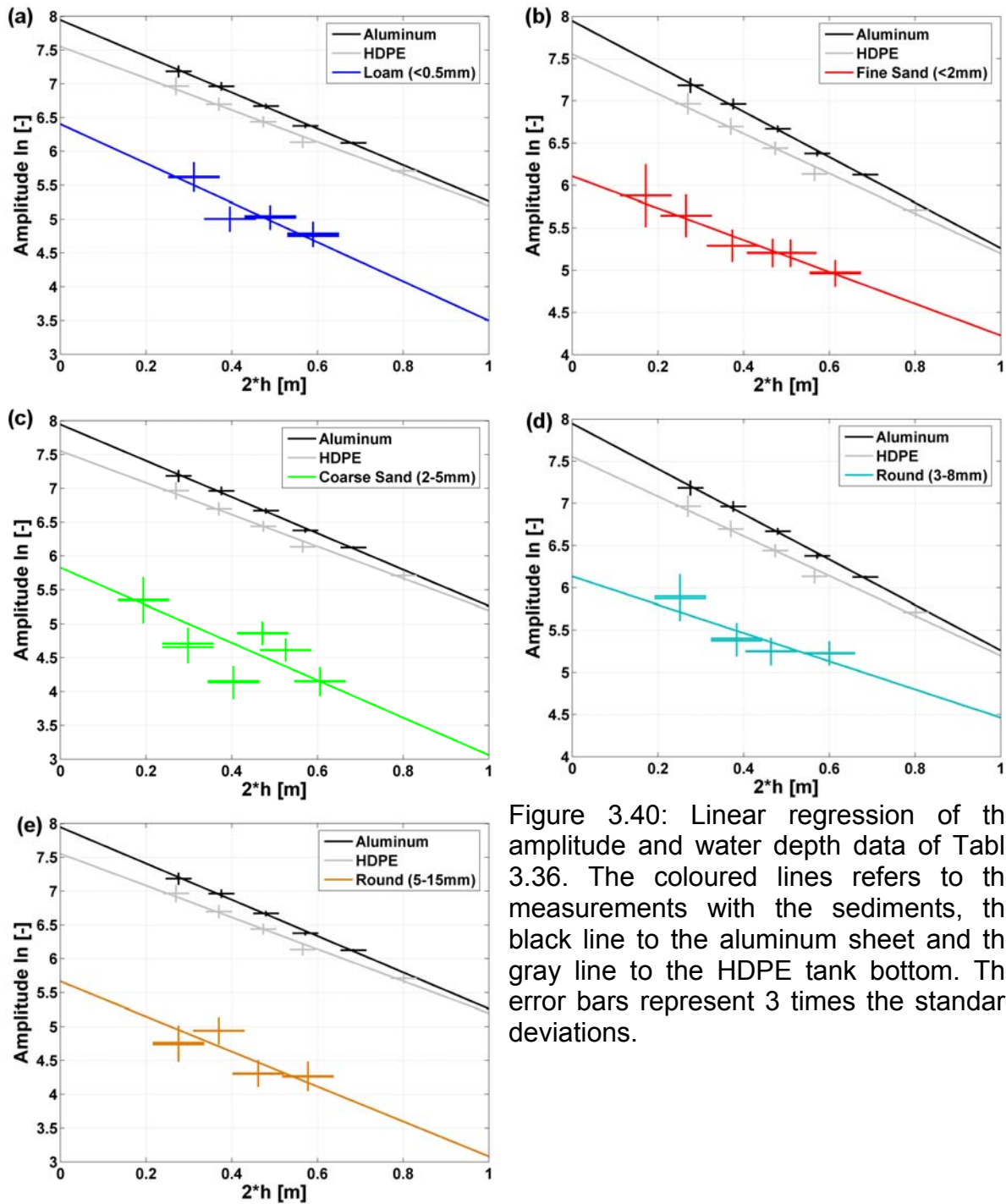

Figure 3.40: Linear regression of the amplitude and water depth data of Table 3.36. The coloured lines refers to the measurements with the sediments, the black line to the aluminum sheet and the gray line to the HDPE tank bottom. The error bars represent 3 times the standard deviations.

Table 3.36: *Experimental data of the GPR test with the sediments used to find the water attenuation coefficient. The X values represent the distance covered by the EM pulse in water $2h_W$, the Y values represent the amplitude A* of the water-sediments reflection corrected for the geometrical attenuation.*

| Material	Position	X 2h [m]	σ(X) σ(2h) [ns]	Y A* [-]	σ(Y) σ(A*) [-]	Position	X 2h [m]	σ(X) σ(2h) [ns]	Y A* [-]	σ(Y) σ(A*) [-]
Loam (<0.5mm)	POS 1	0.59	0.02	4.763	0.0519	POS 3	0.396	0.02	5.0017	0.0624
		0.59	0.02	4.7912	0.0575		0.396	0.02	5.0007	0.0623
		0.59	0.02	4.7517	0.054		0.396	0.02	5.007	0.0605
	POS 2	0.49	0.02	5.0209	0.054	POS 4	0.312	0.02	5.6131	0.0709
		0.49	0.02	5.0205	0.058		0.312	0.02	5.6196	0.0712
		0.49	0.02	5.0463	0.054		0.312	0.02	5.627	0.0711
Fine Sand (<2 mm)	POS 1	0.614	0.02	4.9751	0.0491	POS 4	0.374	0.02	5.2923	0.063
		0.614	0.02	4.9671	0.0463		0.374	0.02	5.2884	0.0626
		0.614	0.02	4.9603	0.0519		0.374	0.02	5.2902	0.0615
	POS 2	0.51	0.02	5.2076	0.0498	POS 5	0.266	0.02	5.6429	0.0837
		0.51	0.02	5.2023	0.0502		0.266	0.02	5.6447	0.0818
		0.51	0.02	5.2022	0.0543		0.266	0.02	5.644	0.0828
	POS 3	0.468	0.02	5.2095	0.0541	POS 6	0.172	0.02	5.88	0.1236
		0.468	0.02	5.2003	0.0538		0.172	0.02	5.8816	0.1221
		0.468	0.02	5.2033	0.0553		0.172	0.02	5.8786	0.1231
Coarse Sand (2-5 mm)	POS 1	0.606	0.02	4.1483	0.0715	POS 4	0.404	0.02	4.1568	0.0701
		0.606	0.02	4.1555	0.0634		0.404	0.02	4.1583	0.0673
		0.606	0.02	4.1563	0.0664		0.404	0.02	4.1345	0.0819
	POS 2	0.526	0.02	4.6161	0.0564	POS 5	0.298	0.02	4.6565	0.079
		0.526	0.02	4.6186	0.0567		0.298	0.02	4.7125	0.0767
		0.526	0.02	4.6092	0.0535		0.298	0.02	4.7066	0.079
	POS 3	0.472	0.02	4.8556	0.0556	POS 6	0.194	0.02	5.3478	0.1096
		0.472	0.02	4.8706	0.0554		0.194	0.02	5.3569	0.11
		0.472	0.02	4.8706	0.0545		0.194	0.02	5.3406	0.1106
Round (3-8 mm)	POS 1	0.6	0.02	5.2	0.0464	POS 3	0.384	0.02	5.3751	0.0616
		0.6	0.02	5.2	0.0477		0.384	0.02	5.3994	0.0608
		0.6	0.02	5.2	0.0453		0.384	0.02	5.4032	0.0608
	POS 2	0.464	0.02	5.2	0.0544	POS 4	0.252	0.02	5.8721	0.0881
		0.464	0.02	5.3	0.0532		0.252	0.02	5.8979	0.0876
		0.464	0.02	5.3	0.0528		0.252	0.02	5.8724	0.0881
Round (5-15 mm)	POS 1	0.578	0.02	4.3	0.0722	POS 3	0.37	0.02	4.9381	0.066
		0.578	0.02	4.3	0.0709		0.37	0.02	4.9427	0.0658
		0.578	0.02	4.3	0.0671		0.37	0.02	4.9376	0.0662
	POS 2	0.462	0.02	4.3	0.0634	POS 4	0.276	0.02	4.7375	0.0849
		0.462	0.02	4.3	0.0641		0.276	0.02	4.7415	0.0824
		0.462	0.02	4.3	0.0665		0.276	0.02	4.7632	0.0839

Table 3.37: *Results of the statistical tests performed for the estimation of the water attenuation coefficient.*

Material	a [-]	b [1/m]	σ(a) [-]	σ(b) [1/m]	χ^2 [-]	q [-]	R^2 [-]
Loam (<0.5mm)	6.4031	-2.905	0.1212	0.26	35.715	0.0001	0.7858
Fine Sand (<2 mm)	6.1086	-1.881	0.0674	0.1422	12.366	0.7185	0.9557
Coarse Sand (2-5 mm)	5.8265	-2.767	0.0966	0.2154	231.6	0	0.4862
Round (3-8 mm)	6.1344	-1.671	0.0914	0.19	33.171	0.0003	0.7977
Round (5-15 mm)	5.6651	-2.584	0.1074	0.243	50.88	0	0.6465
Aluminum	7.9456	-2.6843	0.0538	0.1029	2.8230	0.4197	0.9963
HDPE	7.5537	-2.3550	0.0542	0.0961	8.9573	0.0299	0.9873

Water Attenuation Factor in Frequency Domain

In this section we present the comparison in frequency domain between the water attenuation factor founded in the measurements with the sediments and the values founded in the calibration tests with the aluminum and HDPE reflectors. We pass over the processing description, and we invite the reader to go into the calibration section to further details.


Figure 3.41: Comparison between the water attenuation spectra estimated from the measurements acquired with the sediments on the bottom of the tank and the calibration tests. The colored lines refer to the sediments measurements, the black line to the aluminum reflector the gray line to the HDPE. The error bars represents 3 times the standard deviations. The black star is the value founded with the Open Ended Coaxial Cable test.

Figure 3.41 shows that in all the measurements with the sediments on the bottom of the tank we obtained a less accurate water attenuation spectra. Firstly with the sediments we evaluated wider uncertainties range. Moreover the value obtained with the Open Cable Coaxial Cable is not included in the uncertainties range for all the measurements. Finally the tests with the Coarse Sand (2-5 mm) and Round (5-15mm) are characterized by a spectra with a sharp fell down of the water attenuation at 700 and 900 MHz respectively, this experimentally evidence is difficulty to explain.

Water-Sediment Reflection Coefficient by Amplitude Analysis

The possibility to estimate the reflection coefficient of the interface between water and sediments by the interpretation of the amplitude of reflection is one of the main objectives of this work. In the previous sections we found a first estimation of the water-sediment reflection coefficient by the knowledge of the water permittivity and the bulk permittivity of the bottom sediments. The estimation of the two permittivities involve the knowledge of the velocity of the EM pulse in the two media. In our experimentations we could estimates these quantities because we know all the distances involved in the tests: the sediments thickness and the water depths. On the other hand, in field conditions usually these data are not available an then the velocity analysis previously explained is not suitable. Then the amplitude analysis could represent an effective alternative in the estimation of the water-sediments reflection coefficient, because it does not require further information about the sediments.

We approached the task of the amplitude analysis starting from the simplified radar equation presented in the calibration tests in order to evaluate the water attenuation factor

$$A = rA_0 \cdot \frac{1}{2h_W} \cdot e^{-2 \cdot \alpha \cdot h_W} \tag{3.45}$$

If in equation (3.45) we know the water depth h_W, the water attenuation factor α, the amplitude at the receiver antenna A and finally the amplitude emitted in water A_0, we could put in evidence the water-sediment reflection coefficient r as

$$r = \frac{A_1}{A_0} \cdot e^{2\alpha h} \cdot 2h \tag{3.46}$$

Moreover knowing the uncertainties of each factor of equation (3.46) we could evaluate the uncertainty of the reflection coefficient $\sigma(r)$ as

$$\sigma(r) = 2h \cdot e^{2\alpha h} \cdot \left[\begin{array}{l} \dfrac{\sigma(A_1)}{|A_0|} + \dfrac{|A_1|}{A_0^2} \cdot \sigma(A_0) + \dots \\[2mm] \dots + 2h \cdot \left|\dfrac{A_1}{A_0}\right| \cdot \sigma(\alpha) + \left|\dfrac{A_1}{A_0}\right| \left(\dfrac{1}{h} + 2\alpha\right) \cdot \sigma(h) \end{array} \right] \tag{3.47}$$

Both in our experimentation and in field conditions the main difficult in order to solve equation (3.46) is the lack of information about the amount of signal entered in water. This information is not inferable by the interpretation of the main bang signal, in fact the main bang is a pulse formed by different contributions: the direct wave from the transmitter antenna versus the receiver antenna, the reflection and refraction due to the impedance contrast between the antennas box and water. All these events occur in a short time and it is impossible to discriminate between them. Then the experimental estimate of the amount of signal entered in water it is a challenging task. However we could attempt different ways: the first method could be placing an antenna receiver in water in front of the transmitter antenna. Considering that in the market actually is not available an antenna with a sufficient water proof to resist an immersion, we exclude this procedure.

Then, we attempted to evaluate the signal entered in water by an indirect method. We focused our attention on the amplitude regression performed in the calibration tests to find the water attenuation factor, shown in Figure 3.13 and reproduced in Figure 3.42. The linear regression is described from the equation (3.13), that we reported here to make easier the reading

$$\ln(A) + \ln(2h) = \ln(A_0 R) - 2\alpha h_w \tag{3.48}$$

In the calibration section we explained that the angular coefficient of the amplitude regression is represented by the attenuation factor, instead the intercept of the line with the vertical axes is represented by the term $\ln(A_0 R)$. Moreover considering that for the aluminum reflector the reflection coefficient R is equal to one, we can obtain a rough estimation of the amplitude entered in water from the intercept of the amplitude regression with the vertical axes:

$$A_0 = e^{\text{intercept}} \tag{3.49}$$

and the relative uncertainties

$$\sigma(A_0) = e^{\text{intercept}} \cdot \sigma(\text{intercept}) \tag{3.50}$$

in conclusion we obtain

$$A_0 = 2823 \pm 152 \tag{3.51}$$

Even though we derived the value expressed in equation (3.51) from the test with the aluminum reflector we could adopt this value also for the other tests because al the measurements are performed with the same experimental setup: in particular the antennas, the GPR system and the coupling of the antenna with the water. Figure 3.42 shows an indirect proof of our assumption, in fact the intercept of the HDPE reflector is lower than the one relative to the aluminum reflector. We can explain this evidence if we focus our attention on the value of the water-HDPE reflection coefficient. In fact the water-HDPE reflection coefficient is 0.726, evaluated previously in equation (3.10), lower than the aluminum. Consequently the term $\ln(A_0R)$ for the HDPE reflector should be lower than the aluminum case.
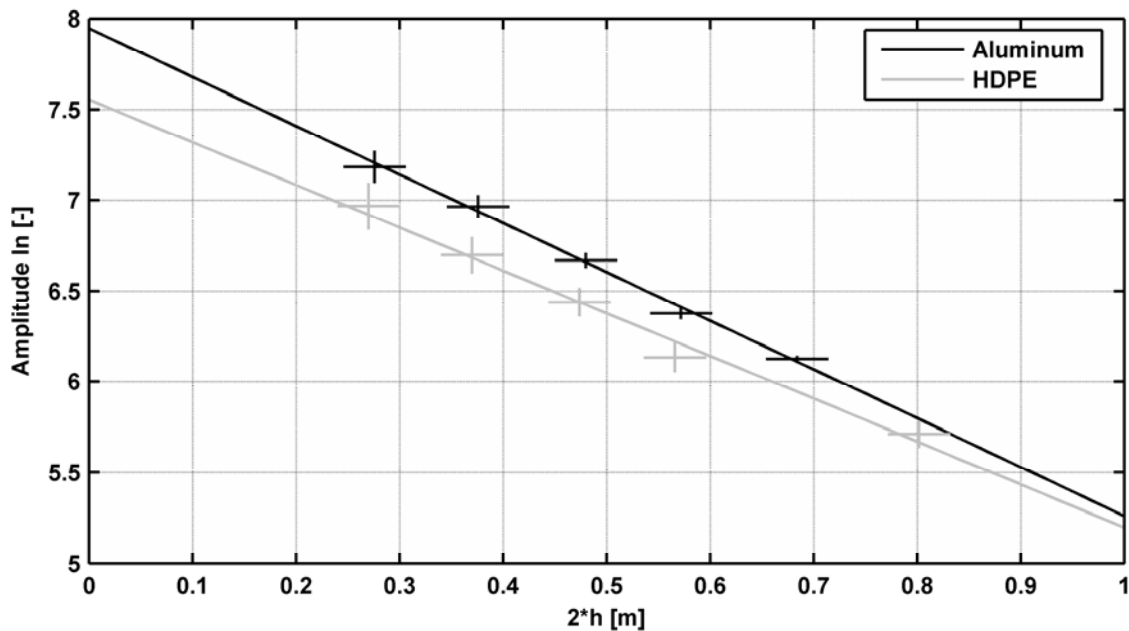
Figure 3.42: *Linear regression of the amplitude data for the estimation of the water attenuation coefficient in the calibration tests. The black line refers to the measurements with the aluminum sheet on the bottom; the gray line refers to the HDPE tank bottom. The error bars represent 3 times the standard deviations.*

Now that we estimate the amplitude entered in the water we are able to estimate the reflection coefficient of the water-sediments impedance contrast by the definition (2.50). In Table 3.38 we reported the reflection coefficient estimated for each GP measurements with the bottom sediments. The mean values for each particulate media investigated are reported in Table 3.39 together with the values estimated by the velocity analysis.

Table 3.38: *Reflection coefficient between water and sediments, obtained from the amplitude analysis of the reflection due to the top particulate media.*

Material	Position	1st measurement		2nd measurement		3rd measurement	
		r	σ(r)	r	σ(r)	r	σ(r)
Loam (<0.5mm)	Pos 1	0.202	0.058	0.208	0.065	0.2	0.059
	Pos 2	0.2	0.056	0.2	0.059	0.205	0.057
	Pos 3	0.152	0.042	0.152	0.041	0.153	0.042
	Pos 4	0.224	0.062	0.226	0.063	0.227	0.065
Fine Sand (<2 mm)	Pos 1	0.267	0.077	0.264	0.076	0.263	0.08
	Pos 2	0.254	0.069	0.253	0.068	0.253	0.07
	Pos 3	0.228	0.061	0.226	0.06	0.226	0.061
	Pos 4	0.192	0.051	0.191	0.05	0.192	0.05
	Pos 5	0.204	0.058	0.205	0.057	0.204	0.057
	Pos 6	0.201	0.066	0.201	0.066	0.201	0.066
Coarse Sand (2-5 mm)	Pos 1	0.114	0.04	0.115	0.038	0.115	0.039
	Pos 2	0.147	0.044	0.147	0.044	0.146	0.043
	Pos 3	0.162	0.046	0.164	0.047	0.164	0.046
	Pos 4	0.067	0.021	0.067	0.021	0.065	0.023
	Pos 5	0.083	0.025	0.088	0.026	0.087	0.026
	Pos 6	0.125	0.042	0.127	0.043	0.124	0.042
Round (3-8 mm)	Pos 1	0.331	0.089	0.331	0.093	0.329	0.091
	Pos 2	0.234	0.062	0.235	0.061	0.235	0.061
	Pos 3	0.214	0.053	0.22	0.054	0.221	0.054
	Pos 4	0.247	0.066	0.254	0.068	0.247	0.066
Round (5-15 mm)	Pos 1	0.119	0.039	0.119	0.04	0.119	0.039
	Pos 2	0.09	0.025	0.091	0.025	0.091	0.025
	Pos 3	0.133	0.034	0.134	0.034	0.133	0.034
	Pos 4	0.085	0.023	0.085	0.023	0.087	0.023

Now we want to focus our attention on the comparison between the reflection coefficient obtained from the velocity and the amplitude analysis. First of all the uncertainties range for the velocity analysis are wider than the ampltidue analysis. This fact is due because the reflection coefficient in the velocity analysys are obtained with a longer seguence of processing, where the error propagation imply a rise of the uncertinties.

We obtained a good match between velocity and amplitude analysis only for two of the five sediments investigated: the fine sand (<2mm) and the round (3-8mm). For the other three case the uncertainties range of the two analysis are not overlapped, in particular for the coarse sand (2-5mm) and the round (5-15mm).

Table 3.39: *Reflection coefficient between water and sediments R, with the relative uncertainties σ(R), obtained by the velocity and amplitude analysis.*

Sediments	Velocity analysis		Amplitude analysis	
	R	σ(R)	R	σ(R)
Loam (<0.5mm)	0.3142	0.0879	0.196	0.056
Fine Sand (<2 mm)	0.2473	0.0989	0.224	0.063
Coarse Sand (2-5 mm)	0.3146	0.1034	0.117	0.036
Round (3-8 mm)	0.2506	0.1019	0.258	0.068
Round (5-15 mm)	0.2756	0.1038	0.107	0.030
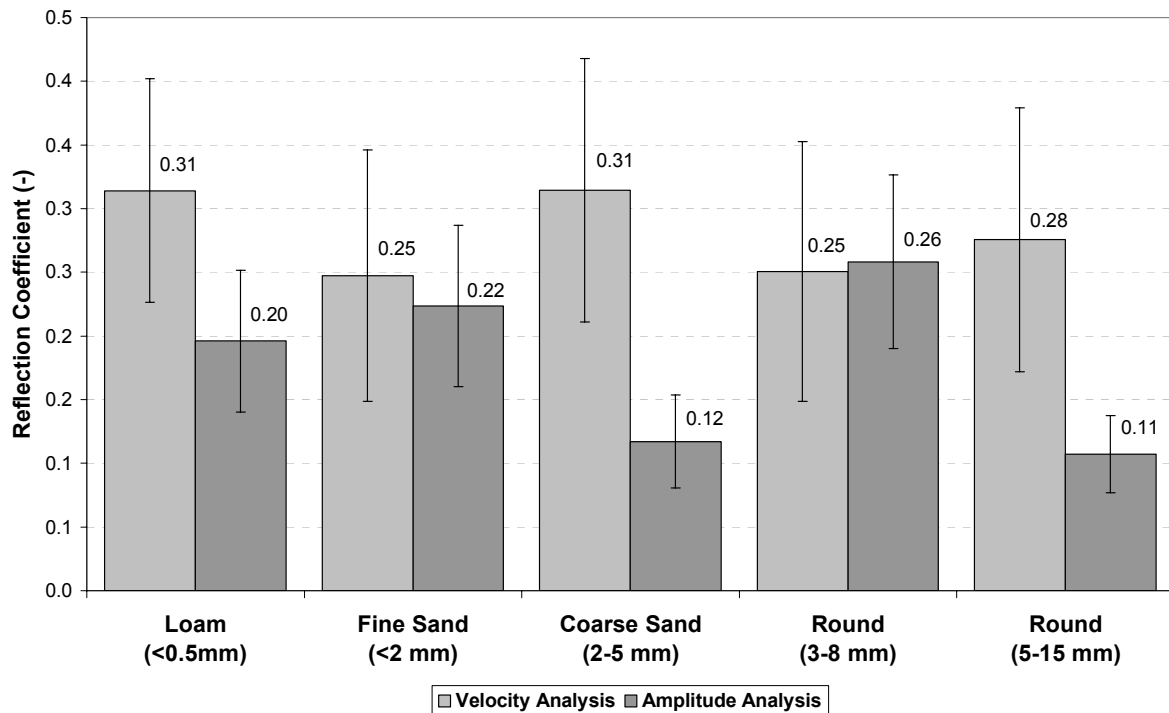
Figure 3.43: *Comparison between the water-sediments reflection coefficients estimated by the velocity and amplitude analysis. The vertical bars represent the uncertainties range ±σ.*

In order to have a comparison term, we collected from different references a collection of reflection coefficients relative to some lacustrine settings, we summarized the values founded in Table 3.40. On the base of the data in Table 3.40 we cold assert that our experimental values of the reflection coefficient are plausible for saturated sediments. In fact, even tough the broad uncertainties ranges obtained in our experiment, the reflection coefficients founded in our experiments are always

lower than 0.4. Then all the reflection coefficients estimated remain under 0.5, the reference value for the water-rock impedance contrast(Placzek and Haeni, 1995). This is an important result because now we can assert that it is plausible the discrimination at least between sediment and rocks.

From Table 3.40 we expected a water-loam reflection coefficient lower than 0.1. In our experiments we obtained from the amplitde analysis a reasonable value, instead the velocity analysis give us a value too high. A better results was achived for the fine sand (<2mm), in fact both the analysis give reflection coefficients comparable with the water-silt available in literature(Placzek and Haeni, 1995). Unluckily for the other sediments investigated we did not found a refernces value, due to the lackage of information available on this argument at the present.

Table 3.40: *Reflection coefficient for some lacustrine settings.*

	Reflection Coefficient	References
Water – Wet sediment	0.28	A-Cubed (1983)
Water – rock	0.5	Ramsey (2005)
Water - limestone	0.5	Placzek and Haeni (1995)
Water – clay	0.1	Placzek and Haeni (1995)
Water – silt	0.2	Placzek and Haeni (1995)
Water - mud	0.05-0.1	Placzek and Haeni (1995)

Sediments Permittivity by Amplitude Analysis

Now we estimate a new value of the bulk permittivity of the bottom sediments from the water-sediments reflection coefficient. Then, we proceed in the opposite way of the velocity analysis. In fact, before we estimate the reflection coefficients by the knowledge of the sediments bulk permittivity and the water permittivity. Instead now we rewrite equation (2.54) in order to estimate the sediments bulk permittivity k_B by the information of the bottom water-sediments reflection coefficients r , evaluated by the amplitude analysis, and of the water permittivity value k_W available form the calibration tests

$$k_B = k_W \cdot \left(\frac{1-r}{1+r}\right)^2 \tag{3.52}$$

After we estimated the uncertainties of the bottom sediments bulk permittivity $\sigma(k_B)$ by the error propagation analysis of equation (3.52)

$$\sigma(K_B) = \left|\frac{(1-r)^2}{(1+r)^2}\right| \cdot \sigma(K_W) + \left|K_W \frac{4 \cdot (r^2 - 1)}{(1+r)^4}\right| \cdot \sigma(r) \tag{3.53}$$

Table 3.41 reports the sediments permittivity and the relative uncertainties, estimated by equation (3.52) and (3.53), for each GPR measurements acquired on the 5 bottom sediments taken in account.

We summarized the values of Table 3.41 with the mean estimation of a bulk permittivity for each particulate media. The results are reported in Table 3.42 together with the bulk permittivity of the bottom sediments estimated by the velocity analysis. We showed the comparison between the two analyses in Figure 3.44. Moreover the uncertainties ranges of the permittivity estimated by the amplitude analysis are wider than the ones obtained from the velocity analysis. The uncertainties ranges of the amplitude analysis are so wide that it is difficult to discriminate between different bottom sediments. The comparison between the two analyses reveals that with the amplitude method we obtained higher values of sediments permittivity. In fact, we obtained a good match between the two analysis only with the round (3-8mm). We explained the higher permittivity founded with the amplitude analysis supposing a vertical gradient of the porosity in the bottom materials.

Table 3.41: *Permittivity of the sediments layer estimated by the analysis of the amplitude of the top of the sediments reflection event.*

Material	Position	1st measurement		2nd measurement		3rd measurement	
		ε_R	$\sigma(\varepsilon_R)$	ε_R	$\sigma(\varepsilon_R)$	ε_R	$\sigma(\varepsilon_R)$
Loam (<0.5mm)	Pos 1	37.1	11.4	36.2	12.0	37.4	11.6
	Pos 2	37.4	11.0	37.4	11.5	36.6	11.1
	Pos 3	45.5	10.7	45.5	10.5	45.3	10.7
	Pos 4	33.8	10.9	33.6	11.0	33.3	11.3
Fine Sand (<2 mm)	Pos 1	28.2	11.1	28.5	11.1	28.7	11.7
	Pos 2	29.7	10.6	29.9	10.6	29.9	10.8
	Pos 3	33.3	10.6	33.6	10.5	33.5	10.6
	Pos 4	38.6	10.6	38.7	10.5	38.7	10.4
	Pos 5	36.7	11.2	36.7	11.0	36.7	11.1
	Pos 6	37.2	12.6	37.2	12.5	37.3	12.6
Coarse Sand (2-5 mm)	Pos 1	53.2	12.0	53.0	11.6	53.0	11.7
	Pos 2	46.5	11.2	46.5	11.3	46.7	11.0
	Pos 3	43.8	11.0	43.4	11.1	43.4	11.0
	Pos 4	64.3	9.5	64.3	9.4	64.7	9.9
	Pos 5	60.3	9.9	59.2	9.9	59.3	10.0
	Pos 6	50.8	11.9	50.6	11.9	51.0	11.9
Round (3-8 mm)	Pos 1	21.2	9.9	21.3	10.2	21.4	10.1
	Pos 2	32.4	10.6	32.3	10.4	32.3	10.4
	Pos 3	35.2	10.0	34.4	10.0	34.3	10.0
	Pos 4	30.6	10.5	29.8	10.5	30.6	10.5
Round (5-15 mm)	Pos 1	52.1	11.6	52.2	11.7	52.2	11.5
	Pos 2	58.5	9.5	58.3	9.6	58.4	9.6
	Pos 3	49.2	9.8	49.0	9.8	49.2	9.9
	Pos 4	59.9	9.3	59.8	9.2	59.3	9.3

In the methods section 3.7.2, we explained that we filled the bottom sediments by subsequent layers. Then It could be possible that the lower layer were in more compacted condition than the upper layers. Consequently it could be possible the presence of a lower area, richer in the solid part and with a lower permittivity. Instead, in the upper part the higher water content imply an higher bulk permittivity. Regard this possible porosity unhomogeneity, we need to take in account that the velocity methods provides a mean permittivity value on the sediments thickness. Instead the amplitude method investigates the upper part of the sediments, probably for a deep of an half of the wavelength (nearly 2cm). Consequently if the hypothesis of an upper part of the sediments mattress richer in water was confirmed, the amplitude methods should provide higher bulk permittivity values.

Table 3.42: *Bottom sediments bulk permittivity k_B, with the relative uncertainties $\sigma(k_B)$, obtained by the velocity and amplitude analysis.*

Sediments	Velocity analysis		Amplitude analysis	
	k_B	$\sigma(k_B)$	k_B	$\sigma(k_B)$
Loam (<0.5mm)	22.9	1.8	38	11.2
Fine Sand (<2 mm)	30.6	2.1	34.1	11.1
Coarse Sand (2-5 mm)	22.9	1.8	53	10.9
Round (3-8 mm)	30.2	2.2	29.7	10.3
Round (5-15 mm)	27.1	2.1	54.8	10.1
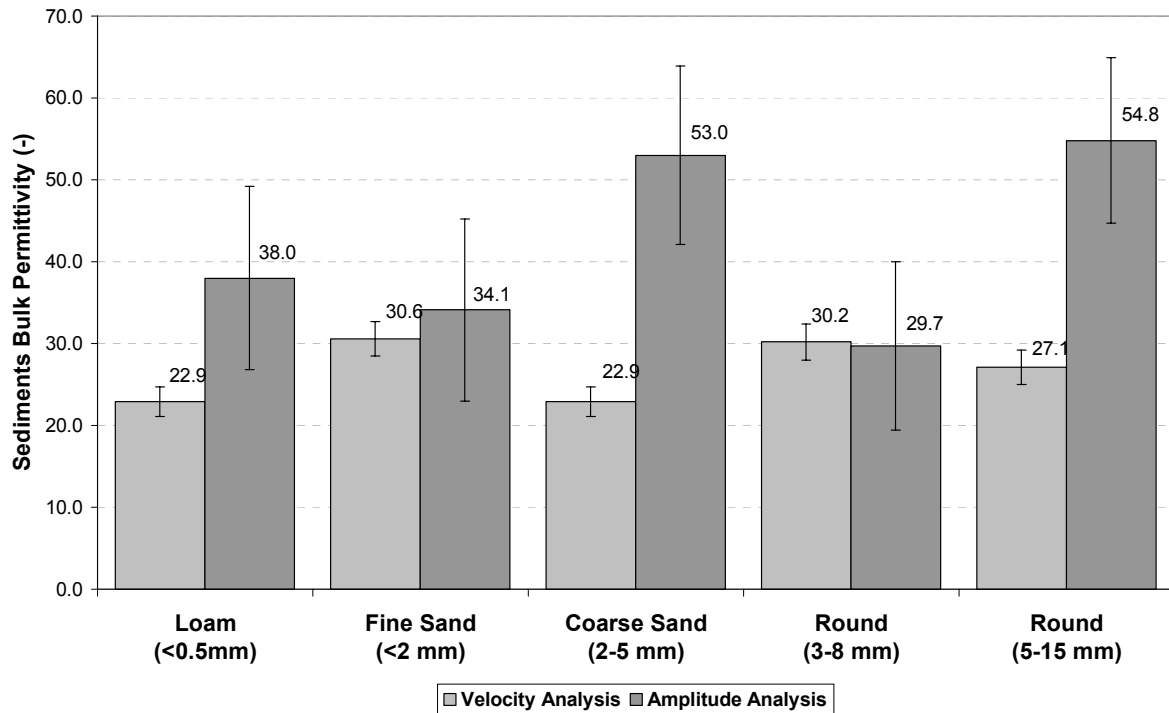
Figure 3.44: *Comparison between the bulk permittivity of the bottom sediments estimated by the velocity and amplitude analysis. The vertical bars represent the uncertainties range ±σ.*

3.8. Correlation between the Material Properties and the GPR measurements

In the following sections, we will show the relations among the electromagnetic properties and the porosity of the particulate media investigated. We found these relations adopting the mixing rules, a set of empirical and theoretical laws. The mixing rules define the permittivity of a multi component system, by the knowledge of the system porosity and the permittivity of each constituent of the system.

Firstly we'll give a brief introduction and review of the mixing rules, focusing the reader attention on their applicability and on the main advantages and disadvantages of each mixing rule taken in account. Then, for the sediments porosities estimation, we selected two of the presented mixing rules: the Bruggemann-Hanai-Sen (BHS) and the Complex Refractive Index Method (CRIM). We evaluated the sediments porosities with both the bulk sediments permittivities value evaluated in the previous sections: one by the velocity analysis and the other by the amplitude analysis. Finally we estimated with the inverse formulae of the mixing rules the bulk sediments permittivities and the water-sediments reflection coefficients from the sediments porosities estimated by direct methods.

3.8.1. Mixing Rules

The dielectric response of any multi-component system will depend upon the volume fraction and permittivity of each individual component (Knight and Abad, 1995). Moreover, the bulk permittivity is a complicated product of the components geometries and the electrochemical and physical interactions among the components (Knight and Endres, 1990). A number of theoretical methods have been proposed to determine the dielectric response of water-saturated sediments. In particular mixing rules provide a basis for predicting expected bulk permittivity values based on specific input parameters. The numerous mixing rules proposed could be fallen within four broad categories: effective medium, empirical and semi-empirical, phenomenological, and volumetric (Knoll, 1996). In Table 3.43 we presented some common mixing rules, subdivided in these categories.

Table 3.43: *Summary of dielectric mixing model categories (Martinez and Byrnes, 2001).*

Volumetric
Method: Relates bulk dielectric properties of a mixture to the dielectric properties of its constituents
Types: Complex Refractive Index Method (CRIM); Arithmetic average; Harmonic average; Lichetenecker-Rother; Time-Propagation (TP)
Advantages: Volumetric data relatively easy to obtain
Disadvantages: Does not account for micro-geometry of components; does not account for electrochemical interaction between components
References: Alharthi and Lange (1987); Birchak et al.(1974), Knoll (1996); Lange (1983); Roth et al.(1990), Lichtenecker and Rother (1931); Wharton et al. (1980)
Empirical and semi-empirical
Method: Mathematical functional relationship between dielectric and other measurable properties
Types: Logarithmic; Polynomial
Advantages: Easy to develop quantitative relationships; able to handle complex materials in models
Disadvantages: There may be no physical justification for the relationship; valid only for the specific data used to develop the relationship and may not be applicable to other data sets
References: Dobson et al.(1985); Olhoeft and Strangway (1975); Topp et al.(1980); Wang and Schmugge (1980)
Phenomenological
Method: Relates frequency dependent behavior to characteristic relaxation times
Types: Cole-Cole; Debye
Advantages: Does not need component properties or geometrical relationships
Disadvantages: Dependent on frequency-specific parameters
References: Power (1997); Ulaby et al.(1986); Wang (1980)
Effective medium
Method: Computes dielectric properties by successive substitutions
Types: Bruggemann-Hanai-Sen (BHS)
Advantages: Accurate for known geometries, valid for particulate media in saturated condition
Disadvantages: Cumbersome to implement; need to choose number of components, initial material, and order and shape of replacement material. It does not take in account the interactions among the different component.
References: Sen et al. (1981); Ulaby et al.(1986)

Volumetric models, for example the one proposed by Lichtenecker and Rother (1931), are semi empirical and provide an average of total permittivity of a sampled volume that is made up of a number of individual components of known permittivities and volume fractions (Huisman et al., 2003). Despite the apparent simplicity of this approach, remarkably good agreement has been found in modeling the dielectric properties of geological materials in the radar frequencies range, in particular with the

Complex Refractive Index Method (CRIM) proposed by Wharton et al. (1980). The CRIM is based on the propagation time along an optical pathway of a single electromagnetic ray (Sambuelli, 2009). However, there are factors such as the solid and fluid phases microgeometry, the solid-fluid interactions, and the frequency of the measurement that are not accounted for in the CRIM (Knight, 2001).

A further approach is the use of empirical relationships. For example the relationship proposed by Topp et al.(1980) is now a standard methods for extracting water content from permittivity measurements (Huebner et al., 2005). One limit of these models are that they predict values for the data used to construct them, but are not widely applicable to data sets consisting of different mineralogies, porosities, or water saturations (Martinez and Byrnes, 2001).

Some model types like phenomenological, that relate frequency dependent behavior to characteristic relaxation times, work well with relatively homogeneous materials such as ice, but are less effective for more complex, heterogeneous materials (Martinez and Byrnes, 2001).

Finally, the effective medium theories (EMT) are rigorous approaches to modeling the dielectric response of geological materials. These types of models take in account effects, like component geometry, in order to predict the dielectric response. We focus our attention on the Bruggeman-Hanai-Sen model (Bruggeman (1935), Hanai (1961), Sen et al.(1981)). The Bruggeman-Hanai-Sen (BHS) model consider a mixture composed of spheres of hosting material and spheres of hosted material and imposed the average field perturbation caused by the two materials to be zero (Sambuelli, 2009). The BHS assumes no interaction between the matrix and the fluid and no scattering, e.g., long wavelength compared to pore and particle sizes (Sneddon et al., 2002).

Considering the above-described limitations of the mixing rule, we adopted for our work two mixing rules widely experimented in similar conditions: the CRIM and the BHS.

3.8.2. Porosity Estimation

In this section, we show how we estimate the porosity from the GPR measurement by the two selected mixing rules: the CRIM and the BHS.

Starting form the CRIM, we can explicit the sediment porosity like

$$\Phi_{CRIM} = \frac{\sqrt{k_B} - \sqrt{k_S}}{\sqrt{k_A} - \sqrt{k_S} + S_w \left(\sqrt{k_W} - \sqrt{k_A} \right)} \tag{3.54}$$

where:

S_w is the water saturation of the mixture;

k_B is the sediments bulk permittivities estimated in the previous sections by the velocity and the amplitude analysis;

k_W is the water permittivity estimated in the calibration tests;

k_S is the permittivity of the solid part of the mixture, dependent of the grain mineralogy.

In the case of saturated sediments, the mixture became biphasic and the water saturation S_W is one, then equation (3.54) could be simplified in

$$\Phi = \frac{\sqrt{k_B} - \sqrt{k_S}}{\sqrt{k_W} - \sqrt{k_S}} \tag{3.55}$$

From equation (3.55) we propagated the uncertainties on the bulk permittivity $\sigma(k_B)$, water permittivity $\sigma(k_B)$ and the permittivity of the solid part $\sigma(k_B)$ in order to find the uncertainties range of the porosity $\sigma(\Phi_{CRIM})$ estimated with the CRIM

$$\sigma\left(\Phi_{CRIM}\right) = \left| \frac{1}{2\sqrt{k_B} \cdot \left(\sqrt{k_W} - \sqrt{k_S} \right)} \right| \cdot \sigma\left(k_B\right) + \left| \frac{\sqrt{k_B} - \sqrt{k_W}}{2\sqrt{k_S} \cdot \left(\sqrt{k_W} - \sqrt{\varepsilon_{R_{solid}}} \right)^2} \right| \cdot \sigma\left(k_S\right) + \dots$$

$$\dots + \left| \frac{\sqrt{k_B} - \sqrt{k_S}}{2\sqrt{k_W} \cdot \left(\sqrt{k_W} - \sqrt{k_S} \right)^2} \right| \cdot \sigma\left(k_W\right) \tag{3.56}$$

Analogously we could define the sediments porosity by the BHS method

$$\Phi_{BHS} = \frac{k_B - k_s}{k_w - k_s} \cdot \left(\frac{k_w}{k_B} \right)^c \tag{3.57}$$

where c is the shape factor, that in the case of spherical grains is equal to 1/3 (Hu and Liu, 2000).

The uncertainties of the sediment porosity estimated by the BHS method is

$$\sigma\left(\Phi_{BHS}\right) = \left|\frac{2k_B + k_S}{3K_B \cdot \left(k_W - k_S\right)} \cdot \left(\frac{k_W}{k_B}\right)^{1/3}\right| \cdot \sigma\left(k_B\right) + \ldots$$

$$\ldots + \left|\frac{\left(k_S - k_B\right) \cdot \left(k_S + 2\varepsilon_{R_{water}}\right)}{3k_W^{2/3} \cdot k_B^{1/3} \cdot \left(k_W - k_S\right)^2}\right| \cdot \sigma\left(k_W\right) + \left|\frac{k_S - k_W}{\left(k_W - k_S\right)^2} \cdot \left(\frac{k_W}{k_B}\right)^{1/3}\right| \cdot \sigma\left(k_S\right)$$

(3.58)

In order to find the sediments porosity by equations (3.55) and (3.57), we need an estimation of the solid part permittivity k_S of the mixture. We estimate k_S for each one of the five sediments investigate by a weighted mean of the minerals permittivity k_{mi}

$$k_S = \left(\sum_i f_i \sqrt{k_{m_i}}\right)^2$$

(3.59)

From the materials section 3.7.1, we derived the volume fraction f_i of each mineral type constituent the grain of the particulate media investigated. We attributed for each mineral the permittivity k_m founded in bibliography and summarized in Table 3.44. Table 3.45 reported the five permittivity of the solid part estimated by equation (3.59).

Table 3.44: *Dielectric constants of common minerals and fluids in the GPR measurements (Martinez and Byrnes, 2001).*

Mineral	k [-]	Frequency [MHz]	References
Albite	7	1	Olhoeft (1989)
Calcite	6.4	1	Olhoeft (1989)
Calcite	7.8–8.5	Radio	Keller (1989)
Gypsum	6.5	750	Martinez and Byrnes (2001)
Halite	5.9	1	Olhoeft (1989)
Kaolinite	11.8	1	Olhoeft (1989)
Mica	6.4	750	Martinez and Byrnes (2001)
Montmorillonite	210	1	Olhoeft (1989)
Olivine	7.2	1	Olhoeft (1989)
Orthoclase	5.6	1	Olhoeft (1989)
Pyroxene	8.5	1	Olhoeft (1989)
Quartz	4.5	1	Olhoeft (1989)
Water	80	1	Lucius et al. (1990)

Table 3.45: *Permittivity estimation of the solid part. We reported the relative volumetric abundance of each type of minerals and the permittivity of each minerals.*

Mineralogy	Quartz	Carbonate	Mica	Feldspar	Greenstones, basic rocks, mafic rocks	Permittivity of the solid part k_S
Mineral Permittivity	4.5	6.4	6.4	6.3	7.85	
			Abundance			
	%	%	%	%	%	
Loam (<0.5mm)	40	-	15	25	20	**5.84**
Fine Sand (<2 mm)	40	-	15	25	20	**5.84**
Coarse Sand (2-5 mm)	50	20	-	-	30	**5.79**
Round (3-8 mm)	50	25	-	-	25	**5.73**
Round (5-15 mm)	25	-	-	-	75	**6.93**

Table 3.46: *Porosity estimation by the two selected mixing rules, the CRIM and the BHS, by the bulk permittivities evaluated by the velocity and amplitude analysis.*

Materials	$K_S \pm \sigma(K_S)$	$K_B \pm \sigma(K_B)$	Amplitude Analysis CRIM $\Phi \pm \sigma(\Phi)$	Amplitude Analysis BHS $\Phi \pm \sigma(\Phi)$	$K_B \pm \sigma(K_B)$	Velocity Analysis CRIM $\Phi \pm \sigma(\Phi)$	Velocity Analysis BHS $\Phi \pm \sigma(\Phi)$
Loam (<0.5mm)	5.84±1	38.2±11.1	0.56±0.17	0.54±0.17	22.9±1.8	0.35±0.06	0.34±0.06
Fine Sand (<2 mm)	5.84±1	34.1±11.1	0.51±0.18	0.49±0.17	30.6±2.1	0.46±0.06	0.44±0.06
Coarse Sand (2-5 mm)	5.79±1	53±10.9	0.72±0.15	0.7±0.15	22.9±1.7	0.35±0.06	0.34±0.06
Round (3-8 mm)	5.73±1	29.7±10.3	0.45±0.18	0.43±0.17	30.2±2.2	0.46±0.07	0.44±0.06
Round (5-15 mm)	6.93±1	54.8±10.1	0.73±0.14	0.72±0.15	27.1±2.1	0.39±0.07	0.38±0.06

Thanks to the estimation of the solid part permittivity, we are now able to evaluate the sediments porosity by equations (3.55) and (3.57). In Table 3.46 we summarized all the physical quantities necessary for this estimation and the resulting porosity. In Table 3.46, we reported for each particulate material the grain permittivity evaluated by equation (3.59) and the sediments bulk permittivities estimated with the velocity and amplitude analysis. We omitted from Table 3.46 the terms of equations (3.55) and (3.57) that are equal for the five particulate materials: the water permittivity k_W and the shape factor c. In particular, we assumed the water permittivity k_W value derived in the calibration tests with the aluminum reflector (k_W=84.1±5.3). Moreover, we assumed spherical grain, then the shape factor c of the BHS formula was assumed equal to 1/3.
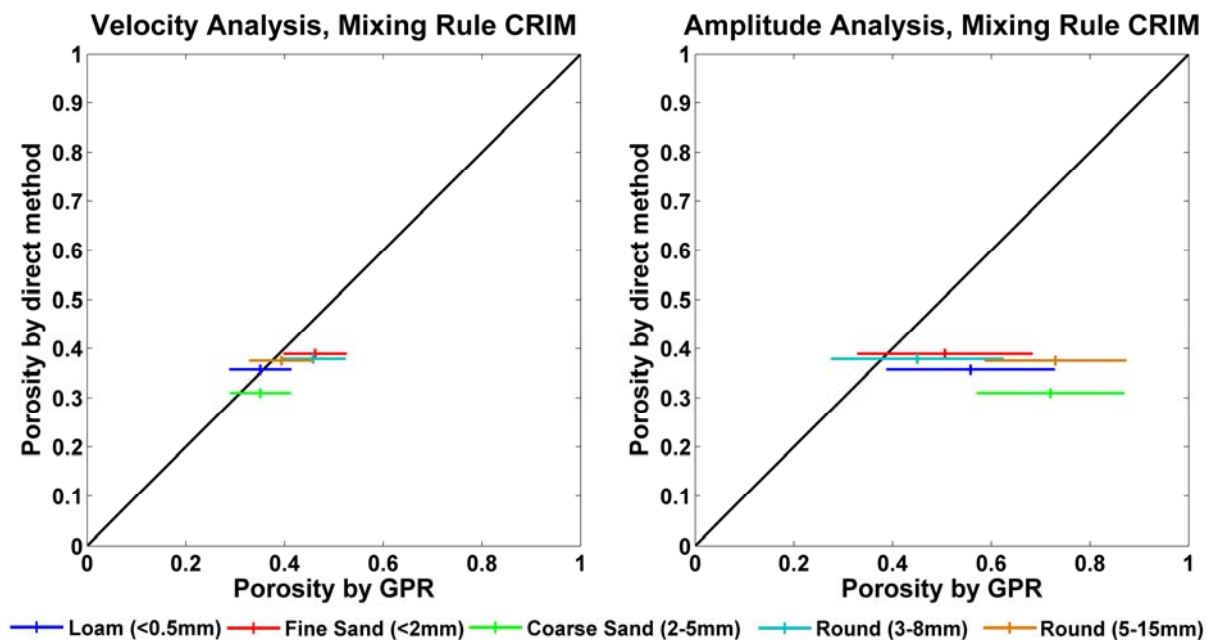
Figure 3.45: *Comparison between the sediments porosity measured by direct methods and the sediments porosity evaluated by GPR, assuming the mixing rules CRIM. The left graph reports the porosity obtained assuming the bulk permittivity derived from the velocity analysis, instead the right the one obtained with the amplitude analysis.*

We compared the sediments porosity evaluated with the mixing rules and reported in Table 3.46, with the porosity measured by direct method and reported in the Methods section 3.7.2. We illustrated this comparison by the graphs shown in Figure 3.45 and Figure 3.46. The ordinate axis of these plots represents the porosity measured by the sediments weighting operation, instead the abscissa axis represents the sediment porosity estimated with the different mixing rules and GPR analysis. Then for each

particulate material we plotted a cross representing the sediments porosities with their uncertainties. The bisectors of the axes, the black lines at 45° cutting the graphs in the middle, represent the perfect mach between the porosities measured by the direct methods and the porosities estimated by GPR. Then, sediments that the porosity estimated by GPR matches the porosity measured by direct methods should intersect with its uncertainties range the black line.
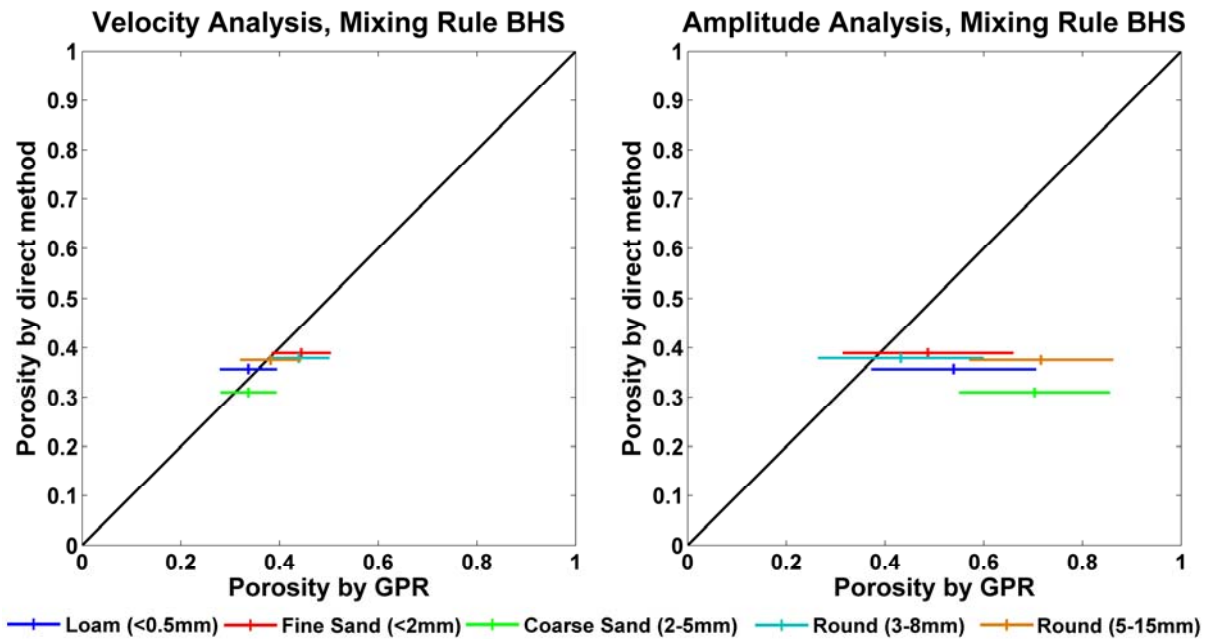
Figure 3.46: *Comparison between the sediments porosity measured by direct methods and the sediments porosity evaluated by GPR, assuming the mixing rules BHS. The left graph reports the porosity obtained assuming the bulk permittivity derived from the velocity analysis, instead the right the one obtained with the amplitude analysis.*

From both Figure 3.45 and Figure 3.46, we can observe that the porosity obtained from the amplitude analysis shows wider uncertainties range than the velocity analysis. The uncertainties ranges of the amplitude analysis are so wide that the porosity estimation became useless, if we consider the porosity range of most of the commons sediments in nature.

The porosities obtained from the velocity analysis are in good agreements with the ones measured by direct methods. In fact with both the mixing rules adopted we have intersections of three materials with the axes bisector, in particular: the loam (<0.5mm), the coarse sand (2-5 mm) and the round (5-15 mm). Moreover the remaining two materials, the fine sand (<2 mm) and the round (3-8 mm), are very closed to the bisector with the mixing rule CRIM and intersect the bisector in the case of the BHS. About the choose of the mixing rule, we can infer from these comparison

that the CRIM and the BHS lead a very similar results, than the selection of the mixing rule in our case is not a primary task. Finally, we can infer that the porosities estimated with the amplitude analysis are always higher than the ones measured by direct methods, then the amplitude analysis tends to overestimate the porosities.

3.8.3.   Modeling the EM Properties from the Porosities Measured

We wanted a further response about the EM properties estimated for the five particulate media: we evaluated the sediment bulks permittivities and the water-sediment reflection coefficients from the porosities measured by the direct methods. Then, we use the mixing rules in the opposite direction respect the previous section. Considering the limited influence of the mixing rule adopted we perform this evaluation only for the CRIM formula. Then we rewrite equation (3.55) to explicit the sediments bulk permittivities k_B

$$k_B = \left[(1-\Phi) \cdot \sqrt{k_S} + \Phi \cdot \sqrt{k_W} \right]^2 \tag{3.60}$$

where now Φ represent the porosity measured by direct methods and k_W continue to be the water permittivity estimated in the calibration tests (k_W=84.1±5.3). About K_s we need to highlight that we should adopt 5 different values according to Table 3.45, one for each particulate media investigated. To improve the clearness of the following figures we select only one value, evaluated as the mean of the five k_S values of Table 3.45.

The relation of the bulk permittivity versus the porosity, evaluated with the CRIM according to equation (3.60), is plotted with black curves in the two graphs of Figure 3.47. In the same graphs, we reported for each particulate media investigated the porosity measured by direct methods and the sediments bulk permittivities evaluated with the amplitude analysis in the bottom graph and with the velocity analysis in the top graph respectively. From Figure 3.47, we could highlight that the trend of the bulk permittivity increase with the sediments porosity. In fact, the bulk permittivity starts from the value of the grain permittivity (K_s=6.02±1) for water saturation null, to reach the water permittivity (k_W=84.1±5.3) when the porosity is unitary. Figure 3.47 confirms the results obtained in the previous sections. In particular only two permittivities value evaluated with the amplitude analysis intersects the theoretically trend of the CRIM: the ones relatives to the fine sand (<2 mm) and the round (3-8 mm). On the contrary the sediments bulk permittivities evaluated with the velocity analysis are in agree with

the the theoretically trend expected by the CRIM. In fact even thought not all materials intersect the CRIM curves, because their uncertainties ranges are very narrow, however they remain very close to the theoretical trend.
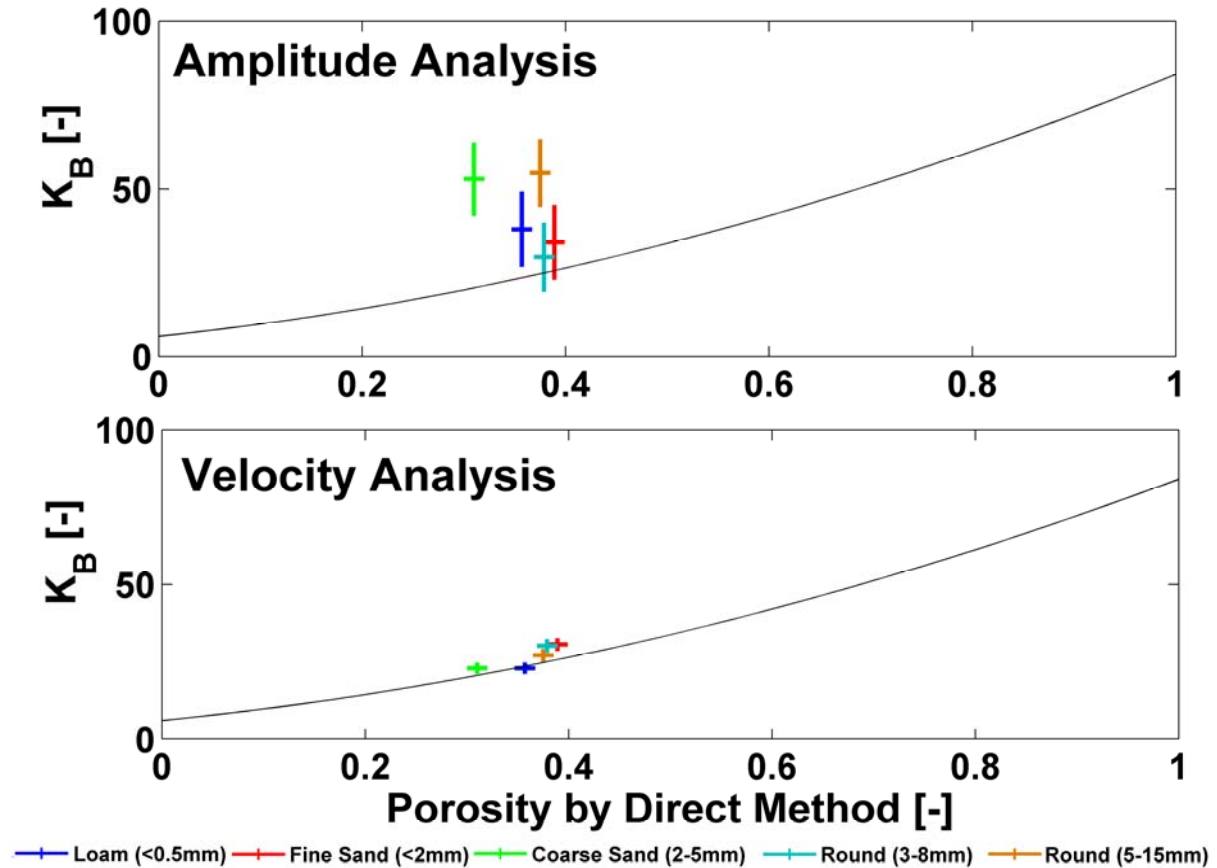

Figure 3.47: *Comparison between the sediments bulk permitivities estimated experimentally by GPR and the values expected thoretically by the CRIM. The black curves are the trend forecast by the CRIM (k_W=84.1±5.3, K_s=6.02±1). The coloured cross represent the permettivities evaluted by the GPR analysis and the porosity measured by direct methods.*

Finally we evaluated the trend of the water-sediments reflection coefficient according to the CRIM. Then, we substituted the sediment bulk permittivities evaluated by equation (3.60) in the simplified relation of the reflection coefficients described by equation (2.54), and we obtained

$$ r = \frac{\sqrt{k_W} - (1-\Phi) \cdot \sqrt{k_s} - \Phi \cdot \sqrt{k_W}}{\sqrt{k_W} + (1-\Phi) \cdot \sqrt{k_s} + \Phi \cdot \sqrt{k_W}} \tag{3.61} $$

In the two graphs of Figure 3.48, we plotted with black curves the relation between the water-sediments reflection coefficients, expected by equation (3.61), versus the porosity. From Figure 3.48, we can observe that the water-sediments reflection

coefficient decrease inversely to the porosity. In fact, for null water saturation we obtain reflection coefficients correspondent to the water-dry grains condition (r=0.58).
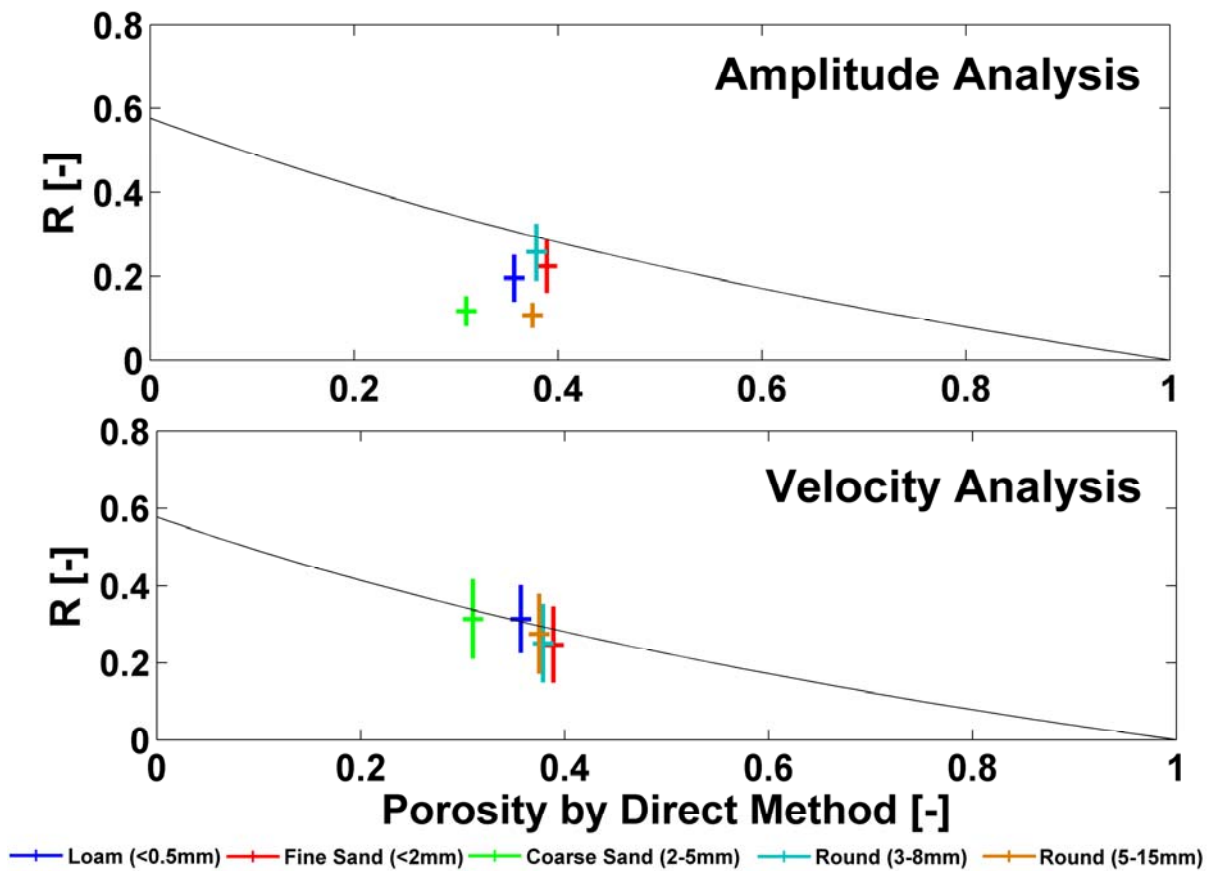
Figure 3.48: *Comparison between the water-sediments reflection coefficients estimated experimentally by GPR and the values expected thoretically by the CRIM. The black curves are the trend forecast by the CRIM (k_W=84.1±5.3, K_s=6.02±1). The coloured cross represent the water-sediments reflection coefficients evaluted by the GPR analysis and the porosity measured by direct methods.*

Instead, when the porosity is unitary, the reflection coefficient is zero because there is not EM impedance contrast. In the same graphs, we added with colored crosses the water-sediments reflection coefficients evaluated by the GPR. In particular, in the top graph the ones relative to the amplitude analysis and in the bottom the ones of the velocity analysis. These water-sediments reflection coefficients are placed in correspondent to the porosity value measured by direct methods. From Figure 3.48 we could highlight again that the water-sediments reflection coefficients provided by the velocity analysis match perfectly the theoretically trend, even though we need to take care about the wide uncertainties range. Instead the amplitude analysis gives back unattended values that do not match the trend forecasted by the CRIM, with the exception of the fine sand (<2 mm) and the round (3-8 mm).

3.9. Discussions

In this section, we want to discuss about the results obtained with the two GPR analysis performed. In particular we would explore why the amplitude analysis give back responses not matched by the theoretically trends of the mixing rules and by the velocity analysis results.

Certainly, we are satisfied by the responses of the velocity analysis. The velocity analysis assures us about the accuracy and the reliability of the experiments with the particulate media. In fact, all the velocities of the EM pulse in water, evaluated by the linear regression of the water depth data versus the two-way-travel-time, are consistent among the different tests and with the values available in bibliography. This point is well proved in Figure 3.36. Consequently, we are confident about the reliability of the water permittivity evaluated with the velocity values. Moreover Figure 3.37 shows like the water permittivities estimated experimentally are conformed with the theoretical trend proposed by Malberg and Maryott (1956).

About the sediments bulk permittivities evaluated by the velocity analysis we do not have a reference values of a direct measure, then we can not assure about their reliability. However their uncertainties ranges are very narrow. Secondly the sediments permittivity estimated are in agree with the values expected from the mixing rules according the porosity measured by direct methods like is shown in Figure 3.47. Moreover the water-sediments reflection coefficients estimated with these values of the bulk sediments permittivity are in agree with the values available in bibliography, like is inferable by Table 3.40. Furthermore there is optimal agreement among the water-sediments reflection coefficients estimated experimentally by the velocity analysis and the values expected theoretically by the mixing rule with the porosity available from the direct measures, like is shown in Figure 3.48. Finally the porosities estimated by the GPR with the velocity analysis are in agreed with the porosities measured by direct methods, like is proven by Figure 3.45 and Figure 3.46.

On the opposite, the responses of the amplitude analysis are more difficult to be interpreted. The first point worthy of attention is the high dispersion of the water attenuation terms, estimated by the linear regression of the amplitude data in time domain, among the different tests with the particulate media, like is inferable by the

interpretation of Table 3.37 and Figure 3.40. On the contrary, the water attenuation terms evaluated in the calibration tests were better in agreement. Moreover the sediments bulk permittivities and the water-sediments reflection coefficients estimated with the amplitude analysis are not consistent with the ones evaluated from the velocity analysis, like is well shown in Figure 3.43. Moreover from Figure 3.47 and Figure 3.48 we can highlight that these values, derived by the amplitude analysis, do not fit the theoretically trend expected by the assumption of the mixing rules with the porosity value provided by the direct methods. Finally the porosity estimated experimentally by the GPR response of the amplitude analysis are not in agreed with the measure of porosities performed by direct methods, like is shown in Figure 3.45 and Figure 3.46.

In order to explain the defect of the amplitude analysis responses we formulated a series of hypothesis. We considered the possible unreliability of the amplitude data provided by the GPR. However, we soon discarded this hypothesis for different reasons. First, the main bang check showed in section 3.6.3 guaranteed us about the high repeatability of the amplitude response of the GPR. Moreover, in the calibration tests, we evaluated water attenuation terms in time domain based on the amplitude data, and the results were consistent among the tests. Furthermore, the water attenuation terms evaluated in frequency domain matched very well the value provided by the Open Ended Coaxial Cable measure.

A further element of our thought is the accuracy of the estimation of the amount of energy emitted from the antenna and entered in water. In fact this value was not evaluated by a direct measure but by an indirect estimation, valid under the assumption explained in section 3.7.4. We cannot completely discard this hypothesis because we can not have a reference term. However, the EM properties evaluated with the amplitude analysis are characterized by high dispersion, that it is difficulty explained by a systematic error like this.

Our principal conjecture is focused on the presence of scattering phenomena in the measures with the particulate media. We discussed about the theory of scattering in section 2.13.3. Let us to consider reliable the velocity of the EM pulse in water estimated in the calibration tests (V_W=0.0327 m/ns). Let us to assume a shift down of the dominant frequency from 1500 MHz toward 700 MHz, according to section 3.6.3. Then, we can evaluate the dominant wavelength of the radar signals with equation

(2.44) equals roughly to 5 cm. Dealing with GPR, it is common recognizable to consider diffraction scattering when the investigated object are bigger than one quarter of the wavelength, then in our case 1.25 cm. Based on this assumption, we selected the sediments for our experimentation, like we explained in the Experimental Design section 3.3 and in the Materials section 3.7.1. However, we cannot exclude that it could be occurred diffraction scattering, of low entity, from sediments grains smaller the one quarter of the dominant wavelength. Some results seem to confirm this hypothesis. In fact all the linear regression of the amplitude data evaluated on the tests with the sediments are statistically worse than the ones performed on the calibration tests. However the problems due to diffraction scattering are less relevant in the field condition of a survey because the antenna frequencies are lower and consequently the dominant wavelength are higher.

Finally, we hypnotized the presence of a vertical gradient of the porosity in the sediments layer investigated. This aspect could justify the different response among the amplitude and velocity analysis. In the methods section 3.7.2, we explained that we filled the bottom sediments by subsequent layers. Then it could be possible that the lower layers were in more compacted condition than the upper layers. Consequently it could be possible the presence of a lower area, richer in the solid part and with a lower permittivity. Instead, in the upper part the higher water content implies a higher bulk permittivity. Regard this possible porosity unhomogeneity, we need to take in account that the velocity methods provides a mean permittivity value on the sediments thickness. Instead, the amplitude method investigates the upper part of the sediments, probably for a deep of an half of the wavelength (nearly 2cm). Consequently, if the hypothesis of an upper part of the sediments mattress richer in water was confirmed, the amplitude methods should provide higher bulk permittivity values, as we verified. However, in the field condition of a survey this problem is less relevant because with lower antenna frequency we could reach higher penetration depth.

3.10. Conclusions

In this chapter we demonstrate that we achieved good assessments of the sediments porosity by GPR techniques only with the interpretation of the velocity of the EM pulse in the sediments. At the same time we highlighted the low reliability of the sediments porosity obtained with the amplitude analysis of the GPR response.

The amplitude analysis was the main objective of this study, because this method better suits the condition of riverine GPR surveys from the water surface of shallow water environments. In fact the application of the velocity analysis requires knowledge about the water depths and the sediments thickness. In field conditions the EM velocity of the GPR pulse in water could be easily known, consequently it could be evaluated the water depths data. On the contrary the sediments thickness is usually one of the tasks to be determined in a geophysical survey.

We can not explain beyond all understanding why the amplitude analysis provided low reliable responses, but we explored a set of hypothesis. First of all we can not rule out the influences of diffraction scattering from objects smaller that one quarter of the GPR dominant wavelength. Secondly we highlight that the two methods probe different penetration depth. In particular the velocity analysis give back a mean response on the sediments layer thickness, instead the amplitude analysis investigate the top of the sediments in function of the frequency adopted. Consequently, in bottom sediments with vertical gradient of the grain size distribution or porosities the two methods could provide different responses. However, both these effects have remarkably lower influence in field conditions. In fact, to achieve sufficient penetration depth in the water, it should be used lower frequencies, which imply diffraction scattering only from very coarse gravel and higher penetration depth in the sediments. Moreover, we found for all the sediment investigated in this work, water-sediments reflection coefficients lower than the values expected for water-rock. Consequently, if the discrimination between different sediments could be problematic, on the other hand the distinction between sediments and rock bottom is easily achievable.

4. Waterborne GPR survey for bottom sediment variability estimation

4.1. Abstract

We conducted an integrated geophysical survey on a stretch of the river Po in order to check the GPR ability to discriminate the variability of riverbed sediments through an analysis of the bottom reflection amplitudes. We conducted continuous profiles with a 200MHz GPR system and a handheld broadband electromagnetic sensor. A conductivity meter and a TDR provided punctual measurements of the water conductivity, permittivity and temperature. The processing and the interpretation of both the GEM-2 and GPR data were enhanced by the reciprocal results and by integration with the punctual measurements of the electromagnetic properties of the water. We used a processing flow that improved the radargram images, and preserved the amplitude ratios among the different profiles, and the frequency content of the bottom reflection signal. We derived the water attenuation coefficient both from the punctual measurements using the Maxwell formulae and from the interpretation of the GPR data, finding an optimal matching between the two values. The GPR measurements provided maps of the bathymetry and of the bottom reflection amplitude. The high reflectivity of the riverbed, derived from the GPR interpretation, agreed with the results of the direct sampling campaign that followed the geophysical survey. The variability of the bottom reflection amplitudes map, which was not confirmed by the direct sampling, could also have been caused by scattering phenomena due to the riverbed clasts which are dimensionally comparable to the wavelength of the radar pulse.

4.2. Introduction

This work deals with the acquisition, processing and interpretation of waterborne GPR to survey bathymetry changes and discriminate between riverbed sediments. We collected GPR data on the Po river (Turin, Italy) in autumn 2005. We also acquired low frequency electromagnetic, TDR, conductivity and temperature measurements during the same campaign (Sambuelli et al., 2007). Some months later we also made a direct sampling of the river bottom.

Monitoring the river erosion and understanding the connection between surface water and underground water are critical environmental issues. Interest in applications of Ground Penetrating Radar to shallow water environments is growing, as shown by the significant number of publications related to this topic. The early applications of GPR in water environments (Annan and Davis, 1977; Kovacs, 1978) were carried out in low conductive media, such as melting water in arctic areas. A high penetration depth can be achieved in such low conductive water: examples exist of sub-bottom penetration in water depths exceeding 25m (Delaney et al., 1992). There are many works, in frozen environments, aimed at obtaining bathymetric maps of ice-covered lakes (Moorman et al., 2001; Schwamborn et al., 2002) and reservoirs (Arcone et al., 1992; Hunter et al., 2003; Best et al., 2005). The improvements in GPR technologies, however, now also allow good penetration in conductive water (Arcone et al., 2006). A system with the emitted power enhanced by a factor of 1000 has also been designed to perform acquisitions in shallow sea water (Abramov et al., 2004) and this system has obtained penetrations of 1-2 m in sediments saturated by salt water.

Thanks to its flexibility and potentiality, GPR is currently a reliable tool for bridge scour assessment (Davidson et al., 1995; Olimpio, 2000; Webb et al., 2000; Park et al., 2004), stream discharge monitoring (Haeni et al., 2000; Melcher et al., 2002; Cheng et al., 2004; Costa et al., 2006); sedimentological studies of bottom deposits (Buynevich and Fitzgerald, 2003; Fuchs et al., 2004; Shields et al., 2004); bathymetric mapping (Moorman and Michel, 1997; Powers et al., 1999; Jol and Albrecht, 2004), and for finding submerged objects like lumber (Jol and Albrecht, 2004). Many authors agree that GPR could provide complementary information to seismic methods, especially in very shallow water where reverberation can prevent the interpretation of subbottom reflectors (Arcone et al., 2006), or when gas in the

sediment prevents seismic signal penetration (Delaney et al., 1992; Mellett, 1995; Powers et al., 1999; Schwamborn et al., 2002). The versatility of GPR is also due to the large flexibility of the surveying setups: case histories report the use of antennas directly coupled to water from the surface (Sellmann et al., 1992; Mellett, 1995); prototypes of submerged antennas (Meyers and Smith, 1998; Tóth, 2004); non contact systems such as helicopter-mounted (Melcher et al., 2002) or rope hanging systems (Costa et al., 2000; Haeni et al., 2000; Cheng et al., 2004); antennas placed on the bottom of non metallic boats (Jol and Albrecht, 2004; Park et al., 2004; Porsani et al., 2004; Bradford et al., 2005).

The potentiality of GPR to detect the composition of a riverbed was already mentioned in early studies (Ulriksen, 1982). In his work, Ulriksen suggested that fine sediments could be identified from strong and smooth reflectors, and moraine from speckled and weak signals, while boulders may produce hyperbolic diffractions. The same qualitative approach to the analysis of basin bottom characteristics has positively been tested by others (Beres and Haeni, 1991; Powers et al., 1999), and in particular Dudley and Giffen (1999) who found an optimal agreement between the GPR results and the direct sampling of the sediments. However, there seems to be a lack of documentation concerning the discrimination of sediment through a quantitative analysis of amplitude. This work aims at providing a methodology to perform an approximate characterization of river bottom sediment through a mapping of the GPR amplitude of reflection (AOR).

The possibility of a quantitative analysis of bottom AOR derives from the following assumptions: the signal transmitted in the water is constant and the river water is homogeneous with respect to the electromagnetic field. We verified the first assumption through preliminary tests, by checking the constancy of the main bang (the first reflection event in a radargram acquired with a near zero offset bistatic antenna) obtained from the water surface. The second assumption is particularly true in shallow rivers, where there is no thermocline and therefore no reflectors before the river bed (Bradford, 2007). We based the corrections of the radargrams for geometrical spreading and water attenuation on this latter assumption. Our methodology is based on the hypothesis that after these corrections have been made, the AOR from the river bed sediments mainly depends on the type of sediments and is uncorrelated to the water depth. However, at least another two

geometrical factors may affect AOR: the slope and the rugosity of the river bottom. As far as the presence of a dipping reflector is concerned, we calculated the gradient of the bathymetry map and verified that more than 95% of the surveyed area has a slope angle below 4°. We hypothesized that the rugosity of the river bottom was negligible compared to the wavelength. This hypothesis, however, was not confirmed by the direct sampling campaign.

Finally, even though we could not estimate the real reflection coefficient, because we did not have information about the amplitude of the signal that entered the water, we considered the possibility of correlating the AOR variability to the variability in the river bed sediments.

4.3. Data Acquisition

In order to test our methodology, we chose a 300m long stretch of the Po river in Turin, in the North-West of Italy. First, we performed a geophysical survey in the autumn of 2005 and then a bottom sampling survey in spring 2006, choosing the sampling points according to the results of the analysis performed on the geophysical data.

Table 4.1: *Acquisition parameters of the IDS K2 GPR*

Antenna Central Frequency	200 MHz
Acquisition rate	6 traces/s
Mean distance between trace	0.3 m
Gain	No
Samples per Trace	2048
Recording Time	400 ns
GPS logging frequency	1 Hz

We carried out the first survey in two steps: first, we collected continuous data with a IDS K2 GPR and a Geophex GEM-2 handheld broadband electromagnetic sensor. Immediately after the continuous acquisitions, we collected punctual measurements of the water permittivity with a Time Domain Reflectometer (TDR) Tektronic 1502c, and of the water conductivity and temperature with a conductivity meter ProfiLine-197.

We referred both acquisitions to the UTM-WGS84 absolute reference system with a real-time kinematic (RTK) GPS positioning. Further details about the boat positioning and tracking can be found in chapter 5.

We used a pulsed radar IDS K2 with a TR200 IDS unit, a 200MHz central frequency bistatic antenna, placed on the flat bottom of a fiberglass boat. We adopted the solution of the antenna placed in the boat and excluded other possibilities. We avoided non contact methods mainly for two reasons: hanging the antenna over the water surface would have caused a widening of the emission cone and multiple patterns in the air and therefore a loss of the horizontal resolution and the introduction of noise in the radargrams. We also excluded a system with a submerged antenna towed on the river bottom for different reasons. First, the antenna cable could have been trapped by submerged objects such as tree trunks, and second, there are documents about the discovery of second world war UXOs in the Turin Po river. Moreover, the choice of the antenna placed on the water surface allows bathymetry estimation. We acquired 10 profiles, 9 parallel to the shorelines and one along a crooked line intersecting the others along four different segments at an approximate angle of 45° (Figure 4.1). All the GPR profiles were acquired using the same configuration with the acquisition parameters reported in Table 4.1.

Table 4.2: *Punctual measurement results: mean and standard deviation, evaluated on 14 points, of the water conductivity, temperature and permittivity at different depths.*

Water Depth (m)	Conductivity (mS/m)		Temperature (°C)		Permittivity (-)	
	Mean	Std	Mean	Std	Mean	Std
0	36.8	0.64	13.3	0.12	85.1	3.35
0.5	36.8	0.48	13.3	0.06	84.1	3.22
1	36.7	0.44	13.2	0.06	85.0	3.21
1.5	36.8	0.42	13.2	0.06	83.3	2.81
2	36.7	0.07	13.3	0.07	-	-
All Depths	36.7	0.46	13.3	0.08	84.4	3.17
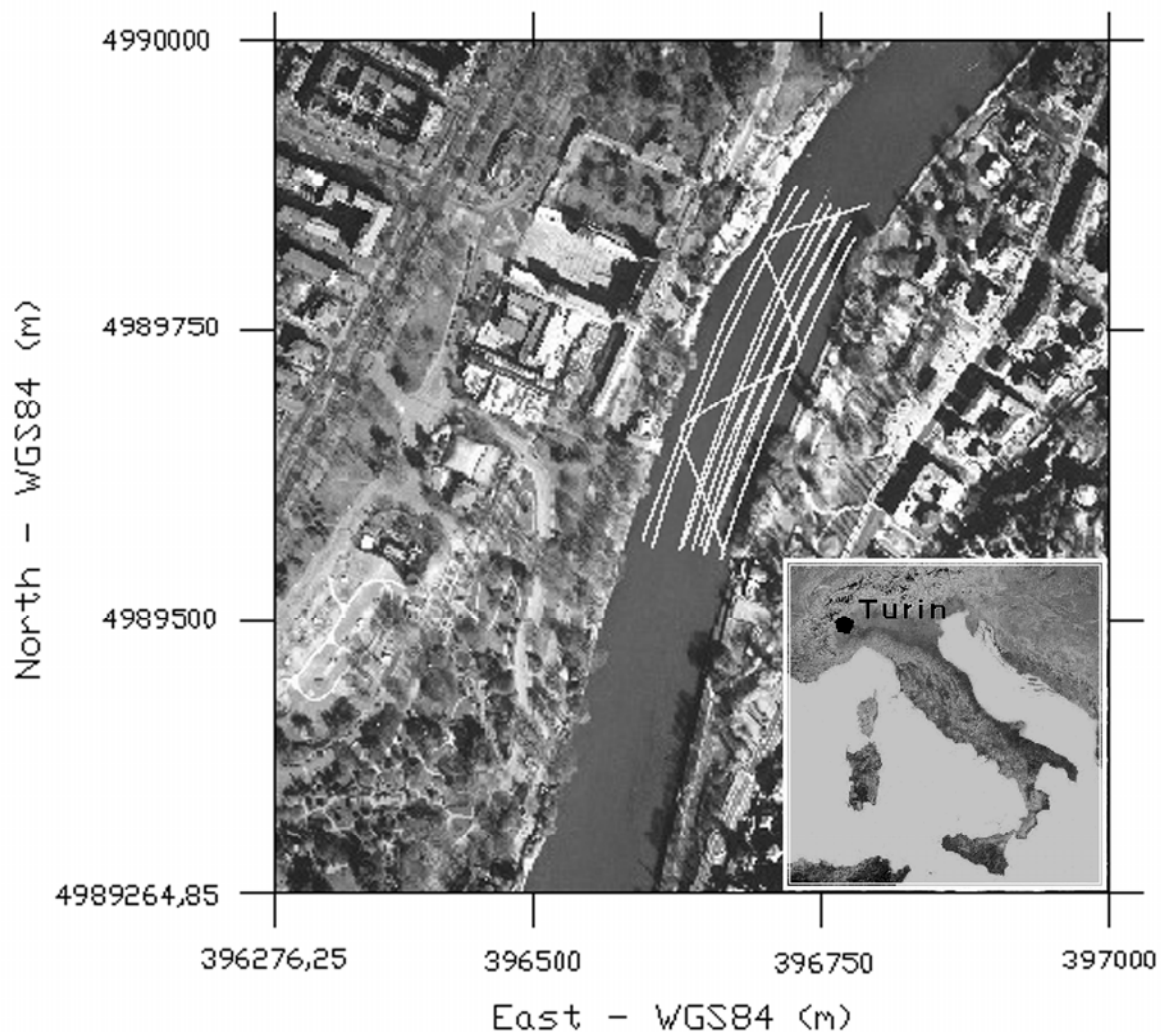
Figure 4.1: *Location of the 10 processed GPR profiles acquired on the Po river in Turin, Italy. The river flows from North to South. Profile 1 is near the western bank, profile 9 is near the east bank, and profile 10 is the crooked one.*

The physical and chemical properties of the water, such as temperature and salinity, influence water conductivity and permittivity which in turn affect the velocity and attenuation of a radar pulse. For example, the vertical gradients of these properties could influence the velocity of the radar waves (Ellison et al., 1996) and consequently the bathymetry accuracy. In order to provide information on the variability of the water properties in the investigated area and to check the vertical gradients, we measured the temperature, conductivity and permittivity from the water surface to a depth of 2m in 0.5m steps (Table 4.2). We took these measurements at 14 points roughly distributed along three lines parallel to the axis of the river: one near the west bank, one near the east bank and the other approximately coincident with the river axis.

We performed the bottom sampling survey in April 2006, when the interpretation of the geophysical survey was established. No flood events occurred between the surveys. We selected 12 points according to two criteria: to scan the bathymetry range and to sample different reflectivity areas. The bottom sampling results are reported in Table 4.3.

Table 4.3: *Riverbed sampling results at each point with a brief description of the sampled sediments, the dimension of the maximum clast collected in the sampling point, its size parameter estimated with equation (4) for a wavelength of 0.16 m, the water depth and the amplitude of reflection (AOR) corresponding to the sampling point.*

Sampling Points	Sample description	Max. clast diameter (cm)	Max. size parameter (-)	Water depth (m)	AOR (dB)
1	4 cobbles with a small amount of sandy silt	6	1.18	1.66	-13.8
2	4 cobbles with a small amount of sandy silt	6	1.18	1.16	-12.7
3	3 cobbles in a gravel matrix with silty sand	9	1.77	1.29	-19.2
4	1 cobble in a silt and gravel matrix	7	1.37	1.24	-7.37
5	Silt with sandy gravel	<1	0.20	1.42	-8.28
6	3 cobbles with sandy-silty gravel	8	1.57	1.61	-11.3
7	1 cobble in a sandy-gravelly silt	7	1.37	1.57	-15.1
8	2 cobbles with sandy-silty pit-run gravel	10	1.96	1.69	-12.7
9	1 cobble covered by silt	9	1.77	2.84	-13.4
10	2 cobbles with pit-run gravel (relatively abundant)	8	1.57	3.05	-10.5
11	Gravel with sand	<1	0.20	2.83	-7
12	2 cobbles in a gravelly-silty sand matrix	6	1.18	2.68	-15.3

4.4. Data Processing

According to the measurements carried out with the conductivity meter and the TDR on the Po water, we obtained the values of the electromagnetic properties reported in Table 4.2 for different water depths. This analysis shows the homogeneity of the water flowing in the surveyed area, and the lack of any significant vertical gradient. We then calculated the average and standard deviation values, shown in Table 4.2, of the conductivity (σ), the permittivity (ε_r) and the temperature (T). We then calculated, with the Maxwell formulae, the attenuation (α), the propagation factor (β), the velocity (v) and the wavelength (λ) of a pulse with a dominant frequency (f) of 200MHz in the water with the aforementioned average values of the electromagnetic parameters and a relative magnetic permeability (μ_r) equal to 1. The results are shown in Table 4.4.

Table 4.4: *Electromagnetic properties of the water estimated with the Maxwell formulae from the conductivity and permittivity measurements.*

ε_r (-)	σ (mS/m)	μ_r (-)	f (MHz)	α (m^{-1})	β (m^{-1})	v (m/ns)	λ (m)
84	36.8	1	200	0.756	38.4	0.033	0.16

Before any processing of the GPR data, we windowed the main bangs of all the traces and we assessed the repeatability of the signal: Figure 4.2 shows all the 8545 raw main bangs of the 10 profiles acquired in the survey. All the signals are very similar and there is overlapping in several points. Similar results are very unusual in terrain acquisitions, but in water applications, it is easy to assure a constant coupling between the antenna, boat and water, while the water impedance usually remains homogeneous along a survey area.

We carried out the data processing to preserve the amplitude ratios among different traces and profiles, and the frequency content of the reflections from the river bottom as much as possible. According to this aim, we processed the data in the following steps.
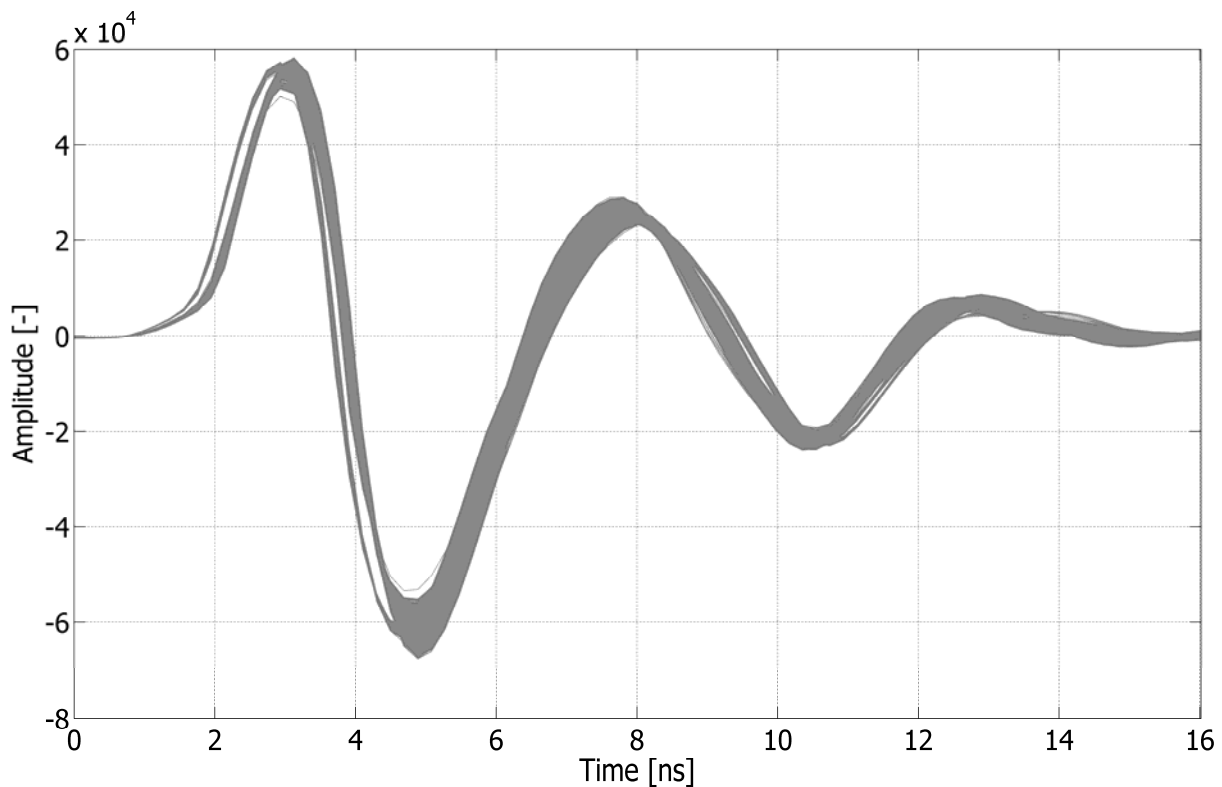
Figure 4.2: *Main bang repeatability. The 8545 raw main bangs of the 10 acquired profiles are plotted. Plot overlapping is due to the high similarity of the traces.*

Zero time correction: we removed the time delay added to the acquisition before the main bang to obtain the "zero" time coinciding with the beginning of the trace.

Dewow: we removed the very low frequency components from all the traces. These undesirable components were present in the signal because the acquisitions were all performed without any filter.

Time cut: after a preliminary check of the profiles, we found that the maximum two-way time (TWT) of the bottom reflection was always less than 180ns. The time cut reduced the trace length from 400 ns to 200 ns.

Background removal: we applied a high pass horizontal filter to all the profiles in order to remove a horizontally coherent component due to a ringing at 200MHz. We applied background removal because two of the next steps, i.e. Divergence compensation and Gain function, would have amplified the amplitude of the ringing.

Divergence compensation: with this operation, we recovered the geometrical attenuation. We could not estimate the radiation pattern of the antennas and it was therefore not taken into account in this correction. The compensation acts on each trace allowing the recovery of the geometrical divergence losses. We multiplied the amplitudes of each sample of each trace by its TWT times the pulse velocity in the

water, thus assuming we were in the Fraunhofer region with spherical loss. This assumption also implicitly means that the down going wave front is spherical and can be approximated locally with a plane wave. The wave then impinges on a flat surface and the up going wave front is plane. This is also equivalent to hypothesizing an image source symmetrical to the real source with respect to the reflecting surface.

After the application of the divergence compensation, we picked the positive maxima AOR of the riverbed and the relative depths. In order to perform the picking operation quickly, we adopted the interpolated auto picking feature available in Sandmeier's Reflex-Win Software. We isolated the reflection events by muting the amplitudes of the traces above and below the bottom reflection in order to guide the auto picking. We estimated the reflection depths with the TWT using a water velocity value equal to 0.033 m/ns. We obtained a depth range from 1 to 3 m, so that we could consider, even in the shallowest condition, the reflection geometry as nearly vertical, the distance between the transmitter and receiver dipoles being equal to 0.19m. The auto picking failed at a limited number of locations where the water depth was greater than 3 m: we did not collect the amplitudes at these locations.

We checked the input signal uniformity, the water homogeneity and the nearly vertical reflection geometry throughout the survey. Then, after the divergence compensation, the AOR should follow an exponential decay with respect to the water depth (Z_W) according to the equation:

$$\frac{AOR}{A_0} = e^{-\alpha \cdot 2 \cdot Z_W} \tag{4.1}$$

where A0 is the amplitude of the wave entering the water and α (m^{-1}) is the water attenuation coefficient. The spherical loss assumption, together with the Rayleigh scattering condition, would then imply that the difference in the AOR from the exponential trend should mainly be given by the difference of electromagnetic characteristics of the reflecting medium, that is, the bottom sediments.

Figure 4.3 shows all the collected picked amplitudes versus twice the water depth together with the least square regression exponential, identified by the equation:

$$AOR = 11540 \cdot e^{-0.743 \cdot 2 \cdot Z_W} \tag{4.2}$$

The value of the attenuation coefficient, 0.743 m^{-1}, estimated from the regression of the AOR, differs by less than 2% from that estimated with the Maxwell relation: 0.756 m^{-1}.

Gain function: with this operation, we recovered the intrinsic attenuation with the attenuation coefficient given by the regression to obtain the AOR of the river bottom sediments.

Time and amplitude reflection picking: with this operation, we picked the times and AOR with the UTM coordinates of each point in order to produce both the final bathymetric and the AOR maps.
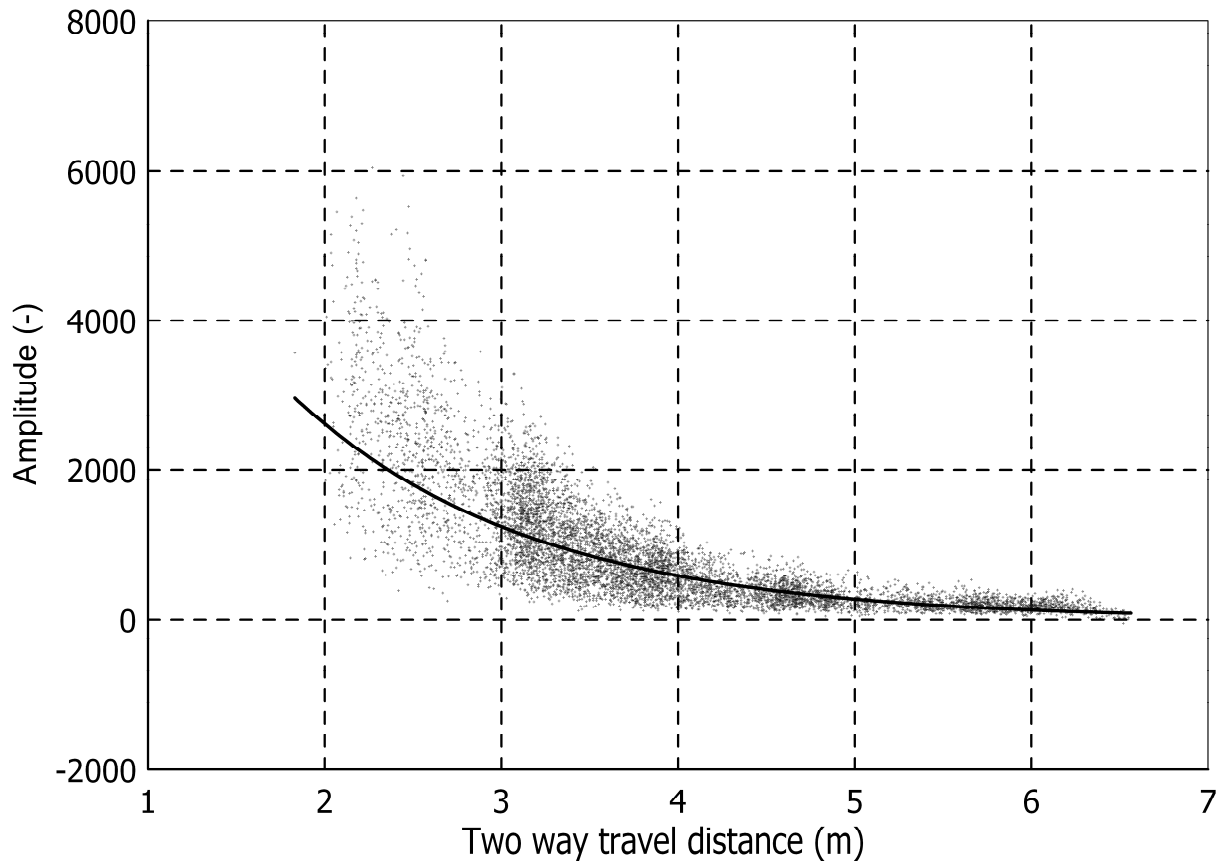
Figure 4.3: *The continuous line represents the least square exponential regression (Equation 2 in the text) on the 8059 amplitudes of reflection (black dots) picked after the divergence compensation, versus the distance travelled by the radar pulse.*

4.5. Results

GPR Sections

The application of the processing flow to the raw data returns improved radargrams. Figure 4.4 shows the comparison between the radargram of profile 4 (the third from the west bank) before and after the processing; both images are plotted with the same amplitude scale. All the processed radargrams show sharp contrasts in the bottom reflections. This high reflectivity prevents an unambiguous identification of the reflections within the sediments.
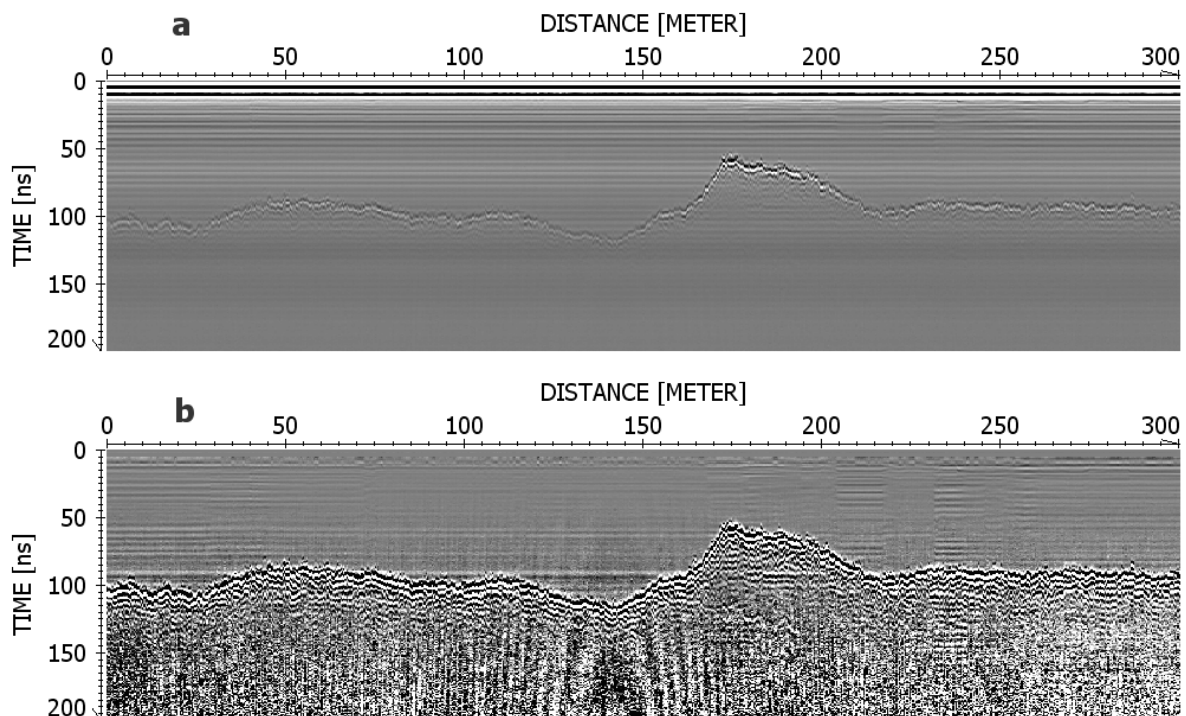
Figure 4.4: *Comparison between the raw (a) and the processed (b) radargrams of profile 4, the third from the west bank. The images are plotted with the same amplitude scale.*

Bathymetric Map

We converted the bottom reflection times into the water depths by using the velocity of the radar waves in the water. We then gridded the results in order to obtain the bathymetric map shown in Figure 4.5. The water depth in the surveyed area increases from the east bank going toward the west bank and almost all the depths are included in the 1-3 m interval. The trend of the bathymetry is in agreement with the fluvial geomorphology. The river, flowing from North-NorthEast to South-

SouthWest, has a slight curvature and the flow has a higher velocity near the west bank.
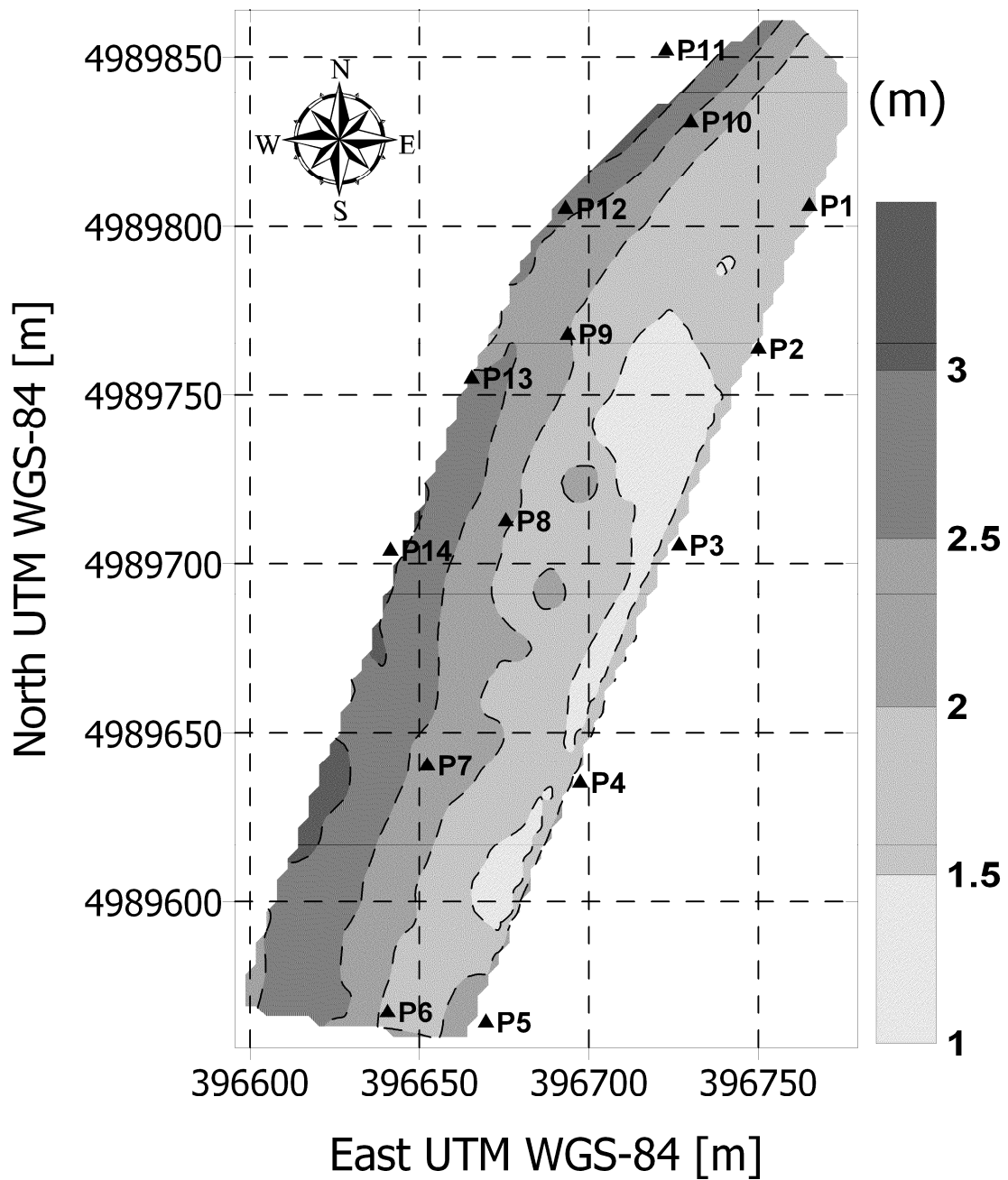
Figure 4.5: *Bathymetric map of the surveyed stretch of the Po river estimated with the GPR Two-way time assuming a radar wave velocity in the water of 0.033 m/ns.*

Reflectivity Map

In order to map the bottom AOR, we converted all the picked amplitude values (AOR) in decibels (AOR $_{[dB]}$) according to:

$$AOR_{[db]} = 20 \cdot \log\left(\frac{AOR}{AOR_{max}}\right)$$

(4.3)

where AOR_{max} is the maximum bottom AOR measured in the surveyed area.

Figure 4.6 shows the bottom AOR map expressed in dB. This map shows only a relative homogeneity of the bottom sediments and is uncorrelated to the bathymetry map shown in Figure 4.5.
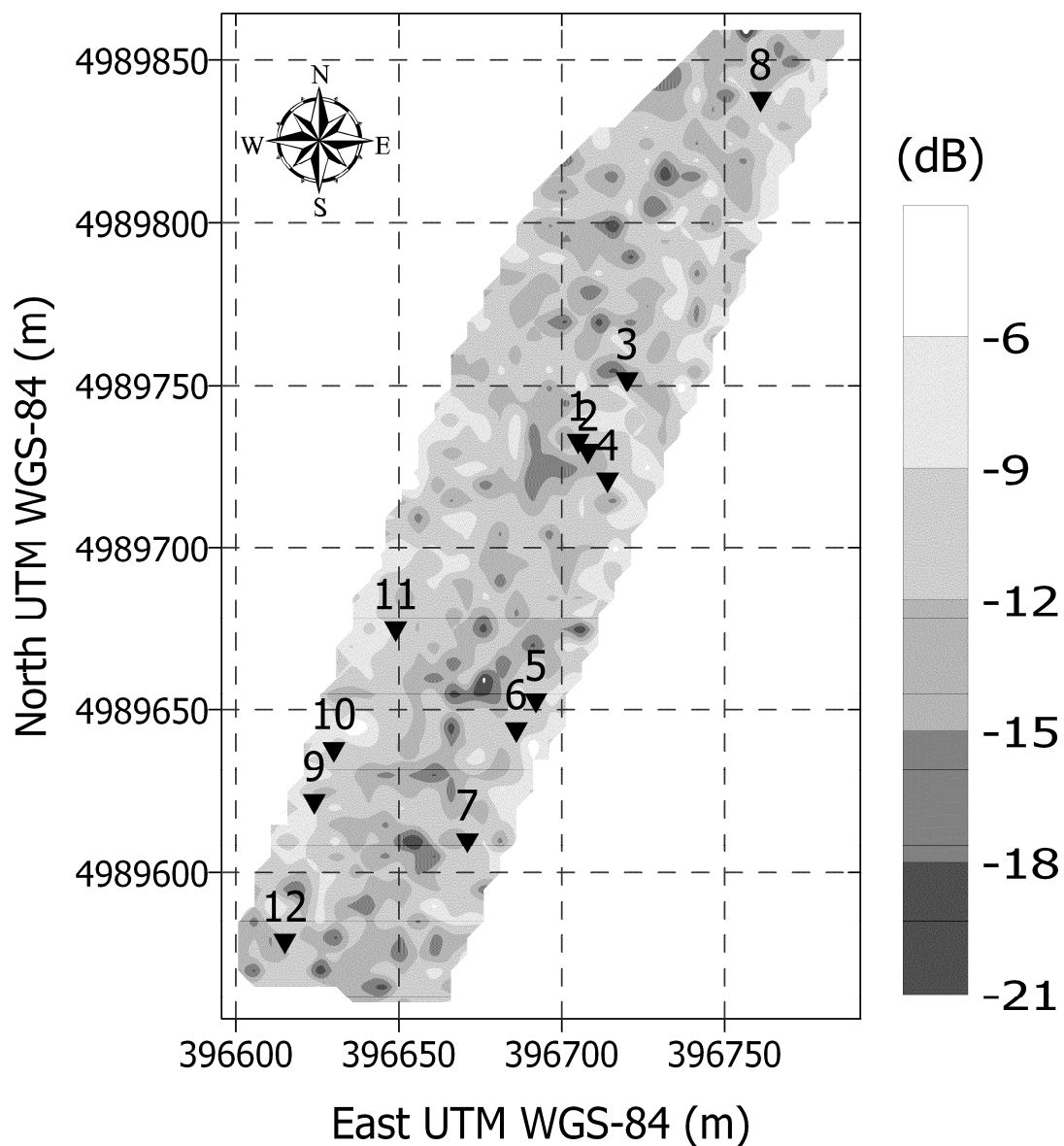
Figure 4.6: *Contour map of the bottom amplitudes of reflection expressed in dB. The twelve black triangles identify the direct sampling points.*

In order to help the interpretation of the bottom AOR map, we graphed all the 8958 amplitude values in the histogram in Figure 4.7. This histogram shows that more than 75% of the area is characterized by values included in the -6dB÷-15dB interval, and we can thus suppose that most of the points have a high AOR. Such a result is in agreement with the radargrams, where the penetration of the signal in the sediments is very poor. Moreover, the sampling surveys revealed the relevant presence of coarse clasts in a sandy matrix, and these sediments have a higher reflectivity than homogeneous fine sediments (Powers et al., 1999; Shields et al., 2004). Finally, the GPR interpretation is in agreement with the electromagnetic survey response described in chapter 5, where resistivity values that are compatible with saturated gravel and coarse clasts were reported. The agreement is more in the widespread high reflectivity in the map, than in a correspondence between high reflectivity and high resistivity areas.
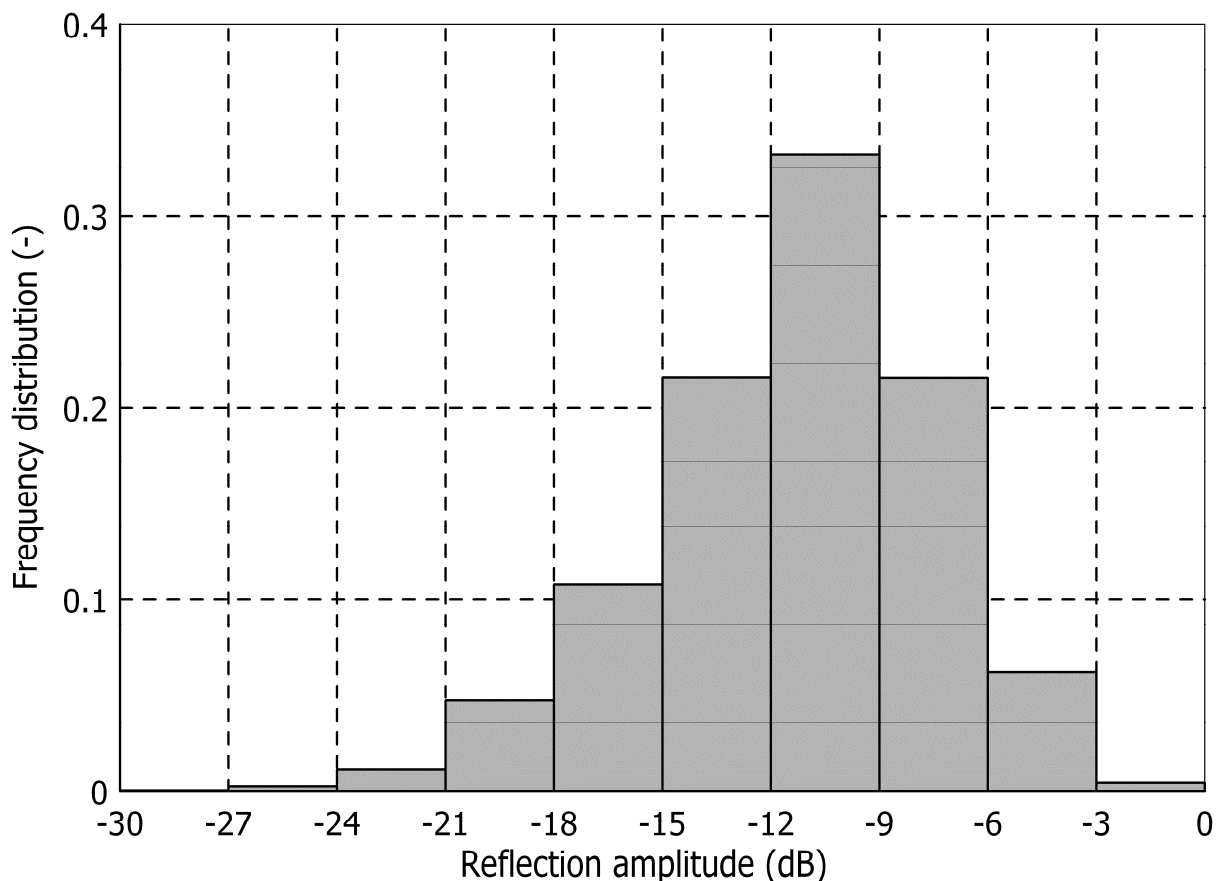
Figure 4.7: *Frequency distribution of the bottom amplitudes of reflection after the application of the processing flow. The histogram was computed from 8958 samples.*

The non homogeneity of the map, with respect to the homogeneity of the direct sampling results, could instead be explained by two main hypothesis: a heterogeneity

of the sediments not detected by the dredging; a non correspondence of the reflector type to the hypothesis we had previously made, particularly with references to the Rayleigh scattering assumption.

The first hypothesis could be confirmed by the observations reported in chapter 5 about the sampling method adopted, and where a non complete uniformity of the bottom sediment conductivity was highlighted.

The second hypothesis could be suggested by the analysis of the ratio between the dominant pulse wavelength and the average pebble diameter. When dealing with scattering problems, it is usual to define a size factor x as:

$$x = \frac{2 \cdot \pi \cdot r}{\lambda}$$

(4.4)

where r is the particle radius and λ is the wavelength. The Rayleigh scattering condition requires x<<1. This condition allows us to consider the heterogeneous material as being homogeneous and, when hit by a plane wave (providing a plane interface), it reflects a plane wave. We have plotted the histograms of the dominant wavelengths of the windowed reflected pulses after the processing in Figure 4.8.
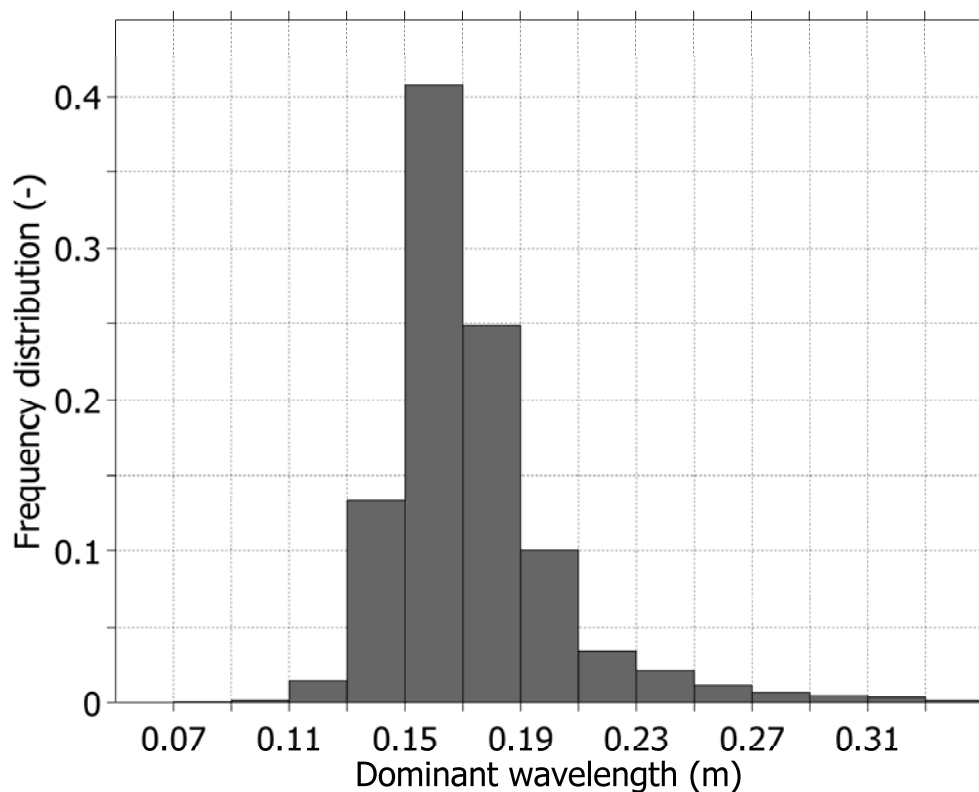
Figure 4.8: *Frequency distribution of the dominant wavelengths estimated from the power spectra of the signal reflected by the river bottom. The histogram was computed from 7678 samples.*

The histogram clearly suggests that the processing flow does not affect the frequency content of the reflected signal, and the dominant wavelength in the water is around 16 cm. This wavelength is about twice the average diameter of many of the sampled pebbles. Based on such a wavelength/particle size ratio, the hypothesis of reflected plane wave cannot therefore be possible, at least at a local scale. In fact, when $x \approx 1$, the Mie solution of Maxwell's equations better describes the scattering. In Mie conditions, the radar cross section of the illuminated object is dependent on its dimension and on the signal wavelength to a great extent. Consequently, the reflected amplitudes toward the receiver are more like a random sum of backscattered diffuse signals rather than a plane wave (Kingsley and Quegan, 1992). Moreover, the Mie condition would prevent the use of a mixing rule approach to give a relation between the reflection coefficient and the permittivity of the sediments, the mixing rules only being valid in the Rayleigh condition (Sihvola and Alanen, 1991).

4.6.   Conclusions

In this work we present results related to GPR data derived from an integrated geophysical survey, where, contemporarily to the GPR measurements, we acquired low induction number electromagnetic multifrequency measurements (GEM-2). We also made some punctual measurements of the water permittivity, conductivity and temperature and carried out a direct sampling survey. Our goal was to distinguish the river bed sediments through a quantitative analysis of the river bottom reflection amplitudes and conductivities.

As far as the quantitative analysis of the bottom reflections is concerned, we first checked the constancy of the signal that entered the water, by checking the main bang repeatability. We then designed the data processing so that it did not significantly affect the frequency content of the signals and preserved the amplitude ratios among the different traces and profiles.

The processing and the interpretation of the GEM-2 and GPR data were enhanced by the reciprocal results and by the integration with the punctual measurements of the electromagnetic properties of the water. The punctual permittivity and conductivity measurements allowed an estimation of the GPR pulse velocity which we then used to obtain a bathymetry map. We used the bathymetry data obtained from the GPR for the transformation of the apparent conductivity data into sediment conductivity. We also calculated the attenuation factor, using the Maxwell formulae applied to the punctual measurements. We used this value, which optimally matched the one estimated in our analysis of the GPR amplitudes, to correct the signal amplitudes and to obtain the AOR map.

However, we did not find an optimal agreement between the GPR interpretation and the direct sampling. While the direct sampling suggests an overall homogeneity of the river bottom, the AOR map shows areas with different values. The difference could be due to scattering phenomena from pluricentimetric clasts and to the method adopted for the direct sampling. As far as the direct sampling is concerned, the Van Veen grab bucket did not provide detailed information on the sediments and a different sampling method should be recommended for geological settings similar to this stretch of the Po river. We did not find a one-to-one relationship between the AOR and the conductivity maps either. Agreement between the two maps and the

direct sampling could only be found in a broad sense. The conductivity values of the river bottom sediments are compatible with coarse saturated materials; the same holds for the high reflectivity of the river bottom. Both these interpretations agree with the coarse clasts obtained from the direct sampling.

With respect to the field settings, the acquisition with the antenna placed on the flat bottom of a fiberglass boat was a good compromise between the quality of the signal and an easy logistic configuration. However, in our opinion, the best solution is an on purpose designed antenna with the dipole submerged in water in order to avoid power losses in the air and to limit the coupling effect between air and water. According to us, the optimum arrangement for a non-seismic river survey could be a multi-sensored boat RTK-tracked with: a GPR, a low frequency conductivity meter, ERT equipment with floating electrodes, and a device for the continuous acquisition of the water permittivity, conductivity and temperature.

5. Study of Riverine Deposits Using EM Methods at a Low Induction Number

5.1. Abstract

We carried out some electromagnetic (EM) profiles along the river Po in the city of Turin (Italy). The aim of this activity was to verify the applicability of low induction number EM multifrequency soundings carried out from a boat in riverine surveys with the intent of determining whether this technique, which is cheaper than air–carried surveys, could be effectively used to define the typology of sediments and to obtain an estimate of the stratigraphy below a riverbed.

We used a GEM-2 (handheld broadband EM sensor) operating with six frequencies to survey the investigated area. A GPR, a conductivity meter and a TDR were used to estimate the bathymetry and to measure the electromagnetic properties of the water. A GPS system, working in RTK mode, was employed to track the route of the boat with centimetric accuracy.

We analyzed the induction number, the depth of investigation (DOI) and the sensitivity of our experimental setup by forward modeling varying the water depth, the frequency and the bottom sediment resistivity. The simulations led to an optimization of the choice of the frequencies that could be reliably used for the interpretation. The 3406 Hz signal had a DOI in the PO water (27 Ωm) of 2.5m and provided sediment resistivities higher than 100 Ωm.

We applied a bathymetric correction to the conductivity data using the water depths obtained from the GPR data. We plotted a map of the river bottom resistivity and compared this map to the results of a direct sediment sampling campaign. The resistivity values (from 120 to 240Ωm) were compatible with the saturated gravel with pebbles in a sandy matrix that resulted from the direct sampling, and with the known geology.

5.2. *Introduction*

Inland waters can be of great interest from several points of view: civil (i.e., water supplies, waterways, resort activities, material dredging, bridge scours, river bar monitoring, harbor and river engineering), environmental (i.e., interactions with shallow aquifers, recharge areas, erosion, submerged unexploded ordnances (UXO) in bombed industrial cities) or disaster planning (i.e., flood prevention and mitigation). Some usual shallow water geophysics techniques and some other techniques borrowed from near-surface geophysics can help to resolve some of the problems such as, for example, bathymetry mapping, riverbed characterization and UXO detection.

Some experiences referring to boat-carried surveys on inland waters can be found in the literature. Ground penetrating radar (GPR) and seismic methods have been utilized to perform riverine surveys. Beres and Haeni (1991) used GPR to study selected stratified-drift deposits in Connecticut. Dudley and Giffen (1999) ran a GPR survey along 50 miles of the Penobscot River, Maine, in the spring of 1999, to produce maps describing the composition and distribution of streambed sediments. Webb et al. (2000) used a GPR to estimate water depths and identify infilled fluvial scour features, acquired at ten different bridge sites in southeastern and central Missouri. Toth (2004) used a new designed GPR combined with seismic methods to survey the river Danube in the centre of Budapest (Hungary).

The aim of our research was to verify the applicability of an EM dipole-dipole methods with a handheld multi-frequency broadband sensor GEM-2 (Won et al., 1996) to define the typology of the streambed sediments. Up to now, frequency domain electromagnetic systems (FDEM) have been rarely utilized in riverine soundings, also because of electromagnetic interference between the transmitted signal and the boat engine. Butler et al. (2004) carried out a survey concerning these applications to delineate the recharge area to a river valley aquifer on the Saint Joint River (City of Fredericton, New Brunswick) using a combination of three geophysical surveys: resistivity imaging along the shoreline, seismic and EM methods carried above the water subsurface. The results of the research were successful and the geophysical interpretations were confirmed by drilling.

Mainly according to the latter reference, we acquired GEM-2 multifrequency data on the Po river in Turin (Figure 5.1).
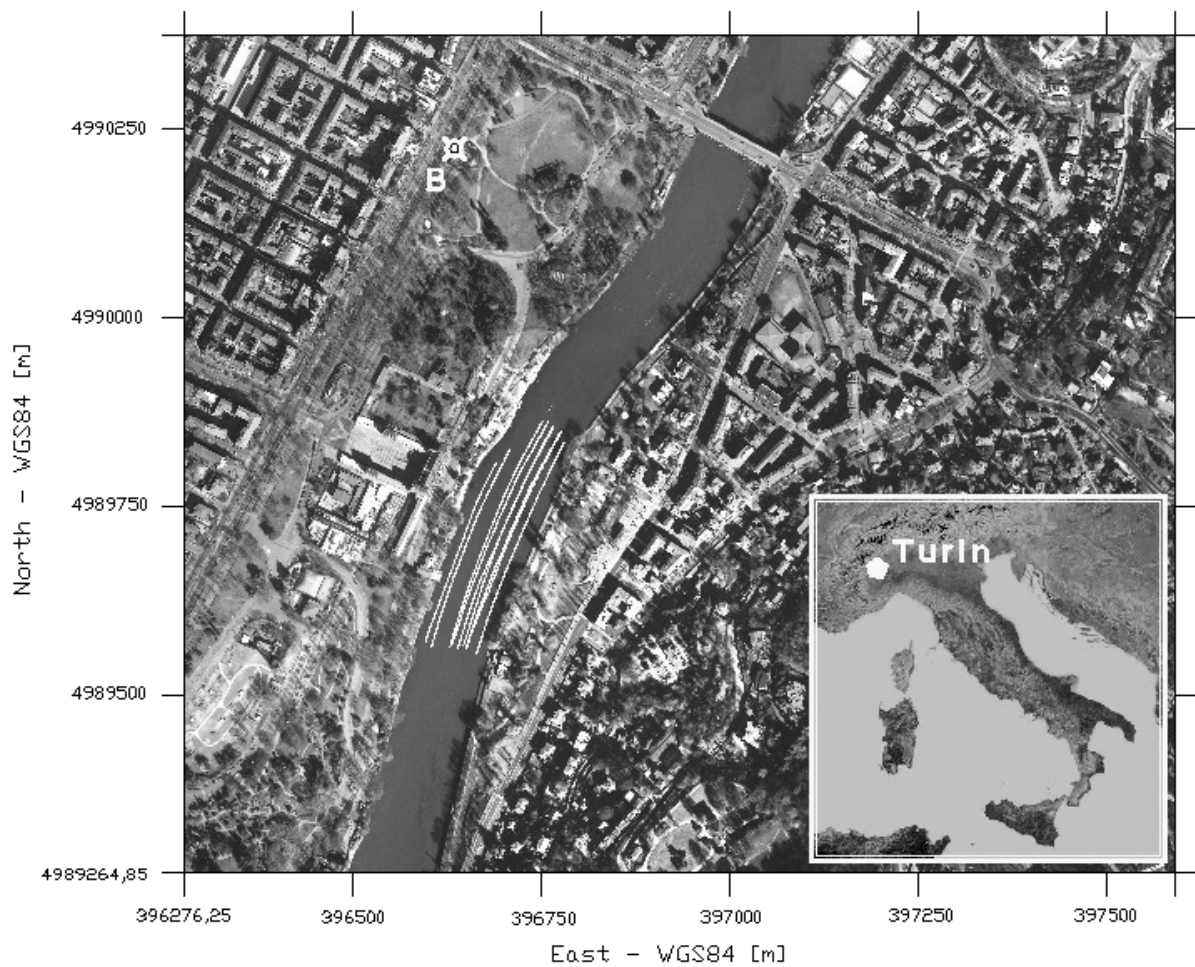
Figure 5.1: *Localization of the investigated area with the survey tracks: the white lines indicate the continuous measurements (GEM-2 and GPR); the white cross in the NW corner of the map indicates the borehole (B) location.*

5.3. Methods

The measurements were conducted along a stretch of the Po River in the city of Turin, near the Valentino park, using the following instruments aboard a motorboat (Figure 5.2):

a Geophex GEM-2, handheld broadband conductivity meter;

a I.D.S. RIS/0 k2, georadar with a TR200 antenna (central frequency 200 MHz);

a Tektronix 1502c, TDR (Time Domain Reflectometer) to measure water permittivity;

a ProfiLine-197, conductivity meter to measure water conductivity and temperature;

two LEICA System 1200 (GPS L1+L2 receivers).

In a first survey, two GPS receivers were placed aboard a boat; one of their antennas was positioned at the stern and the other at the prow of the boat, and both were fixed to the top of a 50 cm wooden pole to assure greater visibility of the antennas and reduce multiple paths. The two receivers were necessary to determine the bearing of the boat and provide a second-by-second geographical reference of the geophysical instruments in an absolute reference system, and to calculate the rotation and translation parameters starting from the knowledge of the antenna positions in both local and global reference systems.
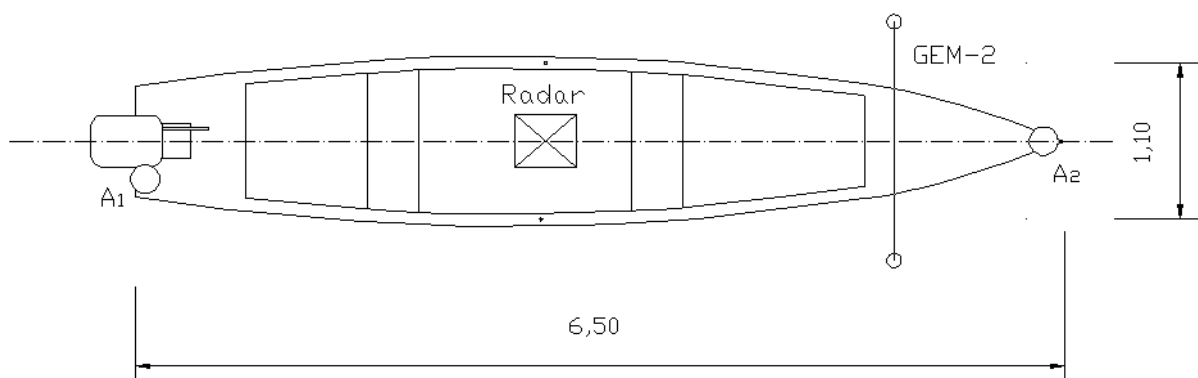
Figure 5.2: *Layout of the motorboat used for the survey: A_1 and A_2 are the DGPS antennas; the dimensions are in meters.*

After placing the GPR and the GEM-2 aboard the boat, all the distances between the GPS antennas and the vertices of the geophysical sensors were measured, in order to create a topographic network to position the barycenters of the sensors within a local reference system that was integral with the boat. During the data processing, the barycentres of the sensors were mapped onto the UTM-WGS84 absolute reference system applying Helmert transformations with seven parameters, that differ

for each surveying instant, in order to move all the GPR and GEM-2 measurements, referred to the barycenters of the sensors, from the local to the absolute reference system.

The GPS RTK technique was adopted to define the trajectory and the bearing of the boat in real time and with an accuracy of a few centimeters. Moreover, it was possible to verify the carrier phases initialization directly on field in real time. The stored raw data were also post-processed: in this way, the quality of the positioning was tested and some gaps in the RTK data, due to physical signal obstructions, were filled. The presence of a GPS network is necessary to obtain good results, in terms of accuracy in wide area surveys. This condition also permits the same coherent reference system to be maintained along trajectories of hundreds of kilometers. For the case study, where only a short river stretch was surveyed, the Politecnico di Torino permanent GPS station, which is located almost 2 km away from the surveying area, was used as the RTK master station. A 1 Hz logging rate for the receivers was set up to synchronize the geophysical instruments with the GPS ones. Since the geophysical instrument positioning does not need an accuracy of a few centimeters, it would also be possible to use low-cost single frequency receivers.

We used the GPR for bathymetric estimation in order to test its suitability for deposit characterization in shallow inland waters. We decided to place the GPR antennas aboard the boat instead of on the river bottom because the antenna cable could get caught up in tree-trunks, branches or even in Second World War UXO. The GPR collected, on average, one trace every 3 cm.

The main problem during the GEM-2 data acquisition was the electromagnetic noise produced by the boat engine; to reduce this interference, we positioned the GEM-2 as far as possible from the engine and we used frequencies higher than 500 Hz (according to the Geophex indications). As we wanted to test the possibility of using a multifrequency broadband sensor to estimate the resistivity of the river bed deposits, during acquisition, we spanned almost the entire GEM-2 frequency range above 500 Hz. The GEM-2 sensor was 0.7 m above the water level and it was set to work using six different frequencies: f_1=775 Hz, f_2=1175 Hz, f_3=3925 Hz, f_4=9825 Hz, f_5=21725 Hz, f_6=47025 Hz. Thus, we obtained six values of apparent resistivity, on average every 0.8 m, theoretically corresponding to six different depths of investigation.

The survey tracks, about 300 m long, are shown in Figure 5.1. The survey started from the north, near the east riverbank and proceeded southward parallel to the shoreline; a new survey was then carried out along a line parallel to the previous one, but sailing in the opposite direction. On the whole, we acquired 11 tracks (10 parallel to the shoreline and the last zigzagging to transect the river). No information was taken in the areas near the shoreline where the trees prevented the reception of the GPS signal.

Table 5.1: *Borehole B stratigraphy (see Figure 5.1 for the borehole location)*

Depth [m]	Geology
0 ÷ 1,00	Top soil
1,00 ÷ 4,00	Sand, gravel and pebbles
4,00 ÷ 6,00	Coarse sand
6,00 ÷ 11,00	Gravel and large pebbles
11,00 ÷ 13,00	Hard 30- 40 cm thick conglomerates, alternated with loose gravel
13,00 ÷ 13,50	Coarse gravel
13,50 ÷ 15,00	Gravel and large pebbles
15,00 ÷ 16,00	Gravel
16,00 ÷ 17,00	Sand and gravel
17,00 ÷ 23,00	Coarse sand and gravel, water table at 17 m (Po water level)
23,00 ÷ 25,00	Gravel and semi -cohesive sand
25,00 ÷ 26,50	Gravel and loose sand
26,50 ÷ 28,00	Gravel
28,00 ÷ 33,50	Gravel and pebbles (lower part of the Holocene alluvium) transgressive over the Miocene
33,50 ÷ 63,00	Grey compact clayey marl
63,00 ÷ 67,00	Hard marl with scarce pebbles

After the GPR and GEM-2 acquisition, we used the conductivity meter and the TDR, keeping the boat still in 14 different points (Figure 5.3) to conduct punctual measurements of the conductivity, temperature and dielectric constant of the water at different depths. In this second survey, the LEIKA GPS allowed us to locate the punctual measurements in points close to the tracks followed in the first survey.

In April 2006, almost five months after the geophysical surveys, the riverbed was sampled utilizing a Van Veen grab bucket. No flood event had occurred in the time that had elapsed from the geophysical survey till the day of the direct sampling

survey. Twelve sampling points (Figure 5.3) were chosen according to the previous geophysical measurements and with the aim of recovering direct information also where the geophysical survey had failed. We were able to position the sampling points with a Garmin GPSMAP 60CS, a GPS system that provided an accuracy of the point locations of about 5 m.

We took 2 or 4 sediment samples for each selected point to obtain an average estimate and to overcome the difficulty of sampling riverbed deposits that were mainly made up of coarse material. However, because of the nature of the deposits, it was impossible to ensure enough material for a complete particle-size analysis.

We also obtained some geological data from a borehole (Figure 5.1 cross B) drilled about 300 m away on the west bank. This borehole reported "coarse gravel, pebbles, gravel and sand" (Table 5.1), from 4 m above the level of the river surface to 17 m below it.
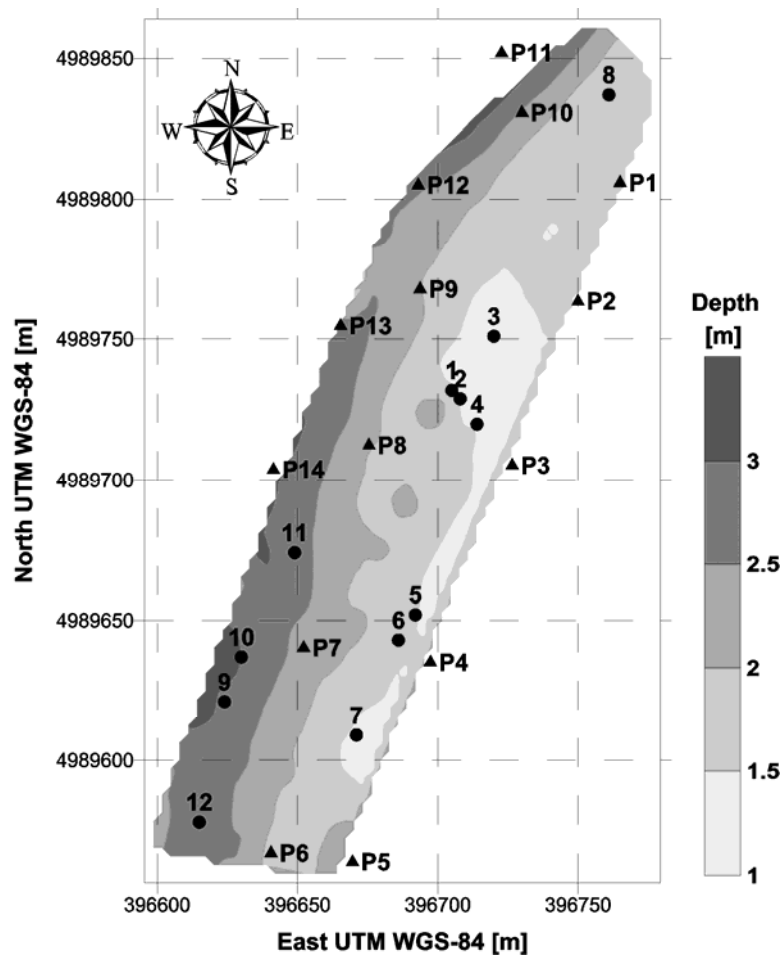
Figure 5.3: *Bathymetric map derived from GPR data: the triangles (P1-P14) refer to the water conductivity and permittivity sampling points; the circles (1-12) refer to river bottom sampling points.*

5.4. Data Processing

The water conductivity meter and the TDR measurements gave nearly constant water resistivity, temperature and permittivity values. The water resistivity was around 27 Ωm, corresponding to a mean conductivity value of 37 mS/m; the temperature was around 13 °C and the relative permittivity was about 84. Table 5.2 reports the values measured at the first and last measurement points, the mean value and the standard deviation on the whole set of points.

Table 5.2: *Conductivity, temperature and permittivity measurements: first point (P1), last point (P14), mean and standard deviation values of 14 points.*

	P1			P14		
Depth (m)	**σ (mS/m)**	**T (°C)**	**ε_r [-]**	**σ (mS/m)**	**T (°C)**	**ε_r [-]**
0	39.1	13.7	89	36.7	13.3	81
0.5	38.5	13.3	90	36.7	13.3	81
1	38.3	13.2	90	36.7	13.3	83
1.5	38.2	13.2	88	36.7	13.3	81
2	-	-	-	36.7	13.3	-
	Mean values (14 pts.)			**Standard deviations (14 pts.)**		
Depth (m)	**σ (mS/m)**	**T (°C)**	**ε_r [-]**	**σ (mS/m)**	**T (°C)**	**ε_r [-]**
0	36.8	13.3	85	0.62	0.12	3
0.5	36.8	13.3	84	0.47	0.06	3
1	36.7	13.3	85	0.43	0.06	3
1.5	36.8	13.3	83	0.41	0.06	3
2	-	13.3	-	-	0.07	-

We processed the GPR raw data utilizing the "Reflex-Win" software. This allowed us to estimate the water depth at each measurement point by picking the time of the bottom reflections at each trace and using the conductivity and permittivity data to calculate the radar pulse velocity. The GPR reflected signals were in a band centered at 200 MHz, corresponding to a wavelength of about 16 cm and gave a depth resolution of about 5 cm. The bathymetric map in Figure 5.3 shows that the depth of the riverbed increases from the east going toward the west riverbank.

We downloaded the raw data logged by the GEM-2 using the "WinGEM" software, obtaining an apparent conductivity profile (mS/m) for each frequency along each

survey track. The raw data power spectra, on average, showed a decrease in energy content below $\lambda \cong 15$ m. The profiles were then low-pass zero-phase filtered (Band-pass filter gain: ≥ -1dB @$\lambda \geq 15$m; Reject-band filter gain: -100dB@$\lambda \leq 6.5$m) in order to remove the highest spatial frequencies (Figure 5.4). This processing was necessary because of the high environmental noise which increased with the lowering of the frequency (Figure 5.5).

Power Spectrum
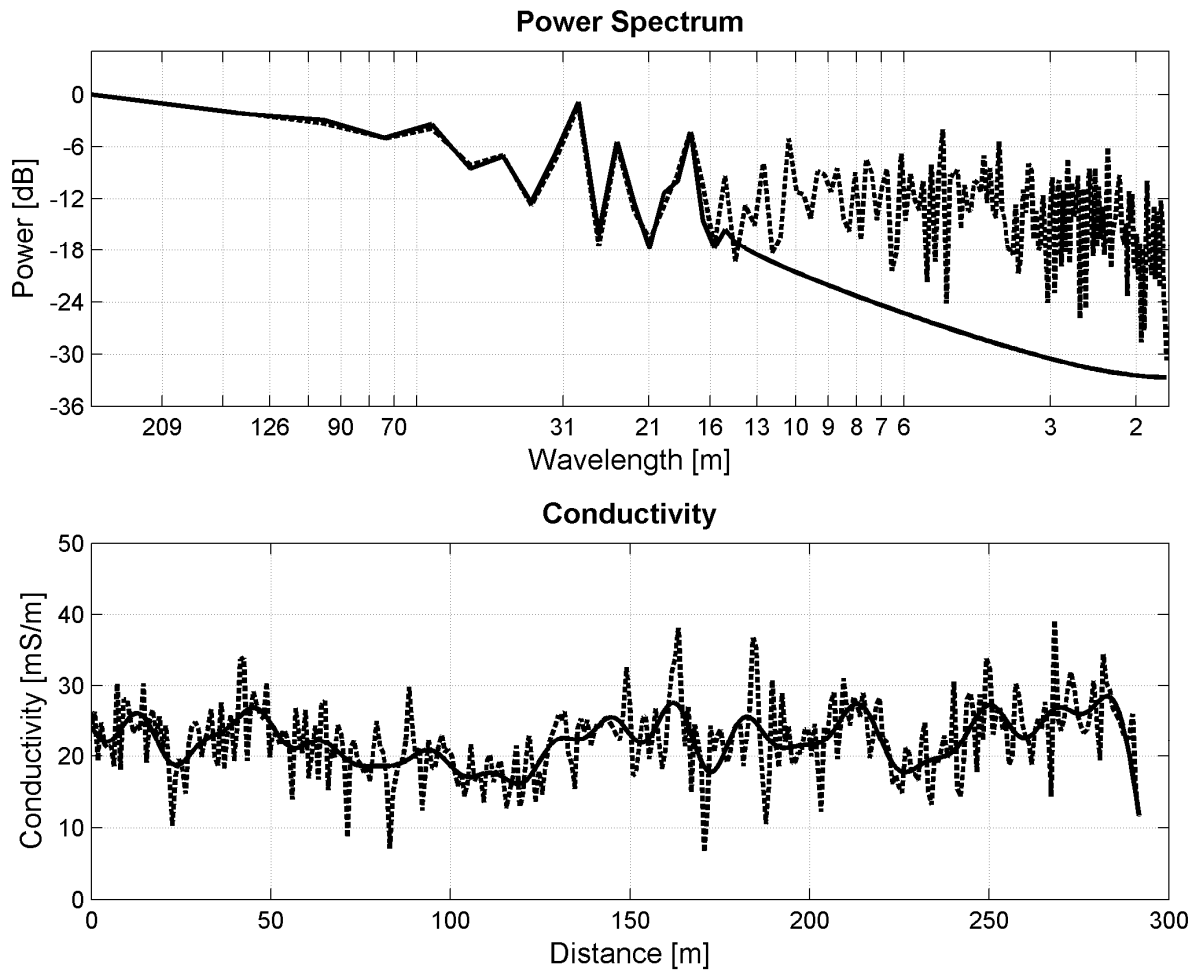
Conductivity

Figure 5.4: *Power spectrum (above) and conductivity profile (below). Comparison between raw (dashed line) and filtered (continuous line) data for track 3 at 3925 Hz (the third track from the West bank).*

The DOI of a handheld conductivity meter depends on many factors: sensor sensitivity, precision, operating frequencies, ambient noise level, target and host properties and intercoil distance. According to Huang (2005), we carried out an analysis to assess: a) the conditions of low induction number, in order to check which frequencies gave a quadrature response that could be converted into conductivity data; b) the capability of the selected frequencies to reliably detect the river bottom

sediment, that is, the DOI; c) the capability to reliably discriminate among sediments having different resistivity, that is, the sensitivity.
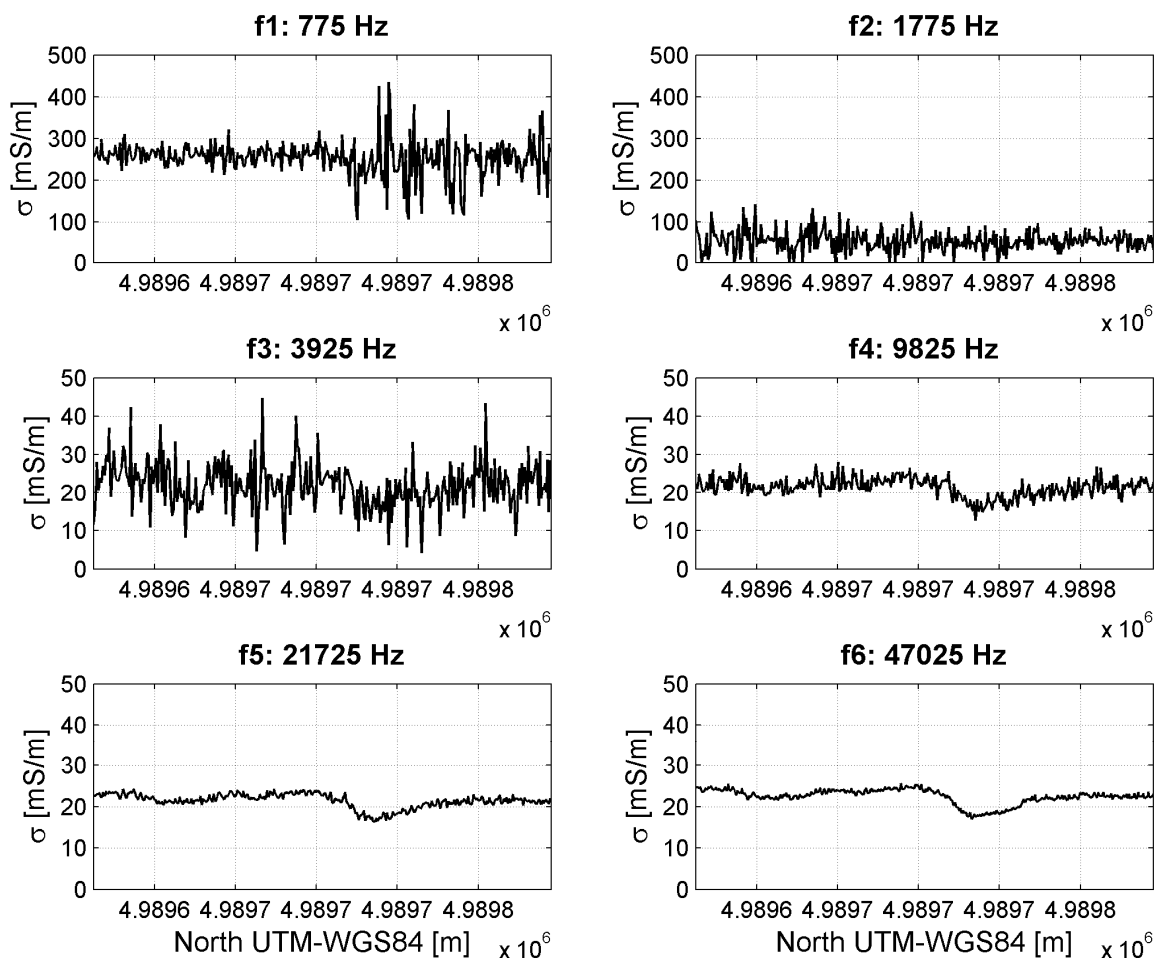
Figure 5.5: *Raw conductivity profiles relative to all frequencies along track 3.*

For this purpose, we conducted a set of simulations that spanned a 500 Hz to 50 kHz frequency range with 6 frequencies per decade, a water resistivity of 27 Ωm, a 1 to 3 m water depth range and a 13.5 to 532 Ωm sediment resistivity range. These latter two ranges were selected on the basis of the bathymetric and the geological data. We carried out this analysis using the Anderson modeling software (1979). We obtained 25 synthetic apparent conductivities (corresponding to five depths in the 1 to 3 m range, as well as 5 resistivity values in the 13.5 to 532 Ωm range) using this simulation at each of the following frequencies: 733.9 Hz, 1077.22 Hz, 3406 Hz, 10772.2 Hz, 23208 Hz and 50000 Hz. We used these results to make comparison with experimental data respectively at 775 Hz, 1175 Hz, 3925Hz, 9825 Hz, 21725 Hz and 47025 Hz.

The apparent conductivity can only be calculated from the quadrature response of the conductivity meter when it operates at an induction number much lower than 1 (McNeill, 1980). Moreover, Huang and Won (2003) demonstrated that the induction number has to be larger then 0.02, otherwise the EM response is small and has a small dependence on the frequency. Therefore, it is possible to only consider reliable those electromagnetic responses that are obtained when the induction number is included in the following range:

$$0.02 < B = \frac{s}{\delta} = \sqrt{\frac{i\omega\sigma\mu_0}{2}}s \ll 1 \qquad (5.1)$$
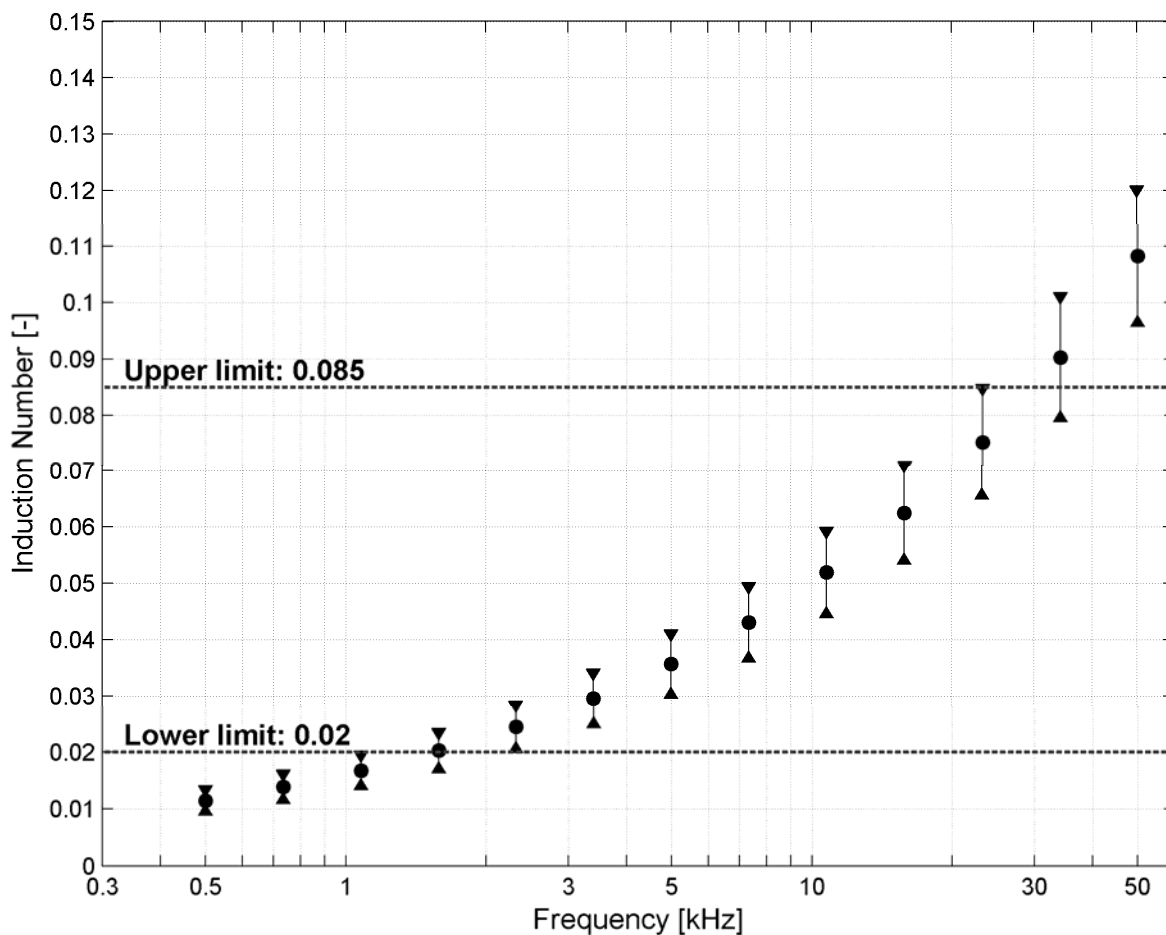
Figure 5.6: *Mean and standard deviation plot graph of the induction numbers estimated from the modeling in the 500-50000 Hz frequency range. Modeling was made assuming: water resistivity 27 Ωm; sediment resistivity from 13.5 to 532 Ωm; water depth from 1 to 3m; inter-coil distance 1.66 m; sensor height above the water 0.7 m.*

Given the GEM-2 inter-coil spacing ($s = 1.66$ m) and the magnetic permeability of free space ($\mu_0 = 4\pi \times 10^{-7}$ H/m), we calculated the mean and standard deviation of the induction numbers relative to the conductivities obtained from the simulation. The

results are shown in the plot of Figure 5.6. We can observe that only the frequencies in the 3 to 22 kHz range produce reliable induction numbers in the 0.02 to 0.085 range (justification of this upper limit is given in the next section). We were then only able to obtain reliable conductivity values from the 3406 Hz, 10772 Hz and 23208 Hz signals.

We then estimated the DOI relative to these three frequencies, with the results of the simulations, for different water depths and sediment resistivities, according to the criterion given by Huang (2005). The results of each frequency are plotted in the graphs of Figure 5.7. Each of these three graphs plots the ratio of the apparent conductivity of a water layer over sediments (σ_a) to the apparent conductivity of an indefinite water layer (σ_{aw}) versus the ratio of the sediment resistivity (ρ_s) to the water resistivity (ρ_w). The two horizontal lines represent the 20% thresholds and the curved lines represent (σ_a/σ_{aw}) at five different water depths. According to the results of these simulations, if we accept a threshold value of 20% - that is, we can detect a sediment if the measured apparent conductivity differs by more than 20% from the apparent conductivity one would have measured above water alone ($\sigma_a/\sigma_{aw}=1$) - the following considerations can be drawn concerning the sensitivity and the DOI.

All the graphs show that there is quite a low sensitivity to the resistivity of the sediments, particularly if the sediments are more resistive than the water (the curves have a very weak slope when $\rho_s>\rho_w$) and that the sensitivity grows as the frequency and the riverbed depth decreases.

We were only able to obtain a very rough capability to discriminate between coarse (>100 Ωm) and finer (<100 Ωm) sediments from the 3406 Hz signal down to a depth of 2.5 m; when the water depth was lower than 1.5 m we were also able to discriminate between sediments with different resistivities. We were only able to obtain a very rough capability to discriminate between coarse (>100 Ωm) and finer (<100 Ωm) sediments from the 10772 Hz signal down to a depth of 2 m; when the water depth was lower than 1 m we were also able to discriminate between sediments with different resistivities. We were only able to obtain a very rough capability to discriminate between coarse (>100 Ωm) and finer (<100 Ωm) sediments from the highest frequency (23208 Hz) down to a depth of 1 m, which was the minimum water depth we encountered in the survey. This means that the information carried by this latter signal is mainly relative to the bathymetry.
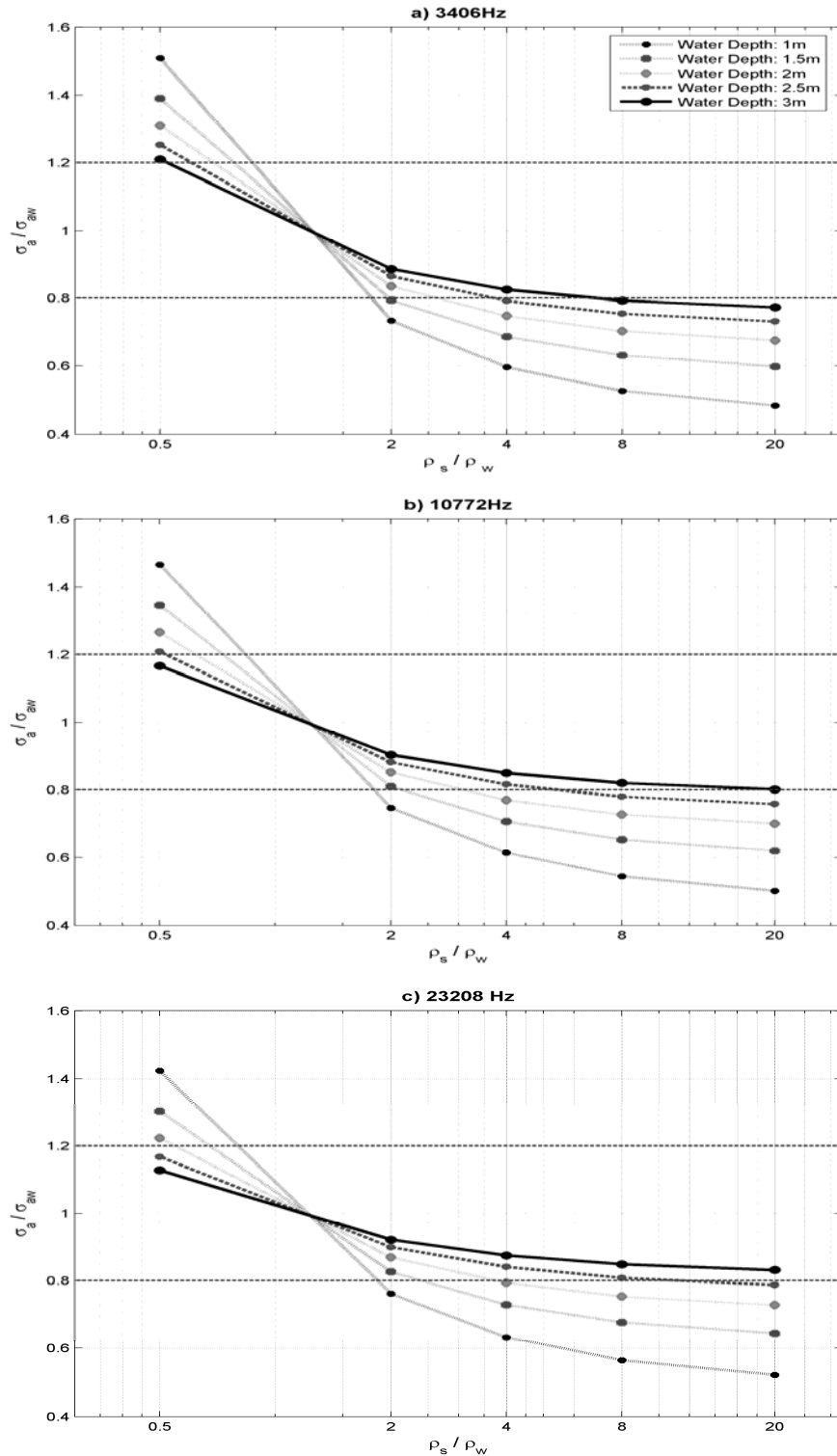
Figure 5.7: *Synthetic apparent conductivity curves (normalized to the apparent conductivity of a water half-space) as a function of sediment resistivity (normalized to water resistivity). The horizontal dashed lines at 0.8 and 1.2 are the DOI thresholds. The parts of the curves outside this interval indicate detectable sediment resistivities. The slope of the curves refers to the sensitivity. The analyzed frequencies were: a) 3406 Hz, b) 10772 Hz and c) 23208 Hz. Modeling was made assuming: water resistivity 27 Ωm; sediment resistivity from 13.5 to 532 Ωm; water depth from 1 to 3m; inter-coil distance 1.66 m; sensor height above the water 0.7 m.*

Finally, the results of the simulations showed that information on sediment resistivity could be drawn, from the 3406 Hz signals, only if both the water depth is lower than 2.5 m and the sediment resistivity is higher than 100 Ωm and, from the 10772 Hz signals, only if both the water depth is lower than 2.0 m and the sediment resistivity is higher than 100 Ωm. In order to analyze a larger area and more reliable data, we only focused attention on the 3925 Hz experimental data.

As suggested by Butler et al. (2004), we then made an approximate bathymetric correction on the whole investigated area. We hypothesized a two-layer model (water-sediment) to estimate the sediment resistivity. The apparent conductivity σ_a of a two-layer model is (McNeill, 1980):

$$\sigma_a = \sigma_1 \left[1 - R_v(Z) \right] + \sigma_2 R_v(Z) \tag{5.2}$$

where Z=z/s is the actual depth divided by the inter-coil spacing s and $R_v(Z)$:

$$R_v(Z) = \frac{1}{\sqrt{4Z^2 + 1}} \tag{5.3}$$

is the cumulative response of the mathematical function $S_v(Z)$:

$$S_v(Z) = \frac{4Z}{\sqrt{(4Z^2 + 1)^3}} \tag{5.4}$$

which describes, for vertical magnetic dipole setting, the relative contribution to the secondary magnetic field, measured at the surface, due to a thin horizontal layer at any given depth z.

Since both GPR and GEM2 measurements were referenced in the UTM-WGS84 absolute coordinate system, it was possible to pair each point where apparent conductivity was measured with the respective water depth z_w and to calculate $Z_w=z_w/s$. As reported above, we measured the true water conductivity with the conductivity meter and obtained an average value σ_w=37 mS/m. Then, we calculated the conductivity of the second layer, which corresponds to the conductivity of the bottom sediment (σ_{sed}) considered as a semi-infinite space at each point of the survey:

$$\sigma_{sed} = \frac{\sigma_a - \left[1 - R_v(Z_w) \right] \sigma_w}{R_v(Z_w)} \tag{5.5}$$

The effect of the water layer was removed through the application of the bathymetric correction.

5.4.1.   Justification of the Selected Upper Limit of the Low Induction Number Condition.

As far as the definition of the upper limit of the low induction number condition expressed in eq.1 is concerned, we worked as follows. We calculated, using the six frequencies (775, 1175, 3925, 9825, 21725 and 47025 Hz) used in the survey, over 21 half spaces with different conductivities (from 0.0037 to 0.104 S/m in steps of 0.005 S/m), the response and the induction number for two horizontal 1.66 m distant coils. We made the calculations of the response with both the simplified form $\left(\dfrac{H_s}{H_p}\right)_{V^S}$

and the "complete" form $\left(\dfrac{H_s}{H_p}\right)_{V^C}$ (McNeill, 1980).

The complete form is:

$$\left(\frac{H_s}{H_p}\right)_{V^C} = \frac{2}{(\gamma \cdot s)^2}\left\{9 - \left[9 + 9 \cdot \gamma \cdot s + 4 \cdot (\gamma \cdot s)^2 + (\gamma \cdot s)^3\right]e^{-(\gamma \cdot s)}\right\} \qquad (5.6)$$

where:

$\gamma = \sqrt{i \cdot \omega \cdot \mu_0 \cdot \sigma}$

$\omega = 2\pi \cdot f$

$f = $ frequency

$\mu_0 = $ free space permeability $\left[4\pi \times 10^{-7}\right]$

$\sigma = $ half space conductivity

$s = $ inter-coil distance

$i = \sqrt{-1}$

The simplified form is:

$$\left(\frac{H_s}{H_p}\right)_{V^S} = \frac{i \cdot \omega \cdot \mu_0 \cdot \sigma \cdot s^2}{4} \qquad (5.7)$$

The induction number is:

$$B = \frac{\sqrt{i \cdot \omega \cdot \mu_0 \cdot \sigma} \cdot s}{\sqrt{2}} \qquad (5.8)$$

We then defined a normalized per-cent difference npd between the imaginary parts of the simplified and the complete form as:

$$npd = \left\{ \left[\mathrm{Im}\left(\frac{H_s}{H_p} \right)_{V^S} - \mathrm{Im}\left(\frac{H_s}{H_p} \right)_{V^C} \right] \middle/ \mathrm{Im}\left(\frac{H_s}{H_p} \right)_{V^C} \right\} \times 100 \qquad (5.9)$$

we plotted the npd versus B and obtained the graph shown in Figure 5.8.

We chose an npd value equal to 10% and obtained an upper limit of B equal to 0.085.
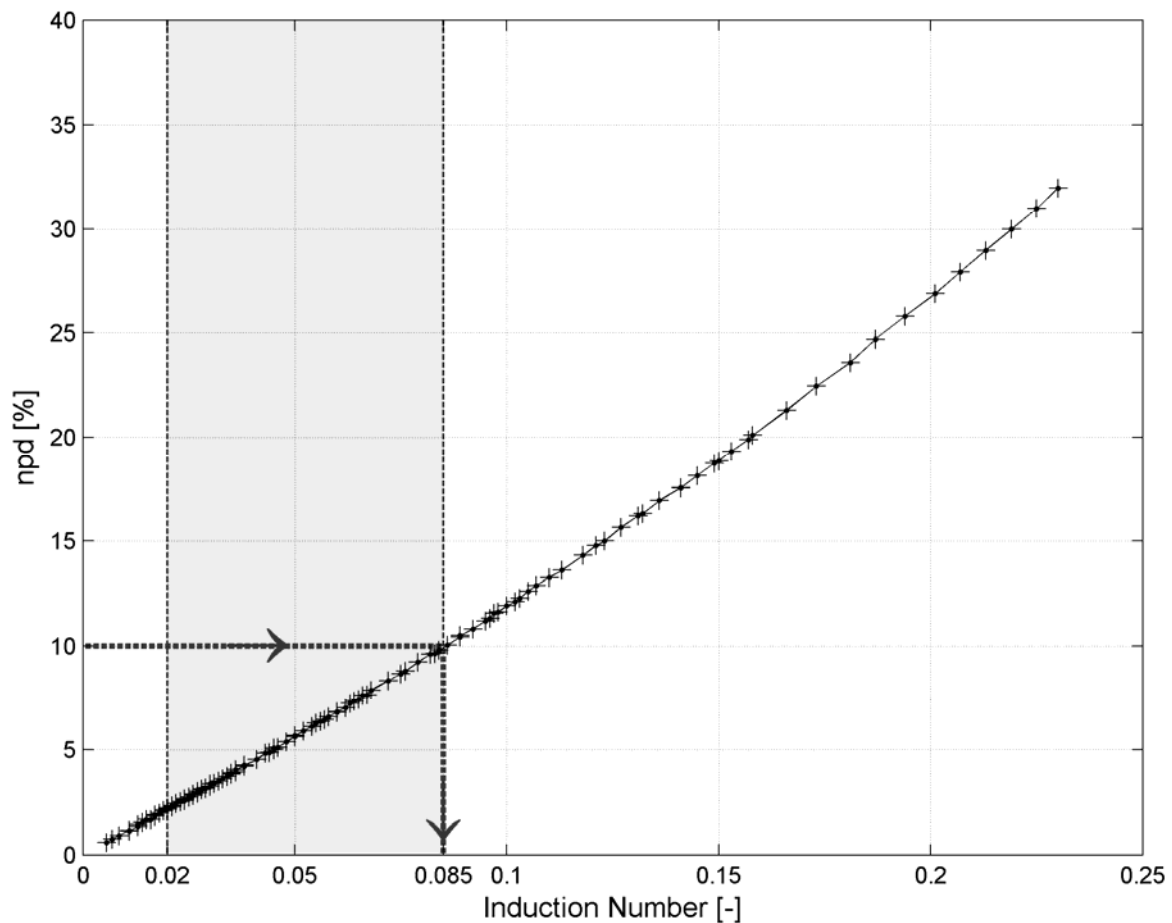
Figure 5.8: *Graph relating the normalized per-cent difference (npd) between the simplified form and the complete form of the quadrature component. The dashed band represents the B value range (0.02 < B < 0.085) that was considered. The upper B limit was obtained, as indicated by the black arrows, considering the largest acceptable npd equal to 10%.*

5.5. *Results*

We plotted a map (Figure 5.9) of the sediment resistivity at 3925 Hz, discarding the data deeper than 2.5 m and with resistivity lower than 100 Ωm. The most frequent resistivity value was 120 Ωm and 75% of the resistivity values were between 100 and 240 Ωm. These data suggest quite a large homogeneity of the deposits, which mainly consist of saturated gravel with pebbles in a sandy matrix; the latter can be prevalent in a lower resistivity area.
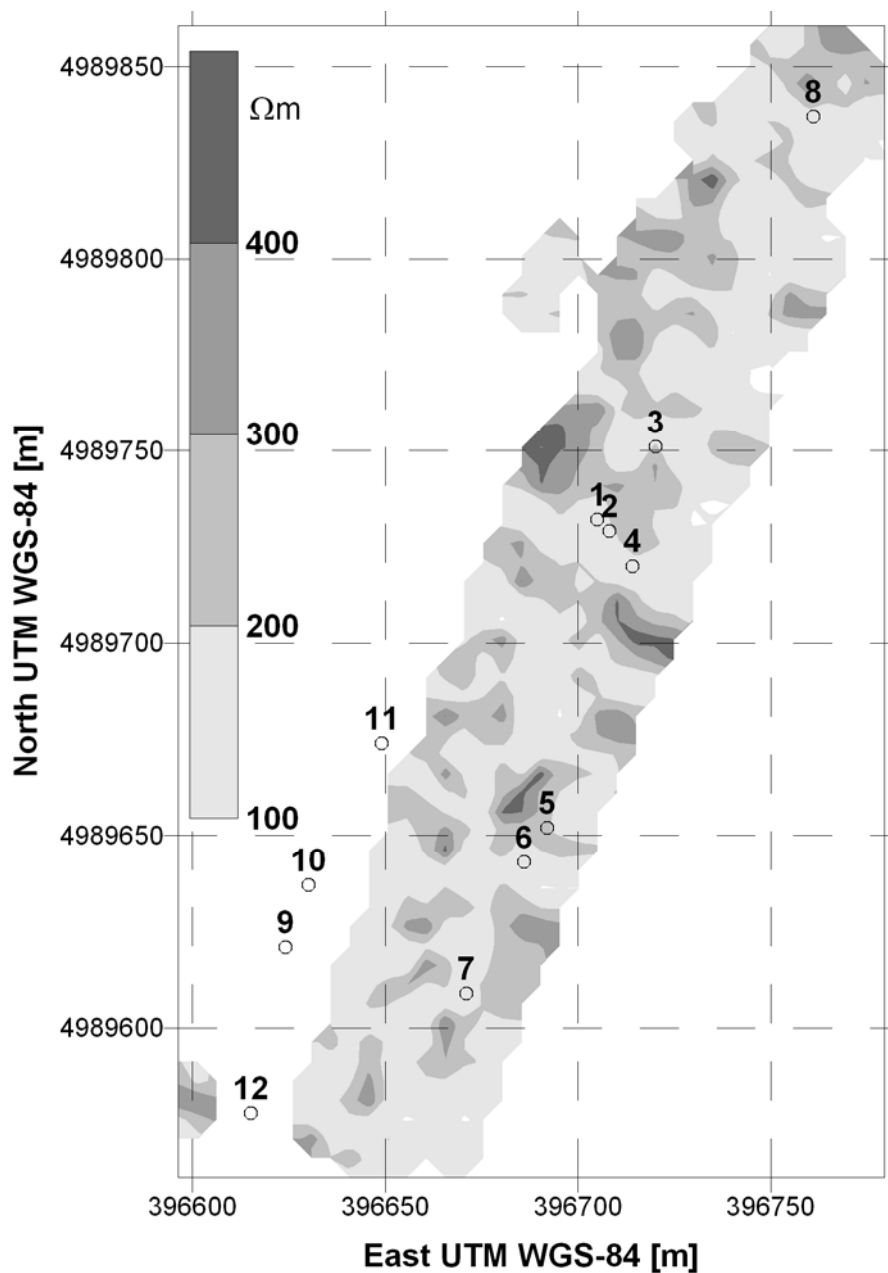

Figure 5.9: *Resistivity map at 3925 Hz, after bathymetry correction. The circles (1-12) refer to the river bottom sampling points. Only points with a water depth of less than 2.5 m were considered.*

As shown in Table 5.3, the top of the riverbed in the surveyed area consists of pebbles and coarse gravel alluviums in a sandy-silty matrix (Figure 5.10). From a careful observation of the samples, it emerges that the alluviums are usually covered by a thin blackish silt film (approximately 1-2 cm), which is rich in organic matter. In the presence of a thicker silt film, it would have been possible to sample a larger amount of sediment but, in our specific case, the grab bucket only managed to scrape off part of the pebbly bottom and pull out huge clasts, in such a way that the finer fraction was very likely to have been underestimated. It is also important to underline that the pebbles had an imbricate structure. This structure did not permit the grab bucket to penetrate, unless one of the two jaws managed to get underneath a pebble. Moreover, even when this happened, the jaws were not able to close completely; therefore the finer material was likely washed away.

Figure 5.10: *Example of coarse riverbed sampled material.*

Pebbly layers occur during floods, when the water speed is high enough to shift coarse clasts along a riverbed. After a flood, during a low water regime, it is possible to observe the deposit of fine suspended sediments in the areas of a river where there is a decrease in the flow-rate compared to the upstream flow-rate. Similar phenomena occur in natural river beds as hollows, meander scars connected to secondary branches or behind obstacles.

A comparison between the sampling description and the average sediment resistivity around the sampling points is shown in Table 5.3. The average resistivity values were obtained from the 3925 Hz map. We averaged the resistivities of the 8 points around the sampling points with the resistivity corresponding to the sampling points.

Table 5.3: *Riverbed sampling results at each point with the corresponding average resistivities. Each average resistivity was obtained from the 3925 Hz map by averaging the resistivity read at the coordinate of the sampling point with the resistivities of the 8 closest points.*

Sampling Points	East UTM-WGS84	North UTM-WGS84	Sample description	Max. clast diameter [cm]	Average resistivity [Ωm]
1	396705	4989732	4 coarse clasts with a small amount of sandy silt	6	180
2	396708	4989729	4 coarse clasts with a little amount of sandy silt	6	215
3	396720	4989751	3 coarse clasts in gravel matrix with silty sand	9	180
4	396714	4989720	1 coarse clast in silt and gravel matrix	7	175
5	396692	4989652	Silt with sandy gravel	<1	225
6	396686	4989643	3 coarse clasts with sandy-silty gravel	8	160
7	396671	4989609	1 coarse clast in sandy-gravelly silt	7	180
8	396761	4989837	2 coarse clasts with sandy-silty pit-run gravel	10	175
9	396624	4989621	1 coarse clast covered by silt	9	-
10	396630	4989637	2 coarse clasts with pit-run gravel (relatively abundant)	8	-
11	396649	4989674	Gravel with sand	<1	-
12	396615	4989578	2 coarse clasts in gravelly-silty sand matrix	6	-

5.6. Conclusions

The sampling of the riverbed sediment only partially confirmed the interpretation of the GEM-2 data filtered and corrected for the bathymetry. We found resistivity values that were compatible with the average results of the direct sampling and with the known geology, but some sampling results did not agree with the resistivity values obtained in the same point. These discrepancies could be due to the following factors: the difficulty in sampling a significant quantity of depositional material due to the heterogeneous and large dimension of the clasts in comparison to the bucket dimensions; a coarser boat location during the direct sampling due to the lower accuracy of the GPS system used in the direct sampling and to the drift of the boat.

The proposed method, however, if carefully planned and if the results are properly processed, seems to be an effective way of estimating river bed conductivity. We conducted a sensitivity analysis, as part of the data processing, to set reliability limits for our results, concerning the frequency, the resistivity range and the depth of investigation. We also proposed a simple method, with a criterion driven by the error accepted in the approximation, to set the upper limit of the low induction number condition. The analysis we carried out should, as far as possible, always be made when designing and processing surveys of this type, according to the adopted inter-coil distances and frequencies.

The EM modeling highlighted a low sensitivity of the method to the sediment resistivity, especially when this is greater than the water resistivity. This effect also prevented a clear correlation between direct sampling and sediment resistivity.

It could be of interest to test this technique in sites where it is possible to find also finer deposits, especially near a main inlet of an artificial or natural lake or where a horizontal variation of the river bed deposits occurs at a decameter scale.

Improvements could also be obtained moving the sensor away from the boat engine which could result in a better signal-to-noise ratio but also in a larger spread-out of the equipment and in a more difficult positioning.

The GPS measurements were very useful, as they assured smooth comparisons and overlaps between the GEM-2 and GPR responses, which was crucial to perform the bathymetric correction. Furthermore, the RTK mode made it possible to obtain knowledge on the coordinates with centimetric accuracy in real time, allowing the

location of punctual measurements, taken with the conductivity meter, near the tracks followed during the continuous measurements (GPR e GEM-2).

6. Conclusions

In this work, we dealt with applications of non-seismic methods in shallow water environments. In particular, we focused the first part of the thesis on the possibilities of ground penetrating radar to discriminate the bottom sediments. In the last part of the work, we dealt with multi-frequency electromagnetic measurements at low induction number conditions.

We start the analysis of the GPR possibilities by laboratory experimentations in controlled settings, described in detail in chapter 3. In this section, we show that we achieved good assessments of the sediments porosity by GPR techniques only with the interpretation of the velocity of the electromagnetic pulse in the sediments. At the same time, we highlighted the low reliability of the sediments porosity obtained with the amplitude analysis of the GPR response. We cannot explain beyond all understanding why the amplitude analysis provided low reliable responses in laboratory, but we explored a set of hypothesis. Firstly, we cannot rule out the influences of diffraction scattering from objects smaller that one quarter of the GPR dominant wavelength. Secondly, we highlight that the two methods probe different penetration depth. In particular the velocity analysis give back a mean response on the sediments layer thickness, instead the amplitude analysis investigate the top of the sediments in function of the frequency adopted. Consequently, in bottom sediments with vertical gradient of the grain size distribution the two methods could provide different responses. However, we were confident that both these effects should have remarkably lower influence in field conditions. In fact, to achieve sufficient penetration depth in the water, it should be used lower frequencies, which imply higher penetration depth in the sediments and diffraction scattering only from very coarse gravel. Moreover, for all the sediment investigated in this work, we found water-sediments reflection coefficients lower than the values expected for water-rock. Consequently, if the reliable discrimination between different sediments could be

problematic, on the other hand the distinction between sediments and rock bottom should be easily achievable.

The analysis of the bottom amplitude of reflection was taken back in account in the interpretation of an integrated geophysical survey performed on a stretch of river PO, described in chapter 4. In this survey contemporarily to the GPR measurements, we acquired low induction number electromagnetic multi-frequency measurements. We also made some punctual measurements of the water permittivity, conductivity and temperature and carried out a direct sampling survey. As far as the quantitative analysis of the bottom reflections is concerned, we first checked the constancy of the signal that entered the water, by checking the main bang repeatability. We then designed the data processing so that it did not significantly affect the frequency content of the signals and preserved the amplitude ratios among the different traces and profiles. The punctual permittivity and conductivity measurements allowed an estimation of the GPR pulse velocity, which we then used to obtain a bathymetry map. We also calculated the attenuation factor, using the Maxwell formulae applied to the punctual measurements. We used this value, which optimally matched the one estimated in our analysis of the GPR amplitudes, to correct the signal amplitudes and to obtain the map of the bottom amplitude of reflections. We did not find an optimal agreement between the GPR interpretation and the direct sampling. While the direct sampling suggests an overall homogeneity of the river bottom, the map of the bottom amplitude of reflections shows areas with different values. The difference could be due to scattering phenomena from pluricentimetric clasts and to the method adopted for the direct sampling. As far as the direct sampling is concerned, the Van Veen grab bucket did not provide detailed information on the sediments and a different sampling method should be recommended for geological settings similar to this stretch of the Po river. In fact, we encountered difficulties in sampling a significant quantity of depositional material due to the heterogeneous and large dimension of the clasts in comparison to the bucket dimensions. Moreover in the direct sampling, we obtained a coarser boat location due to the lower accuracy of the GPS system used and the drift of the boat. With respect to the field settings, the acquisition with the antenna placed on the flat bottom of a fiberglass boat was a good compromise between the quality of the signal and an easy logistic configuration. However, in our opinion, the best solution is an on purpose designed antenna with the dipole

submerged in water in order to avoid power losses in the air and to limit the coupling effect between air and water.

In chapter 5, we dealt with the interpretation of the electromagnetic multi-frequency measurements at low induction number, performed in the integrated geophysical survey on the river PO. The sampling of the riverbed sediment only partially confirmed the interpretation of these data filtered and corrected for the bathymetry. We found resistivity values that were compatible with the average results of the direct sampling and with the known geology, but some sampling results did not agree with the resistivity values obtained in the same point. These discrepancies could be due to the method adopted for the direct sampling. However, the proposed analysis is particularly interesting and innovative, and if carefully planned seems to be an effective way of estimating riverbed conductivities. We conducted a sensitivity analysis, as part of the data processing, to set reliability limits for our results, concerning the frequency, the resistivity range and the depth of investigation. We also proposed a simple method to set the upper limit of the low induction number condition. The electromagnetic modeling highlighted a low sensitivity of the method to the sediment resistivity, especially when this is greater than the water resistivity.

The GPS measurements were very useful, as they assured smooth comparisons and overlaps between the GEM-2 and GPR responses, which were crucial to perform the bathymetric correction. Furthermore, the RTK mode made it possible to obtain knowledge on the coordinates with centimetric accuracy in real time, allowing the location of punctual measurements, taken with the conductivity meter, near the tracks followed during the continuous measurements (GPR e GEM-2).

It could be of interest to test this technique in sites where it is possible to find also finer deposits, especially near a main inlet of an artificial or natural lake or where a horizontal variation of the riverbed deposits occurs at a decameter scale. Improvements could also be obtained moving the sensor away from the boat engine which could result in a better signal-to-noise ratio but also in a larger spread-out of the equipment and in a more difficult positioning.

According to us, the optimum arrangement for a non-seismic river survey could be a multi-sensored boat RTK-tracked with a GPR, a low frequency conductivity meter, a ERT equipment with floating electrodes and a device for the continuous acquisition of the water permittivity, conductivity and temperature.

References

A-Cubed (1983). General State of the Art Review of Ground Probing Radar. Mississauga, Ontario.

Abramov, A.P., A.G. Vasiliev, V.V. Kopeikin and P.A. Morozov (2004). Underwater Ground Penetrating Radar in Archeological Investigation below Sea Bottom. GPR 2004 - 10th International Conference on Ground Penetrating Radar, Delft, The Netherlands.

Alharthi, A. and J. Lange (1987). "Soil Water Saturation: Dielectric Determination." Water Resour. Res. 23.

Allen, D. and T. Dahlin (2007). EC Imaging of acquifers beneath watercourses of the Murray Darling Basin, Australia. High Resolution Geophysics for Shallow Water in 69th EAGE Conference & Exhibition.

Allen, J.B. and L.R. Rabiner (1977). " A unified approach to short-time Fourier analysis and synthesis." Proceedings of the IEEE 65(11): 1558-1564.

Anderson, W.L. (1979). "Numerical integration of related Hankel transforms of orders 0 and 1 by adaptive digital filtering." Geophysics 44(7): 1287-1305.

Annan, A.P. (2001). Ground Penetrating Radar Workshop Notes. S. S. Inc.

Annan, A.P. and J.L. Davis (1977). Impulse Radar Applied To Ice Thickness Measurements and Freshwater Bathymetry. Geological Survey of Canada, Geological Survey of Canada: 63-65.

Annan, A.P., J.L. Davis and D. Gendzwill (1988). "Radar sounding in potash mines, Saskatchewan, Canada." Geophysics 53(12): 1556-1564.

Arcone, S.A., E.F.J. Chacho and A.J. Delaney (1992). "Short-Pulse Radar Detection of Groundwater in the Sagavanirktok River Floodplain in Early Spring." WATER RESOURCES RESEARCH 28(11): 2925-2936.

Arcone, S.A., D. Finnegan and J.E. Laatsch (2006). Bathymetric and Subbottom Surveying in Shallow and Conductive Water. GPR 2006 - 11th International Conference on Ground Penetrating Radar, Columbus Ohio, USA.

Balanis, C.A. (1989). Advanced engineering electromagnetics. New York, Wiley.

Barrett, B., G. Heinson, M. Hatch and A. Telfer (2005). "River sediment salt-load detection using a water-borne transient electromagnetic system." Journal of Applied Geophysics 58(1): 29-44.

Beres, M.J. and F.P. Haeni (1991). "Application of Ground-Penetrating-Radar Methods in Hydrogeologic Studies." Ground Water 29(3): 375-386.

Beres, M.J. and F.P. Haeni (1991). "Application of Ground-Penetrating-Radar Methods in Hydrogeologie Studies." Ground Water 29(3): 375-386.

Best, H., J.P. McNamara and L. Liberty (2005). "Association of Ice and River Channel Morphology Determined Using Ground-penetrating Radar in the Kuparuk River, Alaska." Arctic, Antarctic, and Alpine Research 37(2): 157-162.

Birchak, J.R., C.G. Gardner, J.E. Hipp and J.M. Victor (1974). High dielectric constant microwave probes for sensing soil moisture. Proceedings of the Institute of Electrical and Electronics Engineers.

Bradford, J.H. (2007). Advanced processing and acquisition methods to image within and beneath shallow water bodies with ground-penetrating-radar. High Resolution Geophysics for Shallow Water in 69th EAGE Conference & Exhibition, London.

Bradford, J.H., J.P. McNamara , W. Bowden and M.N. Gooseff (2005). "Measuring thaw depth beneath peat-lined arctic streams using ground-penetrating radar." Hydrological Processes 19(14): 2689-2699.

Brown, W.E. (1972). "Lunar subsurface exploration with coherent radar." Earth, Moon, and Planets 4(1): 113-127.

Bruggeman, D. (1935). "Berechnung verschiedener physikalischer konstanten von heterogenen substanzen." Annalen Der Physik 24: 636-664.

Butler, k.E. (2004). "Delineating recharge to a river valley aquifer by riverine seismic and EM methods." ournal of Environmental & Engineering Geophysics 9: 95-109.

Butler, K.E. (2007). Trends in waterborne electrical and EM induction methods for high resolution sub-bottom imaging. High Resolution Geophysics for Shallow Water in 69th EAGE Conference & Exhibition, London.

Buynevich, I.V. and D.M. Fitzgerald (2003). "High-Resolution Subsurface (GPR) Imaging and Sedimentology of Coastal Ponds, Maine, U.S.A.: Implications for Holocene Back-Barrier Evolution." Journal of Sedimentary Research 73(4): 559-571.

Casanova Alig, R. (2003). Electrostatics. Encyclopedia of Applied Physics. New York, Wiley.

Cheng, R.T., J.W. Gartner, R.R.J. Mason, J.E. Costa, W.J. Plant, K.R. Spicer, F.P. Haeni, N.B. Melcher, W.C. Keller and K. Hayes (2004). Evaluating a Radar-Based, Non Contact Streamflow Measurement System in the San Joaquin River at Vernalis, California. USGS Water-Resources Investigations Report. Menlo Park, California, U.S.G.S.

Cook, J.C. (1960). "Proposed monocycle-pulse VHF radar for airborne ice and snow measurement." Commun. Electr. 51: 588–594.

Cook, J.C. (1974). Status of Ground-Probing Radar and Some Recent Experience. Subsurface Exploration for Underground Excavation and Heavy Construction, American Society of Civil Engineers, Henneker.

Cook, J.C. (1975). "Radar Transparencies Of Mine And Tunnel Rocks." Geophysics 40(5): 865-885.

Costa, J.E., R.T. Cheng, F.P. Haeni, N.B. Melcher, K.R. Spicer, E. Hayes, K. Hayes, W.J. Plant, C. Teague and D. Barrick (2006). "Use of radars to monitor stream discharge by noncontact methods." WATER RESOURCES RESEARCH 42: W07422.

Costa, J.E., K.R. Spicer, R.T. Cheng, F.P. Haeni, N.B. Melcher, E.M. Thurman, W.J. Plant and W.C. Keller (2000). "Measuring Stream Discharge by Non-Contact Methods: A Proof-of-Concept Experiment." Geophysical Research Letters 27(4): 553-556.

Daniels, D.J. (1996). "Surface-penetrating radar." Electronics & Communication Engineering Journal 8(4): 165-182.

Daniels, D.J. (2004). Ground Penetrating Radar (2nd Edition). London, United Kingdom, The Institution of Electrical Engineer.

Daniels, D.J., D.J. Gunton and H.F. Scott (1988). "Introduction to subsurface radar." Radar and Signal Processing, IEE Proceedings F 135(4): 278-320.

Davidson, N.C., M.S.A. Hardy and M.C. Forde (1995). Bridge scour assessment by impulse radar. Radar and Microwave Techniques for Non-Destructive Evalution, IEE Colloquium on, London.

Davis, J.L. and A.P. Annan (1989). "Ground-Penetrating Radar for High-Resolution Mapping of Soil and Rock Stratigraphy." Geophysical Prospecting 37(5): 532-551.

Delaney, A.J., P.V. Sellmann and S.A. Arcone (1992). Sub-bootm Profiling: A comparison of short-pulse radar and acoustic data. Fourth International Conference on Ground Penetrating Radar, Rovaniemi, Finland.

Dobson, M.C., F.T. Ulaby, M.T. Hallikainen and M.A. El-Rayes (1985). "Microwave Dielectric Behavior of Wet Soil-Part II: Dielectric Mixing Models." Geoscience and Remote Sensing, IEEE Transactions on GE-23(1): 35-46.

Dudley, R.W. and S.E. Giffen (1999). Composition and Distribution of Streambed Sediments in the Penobscot River, Maine. USGS Water-Resources Investigations Report. Augusta, Maine, U.S.G.S.

Ellison, W.J., K. Lamkaouchi and J.M. Moreau (1996). "Water: a dielectric reference." Journal of Molecular Liquids 68(2-3): 171-279.

Evans, J.V. (1969). "Radar Studies of Planetary Surfaces." Annual Review of Astronomy and Astrophysics 7(1): 201-248.

Evans, R.L. (2007). "Using CSEM techniques to map the shallow section of seafloor: From the coastline to the edges of the continental slope." Geophysics 72(2): WA105-WA116.

Evans, S. (1963). "Radio techniques for the measurement of ice thickness." Polar Record 11: 406-410.

Evans, S. (1965). "Dielectric properties of ice and snow — a review." Journal of Glaciology 5(42): 773-792.

Fuchs, M., M.J. Beres and F.S. Anselmetti (2004). Combining high-resolution reflection seismic and amphibious GPR methods in lacustrine sedimentology. 12th Mtg. Swiss Sedimentologists, Fribourg, Switzerland.

Gary, B.L. and S.J. Keihm (1978). Interpretation of groundbased microwave measurements of the moon using a detailed regolith properties model. 9th Lunar and Planetary Science Conference, Houston.

Geophysical Survey Systems Inc (1996). Sir® System-2 Operation Manual. North Salem, New Hampshire.

Gloaguen, E., M. Chouteau, D. Marcotte and R. Chapuis (2001). "Estimation of hydraulic conductivity of an unconfined aquifer using cokriging of GPR and hydrostratigraphic data." Journal of Applied Geophysics 47(2): 135-152.

Goldman, M., H. Gvirtzman and S. Hurwitzc (2004). "Mapping saline groundwater beneath the Sea of Galilee and its vicinity using time domain electromagnetic (TDEM) geophysical technique." Israel Journal of Earth Sciences 53(3-4): 187-197.

Greenwood, W.J. and S.K.P. Swarzenski (2006). "Extending Electromagnetic Methods to Map Coastal Pore Water Salinities." Ground Water 44(2): 292-299.

Haeni, F.P., M.L. Buursink, J.E. Costa, N.B. Melcher, R.T. Cheng and W.J. Plant (2000). Ground-Penetrating RADAR Methods Used in Surface-Water Discharge Measurements. GPR 2000 - 8th international conference on Ground penetrating radar, University of Queensland.

Hagfors, T. and D.B. Campbell (1973). "Mapping of planetary surfaces by radar." Proceedings of the IEEE 61(9): 1219-1225.

Hanai, T. (1961). "Dielectric theory on the interfacial polarization for two-phase mixtures." Bull. Inst. Chem. Res. 39: 341–367.

Hu, K. and C.R. Liu (2000). "Theoretical study of the dielectric constant in porous sandstonesaturated with hydrocarbon and water." Geoscience and Remote Sensing, IEEE Transactions on 38(3): 1328-1336.

Huang, H. (2005). "Depth of investigation for small broadband electromagnetic sensors." Geophysics 70(6): G135-G142.

Huang, H. and I.J. Won (2003). "Real-time resistivity sounding using a hand-held broadband electromagnetic sensor." Geophysics 68(4): 1224-1231.

Huebner, C., S. Schlaeger, R. Becker, A. Scheuermann, A. Brandelik, W. Schaedel and R. Schuhmann (2005). Advanced Measurement Methods in Time Domain Reflectometry for Soil Moisture Determination. Electromagnetic Aquametry: 317-347.

Huisman, J.A., S.S. Hubbard, J.D. Redman and A.P. Annan (2003). "Measuring Soil Water Content with Ground Penetrating Radar: A Review." Vadose Zone Journal 2(4): 476-491.

Hulsenbeck (1926). Verfahren zur elektrischen Bodenforschung.

Hunter, L.E., M.G. Ferrick and C.M. Collins (2003). "Monitoring sediment infilling at the Ship Creek Reservoir, Fort Richardson, Alaska, using GPR." Geological Society, London, Special Publications 211(1): 199-206.

Jackson, J.D. (2003). Electrodynamics, Classical Encyclopedia of Applied Physics. New York, Wiley.

Jol, H.M. and A. Albrecht (2004). Searching for submerged lumber with ground penetrating radar: Rib Lake, Wisconsin, USA. GPR 2004 - 10th International Conference on Ground Penetrating Radar, Delft, The Netherlands.

Kadaba, P.K. (1976). Penetration of 0.1 GHz to 1.5 GHz electromagnetic waves into the earth surface for remote sensing applications. IEEE S.E. REGION 3.

Keller, G.V. (1989). Electrical properties. Practical Handbook of Physical Properties of Rocks and Minerals, CRC-Press.

Kingsley, S. and S. Quegan (1992). Understanding Radar Systems. London, McGraw Hill.

Knight, R. (2001). "Ground Penetrating Radar for environmental applications." Annual Review of Earth and Planetary Sciences 29(1): 229-255.

Knight, R. and A. Abad (1995). "Rock/water interaction in dielectric properties: Experiments with hydrophobic sandstones." Geophysics 60(2): 431-436.

Knight, R. and A. Endres (1990). "A new concept in modeling the dielectric response of sandstones: Defining a wetted rock and bulk water system." Geophysics 55(5): 586-594.

Knoll, M.D. (1996). A petrophysical basis for ground-penetrating radar and very early time electromagnetics, electrical properties of sand-clay mixtures. Vancouver, University of British Columbia. PhD: 316.

Kovacs, A. (1978). "Remote detection of water under ice-covered lakes on the North Slope of Alaska." Arctic 31(4): 448-458.

Lambot, S., E.C. Slob, I. van den Bosch, B.A.S.B. Stockbroeckx and M.A.V.M. Vanclooster (2004). "Modeling of ground-penetrating Radar for accurate

characterization of subsurface electric properties." Geoscience and Remote Sensing, IEEE Transactions on 42(11): 2555-2568.

Lange, J.N. (1983). "Microwave properties of saturated reservoirs." Geophysics 48(3): 367-375.

Lichtenecker, K. and K. Rother (1931). "Die Herleitung des logarithmischen Mischungsgesetz es aus allgemeinen Prinzipien der stationären Strömung:." Physikalische Zeitschrift 32: 255-260.

Losito, G., P.L. Aminiti, L. Martelletti, J.M. Grandjean, A. Mazzetti and G. Benvenuti (2007). Marine geoelectrical prospecting for soft structures characterization in shallow water: field and laboratory test. High Resolution Geophysics for Shallow Water in 69th EAGE Conference & Exhibition, London.

Lucius, J.E., G.R. Olhoeft, P.L. Hill and S.K. Duke (1990). Properties and hazards of 108 selected substances. Denver, Colorado.

Malberg, C.G. and A.A. Maryott (1956). "Dieletric constant of water from 0°C to 100°C." Journal of Research of the National Bureau of Standards: 1-8.

Mansoor, N., L. Slater, F. Artigas and E. Auken (2006). "High-resolution geophysical characterization of shallow-water wetlands." Geophysics 71(4): B101-B109.

Martinez, A.D. and A.P. Byrnes (2001). "Modeling dielectric constant values of geologic materials: an aid to ground-penetrating radar data collection and interpretation." Current Research in Earth Sciences.

Maxwell, J.C. (1861). "On Physical Lines of Force." The London, Edinburgh, and Dublin Philosophical Magazine and Journal of Science 1,2: 161-75; 281-91; 338-48.

Maxwell, J.C. (1873). Treatise on Electricity and Magnetism. Oxford.

McNeill, J.D. (1980). Electromagnetic terrain conductivity measurement at low induction numbers. G. L. T. N. TN-6.

Melcher, N.B., J.E. Costa, F.P. Haeni, R.T. Cheng, E.M. Thurman, M. Buursink, K.R. Spicer, E. Hayes, W.J. Plant, W.C. Keller and K. Hayes (2002). "River discharge measurements by using helicopter-mounted radar." Geophysical Research Letters 29(22).

Mellett, J.S. (1995). "Profiling of ponds and bogs using ground-penetrating radar." Journal of Paleolimnology 14(3): 233-240.

Meyers, R.A. and D.G. Smith (1998). Development of an Underwater Ground Penetrating Radar system. GPR 1998 - 7th International Conference on Ground Penetrating Radar, Lawrence, Kansas, USA.

Moorman, B.J., W.M. Last and J.P. Smol (2001). Ground-penetrating radar applications in paleolimnology. Tracking Environmental Change Using Lake Sediments: Physical and Chemical Techniques. Boston, Kluwer Academic Publishers. 2: 23-47.

Moorman, B.J. and F.A. Michel (1997). "Bathymetric mapping and sub-bottom profiling through lake ice with ground-penetrating radar." Journal of Paleolimnology 18(1): 61-73.

Morey, R.M. (1974). Continuous Subsurface Profiling by Impulse Radar. Subsurface Exploration for Underground Excavation and Heavy Construction, American Society of Civil Engineers, Henneker.

Olhoeft, G.R. (1989). Electrical properties of rocks. Physical Properties of Rocks and Minerals. New York, McGraw-Hill.

Olhoeft, G.R. and D.W. Strangway (1975). "Dielectric properties of the first 100 meters of the moon." Earth and Planetary Science Letters 24: 394404.

Olimpio, J.R. (2000). Use of a Ground-Penetrating Radar System to Detect Pre- and Post-Flood Scour at Selected Bridge Sites in New Hampshire, 1996-98. USGS Water-Resources Investigations Report.

Orlando, L. and L. Tramonti (2007). Water bottom electrical tomography in the river tiber. High Resolution Geophysics for Shallow Water in 69th EAGE Conference & Exhibition, London.

Ostro, S.J. (1993). "Planetary radar astronomy." Reviews of Modern Physics 65(4): 1235.

Paine, J.G., H.S. Nance, E.W. Collins and K.L. Niemann (2007). "Quantifying contributions to stream salinity using electromagnetic induction and hydrochemistry in a small Texas coastal-plain basin." Applied Geochemistry 22(10): 2207-2224.

Paris, D.T. and F.K. Hurd (1969). Basic Electromagnetic Theory New York, McGraw Hill.

Park, I., J. Lee and W. Cho (2004). Assessment of Bridge Scour and Riverbed variation by a Ground Penetrating Radar. GPR 2004 - 10th International Conference on Ground Penetrating Radar, Delft, The Netherlands.

Peeples, W.J., W.R. Sill, T.W. May, S.H. Ward, R.J. Phillips, R.L. Jordan, E.A. Abbott and T.J. Killpack (1978). "Orbital Radar Evidence for Lunar Subsurface Layering in Maria Serenitatis and Crisium." JOURNAL OF GEOPHYSICAL RESEARCH 83(B7): 3459-3468.

Pettengill, G.H. (1978). "Physical Properties of the Planets and Satellites from Radar Observations." Annual Review of Astronomy and Astrophysics 16(1): 265-292.

Placzek, G. and F.P. Haeni (1995). Surface-geophysical techniques used to detect existing and infilled scour holes near bridge piers. USGS Water-Resources Investigations Report, USGS

Porcello, L.J., R.L. Jordan, J.S. Zelenka, G.F. Adams, R.J. Phillips, W.E. Brown, Jr., S.H. Ward and P.L. Jackson (1974). "The Apollo lunar sounder radar system." Proceedings of the IEEE 62(6): 769-783.

Porsani, J.L., L. Moutinho and M.L. Assine (2004). GPR Survey in the Taquari River, Pantanal Wetland, West-Central Brazil. GPR 2004 - 10th International Conference on Ground Penetrating Radar, Delft, The Netherlands.

Powers, C.J., F.P. Haeni and S. Spence (1999). Integrated Use of Continuos Seismic-Reflection Profiling and Ground-Penetrating Radar Methods at Jhon's Pond, Cape Cod, Massachutes. SAGEEP 1999 - Symposium on the Application of Geophysics to Environmental and Engineering Problems, Oakland, California.

Powers, M.H. (1997). "Modeling frequency-dependent GPR." The Leading Edge 16(11): 1657-1662.

Powers, M.H. (2004). Migration of Dispersive GPR Data. GPR 2004 - 10th International Conference on Ground Penetrating Radar, Delft, The Netherlands.

Ramsey, M. (2005). "Schlumberg Oilfield Glossary." from http://www.glossary.oilfield.slb.com.

Reynolds, J.M. (1997). An Introduction to Applied and Environmental Geophysics.

Roe, K.C. and D.A. Ellerbruch (1979). Development and testing of a microwave system to measure coal layer thickness up to 25 cm: Pages: 27.

Roth, K., R. Schulin, H. Flühler and W. Attinger (1990). "Calibration of Time Domain Reflectometry for Water Content Measurement Using a Composite Dielectric Approach." Water Resour. Res. 26.

Sambuelli, L. (2009). Uncertainty propagation using some common mixing rules for the modelling and interpratation of electromagnetic data.

Sambuelli, L., S. Leggieri, C. Calzoni and C. Porporato (2007). "Study of riverine deposits using electromagnetic methods at a low induction number." Geophysics 72(5): B113-B120.

Santamarina, J.C. (2001). Soils and Waves. Chichester, England, John Wiley & Sons Ltd.

Schwamborn, G.J., J.K. Dix, J.M. Bull and V. Rachold (2002). "High-resolution seismic and ground penetrating radar-geophysical profiling of a thermokarst lake in the western Lena Delta, Northern Siberia." Permafrost and Periglacial Processes 13(4): 259-269.

Scott, W.J. and F.K. Maxwell (1989). "Marine resistivity survey for granular materials, Beaufort Sea." Canadian Journal of Exploration Geophysics 25: 104-114.

Sellmann, P.V., A.J. Delaney and S.A. Arcone (1992). Sub-bottom surveying in lakes with ground penetrating radar U.S. Army Cold Regions Research and Engineering Laboratory. Hannover, Nwe Hampshire, U.S. Army Cold Regions Research and Engineering Laboratory.

Sen, P.N., C. Scala and M.H. Cohen (1981). "A self-similar model for sedimentary rocks with application to the dielectric constant of fused glass beads." Geophysics 46(5): 781-795.

Shields, G., S. Grossman, M. Lockheed and A. Humphrey (2004). Waterborne Geophysical Surveys on Shallow River Impoundments. SAGEEP 2004 - Symposium on the Application of Geophysics to Environmental and Engineering Problems, Denver, USA.

Sihvola, A.H. and E. Alanen (1991). "Studies of mixing formulae in the complex plane." Geoscience and Remote Sensing, IEEE Transactions on 29(4): 679-687.

Simmons, G., D. Strangway, A.P. Annan, R. Baker, L. Bannister, R. Brown, W. Cooper, D. Cubley, J. Debettencourt, A.W. England, J.K. Groener, G. Jin-Au; Latorraca, J. Meyer, V. Nanda, D. Redman, J. Rossiter, L. Tsang, J. Urner and

R. Watts (1973). Surface Electrical Properties Experiment. A. P. S. R. N. SP-330. Washington, D.C., NASA.

Skolnik, M.I. (1981). Introduction to Radar Systems. Singapore, McGraw Hill Book Company.

Skolnik, M.I. (1990). An Introduction to Impulse Radar. N. M. report. Washington, Naval Research Laboratory.

Skolnik, M.I. (1990). Radar Handbook, Mc Graw Hill.

Smith, J.O. (2007). Mathematics of the Discrete Fourier Transform (DFT) with Audio Applications, Second Edition,. Stanford, BookSurge Publishing.

Smith, S.G. (1997). An introduction to Classical Electromagnetic Radiation. Cambridge, Press Syndacate of the University of Cambridge.

Sneddon, K.W., M.H. Powers, H. Raymond, R.H. Johnson and E.P. Poeter (2002). Modeling Gpr Data to Interpret Porosity and DNAPL Saturations for Calibration of a 3-D Multiphase Flow Simulation. Open-File Report 02-451, USGS

Steenson, B.O. (1951). Radar methods for the exploration of glaciers. Pasadena, California, California Institute of Technology. Ph.D. Thesis.

Swithinbank, C. (1968). "Radio Echo Sounding Of Antarctic Glaciers From Light Aircraft." Association of Scientific Hydrology 79.

Telford, W.M., L.P. Geldart and R.E. Sheriff (1990). Applied Geophysics, 2nd edn. Cambridge (UK), Cambridge University Press.

Thompson, T.W. (1979). "A review of earth-based radar mapping of the moon." Earth, Moon, and Planets 20(2): 179-198.

Topp, G.C., J.L. Davis and A.P. Annan (1980). "Electromagnetic Determination of Soil Water Content: Measurements in Coaxial Transmission Lines." Water Resour. Res. 16.

Tóth, T. (2004). "High resolution geophysics provides optimal results on inland waterways." First Break 22: 45-51.

Ulaby, F.T., R.K. Moore and A.K. Fung (1986). Microwave Remote Sensing: Active and Passive, from Theory to Applications Dedham, Massachusetts, Artech House Publishers.

Ulriksen, C.P.F. (1982). Application of impulse radar to civil engineering. Department of Enineering Geology. Lund, Sweden, Lund University of Technology. Ph.D. Thesis.

Unterberger, R.R. (1978). "Radar Propagation in Rock Salt." Geophysical Prospecting 26(2): 312-328.

Wang, J.R. (1980). "The dielectric properties of soil-water mixtures at microwave frequencies." Radio Sci. 15.

Wang, J.R. and T.J. Schmugge (1980). "An Empirical Model for the Complex Dielectric Permittivity of Soils as a Function of Water Content." Geoscience and Remote Sensing, IEEE Transactions on GE-18(4): 288-295.

Webb, D.J., N.L. Anderson, T. Newton and S. Cardimona (2000). BRIDGE SCOUR: APPLICATION OF GROUND PENETRATING RADAR. Federal Highway Administration and Missouri Department of Transportation special publication, Federal Highway Administration and Missouri Department of Transportation.

Wharton, R.P., G.A. Hazen, R.N. Rau and D.L. Best (1980). Electromagnetic propagation logging - Advances in technique and interpretation:. 55th Annual Technical Conference, Society of Petroleum Engineers of AIME.

Won, I.J., D. Keiswetter, G. Fields and L. Sutton (1996). "GEM-2: A new multifrequency electromagnetic sensor." Journal of Environmental & Engineering Geophysics 1: 129–137.

Wynn, J.C. (1988). "Titanium geophysics: The application of induced polarization to sea-floor mineral exploration." Geophysics 53(3): 386-401.

Xiong, Z. and A.C. Tripp (1997). "Ground-penetrating radar responses of dispersive models." Geophysics 62(4): 1127-1131.

Acknowledgments

Research Laboratory. In particular, I warmly thank Nicolas Espinoza and Douglas D. Cortés, which friendship enriched my experiences at Georgia Tech.

I also warmly thank all my friends. The writing of a dissertation can be a lonely and isolating experience, yet it is obviously not possible without the personal and practical support of friends. Moreover, my sincere gratitude goes to some of them, who remained stood by me in the worst moment and helped me to keep my foot firmly on the ground. Special thanks are due to Maria José for her constant encouragement and support. Finally, many thanks also go to my family, for always granting me enthusiastic and unconditional support.

It is difficult to include in some sentences all the people who give me help in these years. So, please accept my apologize if your name is not listed here.